Optimization-Based Guidance For Satellite Relative Motion

Andrew Charles Rogers

Dissertation submitted to the Faculty of the
Virginia Polytechnic Institute and State University
in partial fulfillment of the requirements for the degree of

Doctor of Philosophy
in
Aerospace Engineering

Craig A. Woolsey, Chair
Robert W. McGwier, Co-Chair
Jonathan T. Black
Gregory D. Earle
Shane D. Ross

April 4, 2016
Blacksburg, Virginia

Keywords: Model Predictive Control, Optimal Control
Astrodynamics, Optimization, Spacecraft Control

Optimization-Based Guidance For Satellite Relative Motion

Andrew C. Rogers

(ABSTRACT)

Spacecraft relative motion modeling and control promises to enable or augment a wide range of missions for scientific research, military applications, and space situational awareness. This dissertation focuses on the development of novel, optimization-based, control design for some representative relative-motion-enabled missions. Spacecraft relative motion refers to two (or more) satellites in nearly identical orbits. We examine control design for relative configurations on the scale of meters (for the purposes of proximity operations) as well as on the scale of tens of kilometers (representative of science gathering missions). Realistic control design for satellites is limited by accurate modeling of the relative orbital perturbations as well as the highly constrained nature of most space systems. We present solutions to several types of optimal orbital maneuvers using a variety of different, realistic assumptions based on the maneuver objectives.

Initially, we assume a perfectly circular orbit with a perfectly spherical Earth and analytically solve the under-actuated, minimum-energy, optimal transfer using techniques from optimal control and linear operator theory. The resulting open-loop control law is guaranteed to be a global optimum. Then, recognizing that very few, if any, orbits are truly circular, the optimal transfer problem is generalized to the elliptical linear and nonlinear systems which describe the relative motion. Solution of the minimum energy transfer for both the linear and nonlinear systems reveals that the resulting trajectories are nearly identical, implying that the nonlinearity has little effect on the relative motion. A continuous-time, nonlinear, sliding mode controller which tracks the linear trajectory in the presence of a higher fidelity orbit model shows that the closed-loop system is both asymptotically stable and robust to disturbances and un-modeled dynamics.

Next, a novel method of computing discrete-time, multi-revolution, finite-thrust, fuel-optimal, relative orbit transfers near an elliptical, perturbed orbit is presented. The optimal control problem is based on the classical, continuous-time, fuel-optimization problem from calculus of variations, and we present the discrete-time analogue of this problem using a transcription-based method. The resulting linear program guarantees a global optimum in terms of fuel consumption, and we validate the results using classical impulsive orbit transfer theory. The new method is shown to converge to classical impulsive orbit transfer theory in the limit that the duration of the zero-order hold discretization approaches zero and the time horizon extends to infinity. Then the fuel/time optimal control problem is solved using a hybrid approach which uses a linear program to solve the fuel optimization, and a genetic algorithm to find the minimizing time-of-flight. The method developed in this work allows mission planners to determine the feasibility for realistic spacecraft and motion models.

Proximity operations for robotic inspection have the potential to aid manned and unmanned systems in space situational awareness and contingency planning in the event of emergency.

A potential limiting factor is the large number of constraints imposed on the inspector vehicle due to collision avoidance constraints and limited power and computational resources. We examine this problem and present a solution to the coupled orbit and attitude control problem using model predictive control. This control technique allows state and control constraints to be encoded as a mathematical program which is solved on-line. We present a new thruster constraint which models the minimum-impulse bit as a semi-continuous variable, resulting in a mixed-integer program. The new model, while computationally more expensive, is shown to be more fuel-efficient than a sub-optimal approximation. The result is a fuel efficient, trajectory tracking, model predictive controller with a linear-quadratic attitude regulator which tracks along a pre-computed "safe" trajectory in the presence of un-modeled dynamics on a higher fidelity orbital and attitude model.

This research was supported by the Ted and Karyn Hume Center for National Security and Technology, the Virginia Space Grant Consortium Graduate Fellowship, and the Association of Old Crows Electronic Warfare Scholarship

What you need, above all else, is a love for your subject, whatever it is. You've got to be so deeply in love with your subject that when curve balls are thrown, when hurdles are put in place, you've got the energy to overcome them.

- Neil deGrasse Tyson

Acknowledgments

I have been very fortunate to have the opportunity to learn from some of the best control and space systems engineers in the world. First, I thank my committee chair Dr. Craig Woolsey for the tremendous help he has provided me over the past few years as I learn to conduct quality research and tackle difficult problems. In addition to being an excellent lecturer, he is also an outstanding mentor who sets a high standard for professionalism and academic excellence. It's safe to argue that the bulk of my knowledge of control systems has come from our numerous enjoyable discussions.

Had it not been for my co-chair Dr. Bob McGwier taking a chance on me when I was little more than an unproven asset that liked satellites, I almost surely would not be where I am today. Working for Bob at the Hume Center has provided me with more interesting and challenging projects than I can count, and exposed me to areas of the Intelligence community that I would never have gotten to experience had it not been for his support.

I have also been fortunate to work very closely with Dr. Jonathan Black, whose enthusiasm and energy for his work is nothing if not infectious. I am very grateful for the countless brainstorming sessions and sanity checks that his experience with space systems engineering has provided me.

I owe Dr. Shane Ross a debt of gratitude for his patience and time as I learned mechanics from him. The three semesters that I had him for the ESM dynamics classes were very beneficial for my understanding of analytical dynamics, and without that background, I would not have enjoyed control theory as much as I do.

I also thank Dr. Greg Earle for his insight during our discussions over "real" satellite systems. His experience in launching and operating satellites provided a valuable sounding board as I tried to incorporate more realism into my research.

My background in dynamics and control has benefited greatly from the wide variety of classes I took, and I thank Dr. Cornel Sultan, Dr. Mazen Farhood, Dr. William Baumann, Dr. Mayuresh Patil, Dr. Chris Hall, Dr. Jeff Borggaard, Dr. Andrew Kurdila, Dr. Scott Hendricks, Dr. Jeff Bolton, Dr. Roger Chang, Dr. Scott Bailey, and Dr. Josh Ellis for sharing their enthusiasm for their subject matter with me. I would like to thank Dr. Troy Henderson for helping me get established in graduate school, putting me in touch with the

Hume Center, and teaching a very enjoyable orbital mechanics course. In addition to the professors at Virginia Tech, I also was fortunate to discuss astrodynamics and control with professors at other institutions. Thank you to Terry Alfriend (Texas A&M) and Andrew Sinclair (Auburn) for our helpful discussions about formation flying.

I am tremendously grateful for the financial support of the Hume Center. The exposure to the numerous unique projects I worked on has been invaluable and eye-opening. I greatly appreciate the encouragement, advice, friendship, and silly discussions with Dr. Charles Clancy, Dr. Joey Ernst, Dr. Chris Headley, Dr. Alan Michaels, Dr. Harold Trease, Mark Goodwin, Sonya Rowe, Thaddeus Koehn, Joe Ziegler, Alex Poetter, Michael Fowler, Zach Leffke, Deirdre Beggs, Kayla Brosie, Kayla Straub, Seth Hitefield, Bill Clark, Ryan Chase, Alan O'Donnell, and all of the other Hume Center folks who have helped me over the years. It has been a lot of fun, and I will certainly miss working with you. Outside of the Hume Center, I have had the pleasure of learning from and working with a number of other students from whom I have been able to learn a lot, and I thank David Allen, Brad Sease, Dr. Brad Atkins, Kevin Nastasi, Dr. John Janeski, Tom Battista, Ben Lutz, Maria Rye, Ryan Stanley, Adam Weisz, Tom Kasmer, Jacob Bean, Dr. Artur Wolek, Mark Palframan, Deva Muniraj, Dr. Dave Grymin, Hunter McLelland, Dr. Haithem Taha, and Dr. Sevak Tahmasian.

I would be remiss if I did not also thank my swim coaches over the years, from age group to varsity, for teaching me to push myself beyond the brink of exhaustion and still thrive. Thank you Ned, Braden, Randy, Leanne, and Don for helping me realize what I'm made of.

I must also thank Ms. Susan Anderson from the math department for her tremendous patience and teaching skill. When I decided to become an engineer, I started my math education from square one, and Susan's outstanding lectures showed me that math is not a subject to be feared.

I also want to thank Ms. Rachel Hall Smith for her help in making sure I navigated the graduate school and AOE procedures successfully.

I cannot express enough gratitude to my parents, Chris and Kathy, and siblings Allison and Patrick, for the 28 years of support and love as I found my passion. You have provided me with an excellent model for how to be a good husband and professional, and I look forward to applying what you've taught me to my next phase in life.

Since meeting my wife Hannah, I have had the extraordinary fortune of having the love and support of my in-laws Mark and Beth, and Hannah's brothers Richard and his fiancée Alexis, Ben and his wife Whitney, and Thomas and their rather large extended family. Thank you for all the great times we've had, and the great times to come.

Finally, I thank my wife Hannah. Without a doubt, your love, encouragement, positivity, and exceptional culinary skills have pushed me to be the best that I can. This degree would not have been possible, nor would it have been as much fun, had it not been for you. I can't wait to see what lies ahead.

Contents

List of Figures

List of Tables

Chapter 1

Introduction

1.1 Motivation

This dissertation focuses on developing new, optimization-based controllers for spacecraft relative motion. The contributions in this work enable both large baseline formation reconfiguration over several orbits as well as very short baseline, rapid response maneuvers. Spacecraft relative motion modeling, control, and estimation is a major area of research in modern astrodynamics and control theory and have been studied for a wide variety of missions. Additionally, relative motion control and estimation have been successfully implemented on missions that have flown or are currently active. There are two primary motivations for building satellite missions around relative motion and multi-vehicle architectures:

1. Distribution of mission objectives among several dedicated agents (e.g. interferometric, *in situ* measurement, and sparse-aperture missions)
2. On-orbit servicing (OOS), robotic inspection, autonomous rendezvous and docking (AR&D)

Several relative motion missions have actually been executed or are still in progress. In the following sections, some example missions enabled by relative motion modeling and control will be briefly described.

1.1.1 Notable Science Missions and Concepts

The **G**ravity **R**ecovery **a**nd **C**limate **E**xperiment (GRACE) [3, 6] uses two satellites in a leader-follower formation (see Figure 1.1) to accomplish the following scientific objectives [69]:

1. Obtain accurate global mean and time-varying models of the Earth's gravity field (a new model every thirty days for five years)
2. Enable a better understanding of ocean surface currents and heat transport
3. Measure changes in sea-floor pressure and ocean mass changes
4. Measure mass balances on ice sheets and glaciers

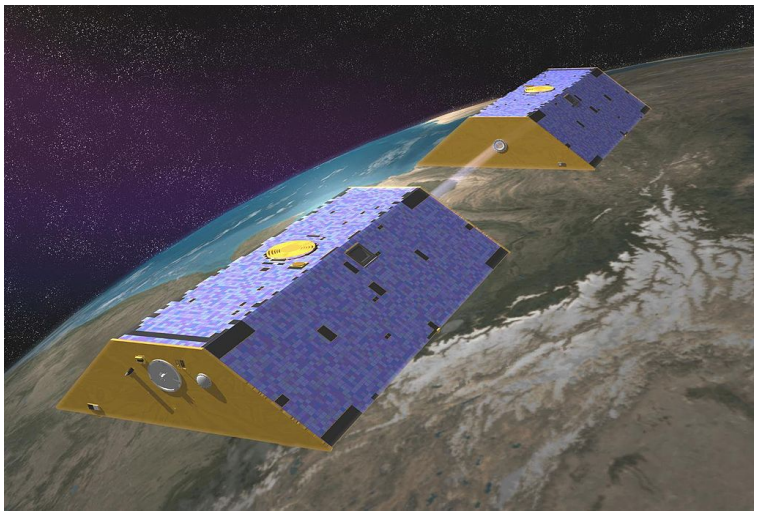

Figure 1.1: Artist's conception of the GRACE formation, credit: NASA

GRACE is still an active mission, and has provided a wealth of scientific data. It is in a naturally decaying orbit and is expected to fully degrade sometime in 2016.

Following the *Ariane-5*'s failed launch of the Cluster-I formation of satellites in 1996 [40], Cluster-II was deployed in a series of launches between July and August 2000. Cluster-II comprises a tetrahedral formation that studies the evolution of the magnetosphere over a complete solar cycle (see Figure 1.2). Cluster-II celebrated 10 years of scientific achievement in February 2011, and continues to operate today [44, 45, 47, 126, 46, 115]. In fact, to date there have been over *2700 referreed papers*, proceedings and theses published based on the science and engineering results from the Cluster-II mission [5]. Cluster-II uses a fairly coarse control method to maintain the formation geometry based on relative orbital elements; for this type of mission this approach is accurate enough to accomplish its science objectives.

Figure 1.2: Artist's depiction of Cluster-II formation, credit: ESA

The Cluster-II mission's success demonstrates the potential for tremendous science return from distributed systems. Another well-known mission that proposed satellite formation flying was the Air Force's TechSat-21 concept [92, 29, 38, 93] which was envisioned using a cluster of small, agile satellites to adapt to new mission parameters or constraints on demand. This project was cancelled in 2003, however elements of the missions concept-of-operations (CONOPS) were incorporated into numerous follow-on studies such as DARPA's F6 (**F**uture, **F**ast, **F**lexible, **F**ree-**F**lying, **F**ractionated **S**pacecraft united by **I**nformation e**X**change) [27] mission concept (artist's depicition seen in Figure 1.3). In this concept, a cluster of small satellites fly in rough formation, and each satellite would be designed to perform a specific subsystem task. The TechSat-21 and F6 concepts effectively replace a single monolithic satellite bus with a swarm of smaller, specialized spacecraft. In the event of a subsystem failure, a new component could be launched at an opportune time while minimizing the down time of the rest of the components.

NASA's **M**agnetospheric **M**ulti**S**cale mission (MMS) [122, 90], which launched on 13 March 2015, involves four satellites flying in a tetrahedral formation [22] in highly elliptical orbits to study magnetic reconnection in the magnetosphere. The mission is intended to build on the successes of the Cluster-II mission but with improved spatio-temporal resolution. Each of the four satellites employ 25 different science instruments that provide unprecedented *in situ* measurements. The MMS satellites required significant improvements to the state of the art for both relative navigation and control to achieve their specific science objective. The satellites have a perigee of about 1.2 Earth radii, and (during Phase 1) an apogee of 12 Earth radii and baselines of 10 km. During Phase 2, their apogee radius will increase to 25 Earth radii. The high eccentricity and relatively long baselines require novel guidance, navigation, and control algorithms to maintain formation and maximize science return.

Figure 1.3: F6 constellation concept, credit: DARPA

1.1.2 Proximity Maneuvering and Control

Proximity operations and relative motion modeling have gone hand-in-hand since the Soviets' first attempts (and failures) of rendezvous between two satellites, *Vostok 3-4* in 1962 and *Vostok 5-6* in 1963. The Soviets learned the hard way that simply launching two satellites into nearly identical orbits is not nearly sufficient to achieve rendezvous. The initial 5-6 kilometer separation soon grew to thousands of kilometers as perturbations and non-commensurate energy levels dramatically affected the relative motion of the satellites.

The United States also got a chance to see first hand how a poor understanding of relative orbital mechanics could affect rendezvous. In 1965, Jim McDivitt's attempt at executing rendezvous between *Gemini 4* and the *Titan* upper stage ended rather anti-climactically when he pointed the capsule directly at the target stage and thrusted forward. For reasons previously unconsidered to NASA (and described quite thoroughly in succeeding chapters of this dissertation), this did not work. It was later realized that thrusting forward increases orbital velocity, and by Kepler's Third Law, changes the orbital period. Following the maneuver, McDivitt's capsule was both above and behind the target stage. This occurred despite Buzz Aldrin's rather thorough analysis in his 1963 dissertation on the subject of guidance for rendezvous between two satellites [7] and Clohessy and Wiltshire's well-known, 1960 paper on terminal guidance for spacecraft rendezvous [35].

The first successful rendezvous happened later in 1965 when Wally Schirra maneuvered *Gemini 6* to within one foot of *Gemini 7* and performed stationkeeping. Proximity operations, and in particular rendezvous have existed almost as long as spaceflight. More recently,

however, more elaborate concepts for proximity operations have emerged.

Rendezvous and docking regularly occurs during unmanned spaceflight. For instance, each resupply mission to the International Space Station requires extremely precise guidance, navigation, and control to ensure safe, reliable operation. Additionally, the AR&D problem has been treated extensively in the spacecraft literature using myriad techniques. A more exotic and less-studied problem is that of circumnavigation for robotic inspection.

The Air Force Research Laboratory's Space Vehicles Directorate commissioned the e**X**perimental **S**mall **S**atellite 10 (XSS-10) program to test proximity guidance and control. AFRL defined the following mission objectives [12]:

- Execute free flight of closed-loop system for a 20 kg micro-satellite
- Closed-loop tracking of space object at less than 500 m
- Perform 270 degree fly-around maneuver based on visual guidance
- Demonstrate stationkeeping and inertial hold near resident space object
- Demonstrate ability to resolve space object at 100 m
- Perform real-time, two-way communications
- Demonstrate life extension mode for micro-satellite
- Record performance parameters and maneuver execution sequences on orbit

The XSS-10 was launched in 2003 on a Delta-II rocket as an auxiliary payload and successfully performed proximity maneuvering and imaging of the upper stage, seen in Figure 1.4.

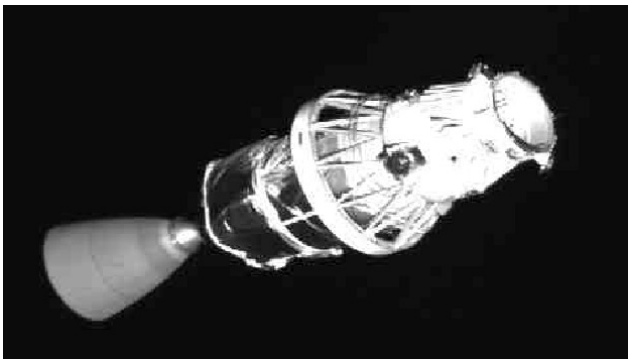

Figure 1.4: Image of Delta-II upper stage taken by XSS-10, credit AFRL

One of the most well-known examples of a free-flying satellite performing autonomous inspection and servicing was DARPA's Orbital Express mission [88, 132, 49, 100], seen in Figure 1.5. The mission's goals, which were successfully executed, were to demonstrate on-orbit servicing, autonomous rendezvous, docking, and capture, fluid transfer (hydrazine fuel) and a battery transfer. The mission was launched in March 2007, and decomissioned in July 2007. The satellites were left to decay naturally.

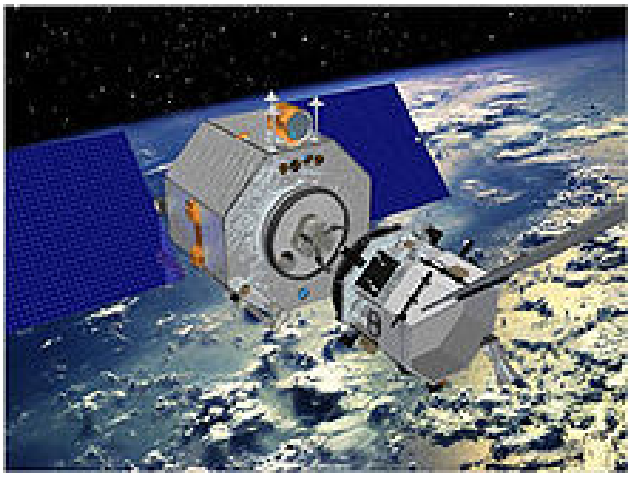

Figure 1.5: Orbital Express ASTRO and NEXTSat, credit: DARPA

Swedish Space Corporation's Prisma project [41, 42, 37] was developed and flew successfully for the purpose of performing autonomous guidance and control of a small satellite near another non-cooperating object (see Figure 1.6). Prisma consists of two satellites, MAIN and TARGET (or the more popular monnikers Mango and Tango). Mango was designed for full 6DOF control authority and is able to perform maneuvers around Tango.

Robotic inspection and servicing were given poignant motivation after damage occurred to two manned spacecraft: the *Mir* space station and the *Columbia* orbiter. *Mir* nearly suffered a disaster when the *Progress M-34* unmanned cargo spacecraft glancingly struck the *Spektr* module on the station (on 24 June 1997) [60]. The resulting hull breach caused a loss of pressure and damaged a solar panel; the damaged module was permanently sealed off and the station was powered down for several weeks while repairs were made. A picture of the external damage can be seen in Figure 1.7.

Fortunately, no crew members were harmed during this event, but it highlighted how even a glancing blow could seriously damage a spacecraft. This was further seen during the *Columbia* tragedy; a piece of foam broke off of the external fuel tank during launch and struck the leading edge of the left wing. The resulting crack in the heat shield caused enough damage that the orbiter disintegrated during re-entry, resulting in the loss of the crew. It was noted that on earlier flights STS-27, STS-45, and STS-87 similar strikes by ice debris and foam had damaged the orbiter, but without hull loss. This event made it

Figure 1.6: Artist's depiction of MAIN and TARGET, credit: ESA

painfully clear that without an effective method of evaluating the damage of the foam strike, seemingly innocuous events could cause severe damage.

A compelling case for robotic inspection and servicing was presented in the *Columbia* Accident Investigation Board's (CAIB) findings [54]. It was determined that on-orbit repair by the astronauts was possible, but considered "high risk" due to the uncertainty over the quality of the repair and the added risk of added damage to the *Columbia*. Furthermore, *Columbia* was not equipped with Canadarm, so an unusual, emergency EVA would be required. Further complicating an emergency EVA was the fact that there was no astronaut EVA training for maneuvering to the wing, however the report indicated that an astronaut *could have* reached the left wing for inspection or repair. Robotic inspection can allow for faster response times and doesn't expose astronauts to potentially hazardous environments.

Since the *Columbia* tragedy, there has been a significant emphasis on robotic servicing and inspection. The **S**pacecraft for the **U**niversal **M**odification of **O**rbits (SUMO) [20] was a program proposed in 2004 by the Naval Research Laboratory to demonstrate the successful execution of machine vision, autonomous guidance, and robotic manipulation of a derelict spacecraft. The program was intended as a risk reduction program that would allow for autonomous servicing and inspection of a non-cooperating satellite.

Another inspection demonstrator, which actually flew before the *Columbia* tragedy on STS-87 in 1997[1], was the **A**utonomous **E**xtravehicular Activity **R**obotic **Cam**era Sprint (AERCam Sprint) [34]. AERCam was a 16 kg, 0.36 m spherical spacecraft which used 12 nitrogen

[1] *Columbia* was actually the orbiter that flew on STS-87

Figure 1.7: Damage to *Mir* seen from *Atlantis* during STS-86, credit: NASA

cold-gas thrusters for attitude and trajectory control, see Figure 1.8. The craft was remotely piloted, however it was able to freely maneuver around the cargo bay of *Columbia* for about 30 minutes. The intent of the AERCam program was to demonstrate the ability of a free-flying satellite to inspect the ISS. NASA developed an autonomous follow-on project called Mini-AERCam, however it never flew.

In the same vein as AERCam, MIT's **S**ynchronized **P**osition **H**old **E**ngage and **R**eorient **E**xperimental **S**atellite (SPHERES) testbed has performed numerous demonstrations of *autonomous* proximity operations [83, 23]. Each SPHERES satellite has a mass of 4.1 kg and can freely move about in the ISS. The spacecraft are strictly for demonstration purposes and are not qualified to fly outside the ISS.

1.2 Literature Survey

1.2.1 Minimum-energy, Under-actuated Maneuvers

Minimum energy transfers near circular orbits, and more generally, Keplerian orbits have been studied quite extensively in the literature. Notable works include Carter and Humi [32], Carter [31], Guelman and Aleshin [57], Pearson [103] and Zanetti [139] . For rendezvous or formation reconfiguration over very small relative distances (when compared with the chief orbit), the Hill-Clohessy-Wiltshire model [35] is typically used because it is a linear, time-invariant approximation of the relative motion, enabling the use of a wide range of tools for analysis and control design. This model assumes a perturbation-free, circular orbit as its reference orbit. In this chapter, we adopt the HCW model assuming that the formation

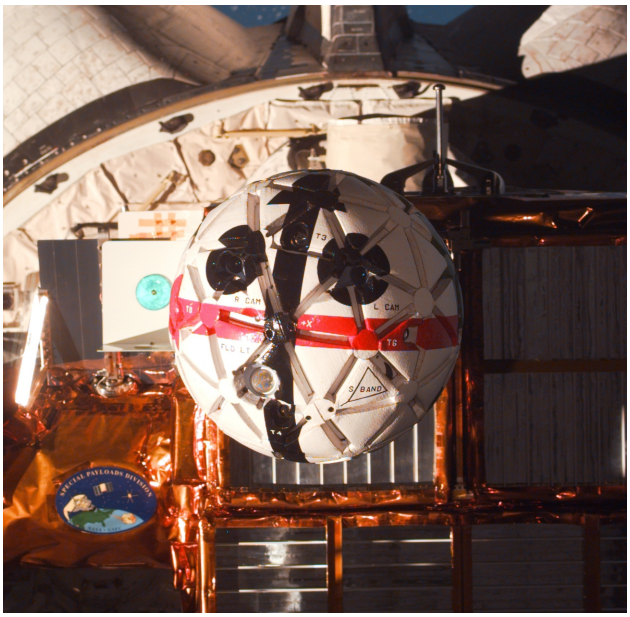

Figure 1.8: AERCam free-flying satellite, credit NASA

reconfiguration takes place quickly, so that the circular orbit approximation is reasonable.

Earlier analyses have assumed that thrust is available in all three directions (radial, in-track and cross-track), in which case the system is completely controllable.The system is also controllable, however, in the case that thrust is available only in the in-track and cross-track directions. McVittie *et al.* [97] used this fact in their work on formation keeping. The under-actuated controllability of the HCW model (and of the general spacecraft relative motion model [111]) is useful property for two reasons. The first is concerned with the mechanical complexity of a satellite; fewer required thrusters means fewer parts that could fail. The second is system robustness; if a single thruster fails for a fully-actuated spacecraft, the system may remain controllable with a reduced number of thrusters. The only requirement is that control authority be maintained in the in-track and cross-track directions.

Independently of the developments in Chapter 3, Huang *et al.* used the Pontryagin Principle to derive optimal controllers for under-actuated rendezvous and reconfiguration [68]. The work in this dissertation differs from their approach in the following ways: 1) explicit analytical expressions for the control laws over any time-of-flight are provided, both in their full form and for certain specific maneuvers where the expressions for the controllers are significantly simplified, 2) we provide necessary and sufficient conditions for global optimality of the under-actuated control laws using results from calculus of variations as well as linear operator theory, and 3) we derive an explicit controllability Gramian, which is also valid over any time-of-flight.

1.2.2 Sliding Mode Tracking Control

Short-time-scale maneuvers for proximity operations were investigated in [79] using the Hill-Clohessy-Wiltshire equations (HCW) which are a linear, time-invariant approximation of the formation flying equations. The authors assume a perfectly circular orbit, and they did not investigate the nonlinear optimal control solution, nor did they consider the linear open loop optimal solution which is also presented here. In contrast, we consider the full nonlinear system, and show the close similarity between the nonlinear optimal transfer and linear optimal transfer. In [59], a nonlinear optimal control solution and neighboring optimal solution were presented for formation flying, however this analysis was done on the scale of a full orbit and using Gauss' Variational Equations (GVE). The GVE are a different parameterization of orbital motion based on variations in the orbital elements. We do not use this approach because the structure of the GVE is not easily amenable to the structural requirements for sliding mode control design (SMC). In [139], the minimum energy transfer problem was solved analytically using the glideslope [103] reference frame, however this solution was valid only for the HCW equations.

Sliding mode control and its myriad variants have been simulated successfully for formation flying. Massey *et al.* [95] studied traditional sliding mode control and "super-twisting" sliding mode control for the HCW equations and treated all nonlinearities as exogenous disturbances. A similar approach was used by Yeh *et al.* [138], however they did include some nonlinear dynamics. Our work differs from theirs in that our controller doesn't just maintain a desired formation, rather we track an optimal maneuver using SMC. Hui and Li [71] used terminal sliding mode control to perform formation reconfigurations on the scale of an orbit or longer. Additionally, the controller we develop is valid for any arbitrarily elliptical orbit, rather than assuming a purely circular orbit.

1.2.3 Trajectory Optimization Near a Perturbed, Elliptical Orbit

Using a standard linear program to minimize the consumed fuel has been explored previously by Richards *et al* [109] where the Hill-Clohessy-Wiltshire equations served as the motion model in optimizing trajectories for robotic inspection. In fact, this work used mixed-integer linear programming to account for plume impingement and collision avoidance, which we do not consider here. Tillerson *et al.* [127] applied linear programming to the formation flying problem with avoidance constraints where a specified formation was maintained in an elliptic orbit, but they didn't consider the effect of J_2. Mueller *et al.* [99] considered a very similar problem as Tillerson *et al.*, but also without the contribution of J_2. Furthermore these three works all assumed fixed time-of-flight for their maneuvers. These earlier papers also did not consider an under-actuated system. The ability to maneuver relative to another spacecraft using only two lines of thrust provides flexibility in case of a thruster failure or, alternatively, enables a designer to reduce the weight and complexity by eliminating unneeded actuators.

Yan and Alfriend [136] explored an approximate solution to the minimum energy transfer using the Gim-Alfriend STM, and used a pseudospectral collocation to approximate the integrals in the minimum energy theorem. This work assumed a fully-actuated system and imposed no constraints on the input forces. Yan and Gong [137] used a finite-horizon, linear-quadratic controller to perform long-term formation maintenance in conjunction with the GA-STM, however this again involved no constraints on the controller. Also, the LQ controller fires continuously whereas the controllers presented in this paper do not, because of the bang-off-bang profile from minimum fuel optimal control. Roscoe *et al.* [113] used the differential orbital element representation of the GA-STM in conjunction with the Maximum Principle and Lawden's primer vector theory, however their analysis explicitly assumed maneuvers were impulsive whereas we assume finite thrust. Gaias *et al.* [52, 50] were able to geometrically derive Δv lower bounds for differential orbital elements, and we use some of their results as a comparison for the proposed method.

The genetic algorithm and other heuristic search algorithms have been used numerous times in previous contributions both to minimize the Δv for a maneuver or to minimize some objective function relating to the quality of a formation of satellites. Kim and Spencer [77] used a binary genetic algorithm to find optimal two- and three-impulse maneuvers for satellite rendezvous. This particular application focused on the solution of the Lambert targeting problem, and did not involve the formation flying assumptions. They were able to get a close agreement with the classical Hohmann and bi-elliptic transfer results, but they do not consider the J_2 perturbation. Sabatini *et al.* [116] applied a genetic algorithm to the problem of finding a set of initial conditions that yield a natural, periodic orbit under the presence of J_2. In addition to the well-known J_2-invariant results (namely, the critical inclination of $i = 63.4°$) they also found two additional drift-free inclinations using the genetic algorithm, corresponding to $i = 49°$ and $i = 131°$. In [1], Abdelkhalik and Mortari used the genetic algorithm again to improve upon some of the results obtained by Kim and Spencer, but this was limited to perturbation-free, low-Earth orbit (LEO) to geostationary Earth orbit (GEO) maneuvers. Luo *et al.* [91] used a hybrid genetic algorithm with simplex method to minimize time-of-flight of rendezvous for the HCW equations, but again, they only consider a circular, unperturbed orbit and do not examine the fuel/time balance that this paper examines. Pontani used a hybrid approach of particle swarm/ indirect method to compute fuel-optimal relative maneuvers using the HCW equations [105]. The contribution of this paper is the use of the GA-STM in the under-actuated, minimum fuel/time optimal control problem. For a given balance between the time-of-flight and the amount of fuel used, we present globally optimal solutions which agree closely with the Δv requirements predicted by impulsive orbit theory.

1.2.4 Constrained Tracking Control

Six degree-of-freedom control studies have been carried out for satellite relative motion, primarily for dynamic synchronization between the relative orbit and relative attitude of two

or more satellites [82, 80, 81]. While those analyses incorporated the effects of various perturbations on the orbit and attitude as a whole, the effect of non-collinear thrusters was not included, nor was the effect of attitude error on thruster alignment. If it is assumed that a thrust system can take any value between $[-u_{\max}, u_{\max}]$ then this assumption can be relaxed since the thrust could be remapped among the thrusters to account for attitude error. If the thrusters are binary, nearly binary or have a relatively large minimum impulse bit, then the thrusters cannot necessarily be remapped. Furthermore, small satellite design is often severely constrained by their payloads, and so the thrusters may not actually be aligned precisely with the center of mass or each other. This assumption is very important for spacecraft proximity operations where small attitude errors can minimize mission performance.

Model predictive control for spacecraft relative motion control has been studied numerous times in the literature for applications ranging from large-scale formation keeping to spacecraft rendezvous and capture [24, 63, 101, 108, 104, 131]. Breger and How [24, 22] use the time-varying Gauss' Variational Equations (GVE) to perform long term formation maintenance for a group of satellites in a highly elliptic orbit. Park *et al.* [101] use model predictive control to approach a moving base platform in a planar setting. Hartley *et al.* [63] develop an entire MPC-based approach and capture system for the Mars Sample Return mission. The MPC formulations vary with respect to the type of cost function used and the constraints imposed. The two most frequently used cost functions in MPC for satellite applications are fuel optimization (see [24, 108, 63]) or quadratic costs similar to LQR (as in [63, 101, 104, 131]). Our work differs from previous studies in that we formulate the MPC problem as a trajectory tracking problem; a fuel-optimal reference trajectory is designed *a priori* and the controller's job is to track along this trajectory in the presence of orbital disturbances and intitial condition error. This is a more general treatment of the problem and allows for an immediate comparison of the performance of the feedback maneuver with the optimal maneuver. Further, we use a 1-norm cost function in addition to the quadratic cost function in the minimization. We find that the 1-norm formulation uses less fuel and provides sparser control activity than the quadratic cost.

Treating the minimum impulse bit of a thruster as a constraint in MPC has been investigated previously as well. The minimum impulse bit (MIB) is the smallest allowable, non-zero thrust provided by a thruster. For small, cold gas thrusters, it's assumed that the MIB is very close to the maximum thrust of the system. This is because the cold gas system typically does not have much throttling capability, so it is essentially a binary thruster. Larsson *et al.* [85] suggested that a semi-continuous variable could be used to encode the MIB into an MPC problem, however they did not implement this strategy since the complexity of mixed-integer programs grows combinatorially with the number of binary constraints. Hartley *et al.* [62] considered other alternatives to using a mixed-integer program and implemented ℓ_{asso} MPC [53] to implement sparsity in the signals:

1. Use continuous thrust (and ignore the problem)
2. Solve the optimization problem and round down any signals below the MIB

3. Use two thrusters with different thrust levels to yield a lower value (differential thrusting)

4. Buffer the low thrusts to a suitable accumulation and execute that signal

The first option is undesirable because it allows any signal in the set $[-u_{\max}, u_{\max}]$ to be applied which is not necessarily a good assumption. The second approach would prevent small signals from being applied, but is sub-optimal in the sense that the signal which is applied to the system may not be the solution to the optimization. Further, it is noted that this can result in the trajectory error states converging to a limit cycle rather than the desired state. This is not necessarily undesirable depending on the mission metrics. The third and fourth options require more modeling to accurately capture the correct signal, and may not be appropriate for thrust systems that are binary or near-binary. In this work, we implement a thrust constraint model similar to the one proposed by Larsson *et al.* and compare it with the second option listed above.

1.3 Summary of Contributions

Chapter 3

The derivation of a closed-form, completely analytical solution to the minimum-energy optimal transfer problem for the HCW equations using only in-track and cross-track thrust is presented. This work was performed independently of [68], however they published a similar solution a few months ahead of this work. The work in this dissertation extends their analysis by accomplishing the following:

1. Explicit, analytical control laws for any arbitrary $t_f > 0$ and any boundary conditions $\boldsymbol{x}_0$ and $\boldsymbol{x}_f$ are presented.
2. An explicit Gramian matrix is derived and verified that it is invertible for any $t_f > 0$, which is necessary and sufficient for controllability. The control law derived with the Gramian is precisely the same as that derived from the Pontryagin Principle, and minimizes the same cost function (the $\mathcal{L}_2$ energy).
3. A proof is presented that the analytical control law is a strong local minimum using calculus of variations and then it is proven that the control law is a global optimum by using the controllability Gramian.
4. Derivation of significantly simplified control laws for certain specific maneuvers in closed-form.

Then the under-actuated maneuver is compared to the fully-actuated maneuver and it is shown that, while slightly more expensive in terms of control energy, the under-actuated maneuver is of the same order of magnitude in terms of cost as the fully-actuated maneuver.

Chapter 4

The circular orbit assumption from Chapter 3 is relaxed and it is assumed that the system is fully-actuated. Chapter 4 contains the following contributions

1. Using the controllability Gramian, a (numerically) computed solution to the fully-actuated, linear optimal rendezvous is presented, and verified by numerically solving the nonlinear optimal transfer problem using the nonlinear equations of motion.
2. A nonlinear, sliding mode, tracking controller is designed to be robust to disturbances of magnitude no larger than that of J_2. Analysis shows that the sliding mode controller is asymptotically stabilizing in the presence of these un-modeled disturbances as well as initial condition error.
3. The controllers in this chapter, both optimal and sub-optimal, work on any relative Keplerian orbit with $e \in [0, 1)$, which allows for a very flexible control design process.

Chapter 5

The focus changes from control design in continuous-time to discrete-time with the goal of developing more realistic control designs. Chapter 5 presented the following contributions

1. The use of the Gim-Alfriend state transition matrix (GA-STM) as the relative motion model for a trajectory optimization problem
2. Using the GA-STM, a method by which to compute fuel-optimal, multi-revolution, finite-thrust, relative orbital transfers near a J_2-perturbed, eccentric orbit using convex programming is developed
3. A demonstration that in the limit the time-discretization approaches zero and the transfer time approaches infinity, the finite-thrust method converges to familiar results from impulsive orbit transfer theory when perturbations are not present
4. A proof that the relative motion model using radial/in-track/cross-track as well as only in-track/cross-track inputs is completely controllable
5. A hybrid technique of convex programming/genetic algorithm to solve the multi-objective fuel/time optimal control problem

The technique used in this chapter allows for the benefit of added modeling fidelity (through the use of relative orbital elements), but with the simplicity of the Cartesian distances and velocities (through the direct linear mapping of orbital elements to Cartesian variables). Moreover, by using the convex programming approach, we guarantee global optimality of the solutions, which is more difficult to do with continuous-time, indirect methods. I also demonstrated that for certain special maneuvers, such as a pure inclination change, the convex program always chooses the nodal crossing to perform a thrust which agrees very closely with results from impulsive transfer theory. This is a very interesting result because no prior structure was imposed on the burns, simply that they minimize the overall cost function.

Chapter 6

The focus shifts from trajectory optimization to discrete-time, model predictive control (MPC) for the application of spacecraft proximity operations. Chapter 6 contains the following novel contributions:

1. A novel coupled orbit and attitude model which is ideal for a small satellite in low-Earth orbit (LEO). This model couples the orbit and attitude together through the thruster input channels. Any attitude error results in the thrust vectors being misaligned with the orbiting axes, and the thrust will in general push the satellite in the wrong direction. Additionally, the model accounts for the potential misalignment of the thrusters with 1) each other and 2) the center of mass; each thrust induces a torque about the center of mass and can cause further attitude error.

2. A reformulation of the classical MPC problem as a trajectory tracing problem. We use a mixed-integer linear program to solve the minimum fuel optimal control problem with collision avoidance constraints. The resulting state and control history is previewed in the prediction.

3. A new method of modeling the minimum impulse bit (MIB) in the trajectory tracking problem. We implemented the MIB as a combinatorial constraint. This results in increased computational effort, but we show that when compared to a sub-optimal approximation of the MIB, the proposed method results in sparser control action, and thus less fuel use. This is compared to another technique which rounds control signals below the minimum bit to zero. It is shown that the new method is able to run faster than real-time for both 1-norm and 2-norm formulations of the problem.

While computationally more expensive, the methods proposed in this chapter can enable small inspector satellites to safely fly around a complex shape (such as the Space Shuttle orbiter or the ISS) while also using sparse control activity.

Following Chapter 6, Chapter 7 contains conclusions of the research are presented as well as recommendations for future work.

1.4 Notation

In this dissertation, significant effort has been made to keep the notation consistent, and in this section the essential mathematical notation is presented.

An n-dimensional Euclidean space is defined as $\mathbb{R}^n$. A real-valued scalar will be denoted by $x \in \mathbb{R}$, whereas a real-valued, n-dimensional vector will be denoted as $\boldsymbol{x} \in \mathbb{R}^n$, and a real-valued matrix in n-by-m dimensional space is given by $\boldsymbol{X} \in \mathbb{R}^{n\times m}$.

This work primarily deals with the control of dynamical systems, and frequently we make use of systems of the form $\dot{\boldsymbol{x}} = \boldsymbol{f}(\boldsymbol{x}, \boldsymbol{u})$. The quantity $\dot{(\cdot)}$ denotes a derivative with respect to time, and $(\cdot)'$ denotes a derivative with respect to a different variable, which will be made clear in the appropriate context. The Jacobian of the vector field $\boldsymbol{f}(\boldsymbol{x}) \in \mathbb{R}^n$ is given by

$$\mathbb{J}(\boldsymbol{x}) = \frac{\partial \boldsymbol{f}(\boldsymbol{x})}{\partial \boldsymbol{x}} = \begin{bmatrix} \frac{\partial f_1}{\partial x_1} & \cdots & \frac{\partial f_1}{\partial x_n} \\ \vdots & \ddots & \vdots \\ \frac{\partial f_n}{\partial x_1} & \cdots & \frac{\partial f_n}{\partial x_n} \end{bmatrix}$$

State transition matrices are written as $\boldsymbol{\Phi}(t_1, t_0) : \boldsymbol{x}(t_0) \mapsto \boldsymbol{x}(t_1)$. Gramian matrices, such as the controllability Gramian are given by $\boldsymbol{W}(t_0, t_1) : \mathbb{R}^n \mapsto \mathbb{R}^n$.

In the trajectory optimization section, we use two different Lagrange multipliers, $\boldsymbol{\lambda}_k$ and $\boldsymbol{\nu}_k$. For the k^{th} inequality constraint in an optimization problem we use $\boldsymbol{\lambda}_k$ and for the k^{th}

equality constraint we use $\boldsymbol{\nu}_k$. For a set $U \subseteq \mathbb{R}^n$, we denote the convex hull of that set as $\text{conv}(U) \subseteq \mathbb{R}^n$.

An identity matrix spanning $\mathbb{R}^n$ is $\mathbb{I}_{n\times n}$, and a matrix of zeros is given by $\mathbf{0}_{n\times n}$. The transpose of a matrix $\boldsymbol{A} \in \mathbb{R}^{n\times m}$ is given by $(\cdot)^T : \mathbb{R}^{n\times m} \mapsto \mathbb{R}^{m\times n}$. The inverse of a square matrix $\boldsymbol{A} \in \mathbb{R}^{n\times n}$ is given by $\boldsymbol{A}^{-1}$. The p-norm of a vector is denoted by $||\cdot||_p$, and when the p is omitted, the reader may assume that the Euclidean norm $p = 2$ is used. For a time-varying vector field $\boldsymbol{f}(\boldsymbol{x}, t)$, its Jacobian will be denoted as $\boldsymbol{A}(t)$, and if elements of the Jacobian are parameterized by a quantity, this will be denoted by $\boldsymbol{A}(t; e)$ where e is the parameter that must be accounted for.

An orthonormal reference frame will be referred to as $\{a\}$ and the basis vectors spanning $\{a\}$ will be denoted $\begin{bmatrix}\hat{\boldsymbol{a}}_1 & \hat{\boldsymbol{a}}_2 & \hat{\boldsymbol{a}}_3\end{bmatrix}$. The rotation from frame $\{a\}$ to frame $\{b\}$ is $\boldsymbol{R}^a_b$.

Chapter 2

Mechanics and Control Preliminaries

In this chapter, the requisite astrodynamics, rigid body dynamics, and control system theory are presented. In particular, the nonlinear and linear relative orbit models, rigid body motion relative to the orbiting frame, and optimal control formulations that we use in later chapters are presented.

2.1 Astrodynamics

2.1.1 Two-Body Problem

Consider the motion of a satellite in orbit around a massive central body. The equations of motion that describe this motion are given by

$$\ddot{\boldsymbol{r}}_{\mathrm{c}} = -\frac{\mu}{||\boldsymbol{r}_{\mathrm{c}}||^3}\boldsymbol{r}_{\mathrm{c}} + \boldsymbol{a}_d(\boldsymbol{r}_{\mathrm{c}}, \dot{\boldsymbol{r}}_{\mathrm{c}}, t) \tag{2.1}$$

where $\boldsymbol{r}_{\mathrm{c}} \in \mathbb{R}^3$ defines the position vector from the center of mass of the central body to the center of mass of the orbiting body, μ is the standard gravitational parameter, and $\boldsymbol{a}_d(\cdot,\cdot,\cdot)$ defines a vector of (possibly time-varying) position and velocity dependent perturbations.

Eq. 2.1 represents a system of three coupled, nonlinear ordinary differential equations which describe the satellite's position and velocity relative to an inertially fixed frame at the center of the central body. The state vector for the equations of motion under the Cartesian parameterization is

$$\begin{bmatrix}\boldsymbol{r}_{\mathrm{c}}^T & \dot{\boldsymbol{r}}_{\mathrm{c}}^T\end{bmatrix}^T = \begin{bmatrix}X & Y & Z & \dot{X} & \dot{Y} & \dot{Z}\end{bmatrix}^T \tag{2.2}$$

Another popular parameterization is the classical orbital elements given by

$$\boldsymbol{e} = \begin{bmatrix}a & e & i & \Omega & \omega & f\end{bmatrix}^T \tag{2.3}$$

where a is the semi-major axis, e is the eccentricity, i is the inclination, Ω is the right-ascension, ω is the argument of periapsis and f is the true anomaly.

Suppose $\boldsymbol{a}_d(\cdot,\cdot,\cdot) = \boldsymbol{0}$, an assumption which can be reasonable for relatively short time-scales. Under this assumption, the angular momentum of the orbit is a constant of motion.

Remark 1. *There are ten classical integrals of motion for the two-body problem; three components of the orbital angular momentum vector, three components of the eccentricity vector, the Hamiltonian, the trajectory equation, the mean motion, and the time or periapsis passage [13]. More recently, an eleventh constant of motion was derived by Sinclair and Hurtado [124]. They noted that the two-body problem can be split into mass-center and relative motion subsystems, and the eleventh constant of motion relates the behavior of the two subsystems.*

We can express the equations of motion in Eq. 2.1 in a different form, namely we use polar coordinates and treat the problem as planar. The equations of motion in this context take the form

$$\ddot{r}_\mathrm{c} = r_\mathrm{c}\dot{\theta}^2 - \frac{\mu}{r_\mathrm{c}^2} \qquad \ddot{\theta} = -\frac{2\dot{r}_\mathrm{c}\dot{\theta}}{r_\mathrm{c}} \tag{2.4}$$

where $\theta = \omega + f$ is called the argument of latitude. This system of equations can explicitly be solved:

$$\begin{aligned} r_\mathrm{c}(\theta) &= \frac{a(1-e^2)}{1+e\cos\theta} & \dot{\theta}(\theta) &= \frac{e\mu\sin\theta}{\sqrt{\mu a(1-e^2)}} \\ \dot{r}_\mathrm{c}(\theta) &= \frac{\sqrt{\mu a(1-e^2)}\,(1+e\cos\theta)^2}{a^2(1-e^2)^2} & \ddot{\theta}(\theta) &= \frac{2\mu e(1+e\cos\theta)^3\sin\theta}{a^3(1-e^2)^3} \end{aligned} \tag{2.5}$$

Eq. 2.5 will be used extensively for the time-varying coefficients in the formation flying equations.

2.1.2 Nonlinear Relative Motion

Consider the relative geometry in Figure 2.1.

Let the inertial frame, which is attached to the center of the central body be given by $\{\hat{\boldsymbol{n}}\} = \begin{bmatrix}\hat{\boldsymbol{X}} & \hat{\boldsymbol{Y}} & \hat{\boldsymbol{Z}}\end{bmatrix}^T$. Similarly, let $\{\hat{\boldsymbol{o}}\}$ be a non-inertial frame attached to the chief satellite be given by $\{\hat{\boldsymbol{o}}\} = \begin{bmatrix}\hat{\boldsymbol{o}}_r & \hat{\boldsymbol{o}}_\theta & \hat{\boldsymbol{o}}_h\end{bmatrix}^T$ where $\hat{\boldsymbol{o}}_r$ points in the radial direction away from the central body, $\hat{\boldsymbol{o}}_h$ points in the direction of the orbital angular momentum and $\hat{\boldsymbol{o}}_\theta$ completes the right-handed triad. This is often called the Local-Vertical, Local-Horizontal reference frame (LVLH). The frame $\{\hat{\boldsymbol{b}}\} = \begin{bmatrix}\hat{\boldsymbol{b}}_1 & \hat{\boldsymbol{b}}_2 & \hat{\boldsymbol{b}}_3\end{bmatrix}^T$ is a body-fixed frame attached to the deputy, which is ignored during the derivation of the trajectory equations. The transformation between $\{\hat{\boldsymbol{n}}\}$ and $\{\hat{\boldsymbol{o}}\}$ is given by

$$\boldsymbol{R}_n^o = \begin{bmatrix} \dfrac{\boldsymbol{r}_\mathrm{c}}{||\boldsymbol{r}_\mathrm{c}||} & \dfrac{\boldsymbol{h}_\mathrm{c}\times\boldsymbol{r}_\mathrm{c}}{||\boldsymbol{h}_\mathrm{c}\times\boldsymbol{r}_\mathrm{c}||} & \dfrac{\boldsymbol{h}_\mathrm{c}}{||\boldsymbol{h}_\mathrm{c}||} \end{bmatrix} \tag{2.6}$$

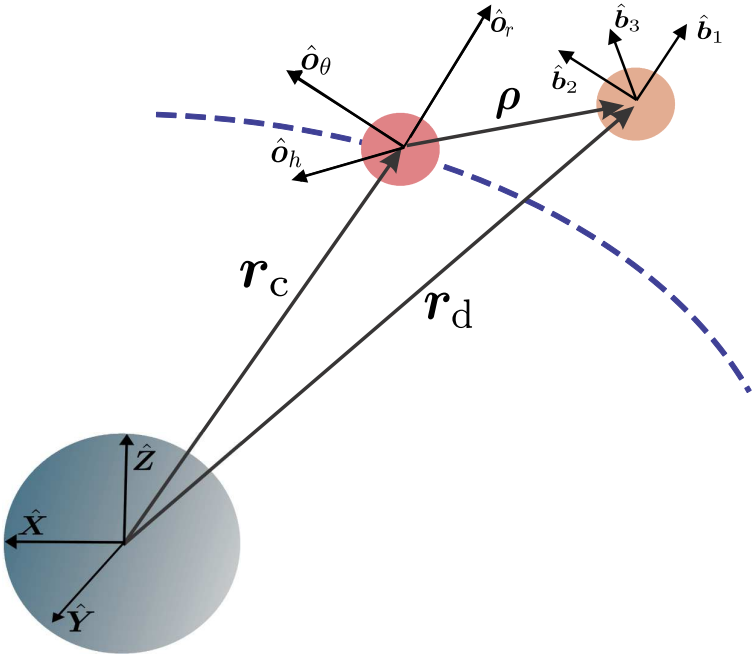

Figure 2.1: Relative orbit geometry

where $\boldsymbol{h}_c = \boldsymbol{r}_c \times \dot{\boldsymbol{r}}_c$ is the specific orbital angular momentum. Now let us consider relative motion in the orbiting frame. The position vector for the deputy in the orbiting frame is

$$\boldsymbol{r}_d = \boldsymbol{r}_c + \boldsymbol{\rho} = \begin{bmatrix} r_c + x & y & z \end{bmatrix}^T \tag{2.7}$$

The angular velocity of the LVLH frame with respect to the inertial frame is $\boldsymbol{\omega}_n^o = \begin{bmatrix} 0 & 0 & \dot{\theta} \end{bmatrix}^T$ with which we write the deputy's velocity with respect to the inertial frame is

$$(\dot{\boldsymbol{r}}_d)_n = (\dot{\boldsymbol{r}}_c + \dot{\boldsymbol{\rho}})_o + S(\boldsymbol{\omega}_n^o)(\boldsymbol{r}_c + \boldsymbol{\rho})_o \tag{2.8}$$

where $S(\cdot)$ is the skew-symmetric, cross product operator satisfying $S(\boldsymbol{a})\boldsymbol{b} = \boldsymbol{a} \times \boldsymbol{b}$ for $\boldsymbol{a}, \boldsymbol{b} \in \mathbb{R}^3$. The deputy's acceleration is

$$(\ddot{\boldsymbol{r}}_d)_n = (\ddot{\boldsymbol{r}}_c + \ddot{\boldsymbol{\rho}})_o + 2S(\boldsymbol{\omega}_n^o)(\dot{\boldsymbol{r}}_c + \dot{\boldsymbol{\rho}})_o + S(\dot{\boldsymbol{\omega}}_n^o)(\boldsymbol{r}_c + \boldsymbol{\rho})_o + S(\boldsymbol{\omega}_n^o)\left[S(\boldsymbol{\omega}_n^o)(\boldsymbol{r}_c + \boldsymbol{\rho})_o\right] \tag{2.9}$$

Using Eq. (2.9) with Eq. (2.1) for the deputy, the equations of motion are

$$(\ddot{\boldsymbol{r}}_c + \ddot{\boldsymbol{\rho}})_o + 2S(\boldsymbol{\omega}_n^o)(\dot{\boldsymbol{r}}_c + \dot{\boldsymbol{\rho}})_o + S(\dot{\boldsymbol{\omega}}_n^o)(\boldsymbol{r}_c + \boldsymbol{\rho})_o + S(\boldsymbol{\omega}_n^o)\left[S(\boldsymbol{\omega}_n^o)(\boldsymbol{r}_c + \boldsymbol{\rho})_o\right] = -\frac{\mu(\boldsymbol{r}_c + \boldsymbol{\rho})}{||\boldsymbol{r}_c + \boldsymbol{\rho}||^3} \tag{2.10}$$

Component-wise, the nonlinear equations of the relative motion (NERM) in terms of the

relative separation are

$$\begin{aligned}
\ddot{x} =& 2\dot{\theta}\dot{y} + \ddot{\theta}y + \dot{\theta}^2 x + \frac{\mu}{r_c^2} - \frac{\mu(x + r_c)}{\left[(r_c + x)^2 + y^2 + z^2\right]^{3/2}} \\
\ddot{y} =& -2\dot{\theta}\dot{x} - \ddot{\theta}x + \dot{\theta}^2 y - \frac{\mu y}{\left[(r_c + x)^2 + y^2 + z^2\right]^{3/2}} \\
\ddot{z} =& -\frac{\mu z}{\left[(r_c + x)^2 + y^2 + z^2\right]^{3/2}}
\end{aligned} \tag{2.11}$$

where r_c, $\dot{r}_c$, $\dot{\theta}$ and $\ddot{\theta}$ satisfy Eq. (2.5). Eq. (2.11) is a nonlinear, time-varying system of equations which (to our knowledge) possesses no analytical solution. The relative motion is parameterized by the eccentricity of the chief's orbit. The effect that the eccentricity has on the relative orbit can be seen in Figure 2.2.

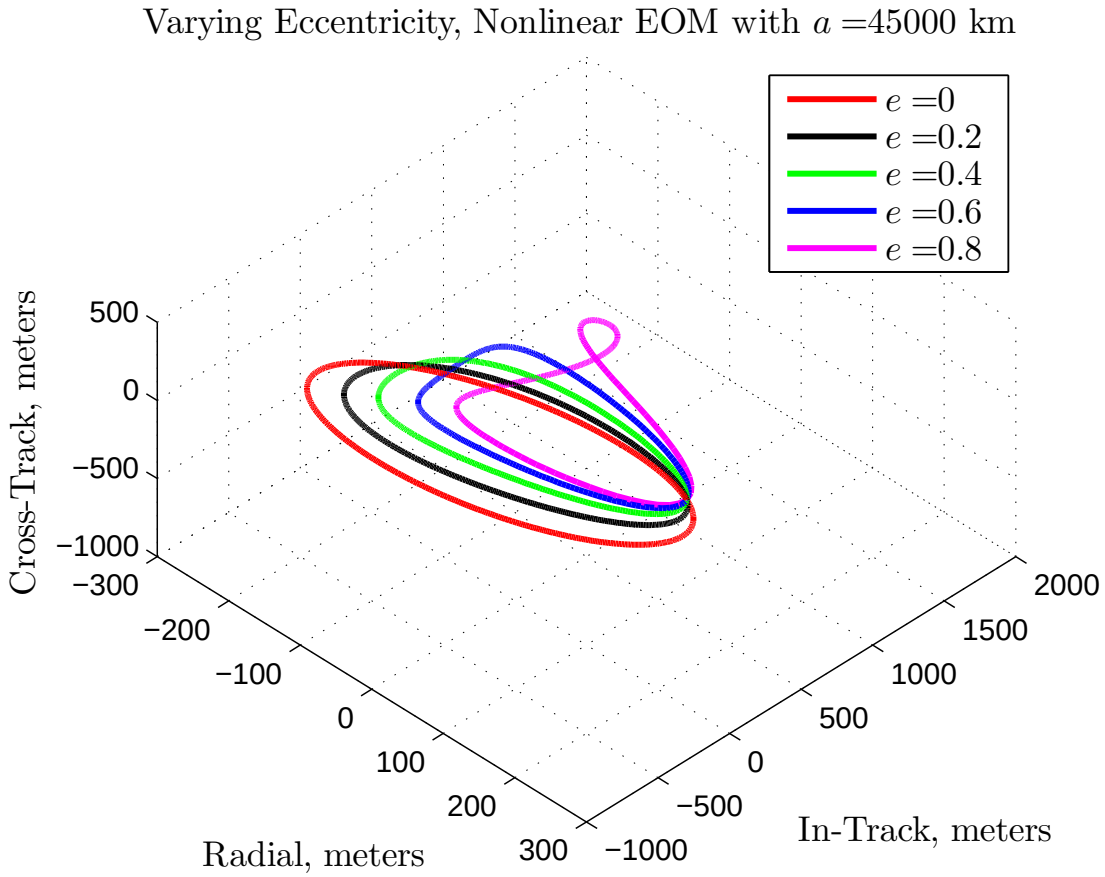

Figure 2.2: Eccentricity warps the relative motion

2.1.3 Linearized Relative Motion

Since a nonlinear system is, in general, much more difficult to work with, we seek a linearized approximation of the nonlinear system which could be beneficial from the standpoint of analysis and control design. Following [10], we can approximate the position of the deputy as

$$\boldsymbol{r}_{\mathrm{d}} = \sqrt{(r_{\mathrm{c}}+x)^2+y^2+z^2} \approx r_{\mathrm{c}}\sqrt{1+2\frac{x}{r_{\mathrm{c}}}}$$

which neglects the contribution in the in-track (y) and cross-track (z) directions to the potential energy. The acceleration due to the conservative force field is the negative gradient of the potential, using the binomial theorem [10, 123]:

$$\boldsymbol{a}_{\mathrm{d,linear}} = -\frac{\mu}{r_{\mathrm{c}}^3}\begin{bmatrix} r_{\mathrm{c}}-2x & y & z \end{bmatrix}^T$$

Now, the linear equations of relative motion (LERM) have the form

$$\begin{aligned} \ddot{x} &= 2\dot{\theta}\dot{y} + \left(\dot{\theta}^2 + 2\frac{\mu}{r_{\mathrm{c}}^3}\right)x + \ddot{\theta}y \\ \ddot{y} &= -2\dot{\theta}\dot{x} - \ddot{\theta}x + \left(\dot{\theta}^2 - \frac{\mu}{r_{\mathrm{c}}^3}\right)y \\ \ddot{z} &= -\frac{\mu}{r_{\mathrm{c}}^3}z \end{aligned} \tag{2.12}$$

and in state space we have

$$\begin{bmatrix} \dot{x} \\ \dot{y} \\ \dot{z} \\ \ddot{x} \\ \ddot{y} \\ \ddot{z} \end{bmatrix} = \underbrace{\begin{bmatrix} 0 & 0 & 0 & 1 & 0 & 0 \\ 0 & 0 & 0 & 0 & 1 & 0 \\ 0 & 0 & 0 & 0 & 0 & 1 \\ \left(\dot{\theta}^2 + 2\frac{\mu}{r_c^3}\right) & \ddot{\theta} & 0 & 0 & 2\dot{\theta} & 0 \\ -\ddot{\theta} & \left(\dot{\theta}^2 - \frac{\mu}{r_c^3}\right) & 0 & -2\dot{\theta} & 0 & 0 \\ 0 & 0 & -\frac{\mu}{r_c^3} & 0 & 0 & 0 \end{bmatrix}}_{=\boldsymbol{A}(t;e)} \begin{bmatrix} x \\ y \\ z \\ \dot{x} \\ \dot{y} \\ \dot{z} \end{bmatrix}$$

For the LERM, it has been shown that bounded relative orbits exist when the initial state for the deputy in the relative frame satisfies

$$\frac{\dot{y}_0}{x_0} = -\frac{n(2+e)}{(1+e)^{\frac{1}{2}}(1-e)^{\frac{3}{2}}} \tag{2.13}$$

where e is the orbital eccentricity. This is a very important result; if this initial condition requirement is not met, the linear system exhibits a secular drift in the in-track direction.

In the orbiting frame, this takes the form of the deputy satellite moving forward relative to the chief or backward depending on what the ratio between the initial radial position and in-track velocity is. From this point forward, this condition will be referred to as the commensurabilty condition.

It is natural to inquire about the quality of the approximation of the LERM: if the NERM are considered (for the time being) to be the "truth," how do the LERM compare? It turns out that the LERM are an excellent approximation of the NERM in the limit that the local space around the chief's orbit can be modeled by Euclidean space. The comparison of the LERM and NERM can be seen in Figure 2.3.

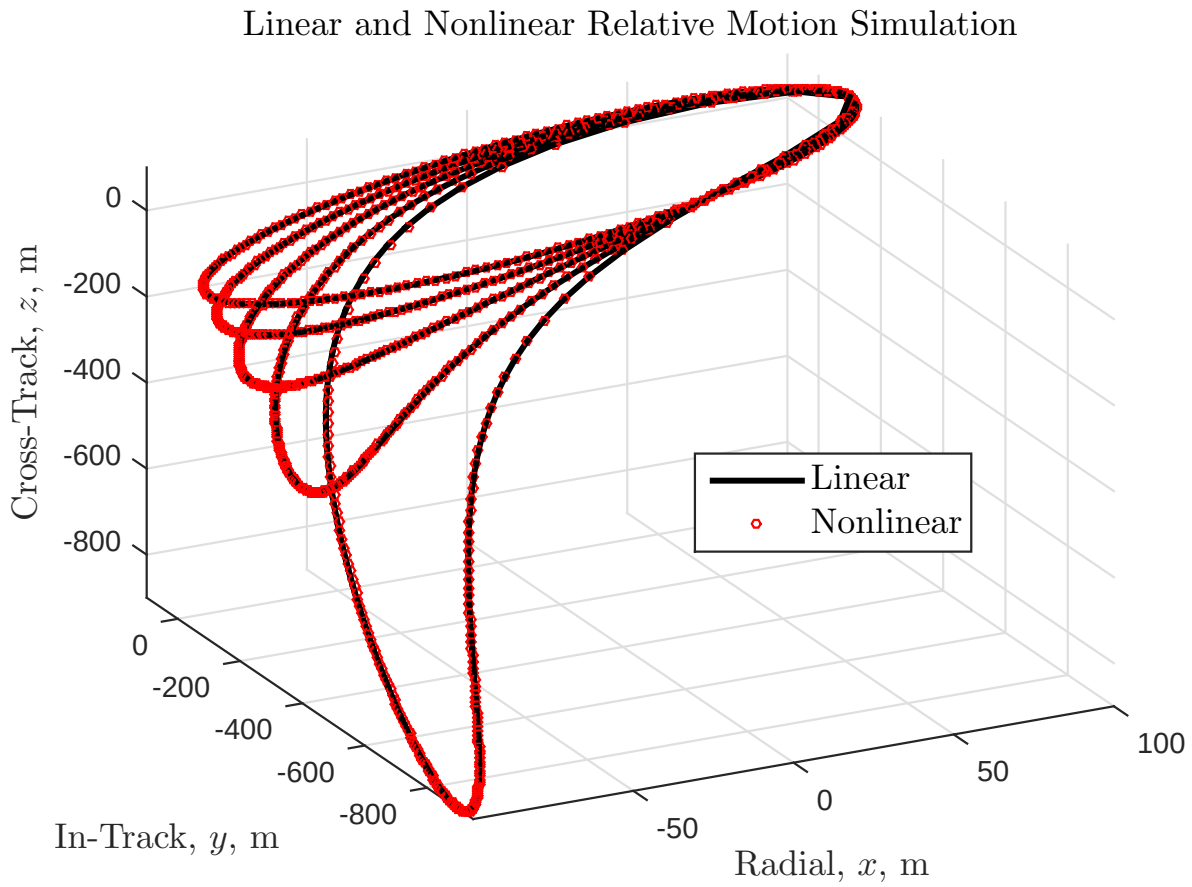

Figure 2.3: For baselines on the order of up to a few kilometers, the difference between the LERM and NERM is nearly indistinguishable

The conclusion we can glean from the comparison shown in Figure 2.3 is that for short baseline maneuvers and/or time-scales, the LERM are the preferred model to work with. Analytically, a linear, time-varying system is easier to work with than a nonlinear system.

Furthermore, for the purposes of optimal control design, using a linear model provides certain guarantees with respect to controllability, optimality etc.

Now we consider the case of vanishing eccentricity. In reality, it is extraordinarily unlikely that the reference orbit will be perfectly circular, particularly when any perturbations are considered, however for nearly-circular orbits (such as the orbits that the Space Shuttle and other LEO objects orbit in or GEO objects) this is a reasonable modeling assumption. In the limit that $e \to 0$, we find that $\dot{\theta} \to n$ and $\ddot{\theta} \to 0$, which makes Eq. (2.12) take the form of the famous Hill-Clohessy-Wiltshire (HCW) equations

$$\begin{aligned} \ddot{x} &= 3n^2 x + 2n\dot{y} \\ \ddot{y} &= -2n\dot{x} \\ \ddot{z} &= -n^2 z \end{aligned} \tag{2.14}$$

In state space, the HCW equations are

$$\begin{bmatrix} \dot{x} \\ \dot{y} \\ \dot{z} \\ \ddot{x} \\ \ddot{y} \\ \ddot{z} \end{bmatrix} = \begin{bmatrix} 0 & 0 & 0 & 1 & 0 & 0 \\ 0 & 0 & 0 & 0 & 1 & 0 \\ 0 & 0 & 0 & 0 & 0 & 1 \\ 3n^2 & 0 & 0 & 0 & 2n & 0 \\ 0 & 0 & 0 & -2n & 0 & 0 \\ 0 & 0 & -n^2 & 0 & 0 & 0 \end{bmatrix} \begin{bmatrix} x \\ y \\ z \\ \dot{x} \\ \dot{y} \\ \dot{z} \end{bmatrix} \tag{2.15}$$

Remark 2. *Note that the state matrix in Eq. (2.15) contains a one-dimensional null-space corresponding to the in-track position y. This physically represents an in-track invariance to initial conditions; the shape of the relative trajectory is not affected by a deputy starting, for example, 200m in front of the chief, or 200m behind the chief. The relative trajectory is just translated forward or backward based on y_0. This ends up being a property of the LERM as well, however it is not immediately apparent upon inspection of the system.*

The commensurability condition becomes

$$\frac{\dot{y}_0}{x_0} = -2n \tag{2.16}$$

The HCW equations are a linear, time-invariant approximation of the motion for which an

analytical solution is readily available

$$\begin{aligned}\boldsymbol{x}(t) &= \boldsymbol{\Phi}(t,0)\boldsymbol{x}_0 \\ &= \begin{bmatrix} 4-3\cos nt & 0 & 0 & \frac{\sin nt}{n} & \frac{2}{n}-\frac{2\cos nt}{n} & 0 \\ -6nt+6\sin nt & 1 & 0 & -\frac{2}{n}+\frac{2\cos nt}{n} & \frac{4\sin nt}{n}-3t & 0 \\ 0 & 0 & \cos nt & 0 & 0 & \frac{\sin nt}{n} \\ 3n\sin nt & 0 & 0 & \cos nt & 2\sin nt & 0 \\ -6n+6n\cos nt & 0 & 0 & -2\sin nt & -3+4\cos nt & 0 \\ 0 & 0 & -n\sin nt & 0 & 0 & \cos nt \end{bmatrix} \begin{bmatrix} x_0 \\ y_0 \\ z_0 \\ \dot{x}_0 \\ \dot{y}_0 \\ \dot{z}_0 \end{bmatrix}\end{aligned} \tag{2.17}$$

where $\boldsymbol{\Phi}(t,0)$ is the matrix exponential for the HCW equations. Analytical solutions to the LERM exist in both the time-domain [26] and the anomaly-domain [135]. The state transition matrices represented in [26] and [135] were not used in the analyses in this dissertation, so they are not included here.

Remark 3. *The state transition matrix in Eq.* (2.17) *forms the basis for the discrete-time relative motion model in Chapter 6.*

2.1.4 Gim-Alfriend Relative Motion Theory

The HCW, LERM and NERM models are generally viewed as good models to use when first studying spacecraft relative motion. The assumptions inherent in their derivation depend entirely on the Keplerian orbit assumption, which, as previously mentioned, is adequate for short time-scale or length-scale maneuvers or missions. For longer maneuver durations, or larger baselines, a more accurate model could be necessary. To this end, we review the essential theory behind the Gim-Alfriend state transition matrix (GA-STM).

The orbiting frame $\{\hat{\boldsymbol{o}}\}$ was previously defined as a Euclidean reference frame which is tangent to the orbit at the point of the chief. This results in linearization error even when the NERM are used [120, 84]. Using a curvilinear reference frame centered at the chief satellite can help mitigate some of the approximation error that accrues from assuming that the space around the chief is Euclidean [10]. Physically, the coordinates (x, y, z) represent the difference in orbital radii, the in-track, arc-length displacement and the cross-track, arc-length displacement respectively. The curvilinear geometry may be seen in Figure 2.4

In reality, the relative motion of the deputy is the result of slight differences in the orbital elements between the chief and deputy. Orbital elements are implicitly expressed in this curvilinear reference frame, and since the deviations are small, linearizing around the small deviations in orbital elements will in general incur a smaller linearization error [9] than using the LVLH reference frame.

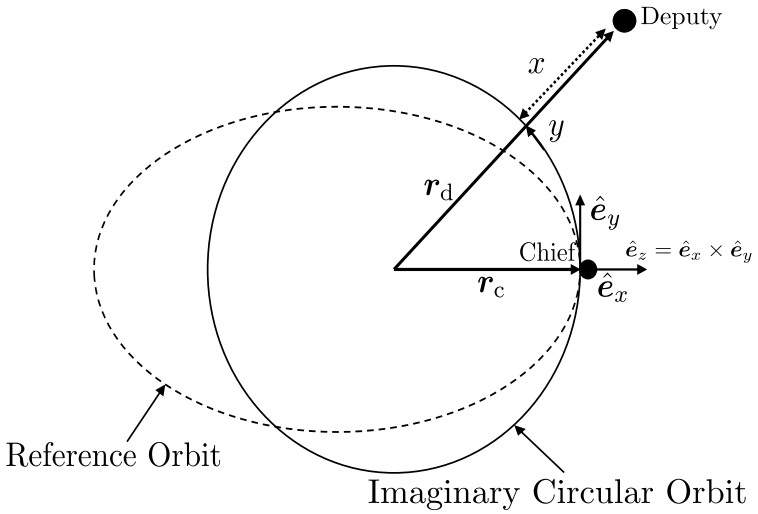

Figure 2.4: The curvilinear reference frame

In the curvilinear reference frame, we now consider the addition of the J_2 perturbation. Previously, we had defined the orbital elements in Eq. (2.3). In the derivation of the GA-STM, the following nonsingular element set is used

$$\boldsymbol{e} = \begin{bmatrix} a & \theta & i & q_1 & q_2 & \Omega \end{bmatrix}^T \tag{2.18}$$

where a, θ, i, and Ω were previously defined and $q_1 = e\cos\omega$ and $q_2 = e\sin\omega$. This set is used because the true anomaly and argument of periapsis are undefined for a circular orbit, and the numerical conditioning of the transformation between mean and osculating orbits is poor for small eccentricities. Denote the difference between the chief and deputy osculating elements as

$$\begin{aligned} \delta\boldsymbol{e} &= \boldsymbol{e}_\mathrm{d} - \boldsymbol{e}_\mathrm{c} \\ &= \begin{bmatrix} \delta a & \delta\theta & \delta i & \delta q_1 & \delta q_2 & \delta\Omega \end{bmatrix}^T \end{aligned} \tag{2.19}$$

and the relative position and velocity expressed in the curvilinear frame is given by the state vector [55]

$$\boldsymbol{x} = \begin{bmatrix} x & \dot{x} & y & \dot{y} & z & \dot{z} \end{bmatrix}^T \tag{2.20}$$

The geometric transformation between the J_2-perturbed differential orbital elements and the curvilinear vector $\boldsymbol{x}(t)$ is given by

$$\boldsymbol{x}(t) = \left[\boldsymbol{M}(t) + \gamma\boldsymbol{N}(t)\right]\delta\boldsymbol{e}(t) \tag{2.21}$$

where $\gamma = 3J_2R_{eq}^2$, $J_2 = 1082.63(10^{-6})$ and $R_{eq} = 6378.137$ km is the equatorial radius of the Earth. The matrix $\boldsymbol{M}(t)$ maps the unperturbed elements into the state vector $\boldsymbol{x}(t)$ and the matrix $\boldsymbol{N}(t)$ contains the elements which are perturbed by J_2. For brevity, we define the matrix

$$\boldsymbol{\Sigma}(t) = \left[\boldsymbol{M}(t) + \gamma\boldsymbol{N}(t)\right] \tag{2.22}$$

The time evolution of the mean orbital elements, $\delta\bar{\boldsymbol{e}}$, due to the J_2 perturbation is given by

$$\delta\bar{\boldsymbol{e}}(t) = \bar{\boldsymbol{\phi}}_{\bar{\boldsymbol{e}}}(t, t_0)\delta\bar{\boldsymbol{e}}(t_0) \tag{2.23}$$

where $\bar{\boldsymbol{\phi}}_{\bar{\boldsymbol{e}}}(t, t_0)$ is the state transition matrix for the mean orbital elements. The differential osculating orbital elements, $\delta\boldsymbol{e}$ can be obtained from the mean elements by computing a matrix $\boldsymbol{D}(t)$ which is given by

$$\boldsymbol{D}(t) = \frac{\partial \boldsymbol{e}}{\partial \bar{\boldsymbol{e}}} = \mathbb{I}_{6\times 6} - J_2 R_{\text{eq}}^2 \left[\boldsymbol{D}^{(\text{lp})}(t) + \boldsymbol{D}^{(\text{sp})_1}(t) + \boldsymbol{D}^{(\text{sp})_2}(t)\right]$$

where (lp) and $(\text{sp})_{1,2}$ refer to long- and short- periodic variations in the elements due to the perturbation. The short-periodic variations occur on the scale of the orbit period. The long-periodic effects are typically manifested over a period of 20-60 days in LEO [128], so for maneuvers on the scale of about 12 hours, such as some of the examples presented in this paper, the long-periodic contribution will be negligible. The mean-to-osculating transformation is given by

$$\begin{aligned} \delta\boldsymbol{e}(t) &= \boldsymbol{D}(t)\delta\bar{\boldsymbol{e}} \\ &= \boldsymbol{D}(t)\bar{\boldsymbol{\phi}}_{\bar{\boldsymbol{e}}}(t, t_0)\delta\bar{\boldsymbol{e}}(t_0) \\ &= \boldsymbol{D}(t)\bar{\boldsymbol{\phi}}_{\bar{\boldsymbol{e}}}(t, t_0)\boldsymbol{D}^{-1}(t_0)\delta\boldsymbol{e}(t_0) \end{aligned} \tag{2.24}$$

Using this expression, the state transition matrix for the curvilinear coordinates $\boldsymbol{x}(t)$ under the influence of J_2 is given by

$$\begin{aligned} \boldsymbol{x}(t) &= \boldsymbol{\Sigma}(t)\boldsymbol{D}(t)\bar{\boldsymbol{\phi}}_{\bar{\boldsymbol{e}}}(t, t_0)\boldsymbol{D}^{-1}(t_0)\boldsymbol{\Sigma}^{-1}(t_0)\boldsymbol{x}(t_0) \\ &= \boldsymbol{\Phi}_{J_2}(t, t_0)\boldsymbol{x}(t_0) \end{aligned} \tag{2.25}$$

where $\boldsymbol{\Phi}_{J_2}(t, t_0)$ is the GA-STM. The elements of the GA-STM are quite long and complex, and the reader is encouraged to refer to [55] or [10] for the complete form[1]. The GA-STM is a closed-form, analytical approximation for the evolution of the deputy satellite relative to the chief under the first-order influence of J_2. In [55], Gim and Alfriend showed that this state transition matrix was valid for all eccentricities and inclinations with the exception of the critical inclination $5\cos^2 i = 1$. The results in [55] indicate that when compared to a nonlinear, numerical simulation of the basic orbit problem with the addition of the J_2-J_6 perturbations, the GA-STM experiences errors on the order of meters over the course of one day in LEO, where J_2 has the strongest effect. From this it may be concluded that this approach would be a useful model for trajectory optimization over long baselines or multiple orbits. Importantly, this model is a *linear* theory which allows for certain guarantees in the control design, e.g. global optimality etc.

[1] A complete Matlab implementation can be found at Github or by cloning the repository with the shell command `git clone git@github.com:acrAstro/satelliteCodes.git`. A companion python implementation is under development in `git@github.com:acrAstro/pysatellite.git`.

Another interesting aspect of the GA-STM is that it is numerically equivalent to the state transition matrix for the unperturbed linear equations of relative motion (LERM) if $J_2 = 0$.

In a later chapter the GA-STM is used to generate fuel-optimal trajectories which take several orbits to complete. Over several orbits, the differential effect of J_2 becomes non-negligible, and we illustrate this in Figure 2.5. Figure 2.5 shows the GA-STM and LERM with the initial condition constraint used in Eq. (2.13), and these two solutions are compared with the orbit equation and J_2-J_6 perturbations included, expressed in the curvilinear frame. The GA-STM is nearly identical to the nonlinear orbit. Conversely, the LERM present a dramatically different solution, and this motivates the use of the GA-STM for trajectory optimization. Initial conditions for J_2-invariant orbits exist which could be used with the GA-STM to ensure that no in-track drift occurs, however this was not used in this analysis.

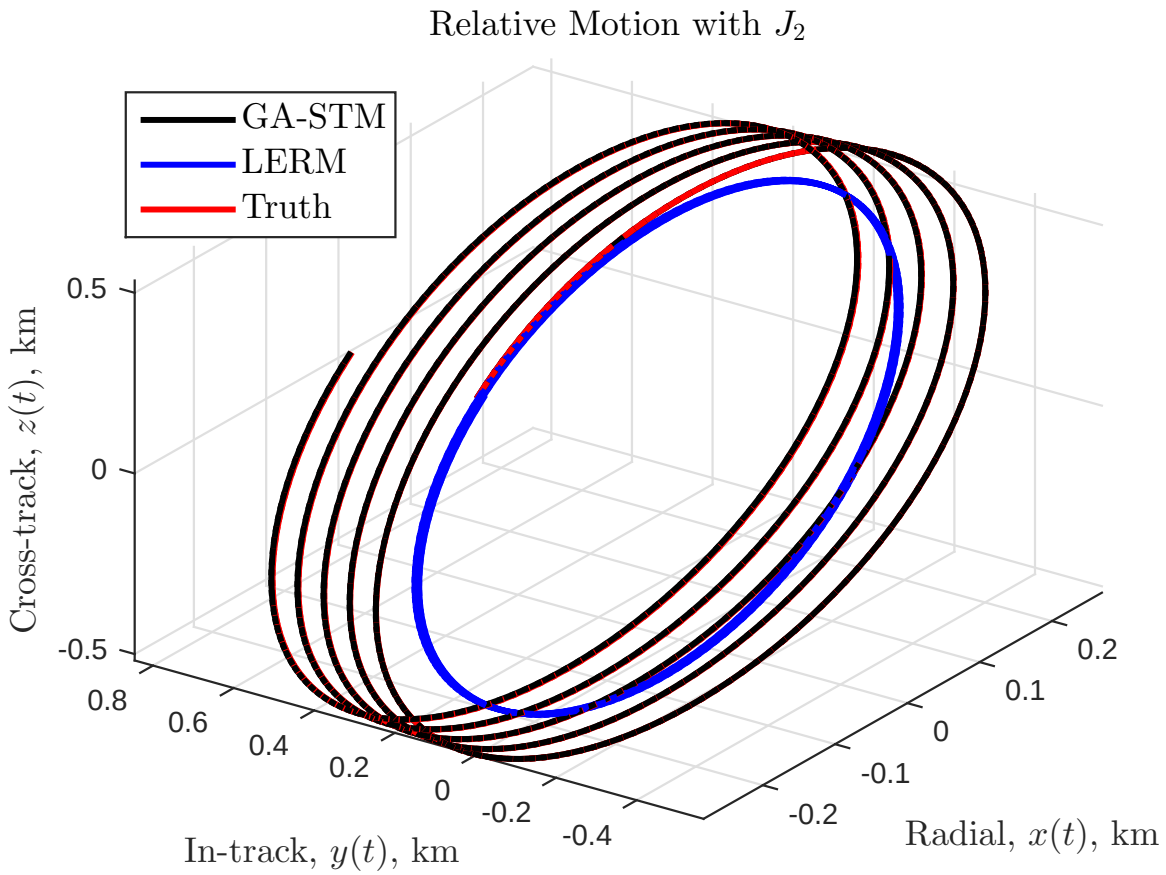

Figure 2.5: J_2 has a rather noticeable effect on the relative motion

2.1.5 Alternative Motion Models

Since the focus of this dissertation is on control design, only a few of the very many relative motion models are used, however, a few other popular models are mentioned here for further reading.

One very popular model is the Tschauner-Hempel model [135]. A change of basis is applied to the LERM which transforms the independent variable from time to true anomaly.

$$\begin{aligned} x'' &= \frac{3}{1+e\cos f}x + 2y' \\ y'' &= -2x' \\ z'' &= -z \end{aligned} \tag{2.26}$$

The benefit of this approach is a simpler state transition matrix than the one provided in [26]. The only downside to using this motion model is that the change of variables must be carefully accounted for when doing control design and analysis because the distances are rescaled by the similarity transformation.

Another model which can be used is the Kechichian system [75]. This model is an exact, nonlinear, time-varying system of differential equations which models relative motion near a dragging and precessing orbiting reference frame. It accounts for the effect of J_2 in terms of the osculating elements, so the resulting motion is more precise, however the highly complex nature of the system can make control design quite difficult.

Gaias *et al.* recently presented a state transition matrix for J_2-perturbed, near-circular relative motion with time-varying differential drag [51]. When used with a mapping from relative orbital elements to Cartesian variables, this model could be used for optimal control design or discrete-time feedback control similarly to the analysis presented on the Gim-Alfriend matrix in Chapter 5.

2.2 Gauss' Variational Equations

Gauss' Variational Equations (GVE) [24, 118, 117] are an exact system of differential equations subject to any number of orbital perturbations:

$$\begin{aligned}
\dot{a} &= \frac{2a^2}{h}\left(e\sin f a_r + \frac{p}{r}a_\theta\right) \\
\dot{e} &= \frac{1}{h}\left(p\sin f a_r + \left((p+r)\cos f + re\right)a_\theta\right) \\
(\dot{i}) &= \frac{r\cos\theta}{h}a_h \\
\dot{\Omega} &= \frac{r\sin\theta}{h\sin i}a_h \\
\dot{\omega} &= \frac{1}{he}\left(-p\cos f a_r + (p+r)\sin f a_\theta\right) - \frac{r\sin\theta\cos i}{h\sin i}a_h \\
\dot{M} &= n + \frac{b}{ahe}\left(\left(p\cos f - 2re\right)a_r - (p+r)\sin f a_\theta\right)
\end{aligned} \tag{2.27}$$

where Kepler's equation provides the relationship between mean anomaly, M, eccentric anomaly, E, and time

$$M = n(t - t_0) = E - e\sin E \tag{2.28}$$

and the eccentric anomaly is related to true anomaly through

$$\tan\left(\frac{f}{2}\right) = \sqrt{\frac{1+e}{1-e}}\tan\left(\frac{E}{2}\right) \tag{2.29}$$

where Eq. 2.27 allows the effect of any arbitrary perturbation on the orbital elements to be studied.

Remark 4. *For the GVE, the orbit cannot be perfectly circular; the Keplerian elements have singularities for circular orbits since argument of periapsis has little meaning when each point is simultaneously periapsis and apoapsis. Alternative forms of the GVE exist for nonsingular elements, equinoctial elements etc., and the reader may refer to [67, 130, 129].*

Two perturbations we consider, particularly in Chapter 6 are the J_2 perturbation and atmospheric drag. The *caveat* to using the GVE to predict the effect of a perturbation on the orbital elements is that the perturbation *must* be expressed in the LVLH reference frame. Consider J_2, which has the form [119]

$$\boldsymbol{a}_{J_2} = -\frac{3}{2}J_2\left(\frac{\mu}{R^2}\right)\left(\frac{R_{eq}}{R}\right)^2\begin{bmatrix}\left(1-5\left(\frac{Z}{R}\right)^2\right)\frac{X}{R} \\ \left(1-5\left(\frac{Z}{R}\right)^2\right)\frac{Y}{R} \\ \left(3-5\left(\frac{Z}{R}\right)^2\right)\frac{Z}{R}\end{bmatrix} \tag{2.30}$$

where $R = \sqrt{X^2 + Y^2 + Z^2}$.

Remark 5. *Simulation of the J_2 perturbation with the GVE requires that 1) at each time step the orbital elements are converted to positions and velocities in the inertial frame (see, for instance Vallado [128]) and 2) the mapping $\boldsymbol{R}_o^n$ be applied to the vector $\boldsymbol{a}_{J_2}$.*

Another perturbation that can have a substantial impact on orbital motion is atmospheric drag. The atmospheric drag acceleration can be written

$$\boldsymbol{a}_{drag} = -\left(\frac{A}{m}\right) C_D \rho \frac{V^2}{2} \hat{\boldsymbol{o}}_v \tag{2.31}$$

where $V = \sqrt{\dot{X}^2 + \dot{Y}^2 + \dot{Z}^2}$, C_D is the drag coefficient, A is the surface area in the velocity direction, m is the mass of the satellite, and $\hat{\boldsymbol{o}}_v$ is the orbital velocity vector expressed in the orbiting frame. The density, ρ can be computed in a number of ways; often an exponential model is used as a first attempt

$$\rho(R) = \rho_0 \boldsymbol{e}^{-\frac{(R - R_0)}{H}} \tag{2.32}$$

where ρ_0 and R_0 are the reference density and orbit radius (typically chosen to be radius and density at periapsis) and H is the atmospheric density scale height.

Remark 6. *Note that in general $\hat{\boldsymbol{o}}_v \neq \hat{\boldsymbol{o}}_\theta$; these vectors are only equal when the orbit is circular.*

The following transformation may be adopted to ensure that the drag perturbation is expressed in the appropriate frame [119]

$$\begin{bmatrix} \hat{\boldsymbol{o}}_r \\ \hat{\boldsymbol{o}}_\theta \end{bmatrix} = \frac{1}{\sqrt{1 + e^2 + 2e\cos f}} \begin{bmatrix} 1 + e\cos f & e\sin f \\ -e\sin f & 1 + e\cos f \end{bmatrix} \begin{bmatrix} \hat{\boldsymbol{o}}_n \\ \hat{\boldsymbol{o}}_v \end{bmatrix} \tag{2.33}$$

and its inverse

$$\begin{bmatrix} \hat{\boldsymbol{o}}_n \\ \hat{\boldsymbol{o}}_v \end{bmatrix} = \frac{1}{\sqrt{1 + e^2 + 2e\cos f}} \begin{bmatrix} 1 + e\cos f & -e\sin f \\ e\sin f & 1 + e\cos f \end{bmatrix} \begin{bmatrix} \hat{\boldsymbol{o}}_r \\ \hat{\boldsymbol{o}}_\theta \end{bmatrix} \tag{2.34}$$

In Chapter 6, the GVE with these perturbations will be used to simulate the controllers on a more realistic orbital model. In theory, any number of perturbations could be included, but for the mission profiles considered in this work, J_2 and atmospheric drag are by far the largest exogenous forces. In fact J_2 is three orders of magnitude larger than the J_3 perturbation.

2.3 Rigid Body Mechanics

Now, consider the motion of a rigid spacecraft in a circular orbit near the orbiting reference frame, seen in Figure 6.1. The rotation between the principal axes of the spacecraft and the orbiting reference frame, $\boldsymbol{R}_o^b$ for some arbitrary orientation can be parameterized by the 3-2-1 Euler angle sequence, where ψ is the yaw angle around the radial unit vector, θ is the pitch angle around the cross-track unit vector, and ϕ is the roll angle about the in-track unit vector, seen in Figure 2.6. The angular velocity of the body with respect to the inertial frame is

$$\boldsymbol{\omega}_n^b = \boldsymbol{\omega}_o^b + \boldsymbol{R}_o^b \boldsymbol{\omega}_n^o \implies \dot{\boldsymbol{\omega}}_n^b = \dot{\boldsymbol{\omega}}_o^b + \dot{\boldsymbol{R}}_o^b \boldsymbol{\omega}_n^o \tag{2.35}$$

where $\boldsymbol{\omega}_n^o = \begin{bmatrix} 0 & 0 & -n \end{bmatrix}^T$ is the constant angular velocity of the orbiting frame with respect to the inertial frame (because we assume the motion is in a circular orbit), and $\boldsymbol{\omega}_n^b$ is the body angular velocity with respect to the orbiting frame. The time-derivative of $\boldsymbol{R}_o^b$ is

$$\dot{\boldsymbol{R}}_o^b = -S(\boldsymbol{\omega}_o^b)\boldsymbol{R}_o^b \tag{2.36}$$

The angular rates in terms of the 3-2-1 Euler angles is

$$\begin{bmatrix} \dot{\psi} \\ \dot{\phi} \\ \dot{\theta} \end{bmatrix} = \frac{1}{\cos\phi} \begin{bmatrix} 0 & \sin\theta & \cos\theta \\ 0 & \cos\phi\cos\theta & -\cos\phi\sin\theta \\ \cos\phi & \sin\phi\sin\theta & \sin\phi\cos\theta \end{bmatrix} \boldsymbol{\omega}_o^b \tag{2.37}$$

The angular displacement of the body axes with respect to the orbiting frame can also be parameterized by the quaternions $\bar{\boldsymbol{q}} = \begin{bmatrix} q_0 & \boldsymbol{q}^T \end{bmatrix}^T$, and the rotation matrix of the body axes with respect to orbiting axes is

$$\boldsymbol{R}_o^b = \begin{bmatrix} q_0^2 + q_1^2 - q_2^2 - q_3^2 & 2(q_1q_2 + q_0q_3) & 2(q_1q_3 - q_0q_2) \\ 2(q_1q_2 - q_0q_3) & q_0^2 - q_1^2 + q_2^2 - q_3^2 & 2(q_2q_3 + q_0q_1) \\ 2(q_1q_3 + q_0q_2) & 2(q_2q_3 - q_0q_1) & q_0^2 - q_1^2 - q_2^2 + q_3^2 \end{bmatrix} \tag{2.38}$$

which can be written more elegantly using the Rodrigues formula

$$\boldsymbol{R}_o^b(\bar{\boldsymbol{q}}) = \mathbb{I}_{3\times 3} + 2q_0 S(\boldsymbol{q}) + 2S^2(\boldsymbol{q}) \tag{2.39}$$

The kinematic equations in terms of quaternions are

$$\begin{bmatrix} \dot{q}_0 \\ \dot{\boldsymbol{q}} \end{bmatrix} = \frac{1}{2} \begin{bmatrix} -\boldsymbol{q}^T \\ [q_0 \mathbb{I}_{3\times 3} + S(\boldsymbol{q})] \end{bmatrix} \boldsymbol{\omega}_o^b \tag{2.40}$$

and the kinematic relationships between the 3-2-1 Euler sequence and kinematics, the mapping between the angular velocities, and associated Euler angle rates are provided in [119, 70, 133]. The dynamic equations including the gravity gradient torque are

$$\dot{\boldsymbol{\omega}}_o^b = \boldsymbol{I}^{-1}\left(-S(\boldsymbol{\omega}_n^b)\boldsymbol{I}\boldsymbol{\omega}_n^b + 3n^2 S(\boldsymbol{r}_1(\bar{\boldsymbol{q}}))\boldsymbol{I}\boldsymbol{r}_1(\bar{\boldsymbol{q}}) + \boldsymbol{\tau}\right) + S(\boldsymbol{\omega}_o^b)\boldsymbol{R}_o^b(\bar{\boldsymbol{q}})\boldsymbol{\omega}_n^o \tag{2.41}$$

where $\boldsymbol{I}$ is the inertia matrix of the satellite, $\boldsymbol{\tau}$ is the control torque and $\boldsymbol{r}_1(\bar{\boldsymbol{q}})$ is the first column of the matrix $\boldsymbol{R}_o^b(\bar{\boldsymbol{q}})$ [133]. Eq (2.41) can be linearized around the equilibrium $\begin{bmatrix}\bar{\boldsymbol{q}}^T & (\boldsymbol{\omega}_o^b)^T\end{bmatrix}^T = \begin{bmatrix}1 & \boldsymbol{0}_{1\times 6}\end{bmatrix}^T$ to yield the state matrix

$$\boldsymbol{A}^r = \begin{bmatrix} 0 & 0 & 0 & 0 & 0 & 0 & 0 \\ 0 & 0 & 0 & 0 & 1/2 & 0 & 0 \\ 0 & 0 & 0 & 0 & 0 & 1/2 & 0 \\ 0 & 0 & 0 & 0 & 0 & 0 & 1/2 \\ 0 & 2n^2\frac{(I_2-I_3)}{I_1} & 0 & 0 & 0 & n\frac{(I_1-I_2+I_3)}{I_1} & 0 \\ 0 & 0 & 8n^2\frac{(I_1-I_3)}{I_2} & 0 & -n\frac{(I_2-I_1+I_3)}{I_2} & 0 & 0 \\ 0 & 0 & 0 & 6n^2\frac{(I_1-I_2)}{I_3} & 0 & 0 & 0 \end{bmatrix} \tag{2.42}$$

and the input matrix

$$\boldsymbol{B}^r = \begin{bmatrix}\boldsymbol{0}_{3\times 4} & \boldsymbol{I}^{-1}\end{bmatrix}^T \tag{2.43}$$

and I_i are the principal moments of inertia. The superscript r indicates the the system describes the rotational dynamics.

Remark 7. *Inspection of Eq.* (2.42) *reveals that the linear state matrix is rank-deficient. Furthermore the pair* $(\boldsymbol{A}^r, \boldsymbol{B}^r)$ *is linearly uncontrollable; however it is stabilizable. This is a result of the quaternion constraint* $\bar{\boldsymbol{q}}^T\bar{\boldsymbol{q}} = 1$. *The redundancy of the quaternion parameterization leads to a one-dimensional, uncontrollable subspace. A different parameterization such as Euler angles or modified Rodrigues parameters can circumvent this, however for model predictive control, this does not significantly affect the control design.*

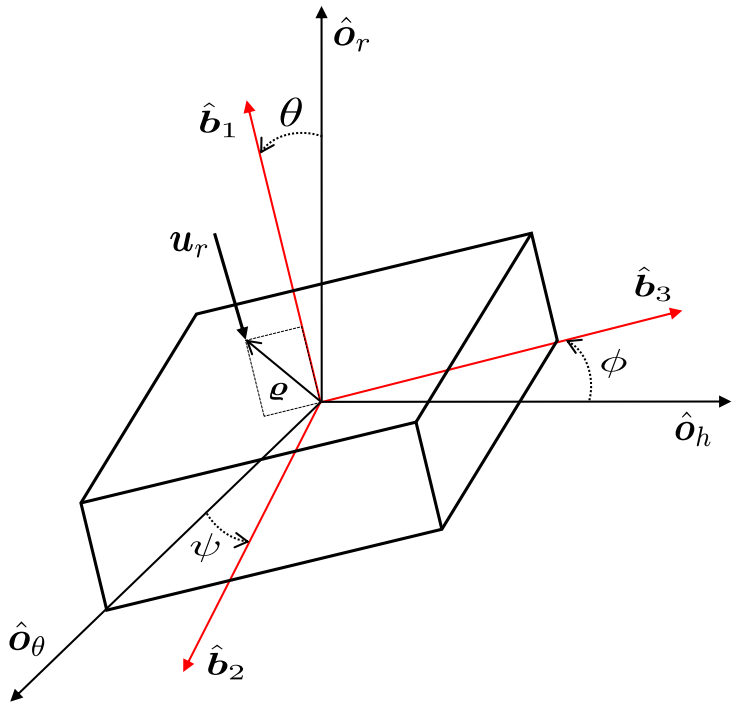

Figure 2.6: Spacecraft body axes relative to orbiting axes

2.4 Optimal Control

In this section, we discuss the Pontryagin Maximum Principle (PMP), and talk briefly about the differences between direct and indirect methods in optimal control.

2.4.1 The Pontryagin Principle

Suppose a system with n states and m control inputs is described by the differential equation [28]

$$\dot{\boldsymbol{x}}(t) = \boldsymbol{f}(\boldsymbol{x}(t), \boldsymbol{u}(t), t) \tag{2.44}$$

where $\boldsymbol{f} : \mathbb{R}^n \times \mathbb{R}^m \mapsto \mathbb{R}^n$ and $t \in \mathbb{R}^+$. Define the set of admissible control signals by $\Omega \subseteq \mathbb{R}^m$. Given an initial set $\boldsymbol{X}_0$ and target set $\boldsymbol{X}_f$, the optimal controller is a piecewise continuous signal $\boldsymbol{u}(t) \in \Omega \subseteq \mathbb{R}^m$, *e.f.* which steers $\boldsymbol{X}_0 \mapsto \boldsymbol{X}_f$ and minimizes the functional $J = \mathbb{R}^n \times \mathbb{R}^m \times \mathbb{R} \mapsto \mathbb{R}$

$$J = \int_{t_0}^{t_f} \ell(\boldsymbol{x}(\tau), \boldsymbol{u}(\tau), \tau)) \, \mathrm{d}\, \tau + \Psi(\boldsymbol{x}(t_f)) \tag{2.45}$$

and maximizes the Hamiltonian

$$\begin{aligned} \hat{\mathcal{H}}(\hat{\boldsymbol{x}}^*(t), \hat{\boldsymbol{\eta}}^*(t)), \boldsymbol{u}^*(t)) &= \arg\max_{\boldsymbol{u} \in \Omega} \, \hat{\mathcal{H}}(\hat{\boldsymbol{x}}^*(t), \hat{\boldsymbol{\eta}}^*(t)), \boldsymbol{u}(t)) \\ &= \arg\max_{\boldsymbol{u} \in \Omega} \, \eta_\ell \, \ell(\boldsymbol{x}(t), \boldsymbol{u}(t), t)) + \boldsymbol{\eta}^T(t) \left[\boldsymbol{f}(\boldsymbol{x}(t), \boldsymbol{u}(t), t) \right] \end{aligned} \tag{2.46}$$

where $(\cdot)^*$ denotes an optimal value. Furthermore, there exists a non-trivial solution to the augmented state and adjoint equations

$$\begin{aligned} \begin{bmatrix} \dot{x}_\ell(t) \\ \dot{\boldsymbol{x}}(t) \end{bmatrix} &= \begin{bmatrix} \ell(\boldsymbol{x}(t), \boldsymbol{u}(t), t) \\ \boldsymbol{f}(\boldsymbol{x}(t), \boldsymbol{u}(t), t) \end{bmatrix} \\ \dot{\hat{\boldsymbol{\eta}}} &= - \begin{bmatrix} 0 & \boldsymbol{0}_{n \times n} \\ \nabla_{\boldsymbol{x}} \ell(\hat{\boldsymbol{x}}^*(t), \boldsymbol{u}^*(t), t) & [\mathbb{J}_{\boldsymbol{x}} \boldsymbol{f}(\hat{\boldsymbol{x}}^*(t), \boldsymbol{u}^*(t), t)]^T \end{bmatrix}^T \hat{\boldsymbol{\eta}} \end{aligned} \tag{2.47}$$

where $\hat{\boldsymbol{\eta}}(t) \triangleq \begin{bmatrix} \eta_\ell(t) & \boldsymbol{\eta}^T(t) \end{bmatrix}^T$ and $\hat{\boldsymbol{x}}(t) \triangleq \begin{bmatrix} x_\ell(t) & \boldsymbol{x}^T(t) \end{bmatrix}^T$ with the terminal condition

$$\Psi(\boldsymbol{x}(t_f)) + \hat{\mathcal{H}}(\boldsymbol{x}(t_f), \boldsymbol{\eta}^*(t_f), \boldsymbol{u}(t_f)) = 0 \tag{2.48}$$

If $\boldsymbol{X}_f$ is not fixed, then

$$\boldsymbol{\eta}(t_f) = \left. \frac{\partial \Psi(\boldsymbol{x}(t_f))}{\partial \boldsymbol{x}} \right|_{\boldsymbol{x}(t) = \boldsymbol{x}(t_f)} \tag{2.49}$$

If $\boldsymbol{X}_{0,f}$ are fixed, the initial and final values of the optimal co-states may be selected to satisfy the transversality conditions

$$\boldsymbol{\eta}^*(t_0) \perp \mathbb{T}_0 \quad \boldsymbol{\eta}^*(t_f) \perp \mathbb{T}_f \tag{2.50}$$

where $\mathbb{T}_{0,f}$ are the spaces tangent to the boundary conditions $\boldsymbol{X}_{0,f}$, respectively. The optimal control problems in this paper are point-to-point problems, which implies that $\mathbb{T}_{0,f} = \mathbf{0}$ and are always satisfied; the transversality conditions provide no further information for solving the boundary value problem, however this was not detrimental to the solutions in this work. Furthermore, for fixed t_f, it is necessary for the Hamiltonian evaluated at the optimal states, co-states and controls to be constant:

$$\hat{\mathcal{H}}(\boldsymbol{x}^*(t), \boldsymbol{\eta}^*(t), \boldsymbol{u}^*(t)) = C^* \tag{2.51}$$

where C^* is an arbitrary constant. Additionally, since $\eta_\ell \neq 0$, it is very common to define the Lagrange multiplier $\boldsymbol{\lambda} = \boldsymbol{\eta}/\eta_\ell$. This definition is used in Chapter 4.

The above developments comprise Pontryagin's Maximum Principle (PMP), which is a necessary condition for the minimization of a functional. The dynamic optimization problem is constrained by the adjoint equations (also called co-states) which are time-varying Lagrange multipliers. If $\Psi(\boldsymbol{x}(t_f)) = 0$ and the problem contains only the running cost (the integral term) then the functional is called a Lagrangian functional; if only the terminal condition is present, then the functional is called a Mayer function. If both terms are present then the functional is called a Bolza functional.

2.4.2 Indirect vs Direct Methods

The PMP is a powerful, general tool for solving optimal control problems, but frequently results in $2n$-dimensional boundary value problems which are not always easily solved. The PMP is known as an *indirect* method wherein the necessary conditions are applied and candidate extrema are identified. Further analysis is typically required to determine whether an extremum is a weak local extremal, strong local extremal etc. [17].

Another approach entirely is to discretize and transcribe the infinite dimensional functional optimization problem into a finite dimensional parameter optimization problem (where the parameters are the states and controls). This is the method applied by software such as GPOPS-II [102]. GPOPS-II uses an *hp*-adaptive, Legendre-Gauss-Radau quadrature, orthogonal collocation method that transcribes the continuous-time optimal control problem to a sparse, nonlinear programming problem (NLP). After the NLP has been solved, the necessary conditions may then be applied to the resulting solution to verify optimality [106].

If the cost function has certain structure (e.g. convexity) and the dynamics/ constraints are linear, then it would make sense to exploit this structure during transcription. Discretizing a linear problem using a zero-order-hold (ZOH) can result in a convex optimization problem (e.g. linear program (LP) or quadratic program (QP) [125, 2] or second-order cone program (SOCP) [18]), which can be solved very efficiently using well-known techniques such as interior point methods etc. [21]. This type of transcription, as well as combinatorial programming extensions (e.g. mixed-integer linear programming or MILP) will be used exclusively in Chapters 5 and 6.

The advantage to transcribing a problem to a convex program is that, despite putting some restrictions on the type of problem one can solve (e.g. nonlinear dynamics can't be used), the resulting optimization problem is guaranteed to be globally optimal due to convexity. As a result, the necessary conditions no longer need to be applied to verify the optimality as they would in a technique such as pseudo-spectral collocation. On the other hand, the optimality of the solution to the convex program only holds in the limit that the linear problem accurately captures the system's behavior. The global optimum of the convex program is not necessarily the optimum of the true nonlinear system.

2.4.3 Controllability and the Minimum Energy Transfer

Some optimal control problems can be solved purely by using the structural properties of linear systems. Consider a linear, time-varying system of the form

$$\dot{\boldsymbol{x}} = \boldsymbol{A}(t)\boldsymbol{x} + \boldsymbol{B}(t)\boldsymbol{u}, \quad \boldsymbol{x}(t_0) = \boldsymbol{x}_0 \tag{2.52}$$

The system is controllable if there exists a piecewise continuous control signal on the interval $t \in [t_0, t_f]$ which drives the system from an initial state $\boldsymbol{x}(t_0)$ to a terminal state $\boldsymbol{x}(t_f)$. The solution to the general linear time-varying system is given by the variation of constants formula

$$\boldsymbol{x}(t_f) = \boldsymbol{\Phi}(t_f, t_0)\boldsymbol{x}_0 + \int_{t_0}^{t_f} \boldsymbol{\Phi}(t_f, \tau)\boldsymbol{B}(\tau)\boldsymbol{u}(\tau)\,\mathrm{d}\,\tau \tag{2.53}$$

where $\boldsymbol{\Phi}(t_f, t)$ is the state transition matrix. To find the input signal $\boldsymbol{u}(t)$ which would drive the system to $\boldsymbol{x}(t_f)$, we use the properties of the linear, time-varying system. First, we pre-multiply both sides of Eq. (2.53) by $\boldsymbol{\Phi}(t_0, t_f)$ and solve for the initial state

$$\boldsymbol{x}_0 = -\int_{t_0}^{t_f} \boldsymbol{\Phi}(t_0, \tau)\boldsymbol{B}(\tau)\boldsymbol{u}(\tau)\,\mathrm{d}\,\tau$$

This defines a linear operator $L(\boldsymbol{u}(t)) : \boldsymbol{C}^m[t_0, t_f] \to \mathbb{R}^n$ [25]. The range-space of this operator defines the set of initial conditions, $\boldsymbol{x}(t_0)$, for which a control signal $\boldsymbol{u} \in C^m[t_0, t_f]$ can drive the state to another state, $\boldsymbol{x}(t_f)$, in a finite time, t_f. Now, the adjoint of the linear operator $L(\cdot)$ is $L^*(\boldsymbol{u}(t)) : \mathbb{R}^n \to C^m[t_0, t_f]$ and is defined by requiring that

$$\langle L(\boldsymbol{u}), \boldsymbol{x}\rangle_{\mathbb{R}^n} = \langle \boldsymbol{u}, L^*(\boldsymbol{x})\rangle_{C^m} \tag{2.54}$$

where $\langle \cdot, \cdot \rangle$ denotes the inner product. By definition, the range of $L(\cdot)$ is in $\mathbb{R}^n$, and the range of $L(\cdot)$ composed with its adjoint, $\mathcal{R}(L \circ L^*)$, is also in $\mathbb{R}^n$, so we can say $\mathcal{R}(L) = \mathcal{R}(L \circ L^*) \in \mathbb{R}^n$. For the left-hand side of Eq. 2.54, we can use the standard inner product on $\mathbb{R}^n$ to write

$$\begin{aligned}\langle L(\boldsymbol{u}), \boldsymbol{x}\rangle_{\mathbb{R}^n} &= \left(-\int_{t_0}^{t_f} \boldsymbol{\Phi}(t_0, \tau)\boldsymbol{B}(\tau)\boldsymbol{u}(\tau)\,\mathrm{d}\,\tau\right)^T \boldsymbol{x} \\ &= -\int_{t_0}^{t_f} \boldsymbol{u}^T(\tau)\boldsymbol{B}^T(\tau)\boldsymbol{\Phi}^T(t_0, \tau)\boldsymbol{x}\,\mathrm{d}\,\tau\end{aligned}$$

For the right-hand side, the inner product on $C^m[t_0, t_f]$ is

$$\langle \boldsymbol{u}, L^*(\boldsymbol{x}) \rangle_{C^m} = -\int_{t_0}^{t_f} \boldsymbol{u}^T(\tau) \boldsymbol{B}^T(\tau) \boldsymbol{\Phi}^T(t_0, \tau) \boldsymbol{x} \, \mathrm{d}\, \tau$$

The adjoint operator of $L(\cdot)$ is then

$$L^*(\boldsymbol{x}) = -\boldsymbol{B}^T(t) \boldsymbol{\Phi}^T(t_0, t) \boldsymbol{x}$$

The composition of the linear operator L and its adjoint L^* is

$$\begin{aligned} L(L^*(\boldsymbol{x})) &= L\left(-\boldsymbol{B}^T(t) \boldsymbol{\Phi}^T(t_0, t)\right) \\ &= \left(\int_{t_0}^{t_f} \boldsymbol{\Phi}(t_0, \tau) \boldsymbol{B}(\tau) \boldsymbol{B}^T(\tau) \boldsymbol{\Phi}^T(t_0, \tau) \, \mathrm{d}\, \tau \right) \boldsymbol{x} \\ &= \boldsymbol{W}_{\mathrm{c}}(t_0, t_f) \boldsymbol{x} \end{aligned}$$

The matrix $\boldsymbol{W}_{\mathrm{c}}(t_0, t_f)$ is the controllability Gramian which defines the operator $L \circ L^* : \mathbb{R}^n \to \mathbb{R}^n$. We require that $\mathcal{R}(L \circ L^*) = \mathbb{R}^n$ which can only be the case if the Gramian is invertible (i.e. has full rank). One controller that drives $\boldsymbol{x}(t_0) = \boldsymbol{x}_0$ to $\boldsymbol{x}(t_f) = \boldsymbol{x}_f$ is given by

$$\boldsymbol{u}^*(t) = -\boldsymbol{B}^T(t) \boldsymbol{\Phi}^T(t_0, t) \boldsymbol{W}_{\mathrm{c}}^{-1}(t_0, t_f) \left(\boldsymbol{x}_0 - \boldsymbol{\Phi}(t_0, t_f) \boldsymbol{x}_f \right) \tag{2.55}$$

where $\boldsymbol{W}_{\mathrm{c}}(t_0, t_f)$ is the controllability Gramian. This controller also minimizes the $\mathcal{L}_2$ energy of the cost function [28] where $\mathcal{L}_2$ is the set of square-integrable functions. In terms of the operators we used to define it, the control law is

$$\boldsymbol{u}^*(t) = L^* \circ (L \circ L^*)^{-1} \left(\boldsymbol{x}_0 - \boldsymbol{\Phi}(t_0, t_f) \boldsymbol{x}_f \right) \tag{2.56}$$

The form $L^* \circ (L \circ L^*)^{-1}$ provides the least-square solution to the under-determined problem of finding a control history that drives the system from $\boldsymbol{x}_0$ to $\boldsymbol{x}_f$.

Remark 8. *This is analogous to manner in which the Moore-Penrose pseudoinverse of a non-square matrix gives a least-square solution to an underdetermined system of linear equations [25]. Note that since this is a least-squares problem constrained by linear dynamics,* $\boldsymbol{u}^*(t)$ *is actually a* global *optimum by convexity [36].*

Chapter 3

Analytical Control Law for Under-actuated, Low-Thrust Formation Reconfiguration

3.1 Introduction

In this chapter, an analytical control law for input-energy-optimal, under-actuated spacecraft relative reconfiguration is derived using the Pontryagin Principle and then verified using the controllability Gramian. Over short time scales, the linearized equations of motion for spacecraft relative motion closely agree with the nonlinear model [112], which makes trajectory optimization using linear techniques useful. The Pontryagin Principle provides only a necessary condition for optimality, however the controllability Gramian provides a necessary and sufficient condition for optimality. The control law that results from using the Gramian is identical to the control law derived using the Pontryagin Principle for the linear system.

Minimum energy transfers near circular orbits, and more generally, Keplerian orbits have been studied quite extensively in the literature. Notable works include Carter and Humi [32], Carter [31], Guelman and Aleshin [57], Pearson [103] and Zanetti [139] . For rendezvous or formation reconfiguration over very small relative distances (when compared with the chief orbit), the Hill-Clohessy-Wiltshire model [35] is typically used because it is a linear, time-invariant approximation of the relative motion, enabling the use of a wide range of tools for analysis and control design. This model assumes a perturbation-free, circular orbit as its reference orbit. In this note, we adopt the HCW model assuming that the formation reconfiguration takes place quickly, so that the circular orbit approximation is reasonable.

Earlier analyses have assumed that thrust is available in all three directions (radial, in-track and cross-track), in which case the system is completely controllable.The system is also

controllable, however, in the case that thrust is available only in the in-track and cross-track directions. McVittie *et al.* [97] used this fact in their work on formation keeping. The under-actuated controllability of the HCW model (and of the general spacecraft relative motion model [111]) is useful property for two reasons. The first is concerned with the mechanical complexity of a satellite; fewer required thrusters means fewer parts that could fail. The second is system robustness; if a single thruster fails for a fully-actuated spacecraft, the system may remain controllable with a reduced number of thrusters. The only requirement is that control authority be maintained in the in-track and cross-track directions.

Independently of the developments in this Chapter, Huang *et al.* used the Pontryagin Principle to derive optimal controllers for under-actuated rendezvous and reconfiguration [68]. This work differs from their approach in the following ways: 1) we give explicit analytical expressions for the control laws over any time-of-flight, both in their full form and for certain specific maneuvers where they are significantly simplified, 2) we provide necessary and sufficient conditions for global optimality of the under-actuated control laws using results from calculus of variations as well as linear operator theory, and 3) we derive an explicit controllability Gramian, which is also valid over any time-of-flight.

The contribution of this chapter is an analytical control law for linearized, under-actuated satellite rendezvous which is guaranteed to minimize the control energy for any time-of-flight $t_f > 0$. The control law is computed first using the Pontryagin Principle, and then verified using the controllability Gramian. The Pontryagin Principle provides necessary conditions for a strong local optimum. Derivation of the controllability Gramian simultaneously provides neccesary and sufficient conditions for controllability as well as a sufficient condition for globally optimal control. We derive the control law and Gramian explicitly for any arbitrary time-of-flight.

3.2 HCW Model

The HCW equations are a widely known model for satellite relative motion near a circular orbit, and are often used in the study of formation flying. Recalling Eq. (2.14) the HCW equations with control forces are:

$$\begin{aligned} \ddot{x} &= 3n^2 x + 2n\dot{y} + u_x \\ \ddot{y} &= -2n\dot{x} + u_y \\ \ddot{z} &= -n^2 z + u_z \end{aligned} \tag{3.1}$$

where $n = \sqrt{\mu/a^3}$ is the mean angular velocity of the chief orbit (μ is the gravitational parameter and a is the orbit semi-major axis). It is easiest to work with the dynamics in normalized form; we scale the distances by the semi-major axis a and set $\mu = 1$, which yields an angular velocity of $n = 1$. We focus on the case when $u_x = 0$; the system is controllable with u_y and u_z only. The state space form form of the HCW equations with only in-track

and cross-track thrust is

$$\dot{\boldsymbol{x}} = \begin{bmatrix} 0 & 0 & 0 & 1 & 0 & 0 \\ 0 & 0 & 0 & 0 & 1 & 0 \\ 0 & 0 & 0 & 0 & 0 & 1 \\ 3 & 0 & 0 & 0 & 2 & 0 \\ 0 & 0 & 0 & -2 & 0 & 0 \\ 0 & 0 & -1 & 0 & 0 & 0 \end{bmatrix} \begin{bmatrix} x \\ y \\ z \\ \dot{x} \\ \dot{y} \\ \dot{z} \end{bmatrix} + \begin{bmatrix} 0 & 0 \\ 0 & 0 \\ 0 & 0 \\ 0 & 0 \\ 1 & 0 \\ 0 & 1 \end{bmatrix} \begin{bmatrix} u_y \\ u_z \end{bmatrix} \tag{3.2}$$

It can be shown that a periodic, closed, relative orbit exists for any initial conditions which satisfy the constraint

$$\dot{y}_0 + 2x_0 = 0 \tag{3.3}$$

which will be referred to as the commensurability conditions. This condition can be understood in the context of the mechanical energy of two separate, circular orbits. Given two orbits with specific energy

$$\mathcal{H}_{1,2} = -\frac{\mu}{2a_{1,2}} \tag{3.4}$$

the orbits will not drift apart (under the restricted, two-body approximation) provided that $\mathcal{H}_1 = \mathcal{H}_2$, which requires that the semi-major axes must be the same [10, 74].

3.3 Optimal Control

The HCW equations are controllable when three inputs (radial, in-track, and cross-track), but this system is also controllable when only in-track and cross-track inputs are used. This property is used to find a minimum energy controller which transfers the spacecraft in the relative frame from some initial state $\boldsymbol{x}_0$ to a final state $\boldsymbol{x}_f$. The control energy is

$$J(\boldsymbol{u}(t), t) = \frac{1}{2} \int_{t_0}^{t_f} \boldsymbol{u}^T(\tau)\boldsymbol{u}(\tau)\, \mathrm{d}\,\tau \tag{3.5}$$

The Pontryagin Principle can be used to find a control law which minimizes Eq. (3.5). Define an augmented Hamiltonian

$$\hat{\mathcal{H}} = \frac{1}{2}\boldsymbol{u}^T(t)\boldsymbol{u}(t) + \boldsymbol{\lambda}^T(t)(\boldsymbol{A}\boldsymbol{x}(t) + \boldsymbol{B}\boldsymbol{u}(t)) \tag{3.6}$$

where $\boldsymbol{\lambda}(t)$ is a vector of Lagrange multipliers which constrain the optimization. A necessary condition for a weak local minimum is the stationarity condition [72]

$$\left.\frac{\partial \hat{\mathcal{H}}}{\partial \boldsymbol{u}(t)}\right|_{\boldsymbol{u}(t)=\boldsymbol{u}^*(t)} = 0 \tag{3.7}$$

The optimal control has the following form

$$\begin{bmatrix} u_y^*(t) \\ u_z^*(t) \end{bmatrix} = - \begin{bmatrix} \lambda_5^*(t) \\ \lambda_6^*(t) \end{bmatrix} \tag{3.8}$$

where $\lambda_{5,6}^*(t)$ are non-trivial solutions to the adjoint equation

$$\dot{\boldsymbol{\lambda}} = -\boldsymbol{A}^T \boldsymbol{\lambda}(t),\ \boldsymbol{\lambda}(t_0) = \boldsymbol{\lambda}_0 \tag{3.9}$$

Now, it is required to solve the adjoint equation, but the initial value $\boldsymbol{\lambda}_0$ is unknown. Assuming that $\boldsymbol{x}_0$ and $\boldsymbol{x}_f$ are known, the resulting boundary value problem may be analytically solved. The Hamiltonian boundary value problem is written in state space in the following form

$$\begin{bmatrix} \dot{\boldsymbol{x}}(t) \\ \dot{\boldsymbol{\lambda}}(t) \end{bmatrix} = \underbrace{\begin{bmatrix} \boldsymbol{A} & -\boldsymbol{B}\boldsymbol{B}^T \\ \boldsymbol{0}_{6\times 6} & -\boldsymbol{A}^T \end{bmatrix}}_{=\hat{\boldsymbol{A}}} \begin{bmatrix} \boldsymbol{x}(t) \\ \boldsymbol{\lambda}(t) \end{bmatrix} \tag{3.10}$$

where $\hat{\boldsymbol{A}}$ is the Hamiltonian matrix and the matrix $\boldsymbol{B}\boldsymbol{B}^T$ is all zeros except the $(5,5)$ and $(6,6)$ position which are -1. Since $\hat{\boldsymbol{A}}$ is time-invariant, the matrix exponential may be used again to determine the evolution of the states and adjoints. Choosing a time-of-flight at which $\boldsymbol{x}(t) = \boldsymbol{x}(t_f)$, the solution is partitioned into blocks

$$\begin{bmatrix} \boldsymbol{x}(t_f) \\ \boldsymbol{\lambda}(t_f) \end{bmatrix} = \begin{bmatrix} \boldsymbol{\Phi}_{\boldsymbol{x}\boldsymbol{x}}(t_f, 0) & \boldsymbol{\Phi}_{\boldsymbol{x}\boldsymbol{\lambda}}(t_f, 0) \\ \boldsymbol{\Phi}_{\boldsymbol{\lambda}\boldsymbol{x}}(t_f, 0) & \boldsymbol{\Phi}_{\boldsymbol{\lambda}\boldsymbol{\lambda}}(t_f, 0) \end{bmatrix} \begin{bmatrix} \boldsymbol{x}(t_0) \\ \boldsymbol{\lambda}(t_0) \end{bmatrix} \tag{3.11}$$

Note that $\boldsymbol{\Phi}_{\boldsymbol{\lambda}\boldsymbol{x}}(t_f, 0) = \boldsymbol{0}_{6\times 6}$. Now, the initial values for the adjoint equations may be computed. From Eq. (3.11), it is straightforward to write

$$\boldsymbol{x}(t_f) = \boldsymbol{\Phi}_{\boldsymbol{x}\boldsymbol{x}}(t_f, 0)\boldsymbol{x}(t_0) + \boldsymbol{\Phi}_{\boldsymbol{x}\boldsymbol{\lambda}}(t_f, 0)\boldsymbol{\lambda}(t_0) \tag{3.12}$$

This can be rearranged to solve for $\boldsymbol{\lambda}(t_0)$

$$\boldsymbol{\lambda}(t_0) = \boldsymbol{\Phi}_{\boldsymbol{x}\boldsymbol{\lambda}}^{-1}(t_f, 0)\left[\boldsymbol{x}(t_f) - \boldsymbol{\Phi}_{\boldsymbol{x}\boldsymbol{x}}(t_f, 0)\boldsymbol{x}(t_0)\right] \tag{3.13}$$

The initial conditions on the adjoint variables may be used to compute the adjoint solution at t_f. Recalling the definition of the optimal control from Eq. (3.8), the optimal control in the in-track direction is

$$u_y(t; t_f) = \sum_{i=1}^{8} q_i \tag{3.14}$$

where the terms q_{1-4} depend on the initial and final positions and the terms q_{5-8} depend on the initial and final velocities, seen in Eq. (3.16) and (3.17). The expressions are lengthy, and the following substitutions are made to condense the equations

$$\begin{aligned} S_t &= \sin t & C_t &= \cos t \\ S_{t_f} &= \sin t_f & C_{t_f} &= \cos t_f \end{aligned} \tag{3.15}$$

The terms q_{1-4} are

$$
\begin{aligned}
q_1 &= x_0\big(-\big(-384t_f^2S_tC_{t_f}+96C_tt_f^2S_{t_f}+1744S_tC_{t_f}+128C_tS_{t_f}\\
&\quad+144C_{t_f}S_{t_f}+144C_tt_f^3+t252t_f^2C_{t_f}-628C_tt_f+680C_tt_fC_{t_f}\\
&\quad-544t_fC_{t_f}-1158tC_{t_f}+36t_f^4S_t+t27t_f^3S_{t_f}-36t_f^3S_tS_{t_f}-492t_f^2S_t\\
&\quad-75t_f^2S_{t_f}-t1254t_fS_{t_f}+1928t_fS_tS_{t_f}-102S_{t_f}-t27t_f^4-117t_f^3\\
&\quad+t315t_f^2+502t_f+90\sin(t-2t_f)-54t\cos(2t_f)-1834S_t+1212t\big)\big)\\
q_2 &= 2x_f\big(64S_tC_{t_f}-52C_tS_{t_f}+32C_tt_f-16t_fC_{t_f}-42tC_{t_f}+12t_f^2S_t\\
&\quad-t12t_fS_{t_f}+42S_{t_f}-t9t_f^2-26t_f+20t_f\cos(t-t_f)-64S_t+42t\big)\\
q_3 &= 4y_0\big((31C_t-25)\big(C_{t_f}-1\big)+37S_tS_{t_f}\big)+\frac{3}{2}y_0(16C_t-13)t_f^2\\
&\quad+t\left(24y_0t_f\big(C_{t_f}+3\big)-96y_0S_{t_f}-\frac{9}{2}y_0t_f^3\right)+6y_0t_f^3S_t\\
&\quad-4y_0t_f\big(8S_{t_f}+10\sin(t-t_f)+27S_t\big)\\
q_4 &= -\frac{1}{2}y_f\big(48C_tt_f^2+t48t_fC_{t_f}+248C_tC_{t_f}-200C_{t_f}-248C_t+12t_f^3S_t\\
&\quad-216t_fS_t-64t_fS_{t_f}-192tS_{t_f}+296S_tS_{t_f}-t9t_f^3-39t_f^2+t144t_f\\
&\quad-80t_f\sin(t-t_f)+200\big)
\end{aligned}
\tag{3.16}
$$

and the terms q_{5-8} are

$$
\begin{aligned}
q_5 &= \dot{x}_0 \big(-160 t_f S_t C_{t_f} - 208 C_t t_f S_{t_f} - 36 t C_{t_f} S_{t_f} + 60 S_t C_{t_f} S_{t_f} \\
&\quad -t9 t_f^3 C_{t_f} - 48 C_t t_f^2 - 39 t_f^2 C_{t_f} + t114 t_f C_{t_f} - 528 C_t C_{t_f} + 426 C_{t_f} \\
&\quad +30 C_t \cos(2t_f) + 498 C_t + t36 t_f^2 S_{t_f} + 116 t_f S_t + 168 t_f S_{t_f} + 6 t S_{t_f} \\
&\quad -16 S_t S_{t_f} - 24 t_f^3 S_t \sin^2\left(\frac{t_f}{2}\right) + t9 t_f^3 + 39 t_f^2 - t84 t_f \\
&\quad +48 t_f^2 \cos(t_f + t) - 24 \cos(2t_f) - 402\big) \\
q_6 &= t\left(30 \dot{x}_f S_{t_f} - 6 t_f \dot{x}_f \left(2 C_{t_f} + 3\right)\right) - 2\left(16 C_t - 13\right) \dot{x}_f \left(C_{t_f} - 1\right) \\
&\quad - 44 \dot{x}_f S_t S_{t_f} + 4 t_f \dot{x}_f \left(4 S_{t_f} + 5 \sin(t - t_f) + 6 S_t\right) \\
q_7 &= -\frac{1}{2} \dot{y}_0 \big(-432 t_f^2 S_t C_{t_f} + 48 C_t t_f^2 S_{t_f} + 2024 S_t C_{t_f} + 408 C_t S_{t_f} \\
&\quad +192 C_{t_f} S_{t_f} + 144 C_t t_f^3 + t288 t_f^2 C_{t_f} - 728 C_t t_f + 552 C_t t_f C_{t_f} C_{t_f} \\
&\quad -440 t_f - 1344 t C_{t_f} + 36 t_f^4 S_t + t36 t_f^3 S_{t_f} - 48 t_f^3 S_t S_{t_f} - 492 t_f^2 S_t \\
&\quad -36 t_f^2 S_{t_f} - t1416 t_f S_{t_f} + 2168 t_f S_t S_{t_f} - 328 S_{t_f} - t27 t_f^4 - 117 t_f^3 \\
&\quad +t315 t_f^2 + 582 t_f + 120 \sin(t - 2t_f) - 72 t \cos(2t_f) - 2144 S_t + 1416 t\big) \\
q_8 &= -\frac{1}{2} \dot{y}_f \big(216 S_t C_{t_f} - 168 C_t S_{t_f} + 96 C_t t_f - 64 t_f C_{t_f} - 144 t C_{t_f} \\
&\quad +36 t_f^2 S_t - t48 t_f S_{t_f} + 136 S_{t_f} - t27 t_f^2 - 78 t_f + 80 t_f \cos(t - t_f) \\
&\quad -216 S_t + 144 t)
\end{aligned}
\tag{3.17}
$$

The cross-track control is

$$
u_z(t; t_f) = \sum_{i=1}^{4} q_i \tag{3.18}
$$

where

$$
\begin{aligned}
q_1 &= \frac{1}{2} z_0 \left(S_{t_f} \sin(t - t_f) - t_f S_t\right) \\
q_2 &= -\frac{1}{2} z_f \left(S_t S_{t_f} - t_f \sin(t - t_f)\right) \\
q_3 &= \frac{1}{2} \dot{z}_0 \left(C_t t_f + S_{t_f} \cos(t - t_f)\right) \\
q_4 &= -\frac{1}{2} \dot{z}_f \left(C_t S_{t_f} + t_f \cos(t - t_f)\right)
\end{aligned}
\tag{3.19}
$$

The in-track and cross-track control expressions are valid for any initial or final condition for which the HCW model still appropriately models the relative dynamics, and any time-of-flight $t_f > 0$.

Now, we show that the optimal control is a strong local minimum by applying the Weierstrass and Legendre-Clebsch necessary conditions. The Weierstrass condition requires that the minimizing controller $\boldsymbol{u}^*(t)$ make the Hamiltonian an absolute minimum at each point on

the minimal path $\boldsymbol{x}^*(t)$. Consider the comparison controller $\bar{\boldsymbol{u}}(t) \neq \boldsymbol{u}^*(t)$. If the Hamiltonian is evaluated at the comparison control, it must be larger than the Hamiltonian evaluated at the optimal controller. Taking the difference of the Hamiltonian evaluated at the comparison control and the Hamiltonian evaluated at the minimizing control (and noting that $\lambda_5 = -u_y^*$ and $\lambda_6 = -u_z^*$) we get that

$$\begin{aligned}\hat{\mathcal{H}}(\bar{\boldsymbol{u}}) - \hat{\mathcal{H}}(\boldsymbol{u}^*) &= \frac{1}{2}\bar{\boldsymbol{u}}^T\bar{\boldsymbol{u}} - \frac{1}{2}(\boldsymbol{u}^*)^T\boldsymbol{u}^* + \boldsymbol{\lambda}^T(\boldsymbol{A}\boldsymbol{x} - \boldsymbol{A}\boldsymbol{x}) + \boldsymbol{\lambda}^T(\boldsymbol{B}\bar{\boldsymbol{u}} - \boldsymbol{B}\boldsymbol{u}^*) \\ &= \frac{1}{2}\left(\bar{u}_y^2 + \bar{u}_z^2 - (u_y^*)^2 - (u_z^*)^2\right) + \lambda_5(\bar{u}_y - u_y^*) + \lambda_6(\bar{u}_z - u_z^*) \\ &= \frac{1}{2}\left[\left(\bar{u}_y - u_y^*\right)^2 + (\bar{u}_z - u_z^*)^2\right] \geq 0\end{aligned} \tag{3.20}$$

which holds $\forall \bar{u}_y \neq u_y^*, \bar{u}_z \neq u_z^*$. The Legendre-Clebsch condition requires that the second partial derivative of the Hamiltonian with respect to each of the controls be a positive semi-definite matrix. Taking these derivatives we get that

$$\frac{\partial}{\partial \boldsymbol{u}}\left(\frac{\partial \hat{\mathcal{H}}}{\partial \boldsymbol{u}}\right) = \mathbb{I}_{2\times 2} > \boldsymbol{0}_{2\times 2} \tag{3.21}$$

Satisfaction of the Weierstrass condition guarantees satisfaction of the Legendre-Clebsch condition [72]. These two conditions are necessary for a strong local minimum. We can prove the candidate is a global minimum by verifying the control law using the Gramian. The linear, time-invariant system

$$\dot{\boldsymbol{x}}(t) = \boldsymbol{A}\boldsymbol{x}(t) + \boldsymbol{B}\boldsymbol{u}(t),\ \boldsymbol{x}(t_0) = \boldsymbol{x}_0 \tag{3.22}$$

where

$$\boldsymbol{B} = \begin{bmatrix}\boldsymbol{0}_{2\times 4} & \mathbb{I}_{2\times 2}\end{bmatrix}^T \tag{3.23}$$

is controllable on $t \in [t_0, t_f]$ iff the matrix

$$\boldsymbol{W}(t_0, t_f) = \int_{t_0}^{t_f} \boldsymbol{\Phi}(\tau, t_0)\boldsymbol{B}\boldsymbol{B}^T\boldsymbol{\Phi}^T(\tau, t_0)\,\mathrm{d}\,\tau \tag{3.24}$$

is nonsingular [25]. Eq. (3.24) is the controllability Gramian matrix, and $\boldsymbol{\Phi}(t, t_0)$ is the state transition matrix for the unforced HCW equations. If Eq. (3.24) is invertible then the controllability matrix

$$\mathbf{C}(\boldsymbol{A}, \boldsymbol{B}) = \begin{bmatrix}\boldsymbol{B} & \boldsymbol{A}\boldsymbol{B} & \boldsymbol{A}^2\boldsymbol{B} & \cdots & \boldsymbol{A}^{n-1}\boldsymbol{B}\end{bmatrix} \tag{3.25}$$

has full row rank. Since the HCW equations are time-invariant, $\boldsymbol{\Phi}(t, t_0)$ is computed using the matrix exponential. Moreover, if Eq. (3.24) is non-singular, then it is guaranteed that a controller exists that minimizes the $\mathcal{L}_2$ input energy in Eq. (3.5). Since Eq. (3.2) is

time-invariant, t_0 may be set to zero without a loss of generality. Recalling Section 2.4.3, the controller which minimizes Eq. (3.5) is

$$\boldsymbol{u}^{\star}(t) = -\boldsymbol{B}^T\boldsymbol{\Phi}^T(0,t)\boldsymbol{W}^{-1}(0,t_f)(\boldsymbol{x}_0 - \boldsymbol{\Phi}(0,t_f)\boldsymbol{x}_f) \tag{3.26}$$

where $\boldsymbol{\Phi}(0,t) = \boldsymbol{\Phi}^{-1}(t,0)$ and the vectors $\boldsymbol{x}_0$ and $\boldsymbol{x}_f$ are boundary conditions for the point-to-point maneuver. The columns $\boldsymbol{w}_i$ of the controllability Gramian for the under-actuated HCW equations for some arbitrary t_f are

$$\boldsymbol{w}_1 = \begin{bmatrix} 6t_f + \sin 2t_f \\ 6t_f \sin t_f + 2(\cos 2t_f - \cos t_f) - 3t_f^2 \\ 0 \\ 3 - 4\cos t_f + \cos 2t_f \\ 2(7\sin t_f - \sin 2t_f - 5t_f) \\ 0 \end{bmatrix} \tag{3.27}$$

$$\boldsymbol{w}_2 = \begin{bmatrix} 6t_f \sin t_f + 2(\cos 2t_f - \cos t_f) - 3t_f^2 \\ 8(t_f + 3t_f\cos t_f - (3+\cos t_f)\sin t_f) + 3t_f^3 \\ 0 \\ 2(2t_f + 3t_f\cos t_f - (3+2\cos t_f)\sin t_f) \\ \frac{1}{2}\left(8 + 9t_f^2 - 8\cos 2t_f - 24t_f \sin t_f\right) \\ 0 \end{bmatrix} \tag{3.28}$$

$$\boldsymbol{w}_3 = \begin{bmatrix} 0 \\ 0 \\ \frac{1}{2}(t_f - \cos t_f \sin t_f) \\ 0 \\ 0 \\ \frac{1}{4}(1 - \cos 2t_f) \end{bmatrix} \tag{3.29}$$

$$\boldsymbol{w}_4 = \begin{bmatrix} 3 - 4\cos t_f + \cos 2t_f \\ 2(2t_f + 3t_f\cos t_f - (3+2\cos t_f)\sin t_f) \\ 0 \\ 2t_f - \sin 2t_f \\ 2(3\cos t_f - \cos 2t_f - 2) \\ 0 \end{bmatrix} \tag{3.30}$$

$$\boldsymbol{w}_5 = \begin{bmatrix} 2(7\sin t_f - \sin 2t_f - 5t_f) \\ \frac{1}{2}\left(8 + 9t_f^2 - 8\cos 2t_f - 24t_f \sin t_f\right) \\ 0 \\ 2(3\cos t_f - \cos 2t_f - 2) \\ 17t_f + 8(\cos t_f - 3)\sin t_f \\ 0 \end{bmatrix} \tag{3.31}$$

$$\boldsymbol{w}_6 = \begin{bmatrix} 0 \\ 0 \\ \frac{1}{4}(1 - \cos 2t_f) \\ 0 \\ 0 \\ \frac{1}{2}(t_f + \cos t_f \sin t_f) \end{bmatrix} \tag{3.32}$$

This Gramian is non-singular for any $t_f > 0$, and when $t_f = 0$, it can be readily seen that the Gramian is a matrix of zeros, the inverse of which is singular. This results in an infinitely large control signal.

The control signal is defined on the set of square-integrable signals, which is infinite dimensional. If there exists a control $\boldsymbol{u}(t) : \boldsymbol{x}_0 \mapsto \boldsymbol{x}_f$, then there exist *infinitely* many control signals which will accomplish the same transfer. The choice of control which minimizes Eq. (3.5) is the minimum-norm solution to the least squares controllability optimization, analogous to the Moore-Penrose pseudo-inverse. The controllability Gramian provides a necessary and sufficient condition for both the controllability of the system as well as the optimality of the choice of $\boldsymbol{u}^*(t)$.

When the complete expressions for $\boldsymbol{B}$, $\boldsymbol{\Phi}(t, 0)$, $\boldsymbol{W}(0, t_f)$, $\boldsymbol{x}_0$, and $\boldsymbol{x}_f$ are combined, we find that the control law is the exact same as that derived using the Pontryagin Principle. We have now guaranteed that the under-actuated control law is a *global minimum* with respect to the $\mathcal{L}_2$ energy.

In the next section, the under-actuated controller is compared with a fully-actuated optimal controller where

$$\boldsymbol{B} = \begin{bmatrix} \mathbf{0}_{3\times3} & \mathbb{I}_{3\times3} \end{bmatrix}^T \tag{3.33}$$

and $\boldsymbol{u}_x = -\lambda_4 \neq 0$.

We note that this control law could be hard-coded into a satellite computer and be used in a receding horizon fashion. As derived in this section, the control law only requires the current measurement $\boldsymbol{x}_0$ and the final state $\boldsymbol{x}_f$ as well as a desired time-of-flight. Since the control law is explicitly derived, it requires no matrix inversions, and since it is derived assuming a circular orbit, Kepler's equation does not need to be solved. As a result the most computationally difficult part of using this control law would be to accurately compute the $\sin(\cdot)$ and $\cos(\cdot)$ functions. We conclude that this control law could be easy to implement on a system in real time.

3.4 Simulations

In this section we simulate the control law developed in the previous section. In addition, the fully-actuated optimal controller (radial, in-track, and cross-track) is also simulated as a comparison. It is expected that, even with the addition of an extra control signal, the fully-actuated system will yield a lower overall energy. Our simulations show this is true, however the control energy for the under-actuated system is of the same order of magnitude which implies that the radial control signal only contributes a small fraction of the overall effort.

In deriving the optimal control law, the HCW equations were normalized so that $\mu = 1$, $a = 1$ so that $n = 1$. As a result, distances are scaled by $1/a$ and velocities are scaled by $1/na$. The boundary conditions are presented in physical units, and the figures reflect this, however the actual simulation uses the normalized quantities.

3.4.1 Radial Maneuver

In the first simulation, the deputy starts at the origin and deploys up to a commensurate relative orbit 400 m above the chief. The maneuver takes place over 1 orbit ($t_f = 2\pi$). The boundary conditions are

$$\begin{aligned} \boldsymbol{x}_0 &= \begin{bmatrix} 0 & 0 & 0 & 0 & 0 & 0 \end{bmatrix}^T \\ \boldsymbol{x}_f &= \begin{bmatrix} 400 & 0 & 0 & 0 & \dot{y}_f & 0 \end{bmatrix}^T \end{aligned} \tag{3.34}$$

Noting that for the 12 boundary conditions only $x_f \neq 0$ and we impose the constraint $\dot{y}_f = -2x_f$ so that the terminal set results in a bounded relative orbit. The optimal control in the in-track direction (in normalized units) is significantly simplified:

$$\begin{aligned} u_y^*(t) = -2x_f \big[& 52t_f - 93t + t_f^2(18t) - 64t_f \cos t - 50t_f \cos(t - t_f) + 93t \cos t_f \\ & + 40t_f \cos t_f + 140 \sin t - 24t_f^2 \sin t - 140 \cos t_f \sin t \\ & + (t_f 30t - 89 + 110 \cos t) \sin t_f \big] \\ u_z^*(t) = 0 & \end{aligned} \tag{3.35}$$

The above expression is valid for any $t_f > 0$, however if t_f is chosen to be 2π, the control law is further simplified

$$\begin{aligned} u_y^*(t) &= -8\pi x_f \left(46 + 18\pi t - 57 \cos t - 24\pi \sin t\right) \\ u_z^*(t) &= 0 \end{aligned} \tag{3.36}$$

The radial maneuver can be seen in Figure 3.1, and the control history can be seen in Figure 3.2. The under-actuated maneuver closely resembles the fully-actuated maneuver; both the shape of the trajectory and the optimal histories. The primary difference, as expected, is that there is radial control action. The cost for the two maneuvers is very close however,

and of the same order of magnitude. In Figure 3.5, we see that the condition in Eq. (2.51) holds for the duration of the orbit.

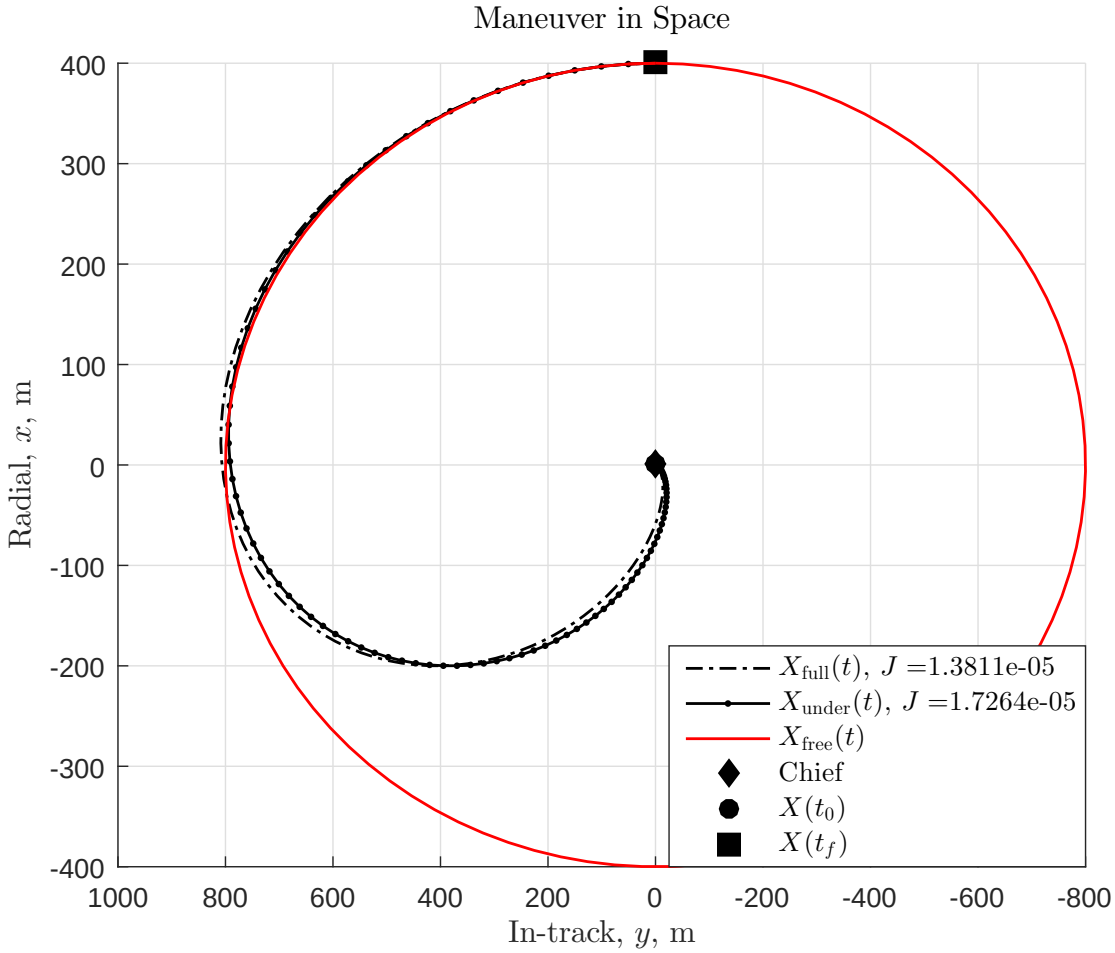

Figure 3.1: Planar trajectory for the reconfiguration maneuver

3.4.2 Leader-Follower Reconfiguration

This simulation demonstrates the planar reconfiguration for a leader-follower formation where the deputy (follower) maneuvers to become the leader. The boundary conditions for the problem are

$$\begin{aligned} \boldsymbol{x}_0 &= \begin{bmatrix} 0 & -200 & 0 & 0 & 0 & \dot{y}_0 & 0 \end{bmatrix}^T \\ \boldsymbol{x}_f &= \begin{bmatrix} 0 & 200 & 0 & 0 & 0 & \dot{y}_f & 0 \end{bmatrix}^T \end{aligned} \tag{3.37}$$

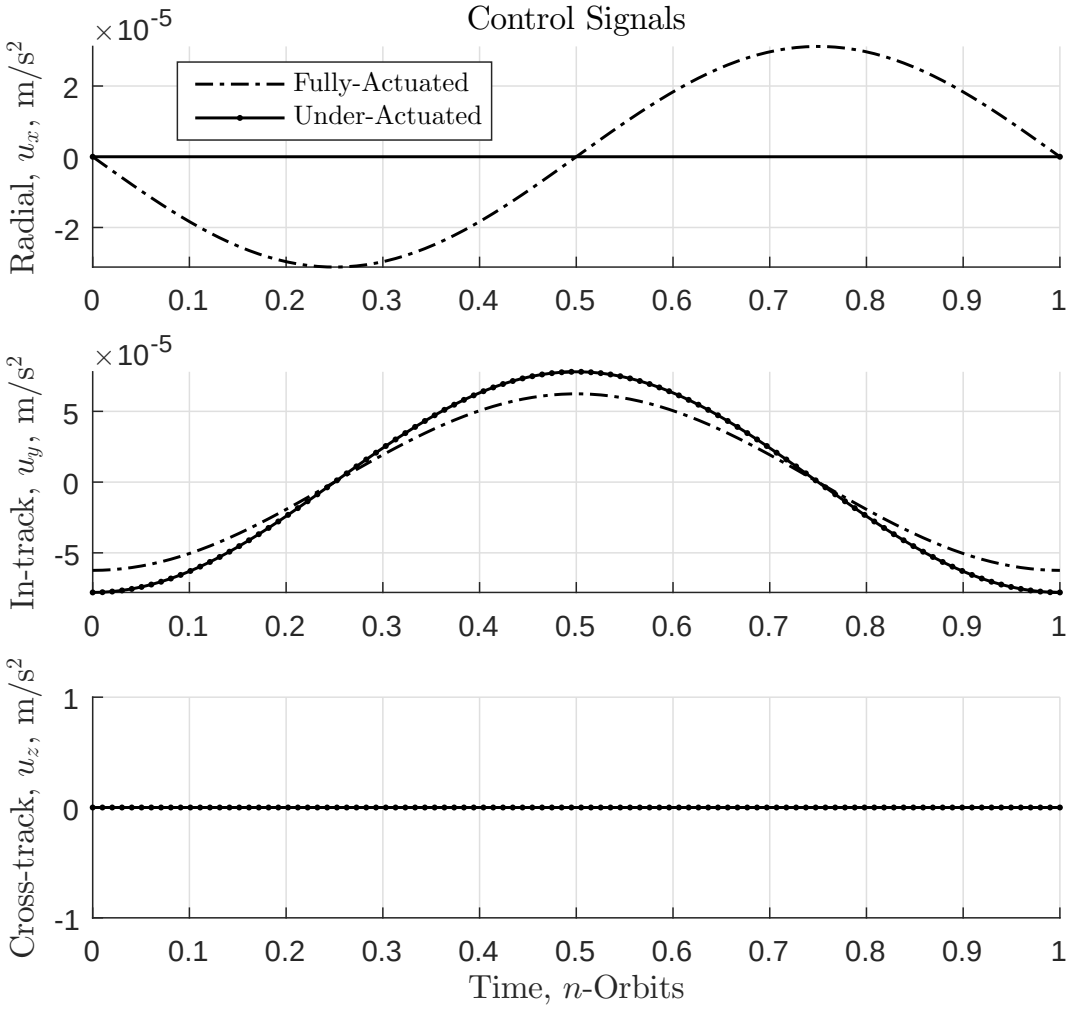

Figure 3.2: Control signals for the reconfiguration maneuver

Again, we have imposed the constraints $y_0 = -2x_0 = 0$ and $y_f = -2x_f = 0$. Substitution of the initial and terminal relative in-track boundary conditions into the formula for $u_y^*(t)$, we get that

$$\begin{aligned} u_y^*(t) = -\frac{1}{2}(y_0 - y_f)\big[&t_f 9t(t_f^2 - 16) - 200 + 39t_f^2 + 8\cos t_f\,(25 - t_f 610 t_f \sin t) \\ &+64(3t + t_f)\sin t_f - 4\sin t(3t_f(t_f^2 - 18) + 74\sin t_f) \\ &-8\cos t(6t_f^2 + 31(\cos t_f - 1) + 10t_f \sin t_f)\big] \\ u_z^*(t) = 0 \end{aligned} \tag{3.38}$$

which is again valid for any $t_f > 0$. Choosing $t_f = 2\pi$, we get a simpler formula for the optimal control

$$\begin{aligned} u_y^*(t) &= 2\pi(y_0 - y_f)\big[96t - 3\pi(13 + 6\pi t) + 48\pi\cos t + 4(6\pi^2 - 37)\sin t\big] \\ y_z^*(t) &= 0 \end{aligned} \tag{3.39}$$

The relative trajectory can be seen in Figure 3.3. As in the previous simulation, the relative trajectory from the under-actuated and fully-actuated systems closely resemble each other, and while the control energy for the fully-actuated system is lower, we can see that the under-actuated maneuver control energy is still of the same order of magnitude. Furthermore, inspection of Figure 3.6 shows that the condition in Eq. (2.51) holds since the Hamiltonian is constant when evaluated at the optimal states, co-states and control.

This maneuver and the previous maneuver demonstrate the relative motion anomaly experienced by the *Gemini* astronauts. For two satellites in a circular orbit, such as the leader-follower configuration, if the follower is commanded to rendezvous with the leader, then thrusting forward is counter-productive. Forward thrust increases the velocity, and by Kepler's Third Law, this results in an increase in the orbital altitude, which then actually slows the follower down relative to the leader. Similarly, for the radial deployment maneuver, the satellite was first required to slow down slightly so that the deputy orbit would drop, and then speed up again to meet the commensurate orbit. The rather simple orbit and control approach provided in this chapter locally demonstrate some of the unique properties of Keplerian orbits.

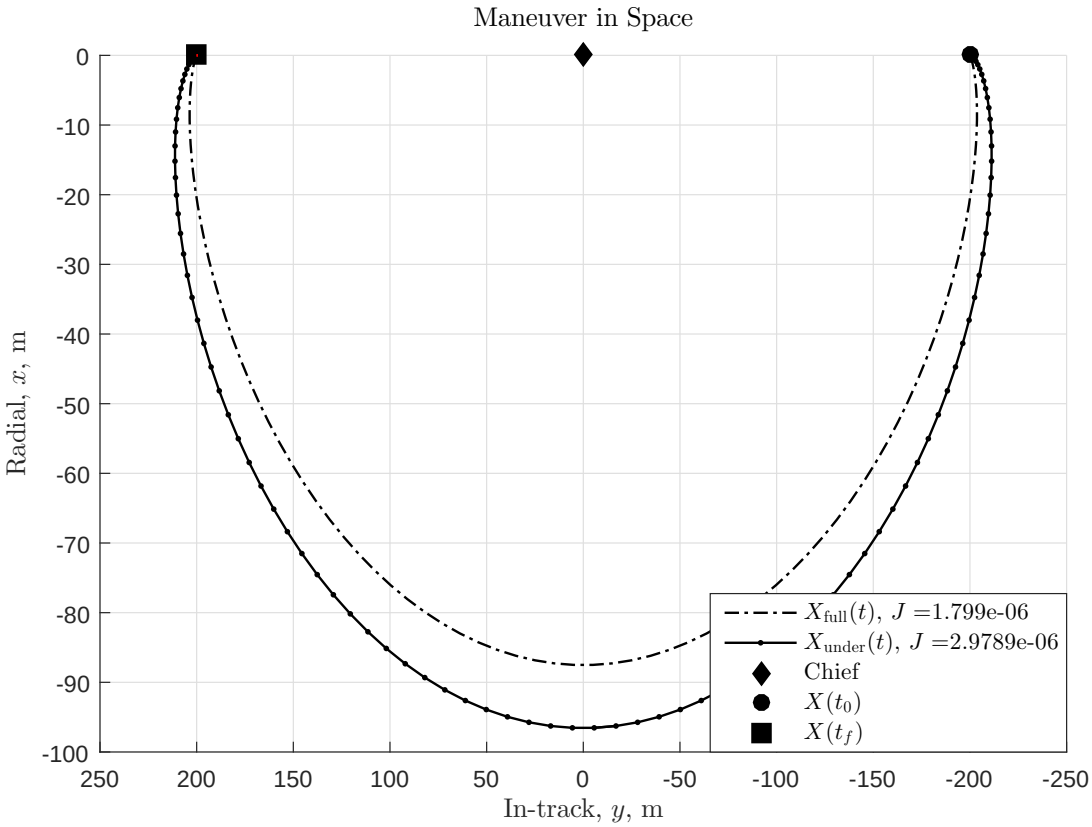

Figure 3.3: Planar trajectory for the leader-follower reconfiguration maneuver

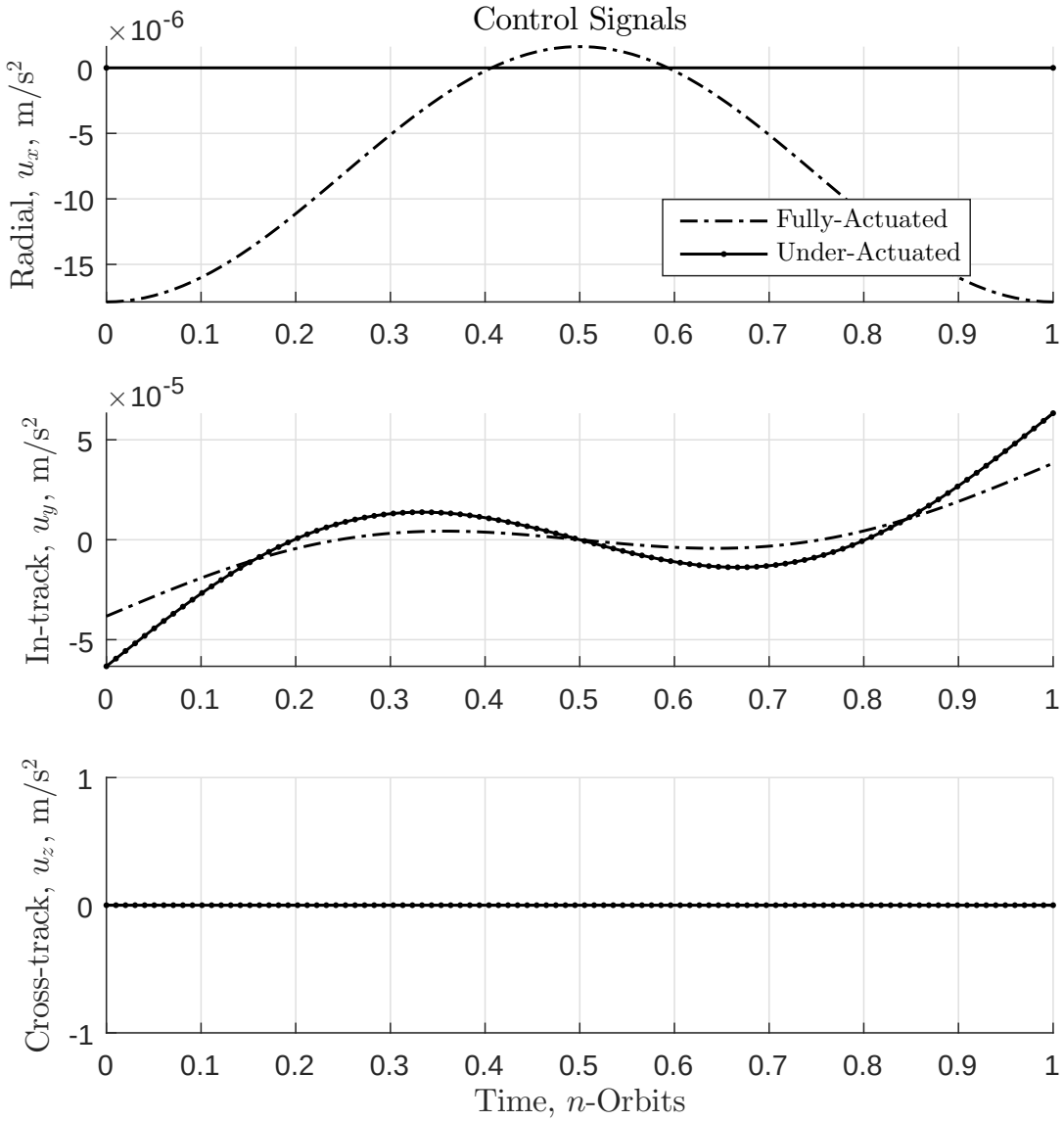

Figure 3.4: Control signals for the leader-follower reconfiguration maneuver

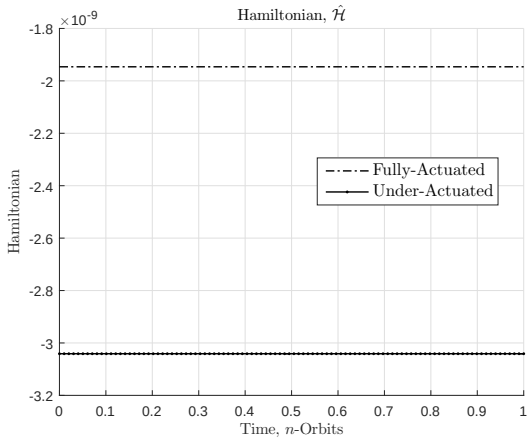

Figure 3.5: Augmented Hamiltonian for the radial, planar, reconfiguration maneuver

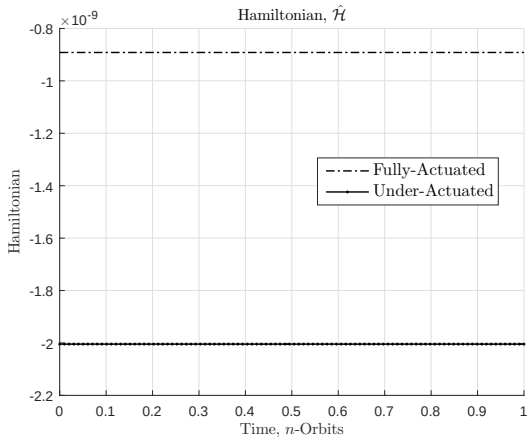

Figure 3.6: Augmented Hamiltonian for the leader-follower reconfiguration maneuver

3.5 Conclusion

This chapter describes the derivation of the necessary and sufficient conditions for a minimum input energy, under-actuated formation reconfiguration problem. The HCW equations are shown to be controllable with only in-track and cross-track thrust. The control laws for both approaches are equivalent, and minimize the $\mathcal{L}_2$ input energy globally. The resulting analytical control laws were applied to several formation reconfiguration examples and demonstrated local manifestations of macroscopic properties of orbits.

Chapter 4

Nonlinear Tracking of Relative Maneuvers in Spacecraft Formations

4.1 Introduction

The problem of spacecraft formation flying has in recent years become increasingly more prevalent in astrodynamics research as an enabling methodology for advanced mission design. Formation flying refers to a broad class of problems. One of the major technological challenges mission designers face is the power-limited nature of most satellites; satellites generally must operate subject to stringent electrical and thrust constraints. We examine a class of minimum energy transfers in perturbed formation flying.

The primary objective we address in this paper is rapid reconfiguration of a two satellite formation in an arbitrarily eccentric orbit. It is important to note that we are only performing control on one of the satellites. We include the effect of J_2 as a bounded, finite approximation of the maximum disturbance that a two satellite formation would experience in a short time-scale maneuver, meaning one that occurs in less than one orbit. The short time-scale serves as our justification for not using a high-fidelity orbital model.

This chapter is structured as follows. In Section 4.2, we present the orbital model used for this analysis. In Section 4.3.2 we study the optimal trajectory generation for this system. Section 4.3.1 presents the nonlinear, time-varying boundary value problem that arises in the elliptical orbit transfer problem. Section 4.3.2 presents a different approach in which a simplified gravitational field model yields a linear, time-varying system, but we minimize the same cost function. We find that the two approaches agree nearly exactly. In Section 4.4, we use the linear optimal trajectory presented from Section 4.3.2 as a reference trajectory and present a sliding mode tracking controller to track this trajectory in the presence of orbital disturbances on the order of the J_2 perturbation or less. In Section 4.5, we present comparative results that demonstrate the performance of the nonlinear and linear optimal

controllers, and find that the sliding mode tracking controller accomplishes the desired transfer with thrust performance on the same order of magnitude as the optimal controllers.

4.2 System Model

Consider the relative geometry in Figure 2.1. Using Eq. (2.11), the nonlinear equations are

$$\begin{aligned}
\ddot{x} =& 2\dot{\theta}\dot{y} + \ddot{\theta}y + \dot{\theta}^2 x + \frac{\mu}{r_{\mathrm{c}}^2} - \frac{\mu(x + r_{\mathrm{c}})}{\left[(r_{\mathrm{c}} + x)^2 + y^2 + z^2\right]^{3/2}} + f_r \\
\ddot{y} =& -2\dot{\theta}\dot{x} - \ddot{\theta}x + \dot{\theta}^2 y - \frac{\mu y}{\left[(r_{\mathrm{c}} + x)^2 + y^2 + z^2\right]^{3/2}} + f_\theta \\
\ddot{z} =& -\frac{\mu z}{\left[(r_{\mathrm{c}} + x)^2 + y^2 + z^2\right]^{3/2}} + f_h
\end{aligned} \tag{4.1}$$

where f_i are the components of the exogenous disturbances, $\boldsymbol{f}_e$, mapped into the relative frame, and r_{c}, $\dot{r}_{\mathrm{c}}$, $\dot{\theta}$ and $\ddot{\theta}$ are given in Eq. (2.5).

In this work, we are assuming that the maneuvers happen on a time scale that is much less than that of the orbital motion. The natural frequency of the orbit is $n = \sqrt{\mu/a^3}$ where a is the semi-major axis. Thus, the orbital period is equal to $P = 2\pi/n$. It is widely known that the J_2 disturbance is several orders of magnitude larger than any other orbital perturbation [119, 13, 128, 134]. Over the short time-scales considered in this work it is reasonable to neglect all perturbations other than J_2. The J_2 acceleration on the chief is given by [13]

$$\boldsymbol{a}_{J_2} = -\frac{3}{2} J_2 \left(\frac{\mu}{R^2}\right)\left(\frac{R_{eq}}{R}\right)^2 \begin{bmatrix} \left(1 - 5\left(\frac{Z}{R}\right)^2\right)\frac{X}{R} \\ \left(1 - 5\left(\frac{Z}{R}\right)^2\right)\frac{Y}{R} \\ \left(3 - 5\left(\frac{Z}{R}\right)^2\right)\frac{Z}{R} \end{bmatrix} \tag{4.2}$$

where $J_2 = 1082.63 \times 10^{-6}$. This expresses the acceleration in the inertial frame. A similar model can easily be written by using the definition for the deputy's position vector in the $\{n\}$-frame. The formation flying equations in Eq. (2.11) are expressed in the orbiting frame, and the difference between the disturbance on the chief and deputy will be used as the disturbance in the orbiting frame. Let

$$\boldsymbol{d} = \boldsymbol{R}_n^o(\boldsymbol{f}_e^{\mathrm{d}} - \boldsymbol{f}_e^{\mathrm{c}}) \tag{4.3}$$

where $\boldsymbol{f}_e^{\mathrm{d}}$ refers to the exogenous forcing function on the deputy and $\boldsymbol{f}_e^{\mathrm{c}}$ refers to the forces on the chief. The components of $\boldsymbol{d}$ are incorporated into Eq. (2.11) and provide a level of uncertainty in the model which we hope to attenuate with a robust controller.

We can make an approximation to the nonlinear system that yields a linear system with time-varying coefficients. Following [10], we can approximate the position of the deputy as

$$\boldsymbol{r}_{\mathrm{d}} = \sqrt{(r_{\mathrm{c}} + x)^2 + y^2 + z^2} \approx r_{\mathrm{c}} \sqrt{1 + 2\frac{x}{r_{\mathrm{c}}}}$$

which neglects the contribution in the in-track (y) and cross-track (z) directions to the potential energy. The acceleration due to the conservative force field is the negative gradient of the potential, using the binomial theorem [10, 123]:

$$\boldsymbol{a}_{\mathrm{d}} = -\frac{\mu}{r_{\mathrm{c}}^3} \begin{bmatrix} r_{\mathrm{c}} - 2x & y & z \end{bmatrix}^T$$

Now, the linear equations of relative motion (LERM) have the form of Eq. (2.12)

$$\begin{aligned} \ddot{x} &= 2\dot{\theta}\dot{y} + \left(\dot{\theta}^2 + 2\frac{\mu}{r_{\mathrm{c}}^3}\right) x + \ddot{\theta} y \\ \ddot{y} &= -2\dot{\theta}\dot{x} - \ddot{\theta} x + \left(\dot{\theta}^2 - \frac{\mu}{r_{\mathrm{c}}^3}\right) y \\ \ddot{z} &= -\frac{\mu}{r_{\mathrm{c}}^3} z \end{aligned} \tag{4.4}$$

Recall that r_{c} and θ are taken to be known functions of time satisfying Eq. (2.5) for the chief. For the LERM, it has been shown that bounded relative orbits exist when the initial state for the deputy in the relative frame satisfies

$$\frac{\dot{y}_0}{x_0} = -\frac{n(2+e)}{(1+e)^{\frac{1}{2}}(1-e)^{\frac{3}{2}}} \tag{4.5}$$

where e is the orbital eccentricity. This is a very important result; if this initial condition requirement is not met, the linear system exhibits a secular drift in the in-track direction. In the orbiting frame, this takes the form of the deputy satellite moving forward relative to the chief or backward depending on what the ratio between the initial radial position and in-track velocity is. From this point forward, condition (4.5) will be referred to as the commensurabilty condition.

4.3 Optimal Transfer Trajectory

We now address the problem of computing the optimal transfer trajectory which will serve as the reference trajectory in a later section of this paper. We present two solutions to a minimum-energy, continuous-thrust, point-to-point optimal control problem. The first approach is to use the Pontryagin Maximum Principle to minimize the control energy using the nonlinear system model in Eq. (2.11). The second approach minimizes the same control energy but subject to the LERM. This approach relies on linear operator theory. For this section we deal with the restricted, idealized case in which there are no exogenous disturbances.

4.3.1 Nonlinear Optimal Transfer

In the context of proximity operations and rendezvous for spacecraft formation flying, it can be advantageous to manipulate the relative orbit using minimum control which corresponds to minimum energy expenditure [103],[139]. Let the performance objective be

$$\min_{\boldsymbol{u}\in\Omega} J(\boldsymbol{u}(\cdot)) = \frac{1}{2}\int_{t_0}^{t_f} \boldsymbol{u}^T\boldsymbol{u}\,\mathrm{d}\,\tau \tag{4.6}$$

subject to the dynamic constraint of Eq. (2.11).

We can define the initial and target sets to be $\boldsymbol{X}_0 = \{\boldsymbol{x}(t_0)\}$ and $\boldsymbol{X}_f = \{\boldsymbol{x}(t_f)\}$ respectively, and assume that $t_f < \infty$. Furthermore, let the set of admissible controllers be

$$\boldsymbol{u} \in \Theta \subseteq C^m[t_0, t_f] \tag{4.7}$$

where $C^m[t_0, t_f]$ is the set of control signals which are continuous on the interval $[t_0, t_f]$. For this problem, the augmented Hamiltonian is

$$\hat{\mathcal{H}} = \frac{1}{2}\eta_0\boldsymbol{u}^T\boldsymbol{u} + \boldsymbol{\eta}^T\boldsymbol{f}(\boldsymbol{x},\boldsymbol{u},t) \tag{4.8}$$

The necessary condition for a local extremal requires that

$$\frac{\partial\hat{\mathcal{H}}}{\partial\boldsymbol{u}} = \boldsymbol{0} \tag{4.9}$$

Carrying out this derivative, we see that the optimal control for the NERM is given by

$$\boldsymbol{u}^* = \begin{bmatrix} u_x^* & u_y^* & u_z^* \end{bmatrix}^T = \begin{bmatrix} -\frac{\eta_4}{\eta_0} & -\frac{\eta_5}{\eta_0} & -\frac{\eta_6}{\eta_0} \end{bmatrix}^T \tag{4.10}$$

where η_0 and $\eta_{4,5,6}$ satisfy the following adjoint equation:

$$\dot{\hat{\boldsymbol{\eta}}} = -\left[\hat{\boldsymbol{A}}\right]^T\hat{\boldsymbol{\eta}} \tag{4.11}$$

where $\hat{\boldsymbol{\eta}} = \begin{bmatrix} \eta_0 & \boldsymbol{\eta}^T \end{bmatrix}^T$ and

$$[\hat{\boldsymbol{A}}]^T = \begin{bmatrix} 0 & \boldsymbol{0}_{n\times n} \\ \nabla_{\boldsymbol{x}}\ell(\hat{\boldsymbol{x}}^*,\boldsymbol{u}^*) & [\mathbb{J}_{\boldsymbol{x}}\boldsymbol{f}(\hat{\boldsymbol{x}}^*,\boldsymbol{u}^*)]^T \end{bmatrix} \tag{4.12}$$

For this problem, with this particular cost function, the Lagrange multiplier η_0 which is associated with the Lagrangian can be divided through since it will actually be an arbitrary,

nonzero constant. Let $\boldsymbol{\lambda} = \frac{\boldsymbol{\eta}}{\eta_0}$. Now, the adjoint equations have the following form

$$\begin{aligned}
\dot{\lambda}_1 =& -\frac{3\lambda_6\mu(r+x)z}{\gamma^5} - \lambda_4\left(\frac{3\mu(r+x)^2}{\gamma^5} - \frac{\mu}{\gamma^3} + \dot{\theta}^2\right) \\
&-\lambda_5\left(\frac{3\mu(r+x)y}{\gamma^5} - \ddot{\theta}\right) \\
\dot{\lambda}_2 =& -\frac{3\lambda_6\mu yz}{\gamma^5} - \lambda_5\left(\frac{3\mu y^2}{\gamma^5} - \frac{\mu}{\gamma^3} + \dot{\theta}^2\right) \\
&-\lambda_4\left(\frac{3\mu(r+x)y}{\gamma^5} + \ddot{\theta}\right) \\
\dot{\lambda}_3 =& -\frac{3\lambda_4\mu(r+x)z}{\gamma^5} - \lambda_6\left(\frac{3\mu z^2}{\gamma^5} - \frac{\mu}{\gamma^3}\right) - \frac{3\lambda_5\mu zy}{\gamma^5} \\
\dot{\lambda}_4 =& 2\lambda_5\dot{\theta} - \lambda_1 \\
\dot{\lambda}_5 =& -\left(\lambda_2 + 2\lambda_4\dot{\theta}\right) \\
\dot{\lambda}_6 =& -\lambda_3
\end{aligned} \tag{4.13}$$

where

$$\gamma = \left[(r_\mathrm{c}+x)^2 + y^2 + z^2\right]^{1/2} \tag{4.14}$$

and r_c, $\dot{\theta}$ and $\ddot{\theta} = -\frac{2\dot{r}_\mathrm{c}\dot{\theta}}{r_\mathrm{c}}$ are taken to be known functions of time, from Eq. (2.5). The optimal control vector is thus:

$$\boldsymbol{u}^* = \begin{bmatrix} -\lambda_4 & -\lambda_5 & -\lambda_6 \end{bmatrix}^T \tag{4.15}$$

We have identified the initial and target sets for the state variables, but we need to define the initial or target values for the adjoint states. In general, the transversality conditions at the boundaries of the problem can be used to find the tangent space normal to the vector field given by Eq. (2.11) and this can provide boundary conditions for the adjoint vector field. For this problem, since this problem is formulated as point-to-point, the transversality conditions provide no extra information about the problem. We are thus left with a nonlinear, two-point boundary value problem defined by the state and adjoint vector fields and will need to solve it numerically to compute the optimal trajectory.

In numerical simulations, an initial guess of $\boldsymbol{\lambda} = \mathbf{0}$ for the boundary value problem solver `bvp4c` in Matlab was provided and an optimal solution was found. We also used GPOPS-II [102] which is faster and easier to use than Matlab's boundary value problem solver. In general, a poor initial guess can dramatically change the outcome of the optimization, but for this particular formulation, no issues were found with this guess. In the succeeding section we present a linear controller which minimizes the same cost function given in Eq. (4.6). This approach requires 1) the solution to initial or final value problems and 2) the invertibility of the controllability Gramian.

The approximation that leads to the LERM is very good, and in numerical analysis we find that the linear and nonlinear optimal solutions agree nearly exactly. The trajectories used for the robust tracking controller presented later are all computed using the linear optimal solution.

4.3.2 Linear Optimal Transfer

Consider a linear, time-varying system of the form

$$\dot{\boldsymbol{x}} = \boldsymbol{A}(t)\boldsymbol{x} + \boldsymbol{B}(t)\boldsymbol{u}, \quad \boldsymbol{x}(t_0) = \boldsymbol{x}_0 \tag{4.16}$$

The system is controllable if there exists a piecewise continuous control signal on the interval $t \in [t_0, t_f]$ which drives the system from an initial state $\boldsymbol{x}(t_0)$ to a terminal state $\boldsymbol{x}(t_f)$. The solution to the general linear time-varying system is given by the variation of constants formula

$$\boldsymbol{x}(t_f) = \boldsymbol{\Phi}(t_f, t_0)\boldsymbol{x}_0 + \int_{t_0}^{t_f} \boldsymbol{\Phi}(t_f, \tau)\boldsymbol{B}(\tau)\boldsymbol{u}(\tau)\,\mathrm{d}\,\tau \tag{4.17}$$

where $\boldsymbol{\Phi}(t_f, t)$ is the state transition matrix. To find the input signal $\boldsymbol{u}(t)$ which would drive the system to $\boldsymbol{x}(t_f)$, we use the properties of the linear, time-varying system. First, we pre-multiply both sides of Eq. (4.17) by $\boldsymbol{\Phi}(t_0, t_f)$ and solve for the initial state

$$\boldsymbol{x}_0 = -\int_{t_0}^{t_f} \boldsymbol{\Phi}(t_0, \tau)\boldsymbol{B}(\tau)\boldsymbol{u}(\tau)\,\mathrm{d}\,\tau$$

This defines a linear operator $L(\boldsymbol{u}(t)) : \boldsymbol{C}^m[t_0, t_f] \to \mathbb{R}^n$ [25]. The range-space of this operator defines the set of initial conditions, $\boldsymbol{x}(t_0)$, for which a control signal $\boldsymbol{u} \in C^m[t_0, t_f]$ can drive the state to another state, $\boldsymbol{x}(t_f)$, in a finite time, t_f. Now, the adjoint of the linear operator $L(\cdot)$ is $L^*(\boldsymbol{u}(t)) : \mathbb{R}^n \to C^m[t_0, t_f]$ and is defined by requiring that

$$\langle L(\boldsymbol{u}), \boldsymbol{x}\rangle_{\mathbb{R}^n} = \langle \boldsymbol{u}, L^*(\boldsymbol{x})\rangle_{C^m} \tag{4.18}$$

where $\langle \cdot, \cdot \rangle$ denotes the inner product. By definition, the range of $L(\cdot)$ is in $\mathbb{R}^n$, and the range of $L(\cdot)$ composed with its adjoint, $\mathcal{R}(L \circ L^*)$, is also in $\mathbb{R}^n$, so we can say $\mathcal{R}(L) = \mathcal{R}(L \circ L^*) \in \mathbb{R}^n$. For the left-hand side of Eq. 4.18, we can use the standard inner product on $\mathbb{R}^n$ to write

$$\begin{aligned}\langle L(\boldsymbol{u}), \boldsymbol{x}\rangle_{\mathbb{R}^n} &= \left(-\int_{t_0}^{t_f} \boldsymbol{\Phi}(t_0, \tau)\boldsymbol{B}(\tau)\boldsymbol{u}(\tau)\,\mathrm{d}\,\tau\right)^T \boldsymbol{x} \\ &= -\int_{t_0}^{t_f} \boldsymbol{u}^T(\tau)\boldsymbol{B}^T(\tau)\boldsymbol{\Phi}^T(t_0, \tau)\boldsymbol{x}\,\mathrm{d}\,\tau\end{aligned}$$

For the right-hand side, the inner product on $C^m[t_0, t_f]$ is

$$\langle \boldsymbol{u}, L^*(\boldsymbol{x})\rangle_{C^m} = -\int_{t_0}^{t_f} \boldsymbol{u}^T(\tau)\boldsymbol{B}^T(\tau)\boldsymbol{\Phi}^T(t_0, \tau)\boldsymbol{x}\,\mathrm{d}\,\tau$$

The adjoint operator of $L(\cdot)$ is then

$$L^*(\boldsymbol{x}) = -\boldsymbol{B}^T(t)\boldsymbol{\Phi}^T(t_0,t)\boldsymbol{x}$$

The composition of the linear operator L and its adjoint L^* is

$$\begin{aligned} L(L^*(\boldsymbol{x})) &= L\left(-\boldsymbol{B}^T(t)\boldsymbol{\Phi}^T(t_0,t)\right) \\ &= \left(\int_{t_0}^{t_f} \boldsymbol{\Phi}(t_0,\tau)\boldsymbol{B}(\tau)\boldsymbol{B}^T(\tau)\boldsymbol{\Phi}^T(t_0,\tau)\,\mathrm{d}\,\tau\right)\boldsymbol{x} \\ &= \boldsymbol{W}_{\mathrm{c}}(t_0,t_f)\boldsymbol{x} \end{aligned}$$

The matrix $\boldsymbol{W}_{\mathrm{c}}(t_0,t_f)$ is the controllability Gramian which defines the operator $L \circ L^* : \mathbb{R}^n \to \mathbb{R}^n$. We require that $\mathcal{R}(L \circ L^*) = \mathbb{R}^n$ which can only be the case if the Gramian is invertible (i.e. has full rank). One controller that drives $\boldsymbol{x}(t_0) = \boldsymbol{x}_0$ to $\boldsymbol{x}(t_f) = \boldsymbol{x}_f$ is given by

$$\boldsymbol{u}^*(t) = -\boldsymbol{B}^T(t)\boldsymbol{\Phi}^T(t_0,t)\boldsymbol{W}_{\mathrm{c}}^{-1}(t_0,t_f)\left(\boldsymbol{x}_0 - \boldsymbol{\Phi}(t_0,t_f)\boldsymbol{x}_f\right) \tag{4.19}$$

where $\boldsymbol{W}_{\mathrm{c}}(t_0,t_f)$ is the controllability Gramian. This controller also minimizes the $\mathcal{L}_2$ energy of the cost function [28] where $\mathcal{L}_2$ is the set of square-integrable functions. Another important property of this particular control law is that we can express it in terms of the operators we used to define it:

$$\boldsymbol{u}^*(t) = L^* \circ (L \circ L^*)^{-1}\left(\boldsymbol{x}_0 - \boldsymbol{\Phi}(t_0,t_f)\boldsymbol{x}_f\right) \tag{4.20}$$

This form $L^* \circ (L \circ L^*)^{-1}$ provides the least-square solution to the under-determined problem of finding a control history that drives the system from $\boldsymbol{x}_0$ to $\boldsymbol{x}_f$. This is analogous to manner in which the Moore-Penrose pseudoinverse of a non-square matrix gives a least-square solution to a system of linear equations which lacks a unique solution [25].

The Gramian is numerically computed as the solution to the following final value problem

$$\dot{\boldsymbol{W}}(t,t_f) = \boldsymbol{A}(t)\boldsymbol{W}(t,t_f) + \boldsymbol{W}(t,t_f)\boldsymbol{A}^T(t) - \boldsymbol{B}(t)\boldsymbol{B}^T(t), \quad \boldsymbol{W}(t_f,t_f) = \boldsymbol{0} \tag{4.21}$$

Furthermore the state transition matrix for a given time is the solution to the initial value problem

$$\dot{\boldsymbol{\Phi}}(t,t_0) = \boldsymbol{A}(t)\boldsymbol{\Phi}(t,t_0), \quad \boldsymbol{\Phi}(t_0,t_0) = \mathbb{I} \tag{4.22}$$

Remark 9. *We note that it is important to check the Gramian for the following properties since the Gramian is being computed numerically:*

- *Symmetry ($\boldsymbol{W}_{\mathrm{c}}(t_0,t_f) = \boldsymbol{W}_{\mathrm{c}}^T(t_0,t_f)$)*
- *Positive-definiteness ($\lambda_i > 0$) for each λ_i of $\boldsymbol{W}_{\mathrm{c}}(t_0,t_f)$*

It is also advantageous, particularly for very short time-horizons, to examine the condition number of the Gramian; an ill-conditioned Gramian matrix could result in near-singular inverses. This is a result of the numerical analysis and can be manipulated by increasing the relative and absolute tolerances in the numerical integration of the system.

4.4 Sliding Mode Tracking Control

We return to our original nonlinear system in Eq. (2.11) and include the disturbance vector, $\boldsymbol{d}$, resulting from J_2 in the dynamics. Define the change of variables

$$\boldsymbol{\eta} = \boldsymbol{x} - \boldsymbol{x}^d \tag{4.23}$$

where $\boldsymbol{x}^d$ is the desired trajectory computed from the optimal control solution. Furthermore, define

$$\boldsymbol{\xi} = \dot{\boldsymbol{\eta}} = \dot{\boldsymbol{x}} - \dot{\boldsymbol{x}}^d \tag{4.24}$$

We can express the system in Eq. (2.11) in the following form:

$$\begin{aligned} \dot{\boldsymbol{\eta}} =& \boldsymbol{f}_a(\boldsymbol{\eta}, \boldsymbol{\xi}) \\ \dot{\boldsymbol{\xi}} =& \boldsymbol{f}_b(\boldsymbol{\eta}, \boldsymbol{\xi}) + \boldsymbol{G}\boldsymbol{u} + \boldsymbol{d} - \ddot{\boldsymbol{x}}^d \end{aligned} \tag{4.25}$$

where we let

$$\boldsymbol{f}_b(\boldsymbol{\eta}, \boldsymbol{\xi}) = \mathcal{A}\begin{bmatrix} \boldsymbol{x}^T & \dot{\boldsymbol{x}}^T \end{bmatrix}^T + \boldsymbol{N} \tag{4.26}$$

and $\mathcal{A}$ is

$$\mathcal{A} = \begin{bmatrix} \dot{\theta}^2 & \ddot{\theta} & 0 & 0 & 2\dot{\theta} & 0 \\ -\ddot{\theta} & \dot{\theta}^2 & 0 & -2\dot{\theta} & 0 & 0 \\ 0 & 0 & 0 & 0 & 0 & 0 \end{bmatrix} \tag{4.27}$$

and $\boldsymbol{N}$ is

$$\boldsymbol{N} = \begin{bmatrix} \frac{\mu}{r_c^2} - \frac{\mu(r_c+x)}{((r_c+x)^2+y^2+z^2)^{3/2}} \\ -\frac{\mu y}{((r_c+x)^2+y^2+z^2)^{3/2}} \\ -\frac{\mu z}{((r_c+x)^2+y^2+z^2)^{3/2}} \end{bmatrix} \tag{4.28}$$

Following the approach in Khalil [76], the first step in SMC design is to treat the velocities as virtual control inputs and choose a function $\boldsymbol{\phi}(\boldsymbol{\eta})$ such that the kinematic subsystem is asymptotically stable. Choosing

$$\boldsymbol{f}_a(\boldsymbol{\eta}, \boldsymbol{\xi}) = \boldsymbol{\phi}(\boldsymbol{\eta}) = -\boldsymbol{K}\boldsymbol{\eta} \tag{4.29}$$

We define the sliding manifold to be

$$\boldsymbol{z} = \boldsymbol{\xi} - \boldsymbol{\phi}(\boldsymbol{\eta}) = \boldsymbol{\xi} + \boldsymbol{K}\boldsymbol{\eta} \tag{4.30}$$

where $\boldsymbol{K}$ is positive definite. Taking the derivative of $\boldsymbol{z}$ we find that

$$\dot{\boldsymbol{z}} = \mathcal{A}\begin{bmatrix} \boldsymbol{x} \\ \dot{\boldsymbol{x}} \end{bmatrix} + \boldsymbol{N} + \boldsymbol{G}\boldsymbol{u} + \boldsymbol{d} - \ddot{\boldsymbol{x}}^d - \frac{\partial \boldsymbol{\phi}}{\partial \boldsymbol{\eta}}\boldsymbol{f}_a(\boldsymbol{\eta}, \boldsymbol{\xi}) \tag{4.31}$$

At this point we partition the controller into two terms: one part of the controller, $\boldsymbol{u}_{\text{eq}}$ cancels out the nominal dynamics and the other part of the controller, $\tilde{\boldsymbol{v}}$, will be designed to attenuate the uncertainty from $\boldsymbol{d}$. The controller is

$$\begin{aligned}\boldsymbol{u} =& \boldsymbol{G}^{-1}\left(-\boldsymbol{f}_b(\boldsymbol{\eta},\boldsymbol{\xi}) + \frac{\partial \boldsymbol{\phi}}{\partial \boldsymbol{\eta}}\boldsymbol{f}_a(\boldsymbol{\eta},\boldsymbol{\xi}) + \tilde{\boldsymbol{v}}\right) \\ =& -\left(\mathcal{A}\begin{bmatrix}\boldsymbol{x}\\ \dot{\boldsymbol{x}}\end{bmatrix} + \boldsymbol{N} - \ddot{\boldsymbol{x}}^d\right) + \frac{\partial \boldsymbol{\phi}}{\partial \boldsymbol{\eta}}\boldsymbol{\xi} + \tilde{\boldsymbol{v}}\end{aligned} \tag{4.32}$$

This makes the dynamics along the sliding manifold

$$\dot{\boldsymbol{z}} = \tilde{\boldsymbol{v}} + \boldsymbol{\Delta} \tag{4.33}$$

For the disturbance vector, we assume that the magnitude of the disturbance is bounded and satisfies the inequality

$$||\boldsymbol{\Delta}|| \leq a||\boldsymbol{d}|| + k||\tilde{\boldsymbol{v}}|| \tag{4.34}$$

Now, choose the following Lyapunov function for each component of the sliding mode [76]

$$V_i = \frac{1}{2}z_i^2, \quad i = 1,2,3 \tag{4.35}$$

Its Lyapunov rate is

$$\dot{V}_i = z_i\dot{z}_i = z_i\tilde{v}_i + z_i\Delta_i \tag{4.36}$$

This yields the following inequality [76]

$$z_i\tilde{v}_i + z_i\Delta_i \leq z_i\tilde{v}_i + |z_i|\left(a||\boldsymbol{d}|| + k||\tilde{\boldsymbol{v}}||_\infty\right) \tag{4.37}$$

Let

$$\tilde{v}_i = -\beta(\boldsymbol{x})\,\text{sgn}(z_i),\ \beta(\boldsymbol{x}) \geq \frac{a||\boldsymbol{d}||}{1-k} + b_0,\ \forall \boldsymbol{x} \in \mathcal{D}, b_0 > 0 \tag{4.38}$$

where $a > 0$, $b_0 > 0$ and $k > 0$ and $\mathcal{D}$ is a neighborhood about the origin. This makes the Lyapunov rate

$$\begin{aligned}\dot{V}_i \leq& \left(-\beta(\boldsymbol{x}) + a||\boldsymbol{d}|| + k\beta(\boldsymbol{x})\right)|z_i| \\ \leq& \left(-a||\boldsymbol{d}|| - (1-k)b_0 + a||\boldsymbol{d}||\right)|z_i|\end{aligned} \tag{4.39}$$

Now, we have

$$\dot{V}_i \leq -b_0(1-k)|z_i| \tag{4.40}$$

which guarantees that any trajectory which is not on the manifold $\boldsymbol{z} = \boldsymbol{0}$ will reach it in finite time. This also guarantees that trajectories already on the manifold $\boldsymbol{z} = \boldsymbol{0}$ will not leave it. The final form for the controller that accomplishes this transfer is

$$\boldsymbol{u} = -\left(\boldsymbol{f}_b(\boldsymbol{\eta},\boldsymbol{\xi})\right) + \frac{\partial \boldsymbol{\phi}}{\partial \boldsymbol{\eta}}\boldsymbol{\xi} - \frac{1}{1-k}\left(a||\boldsymbol{d}|| + b_0\right)\text{sgn}(\boldsymbol{z}) \tag{4.41}$$

A common issue with the bang-bang structure of the sliding mode control due to the signum function, seen in Figure 4.1, is that the system cannot be locally Lipschitz continuous. Operationally, this also results in the system "chattering" back and forth around the sliding manifold, seen in Figure 4.2. For a physical system, this could result in 1) excessive control activity which can wear out the actuators and 2) the system can stabilize to a limit cycle around the equilibrium point (rather than the equilibrium point itself). We make a con-

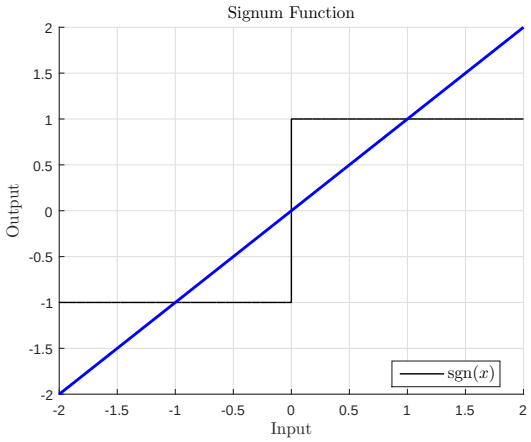

Figure 4.1: Signum function

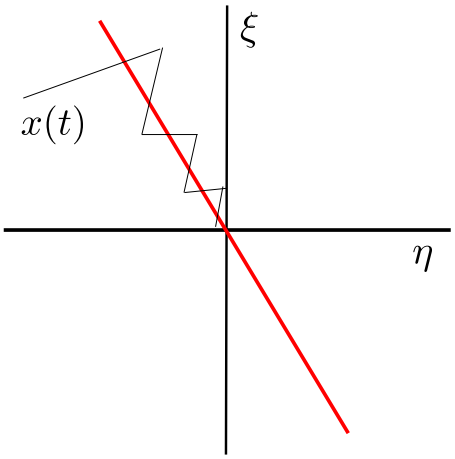

Figure 4.2: Chattering around sliding mode in the z phase space

tinuous approximation of the signum function with a saturation function which is defined as

$$\operatorname{sgn}(x) \approx \operatorname{sat}(x;\epsilon) = \begin{cases} \frac{x}{\epsilon} & \text{if } |x| \leq |\epsilon| \\ \operatorname{sgn} x & \text{if } |x| > \epsilon \end{cases}$$

With this approximation we get a similar form for the control law

$$\boldsymbol{u} = -\left(\boldsymbol{f}_b(\boldsymbol{\eta},\boldsymbol{\xi})\right) + \frac{\partial \boldsymbol{\phi}}{\partial \boldsymbol{\eta}}\boldsymbol{\xi} - \frac{1}{1-k}\left(a||\boldsymbol{d}|| + b_0\right)\operatorname{sat}(\boldsymbol{z};\epsilon) \tag{4.42}$$

The saturation function, seen in Figure 4.3, results in a "boundary layer" around the sliding manifold, seen in Figure 4.4. For the "true" bang-bang control law, once the system reaches the sliding manifold, it stays there for all time. In the saturation relaxation, one the system enters the boundary layer, it remains in the boundary layer for all time. Once there, the system may oscillate around the manifold, and this oscillation can be tuned specifically to suit the needs of the objective.

The vector $\boldsymbol{d}$ for this problem represents a bounded disturbance on the order of the J_2 perturbation. It is well-known [138, 95, 134] that the J_2 perturbation is the most dominant perturbation. We can take the disturbance to be bounded by $d_i \leq 10^{-4}$ m/s^2 to account for the worst-case exogenous forcing on the system.

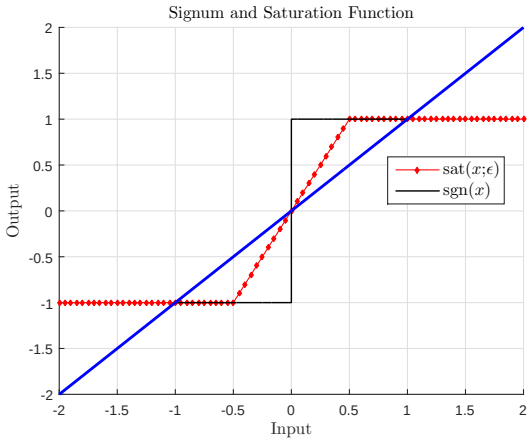

Figure 4.3: Saturation function

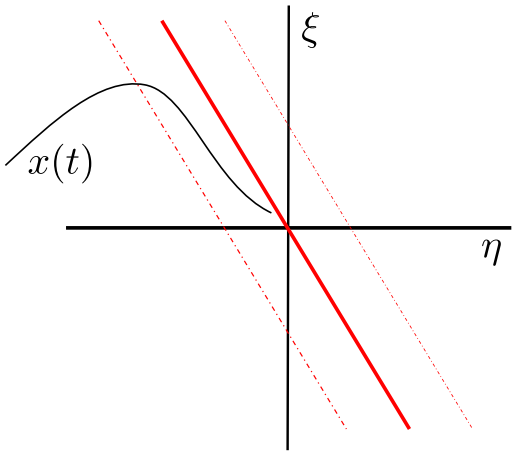

Figure 4.4: Boundary layer in the z phase space

4.5 Numerical Analysis

To simulate the controllers that we have designed, we chose a rendezvous maneuver. We assume that the deputy satellite has a mass of 100 kg with a fuel-mass fraction of 0.06. The initial orbit for the chief is:

$$\boldsymbol{X}_c^0 = \begin{bmatrix} 9000 & 0 & 0 & 0 & 8.93 & 0 \end{bmatrix}^T \tag{4.43}$$

where units are in kilometers and kilometers/ sec. This corresponds to a semi-major axis of 45000 km, an eccentricity of $e = 0.8$, and $i = \Omega = \omega = f_0 = 0$ where these parameters are respectively the inclination, right-ascension, argument of periapsis and true anomaly of the chief. The deputy's initial position and velocity are:

$$\boldsymbol{X}_d^0 = \begin{bmatrix} 1000 & -1000 & 1000 & 0 & \dot{y}_d^0 & 0 \end{bmatrix} \tag{4.44}$$

where $\dot{y}_d^0$ is the initial in-track velocity given by the commensurability conditions in Eq. (4.5) and the units are in meters and meters/ sec. The target set for the deputy is a point one meter directly behind the chief at zero relative velocity:

$$\boldsymbol{X}_d^f = \begin{bmatrix} 0 & -1 & 0 & 0 & 0 & 0 \end{bmatrix} \tag{4.45}$$

We wish to accomplish the transfer in 1200 seconds which is a fairly aggressive maneuver; numerous other contributors achieve maneuvers typically on the order of one orbit. For our first simulation we compare the nonlinear and linear optimal solutions. Figure 4.5 shows the relative, optimal position history of the maneuver, as can be seen, the nonlinear and linear solutions agree nearly exactly. Investigation of Figure 4.6 and 4.7 shows that the position histories and control histories match almost perfectly as well. This further reinforces

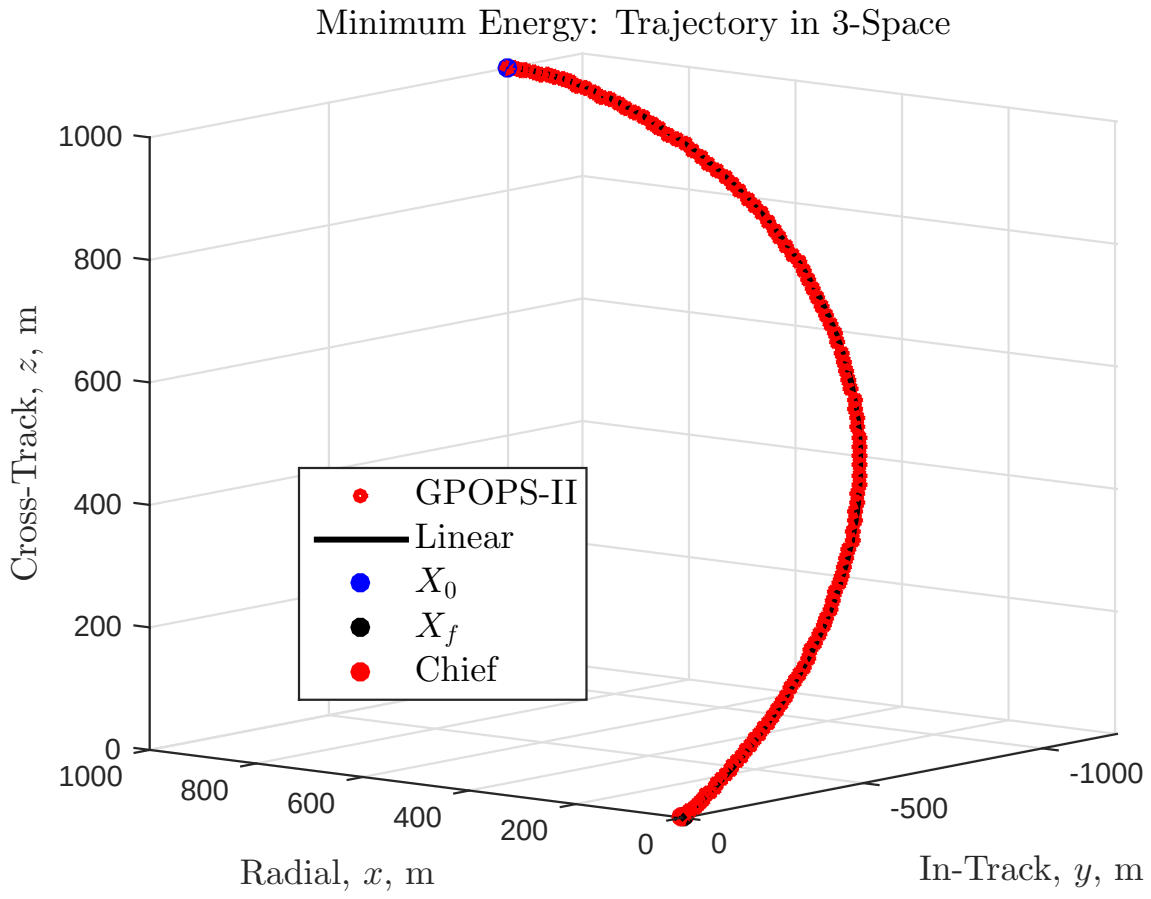

Figure 4.5: Nonlinear and linear optimal transfer solution

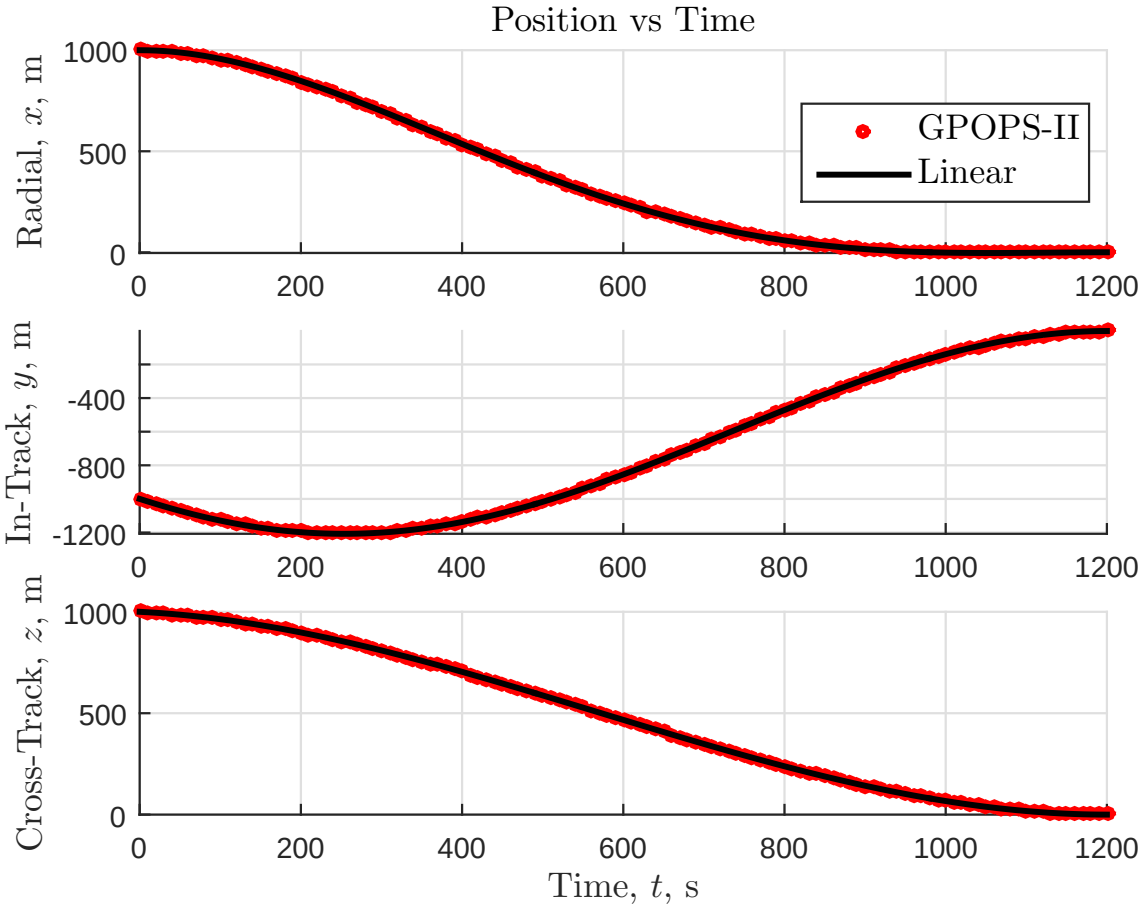

Figure 4.6: Position histories for the optimal control problem in the absence of disturbing forces. The linear and nonlinear solutions are nearly identical.

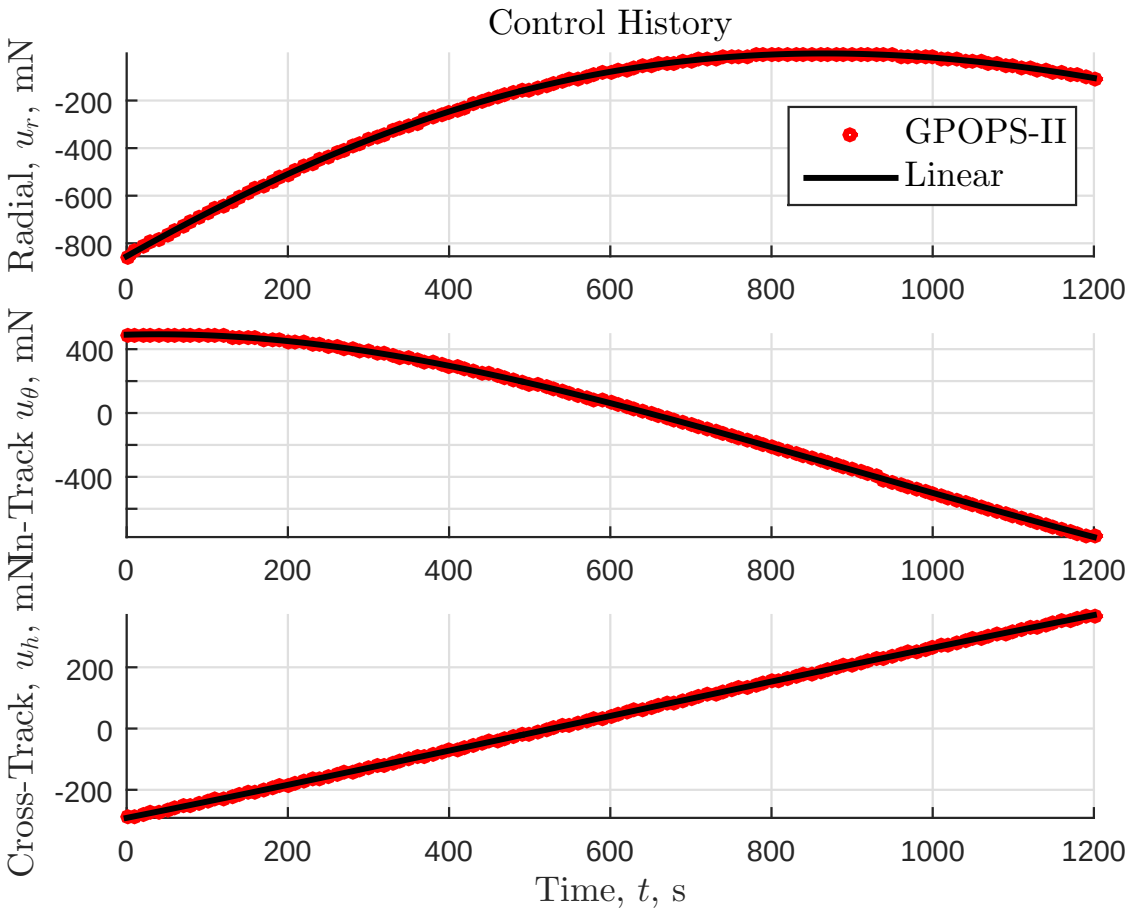

Figure 4.7: Control component history, again, nonlinear and linear are nearly identical

our claim that the LERM provide a sufficiently accurate model compared to the nonlinear "truth."

Next we use the linear optimal solution we computed to serve as a reference trajectory in the presence of the nonlinear, perturbed dynamics. Furthermore, we give the deputy a 5% error in the initial conditions. We tune the sliding mode controller with the following parameters:

$$\boldsymbol{K} = 0.067\mathbb{I},\ k = 0.99,\ a = 1,\ b_0 = 1e-4,\ \epsilon = 0.01 \tag{4.46}$$

In Figure 4.8, we can see that even with a 5% error in the initial conditions, the SMC tracking controller can drive the satellite onto the reference trajectory. In Figure 4.9, we see the relative position error. As we can see, the controller certainly drives the relative position error to zero and tracks the reference trajectory almost exactly. In Figure 4.12, we can see the optimal thrust magnitude and tracking thrust magnitude plotted with each other. The controller initially applies a larger thrust than the optimal controller, and we can see that the thrust magnitude increases when the sliding manifold is reached.

4.6 Conclusions

We have shown that the minimum energy transfer problem from linear optimal control theory compares almost exactly with the solution to the nonlinear boundary value problem that arises from the Maximum Principle. The close agreement between the two solutions leads us to believe that this method of trajectory generation provides a new and useful approach to the problem of spacecraft formation reconfiguration. We also presented a sliding mode controller that worked on very highly eccentric orbits and was able to track an aggressive, short-time-scale maneuver.

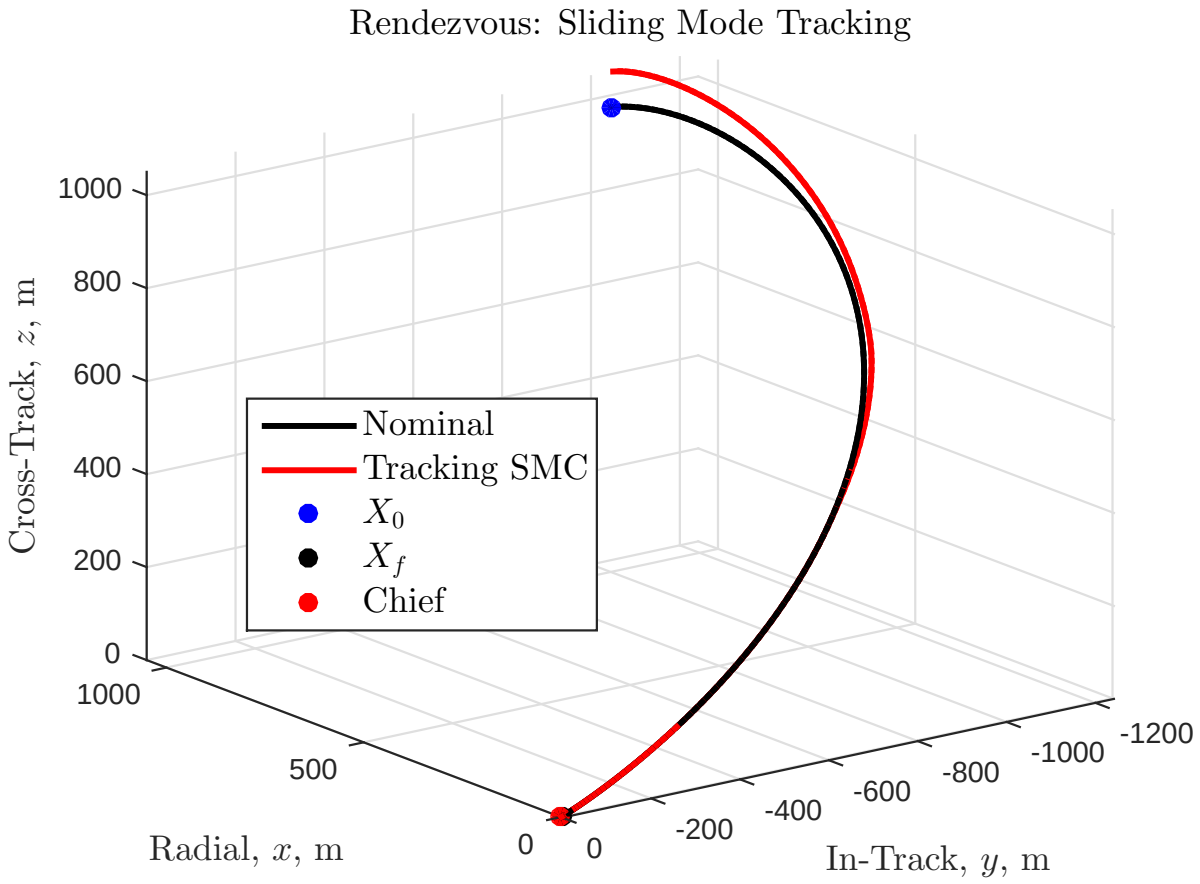

Figure 4.8: Trajectory in space. Notice that although the tracking controller starts with significant error, it is able to successfully recover and track the desired trajectory.

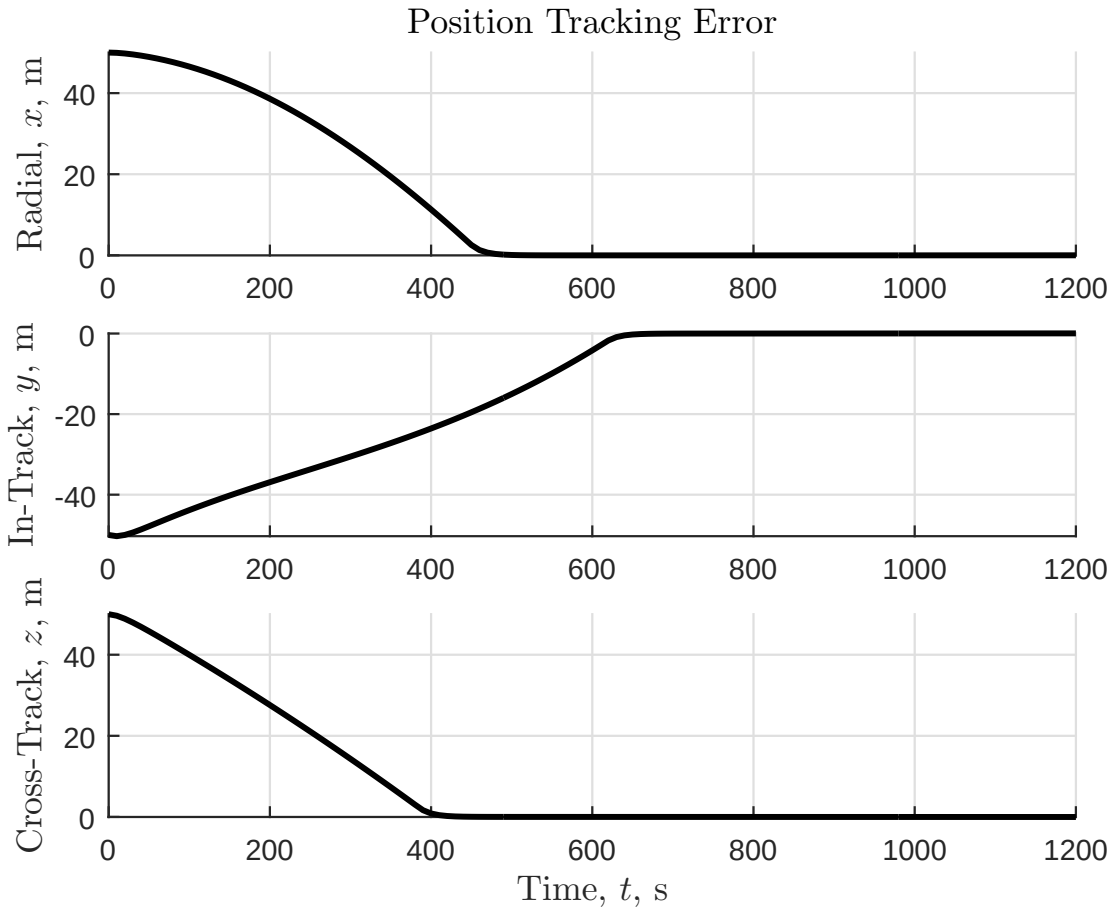

Figure 4.9: Relative position error (based on reference trajectory) over time

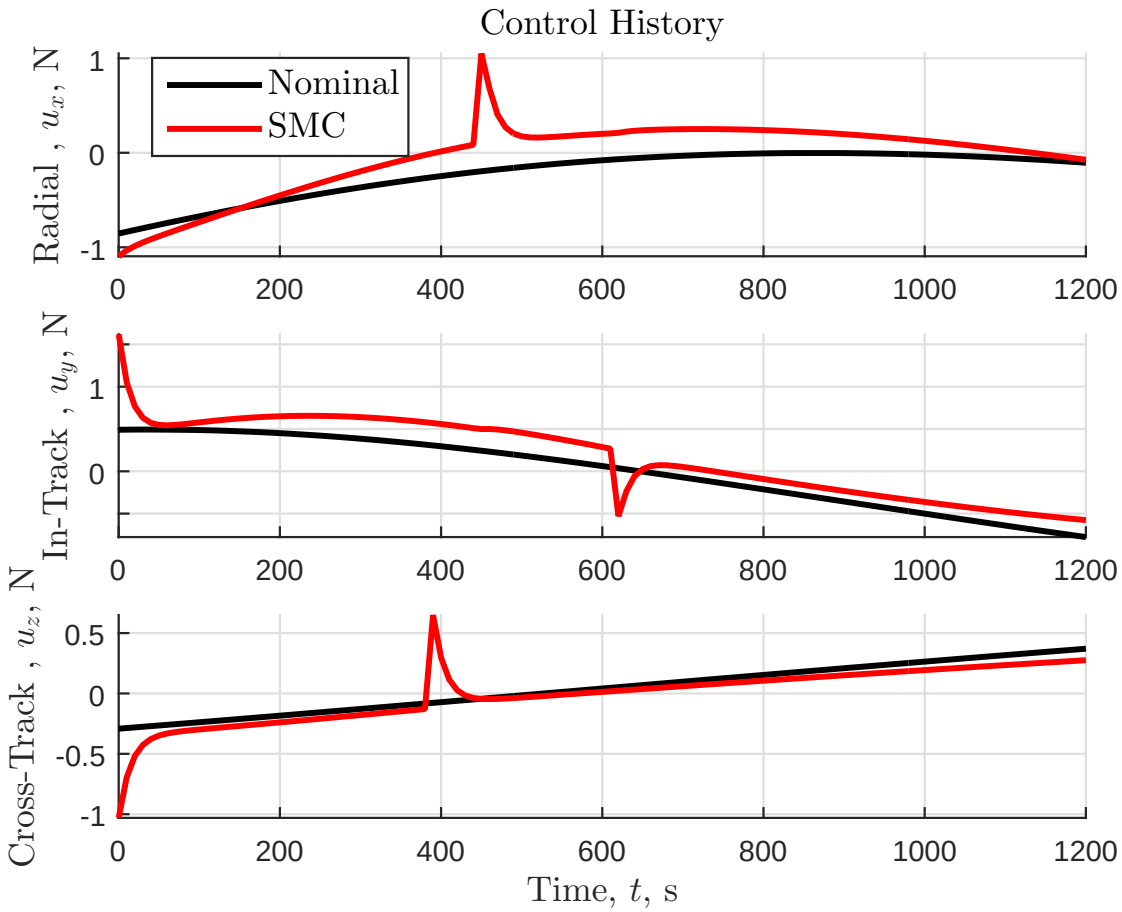

Figure 4.10: Control component history

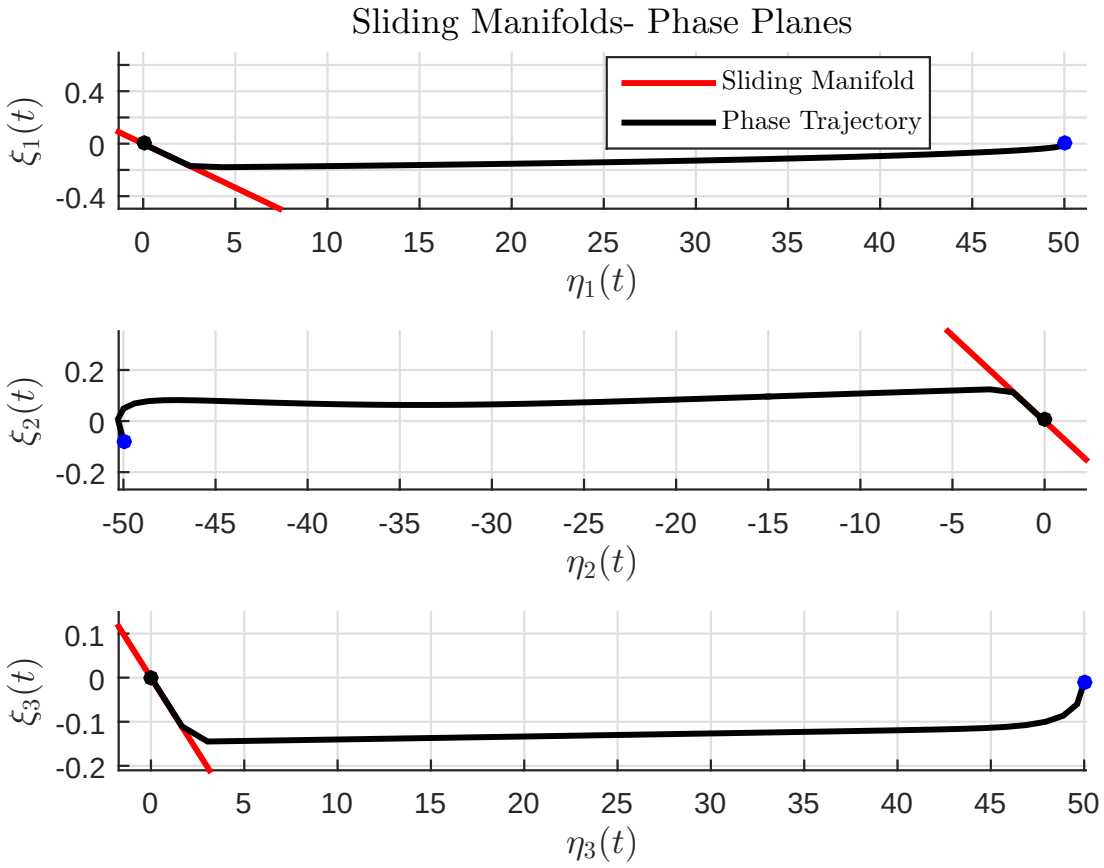

Figure 4.11: Sliding mode phase portrait

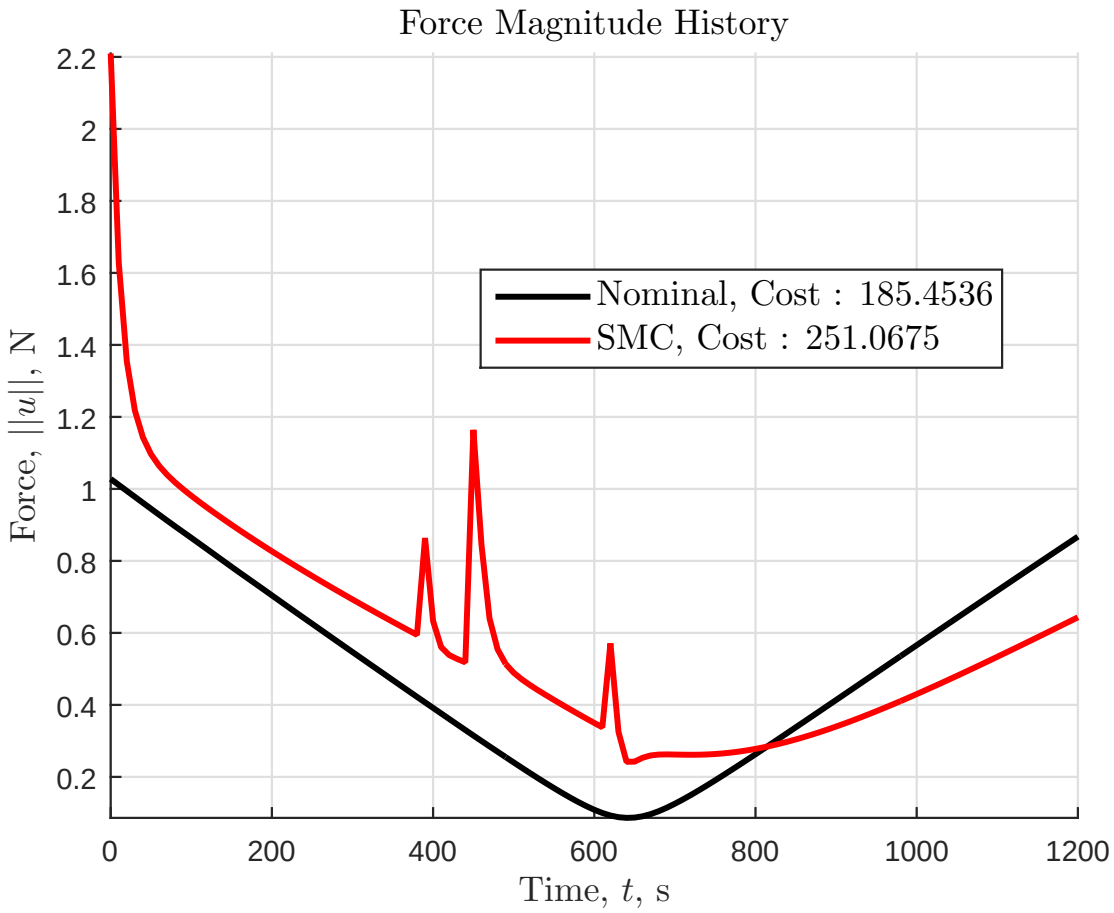

Figure 4.12: Thrust magnitudes over the course of the maneuver

Chapter 5

Fuel/Time Optimal Relative Trajectories for a Satellite Near a Perturbed, Elliptical Orbit

5.1 Introduction

Modeling and control of the relative motion between two or more satellites has been extensively studied for numerous applications in recent years. Effective relative motion modeling and control can enable a wide variety of missions. Potential applications examined have included small length/time scale missions such as proximity operations and rendezvous as well as large-scale, widely dispersed formations for sparse aperture imaging systems and other distributed data collection systems [43].

One compelling application for satellite formation flying implementation is ionospheric measurement and mapping. The ionosphere plays an important role in atmospheric electricity and has a pronounced effect on the propagation of radio waves. The ionosphere is vitally important for radio communications, yet certain aspects of it are not well understood. Plasma irregularities spanning multiple length scales are prevalent throughout the ionosphere and give rise to many interesting phenomena. The spatially and temporally varying structures arising from persistent instabilities can make communication difficult. These plasma irregularities produce scintillation which in turn affects radio signals. This makes it difficult or impossible to communicate through auroras or through the equatorial-spread-F [110]. The Air Force Research Lab launched the **C**ommunications/ **N**avigation **O**utage **F**orecasting **S**ystem satellite in 2008 to study some of these effects, but since it was a single, monolithic system, it lacked the capability to simultaneously measure different sections of the plasma instabilities. Large-scale, distributed, remote sensing systems such as the **Super D**ual **A**urora **R**adar **N**etwork (SuperDARN) [33] can measure huge scale traveling iono-

spheric disturbances (TIDs), but can have difficulty with measurements on the scale of 1 km- 10 km. In this context, a distributed system of small satellites can be deployed to take measurements and loosely keep formation while transmitting data to a central node which would communicate with the ground. The distributed architecture would give improved flexibility and resolution.

Trajectory planning and optimization is an important part of mission design for space vehicles. It plays a particularly important role in small satellite mission design due to the limited control authority that is generally available. A higher fidelity relative motion model used in the optimization of a spacecraft trajectory could reduce the amount of feedback required to stay on course since more external perturbations would be accounted for explicitly in the optimization.

This chapter focuses on the development and analysis of a method of trajectory planning which solves the fuel/time optimal control problem . The results in this paper are broad and could be applied to many different relative motion problems, however in our simulations we assume that the satellite is "small" (15 kg) and base the optimization on a thruster whose design constraints are not easily incorporated into more traditional impulsive analyses.

The contributions of this chapter are twofold. First, the Gim-Alfriend state transition matrix (GA-STM) is used as the relative motion model for control design as discussed in Chapter 2. The GA-STM is a powerful tool which provides greater orbit prediction accuracy over the classical linear equations of relative motion (LERM) given by Lawden [55, 8]. The GA-STM also does not require the integration of any differential equations. This is advantageous since modeling the differential J_2 perturbation and higher order gravitational perturbations for relative motion can be very difficult, and the effects of inaccurate modeling can become amplified during numerical integration and long-term propagation. The GA-STM is an exact, analytical, *linear* relative motion model that is valid at any eccentricity or inclination except the critical inclination given by $5\cos^2 i = 1$. The critical inclination, which is approximately $i = 63.4°$, is the angle at which the mean argument of perigee will not change, a well-known result from Lagrange's Planetary Equations [128].

The GA-STM provides a trajectory planner with a higher fidelity model, but since the model is linear, the theory of linear, time-varying systems can be used to study its structural characteristics. Furthermore, from the standpoint of optimal control, since the dynamics are linear, convex optimization may be used to develop optimal control strategies. By convexity, any feasible solution to a convex program is guaranteed to be the global optimum, and the solution time for a given problem scales slowly with respect to the number of optimization variables [21]. Using the GA-STM in conjunction with a convex program to compute the control laws yields more realistic trajectories, which is especially advantageous over long maneuver times or for long baselines, where the effects of differential J_2 become much more pronounced.

The second contribution in this chapter is an analysis of the family of trajectories that arise from solving the minimum fuel/time optimal control problem. In this chapter, the satellite

is assumed to be under-actuated, thrusting only in the velocity and orbit-normal directions (in- and cross-track). The fuel use is optimized via a standard linear program and then the fuel/time cost function is analyzed via a genetic algorithm. This global optimization technique is used because, for a desired balance between the time-of-flight and fuel use, the structure of the cost function is highly multi-modal for longer maneuver horizons, and there exist numerous local minima. The existence of these minima implies that for a given initial and target set in the relative frame, there exist multiple sub-optimal maneuvers that will be the minimum fuel transfer for a particular time-of-flight, even if the maneuver isn't globally optimal with respect to the fuel/time optimization. The numerous possible minima allow for a large design space for trajectory planners to explore, and thus a flexible framework which can be applied to a wide variety of maneuvers.

In this chapter, we expand on previous contributors' work by using the GA-STM in conjunction with a linear program to develop under-actuated, optimal trajectories for satellites with realistic hardware constraints in the presence of an eccentric, J_2-perturbed orbit. We also minimize a cost function which reflects the balance between the time-of-flight and the amount of fuel used with a genetic algorithm and show that we are able to obtain globally optimal solutions. These globally optimal solutions result in Δv expenditures that closely resemble results of impulsive orbit theory. Additionally, even though we present analysis of specific maneuvers, the method in this paper can be used in any arbitrary formation reconfiguration problem for which the GA-STM is a suitable relative motion model.

The remainder of the chapter is organized as follows. First, the essential theory behind the GA-STM theory is presented. It should be noted that the actual form for the elements of this state transition matrix are extremely long and complex, and so they have not been included in this paper (see [55] or [10]). The general structure of a fuel/time optimal control problem is presented using the Maximum Principle (MP), which provides insight into the structure of the optimal control policy. Then, the minimum fuel optimal control problem is cast as a standard linear program, and solved for a fixed time-of-flight. Following this development, the fuel/time optimal control problem is solved with a hybrid method: a linear program finds the minimum fuel control history and a genetic algorithm minimizes the time-of-flight for a given fuel/time penalty parameter. The control approach is applied to two separate mission profiles: 1) a trajectory plan to change the relative inclination only (cross-track only maneuver) and 2) a trajectory plan to change the relative semi-major axis only (in-track/ radial motion only). These two plans are considered because the results can be validated using fundamental results from orbital mechanics, namely the plane change and differential semi-major axis change. Our results match the required Δv well, and the discrepancies between the two results can easily be accounted for based upon the assumptions made for the maneuvers. The results presented also reflect the ease with which the GA-STM can be used to plan fuel/time optimal controllers compute optimal controllers.

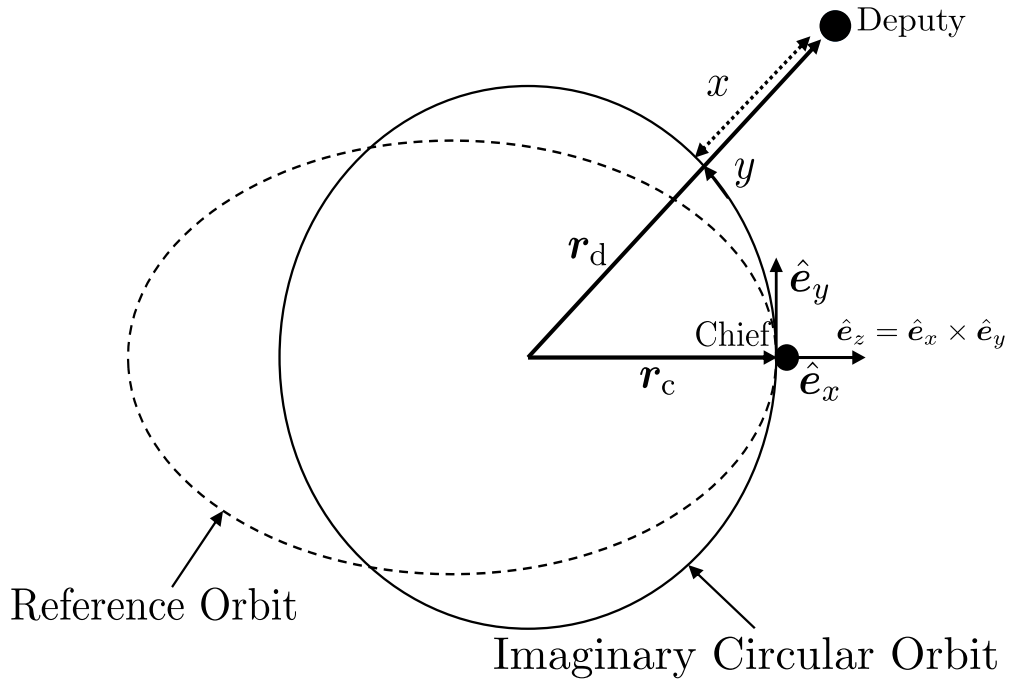

Figure 5.1: The curvilinear reference frame

5.2 Gim-Alfriend Relative Motion Theory

In this section, the necessary background on the Gim-Alfriend relative motion theory [55],[10] from Chapter 2.1.4, is presented.

Consider the J_2-perturbed, elliptic orbit of a satellite whose state is parameterized by the nonsingular element set $\boldsymbol{e} = (a, \theta, i, q_1, q_2, \Omega)^T$ where a is the semi-major axis, $\theta = \omega + f$ is the argument of latitude, ω is the argument of periapsis and f is the true anomaly, i is the inclination, $q_1 = e\cos\omega$, $q_2 = e\sin\omega$, e is the eccentricity of the chief orbit and Ω is the right ascension. Denoting the chief satellite's element set as $\boldsymbol{e}_c$ and the deputy's as $\boldsymbol{e}_d$, the differential orbital elements describing their separation is $\delta\boldsymbol{e} = \boldsymbol{e}_d - \boldsymbol{e}_c$, consistent with the notation in [55]. The relative state in the local-vertical, local-horizontal reference frame (LVLH) is given by the vector $\boldsymbol{x}(t) = (x, \dot{x}, y, \dot{y}, z, \dot{z})^T$. The geometry of the LVLH frame can be seen in Figure 5.1. Note that the LVLH frame is curvilinear; x denotes the difference in the orbital radii of the deputy and chief, and y and z denote curvilinear distances along imaginary circular orbits along the direction of motion and perpendicular to the orbital motion of the chief, respectively (see Figure 5.1). The curvilinear approximation has the advantage that it can reduce the linearization error for the formation flying problem. The geometric transformation between the J_2-perturbed differential orbital elements and the

curvilinear vector $\boldsymbol{x}(t)$ is given by

$$\boldsymbol{x}(t) = [\boldsymbol{M}(t) + \gamma \boldsymbol{N}(t)]\, \delta \boldsymbol{e}(t) \tag{5.1}$$

where $\gamma = 3J_2 R_{eq}^2$, $J_2 = 1082.63 \times 10^{-6}$ and $R_{eq} = 6378.137$ km is the equatorial radius of the Earth. The matrix $\boldsymbol{M}(t)$ maps the unperturbed elements into the state vector $\boldsymbol{x}(t)$ and the matrix $\boldsymbol{N}(t)$ contains the elements which are perturbed by J_2. For brevity, the matrix $[\boldsymbol{M}(t) + \gamma \boldsymbol{N}(t)]$ will be denoted by $\boldsymbol{\Sigma}(t)$.

The time evolution of the mean orbital elements, $\delta \bar{\boldsymbol{e}}$, due to the J_2 perturbation is

$$\delta \bar{\boldsymbol{e}}(t) = \bar{\boldsymbol{\phi}}_{\bar{\boldsymbol{e}}}(t, t_0) \delta \bar{\boldsymbol{e}}(t_0) \tag{5.2}$$

where $\bar{\boldsymbol{\phi}}_{\bar{\boldsymbol{e}}}(t, t_0)$ is the state transition matrix for the mean orbital elements. The differential osculating orbital elements, $\delta \boldsymbol{e}$ can be obtained from the mean elements by computing a matrix

$$\boldsymbol{D}(t) = \frac{\partial \boldsymbol{e}}{\partial \bar{\boldsymbol{e}}} = \mathbb{I}_{6\times 6} - J_2 R_{\text{eq}}^2 \left[\boldsymbol{D}^{(\text{lp})}(t) + \boldsymbol{D}^{(\text{sp})_1}(t) + \boldsymbol{D}^{(\text{sp})_2}(t) \right] \tag{5.3}$$

where (lp) and $(\text{sp})_{1,2}$ refer to long- and short-periodic variations in the elements due to the perturbation. The short-periodic variations occur on the scale of the orbit period. The long-periodic effects are typically manifested over a period of 20-60 days in LEO [128], so for maneuvers on the scale of about 12 hours the long-periodic contribution will be negligible. The mean-to-osculating transformation is

$$\delta \boldsymbol{e}(t) = \boldsymbol{D}(t) \delta \bar{\boldsymbol{e}} = \boldsymbol{D}(t) \bar{\boldsymbol{\phi}}_{\bar{\boldsymbol{e}}}(t, t_0) \delta \bar{\boldsymbol{e}}(t_0) = \boldsymbol{D}(t) \bar{\boldsymbol{\phi}}_{\bar{\boldsymbol{e}}}(t, t_0) \boldsymbol{D}^{-1}(t_0) \delta \boldsymbol{e}(t_0) \tag{5.4}$$

Using this expression, the state transition matrix for the curvilinear coordinates $\boldsymbol{x}(t)$ under the influence of J_2 is

$$\begin{aligned} \boldsymbol{x}(t) &= \boldsymbol{\Sigma}(t) \boldsymbol{D}(t) \bar{\boldsymbol{\phi}}_{\bar{\boldsymbol{e}}}(t, t_0) \boldsymbol{D}^{-1}(t_0) \boldsymbol{\Sigma}^{-1}(t_0) \boldsymbol{x}(t_0) \\ &= \boldsymbol{\Phi}_{J_2}(t, t_0) \boldsymbol{x}(t_0) \end{aligned} \tag{5.5}$$

The elements of the matrices in Eq. (5.5) are quite long and complex; the interested reader may refer to [55] or [10] for the complete form. The GA-STM is a closed-form, analytical approximation for the evolution of the deputy satellite relative to the chief under the influence of J_2. In [55], Gim and Alfriend showed that this state transition matrix is valid for all eccentricities and inclinations with the exception of the critical inclination. The results in [55] indicate that when compared to a nonlinear, numerical simulation of the basic orbit problem with the addition of the J_2-J_5 perturbations, the GA-STM experiences errors on the order of meters over the course of one day in LEO, where J_2 has the strongest effect. From the results in [55] it may be concluded that this approach can be a useful model for trajectory optimization over long baselines or multiple orbits. Importantly, this model is a *linear* theory which allows for certain guarantees in the control design, e.g. global optimality etc.

The GA-STM is a unique approach to modeling the relative motion because it requires no integration of differential equations. Indeed, in the succeeding sections of this paper, we compute the control law and then simulate the system by solving a series of difference equations formulated using the GA-STM.

5.3 Trajectory Optimization

In this section, the general theory of minimum fuel and time/fuel optimal control is presented in the context of the Maximum Principle. We then show how the continuous-time optimal control problem is turned into a discrete-time, convex programming problem.

5.3.1 Minimum Fuel and Time/Fuel Optimization

Consider the general, point-to-point optimal control problem

$$\begin{aligned} &\min_{\boldsymbol{u}_i(t)\in U} \int_{t_0}^{t_f} \sum_{i=1}^{m} |u_i(\tau)| \,\mathrm{d}\,\tau \\ \text{subject to: } &\dot{\boldsymbol{x}}(t) = \boldsymbol{A}(t)\boldsymbol{x}(t) + \boldsymbol{B}(t)\boldsymbol{u}(t) \\ &\boldsymbol{x}(t_0) = \boldsymbol{x}_0 \quad \boldsymbol{x}(t_f) = \boldsymbol{x}_f \\ &U = [-u_{\max}, u_{\max}] \end{aligned} \tag{5.6}$$

where t_0 and t_f are fixed and U is the set of admissible controllers, $u_{min} = -u_{max}$. Using Pontryagin's Maximum Principle [28],[78], the Hamiltonian is

$$\mathcal{H}(\boldsymbol{x}(t), \boldsymbol{\lambda}(t), \boldsymbol{u}(t), t) = \sum_{i=1}^{m} |u_i(t)| + \boldsymbol{\lambda}^T(t) \left[\boldsymbol{A}(t)\boldsymbol{x}(t) + \boldsymbol{B}(t)\boldsymbol{u}(t)\right] \tag{5.7}$$

where $\boldsymbol{\lambda}$ is the vector of co-state (or adjoint) variables. The optimal control is the value of $u_i(t)$ for which the Hamiltonian takes its maximum value:

$$\begin{aligned} u_i^*(t) &= \arg\max_{u_i(t)\in U} \mathcal{H}(\boldsymbol{x}^*(t), \boldsymbol{\lambda}^*(t), \boldsymbol{u}^*(t), t) \\ &= -\operatorname{dez}\left(b_{ij}(t)\lambda_i^*(t)\right) \end{aligned} \tag{5.8}$$

where $(\cdot)^*$ denotes an optimal value, and $\operatorname{dez}(\cdot)$ is the deadzone function defined by

$$u_i^*(t) = \begin{cases} u_{\max} & \text{if } b_{ij}\lambda_i^* > 1 \\ -u_{\max} & \text{if } b_{ij}\lambda_i^* < -1 \\ 0 & \text{if } |b_{ij}\lambda_i^*| \leq 1 \end{cases}$$

The general structure of the minimum fuel optimal control is a bang-off-bang profile where the controller takes on either the maximum input or no input. The adjoint variables satisfy the following equation

$$\dot{\boldsymbol{\lambda}}(t) = -\boldsymbol{A}^T(t)\boldsymbol{\lambda}(t) \implies \boldsymbol{\lambda}^*(t) = \boldsymbol{\Phi}^T_{\boldsymbol{A}(t)}(t_0, t)\boldsymbol{\lambda}^*(t_0) \tag{5.9}$$

where $\boldsymbol{\Phi}_{\boldsymbol{A}(t)}(t, t_0)$ is the transition matrix associated with the dynamics given by $\dot{\boldsymbol{x}}$. While it would seem that the optimal control problem has been solved, the initial values of the costates still have not been determined. Since this is a point-to-point problem, transversality conditions will not give any extra information about the problem at the boundaries, and so for this particular approach the problem must be solved using a numerical technique such as shooting or collocation.

The minimum time/fuel optimal control problem is formulated exactly as in Eq. 6.26, however the running cost is now given by

$$\min_{\boldsymbol{u}(t)\in U} \int_{t_0}^{t_f} 1 + \alpha \sum_{i=1}^{m} |u_i(\tau)| \, \mathrm{d}\, \tau \tag{5.10}$$

with t_f being a free variable, and the additional boundary constraint $\mathcal{H}(t_f) = 0$. The optimal control profile will remain a bang-off-bang signal, however in this problem, the parameter α serves to also establish the relative importance of the maneuver time relative to the control signal.

5.3.2 Linear Programming Solution

Rather than use numerical techniques such as shooting or collocation, one may convert the problem to a linear program, a method for which there exist well-established, reliable techniques for finding a *global* minimum. The solution to a general linear time-varying system is the variation of constants formula

$$\boldsymbol{x}(t) = \boldsymbol{\Phi}(t, t_0)\boldsymbol{x}(t_0) + \int_{t_0}^{t_f} \boldsymbol{\Phi}(t, \tau)\boldsymbol{B}(\tau)\boldsymbol{u}(\tau) \, \mathrm{d}\, \tau \tag{5.11}$$

Imposing a zero-order-hold (ZOH) with sample time T_s on the input, the discrete form of the variation of constants formula for the $(k+1)^{\text{th}}$ time-step given the state and input at the k^{th} time-step is

$$\boldsymbol{x}_{k+1} = \boldsymbol{\Phi}((k+1)T_s, kT_s)\boldsymbol{x}_k + \int_{kT_s}^{(k+1)T_s} \boldsymbol{\Phi}((k+1)T_s, \tau)\boldsymbol{B}(\tau) \, \mathrm{d}\, \tau \, \boldsymbol{u}_k \tag{5.12}$$

Define the matrices [114]:

$$\begin{aligned} \boldsymbol{A}_k &= \boldsymbol{\Phi}((k+1)T_s, kT_s) \\ \boldsymbol{B}_k &= \int_{kT_s}^{(k+1)T_s} \boldsymbol{\Phi}((k+1)T_s, \tau)\boldsymbol{B}(\tau) \, \mathrm{d}\, \tau \end{aligned} \tag{5.13}$$

A recursion model is built up over $N-1$ samples

$$\begin{aligned}
\boldsymbol{x}_1 &= \boldsymbol{A}_0\boldsymbol{x}_0 + \boldsymbol{B}_0\boldsymbol{u}_0 \\
\boldsymbol{x}_2 &= \boldsymbol{A}_1\boldsymbol{x}_0 + \boldsymbol{B}_1\boldsymbol{u}_1 \\
&= \boldsymbol{A}_1\boldsymbol{A}_0\boldsymbol{x}_0 + \boldsymbol{A}_1\boldsymbol{B}_0\boldsymbol{u}_0 + \boldsymbol{B}_1\boldsymbol{u}_0 \\
&\vdots \\
\boldsymbol{x}_N &= \boldsymbol{A}_{N-1}\boldsymbol{A}_{N-2}\cdots\boldsymbol{A}_1\boldsymbol{A}_0\boldsymbol{x}_0 + \boldsymbol{A}_{N-1}\boldsymbol{A}_{N-2}\cdots\boldsymbol{A}_1\boldsymbol{B}_0\boldsymbol{u}_0 + \cdots \\
&\quad \boldsymbol{A}_{N-1}\boldsymbol{B}_{N-2}\boldsymbol{u}_{N-2} + \boldsymbol{B}_{N-1}\boldsymbol{u}_{N-1}
\end{aligned} \tag{5.14}$$

Let $\boldsymbol{x}_N = \boldsymbol{x}_f$, which is the terminal boundary condition, the product $\boldsymbol{A}_{N-1}\cdots\boldsymbol{A}_0$ gives the unforced response of the system to the initial state $\boldsymbol{x}_0$ at the final time step $k = N$. Define a new vector, which is the terminal equality constraint

$$\boldsymbol{b}_{eq} = \boldsymbol{x}_N - \boldsymbol{A}_{N-1}\cdots\boldsymbol{A}_0\boldsymbol{x}_0 \tag{5.15}$$

The products $\boldsymbol{A}_{N-1}\cdots\boldsymbol{A}_0\boldsymbol{B}_0$ and so on may be thought of as the convolution between the free response and the control input at each sampling instant; as time progresses the current state is a product of the input at the current time plus all of the control inputs leading up to that point.

In order to put the problem in the form of a standard linear program, we define a new pair of input vectors $\boldsymbol{u}_k^+$ and $\boldsymbol{u}_k^-$, since the standard form of a linear program requires that the decision variables be greater than or equal to zero. Each component of $\boldsymbol{u}_k^+$ and $\boldsymbol{u}_k^-$ is non-negative and bounded above by $u_{\max}$. At the end of the optimization, the positive and negative control signals are recombined by[125]

$$\boldsymbol{u}_k \;=\; \boldsymbol{u}_k^+ - \boldsymbol{u}_k^- \tag{5.16}$$

Now, a new matrix $\bar{\boldsymbol{B}}_k$ can be defined to incorporate both the positive and negative variables into the convolution history

$$\bar{\boldsymbol{B}}_k = \begin{bmatrix}\boldsymbol{B}_k & -\boldsymbol{B}_k\end{bmatrix} \tag{5.17}$$

A convolution matrix can be computed

$$\boldsymbol{A}_{eq} = \begin{bmatrix}\boldsymbol{A}_{N-1}\cdots\boldsymbol{A}_1\bar{\boldsymbol{B}}_0 & \cdots & \boldsymbol{A}_{N-1}\bar{\boldsymbol{B}}_{N-2} & \bar{\boldsymbol{B}}_{N-1}\end{bmatrix} \tag{5.18}$$

and the vector of decision variables is

$$\tilde{\boldsymbol{U}} = \begin{bmatrix}(\boldsymbol{u}_0^+)^T & (\boldsymbol{u}_0^-)^T & (\boldsymbol{u}_1^+)^T & (\boldsymbol{u}_1^-)^T & \cdots & (\boldsymbol{u}_{N-1}^+)^T & (\boldsymbol{u}_{N-1}^-)^T\end{bmatrix}^T \tag{5.19}$$

The standard linear program can be written as

$$\begin{aligned}
&\min_{\boldsymbol{u}_k^+,\boldsymbol{u}_k^-} \sum_{k=0}^{N-1}\left[\boldsymbol{u}_k^+ + \boldsymbol{u}_k^-\right] \\
&\text{subject to } \boldsymbol{A}_{eq}\tilde{\boldsymbol{U}} = \boldsymbol{b}_{eq} \\
&\qquad \boldsymbol{u}_k^+ \geq \boldsymbol{0}_{m\times 1}, \quad \boldsymbol{u}_k^+ \leq u_{\max}\boldsymbol{1}_{m\times 1} \\
&\qquad \boldsymbol{u}_k^- \geq \boldsymbol{0}_{m\times 1}, \quad \boldsymbol{u}_k^- \leq u_{\max}\boldsymbol{1}_{m\times 1}
\end{aligned} \tag{5.20}$$

where $\mathbf{0}_{m\times 1}$ defines a vector of zeros and $\mathbf{1}_{m\times 1}$ defines a vector of ones and m is the number of input channels in each direction. The control constraint set defines the vertices of a convex polytope. By convexity, if a minimum for Eq. 5.20 exists, it will be a global minimum. For this paper, Matlab's primal-dual interior point algorithm was used.

The method presented for Eq. 5.20 assumes a fixed final time, the minimum value of which will not generally be the same for the minimum fuel/time problem. The minimum fuel/time cost function in Eq. 5.10 is a functional mapping $J : \mathbb{R}\times\mathbb{R}^m \to \mathbb{R}$. In the linear programming context, the cost functional takes the form

$$J_{LP}(||\boldsymbol{u}(t_f)||_1, t_f; \alpha) = t_f + \alpha \underbrace{\sum_{k=0}^{N-1} \left[\boldsymbol{u}_k^+ + \boldsymbol{u}_k^-\right]}_{=||\boldsymbol{u}(t_f)||_1} \tag{5.21}$$

In proximity operation scenarios with a sufficiently short time horizon, the cost function in Eq. (5.21) has a unique minimum. One approach to determining the time which minimizes Eq. 5.21 is to use a golden section algorithm [125] or similar single dimensional search in conjunction with the linear programming output to determine the minimum time-of-flight. Generally this will only work if it is known that there exists only one minimum. This approach allows a trade space analysis of the weighted fuel/time optimal control problem while using the convexity guarantees of the linear program.

For longer maneuver horizons involving multiple orbits, such as large-scale reconfiguration maneuvers, the functional in Eq. 5.21 becomes multi-modal with numerous local minima for a given values of α. In this instance, a golden section search is not guaranteed to converge to the global minimum. Two approaches can be used here: 1) an iterative search to find several candidate minima, at which point the golden section search could be used or 2) a global optimization technique such as a continuous genetic algorithm [64]. The latter approach is employed in this paper.

The structure of the cost functional, namely the locations of the minima, can be difficult to determine for a given value of α. This serves as the justification for using the genetic algorithm; given a sufficiently large solution space and a diverse initial population, the algorithm will tend to converge to the global minimum. The trajectory planner is only required to provide an upper and lower bound on the time-of-flight.

While providing a minimum which is possibly global, the genetic algorithm does have some limitations. The limitations of the genetic algorithm lie primarily in the stochastic nature of the evolution of the population. Provided enough diversity exists in the first generation of the algorithm, i.e. there exists a wide enough spread in the decision variables, the algorithm can converge to a global minimum. It is important to note, however, that there does not currently exist a formal proof of convergence for the genetic algorithm, nor does there even exist a lower bound on the number of function evaluations needed for convergence. A hybrid approach could be used where the genetic algorithm is used to get "close" to a global minimum at

which point a local minimum search algorithm with a guarantee of convergence could be used, however this approach was not employed here.

5.4 Trajectory Design using the GA-STM

In this section, we apply the method outlined in the previous section to the problem of deploying a large-baseline formation of satellites with realistic thruster constraints incorporated into the optimization.

5.4.1 Thruster Allocation and Reachability

Recall that the ordering of the variables in the state vector used by the GA-STM is given by $\boldsymbol{x} = (x, \dot{x}, y, \dot{y}, z, \dot{z})^T$. If the satellite is fully actuated, the input matrix is

$$\boldsymbol{B}(t) = \frac{1}{m_\mathrm{d}} \begin{bmatrix} 0 & 0 & 0 & 0 & 0 & 1 \\ 0 & 0 & 0 & 1 & 0 & 0 \\ 0 & 1 & 0 & 0 & 0 & 0 \end{bmatrix}^T \tag{5.22}$$

Yan and Alfriend [136] showed the controllability of the fully-actuated GA-STM model by computing a minimum-energy controller. Furthermore, the authors of the current work showed in [111] that the general time-varying form of the formation flying problem is completely controllable using only two control inputs, one in the in-track, y, direction and one in the cross-track, z, direction. The under-actuated control input matrix is

$$\boldsymbol{B}(t) = \frac{1}{m_\mathrm{d}} \begin{bmatrix} 0 & 0 & 0 & 0 & 0 & 1 \\ 0 & 0 & 0 & 1 & 0 & 0 \end{bmatrix}^T \tag{5.23}$$

Due to the complexity of the GA-STM and the presence of transcendental terms relating time, true anomaly and mean anomaly (through Kepler's equation), a closed-form reachability Gramian is difficult if not impossible to compute. However, a numerical investigation over a wide range of eccentricities, inclinations and time spans reveals that the Gramian matrix given by [114]

$$\boldsymbol{W}_{J_2}(k_0, k_f) = \sum_{j=k_0}^{k_f-1} \boldsymbol{\Phi}_{J_2}(k_f, j+1) \boldsymbol{B}(j) \boldsymbol{B}^T(j) \boldsymbol{\Phi}_{J_2}^T(k_f, j+1) \tag{5.24}$$

is nonsingular for both the $\boldsymbol{B}(t)$ in Eq. (5.22) and Eq. (5.23). It follows that the system is completely reachable using thrust in the radial, in-track and cross-track directions, or just in-track and cross-track. The only inclination(s) for which this condition does not hold is near the critical inclination, given by the roots of $5\cos^2 i = 1$ where the denominators in the GA-STM which contain this expression become singular.

The positive-definiteness of the reachability Gramian guarantees the existence of a non-unique control law which will accomplish a desired transfer from $\boldsymbol{x}_0 \rightarrow \boldsymbol{x}_N$. The under-actuated reachability property physically means that the radial and in-track positions and velocities may be reached using only in-track thrust, and the cross-track position and velocity may be controlled using the cross-track thrust. This property reflects results from classical orbital maneuver theory. For example, planar maneuvers such as the Hohmann transfer, bi-elliptic transfer and one-tangent burn maneuvers require thrusts purely in the velocity direction; no radial thrust is required to accomplish the maneuver.

5.4.2 Validation

Before using the proposed linear programming solution to develop fuel/time optimal trajectories around a perturbed, elliptical orbit, we compare the linear programming solution for the GA-STM with $J_2 = 0$ and $e = 0$ to two well-known results from impulsive orbit transfer theory. We note that the fuel usage (Δv with units of m/s) should be no less than that predicted by impulsive orbit transfer theory because we assume a finite-time maneuver which, in general, is not as efficient as an impulsive maneuver. On the other hand, analyzing the maneuvers with finite thrust allows for comparison of a realistic, flight proven thruster with the impulsive maneuver.

Differential Inclination Change

Impulsive maneuvers can be derived geometrically [52, 50] or from Gauss' Variational Equations [117]. The Δv required to perform a pure relative inclination change in terms of orbital elements is

$$\Delta v_{\delta i} = \frac{h \delta i}{r \cos \theta_c} = na\delta i \tag{5.25}$$

where (for a pure inclination change) θ_c is the argument of latitude at the node crossing. Table 5.1 contains the model data for a sample inclination change. The deputy starts at the origin of the LVLH frame and performs a pure cross-track maneuver. The satellite thruster parameters are based on the Aerojet MR-103M Minimum Impulse Thruster rocket (P/N 34211-301) [4]. The MR-103M provides 0.22 N of thrust and has a specific impulse of 206 seconds. The mass of the rocket is 0.16 kg, so the total mass for four thrusters (mounted in the $\pm$ in-track and $\pm$ cross-track directions) would be about 0.64 kg. The satellite is assumed to have a mass of 15 kg, and for this analysis, the change in mass (which is used to calculate Δv) is less than 1% of the original mass, so we assume it is negligible.

The minimum predicted Δv required for the pure relative inclination change is 26.97 m/s. In Figure 5.2, the Δv as a function of the time-of-flight is shown. As expected the finite thrust approach does not quite match the Δv of the pure impulsive maneuver, seen in Figure 5.2. The reason for this stems from the assumptions on the two models. The finite thrust time

Table 5.1: Parameters for circular, unperturbed relative inclination change

Parameter	Value
Chief init. state, $(a, \theta, i, q_1, q_2, \Omega)$	$(6678 \text{ km}, 0 \text{ deg}, 28 \text{ deg}, 0, 0, 45 \text{ deg})$
Deputy init. state, $(x, \dot{x}, y, \dot{y}, z, \dot{z})$	$(0 \text{ m}, 0 \text{ m/s}, 0 \text{ m}, 0 \text{ m/s}, 0 \text{ m}, 0 \text{ m/s})$
Deputy final state, $(\delta a, \delta\theta, \delta i, \delta q_1, \delta q_2, \delta\Omega)$	$(0 \text{ m}, 0 \text{ deg}, 0.2 \text{ deg}, 0, 0, 0 \text{ deg})$
Max thrust, u_{max}	0.22 N
Specific impulse, I_{sp}	206 s
Deputy mass, m_{d}	15 kg

means that the maneuver cannot be performed as an exact impulse at the node crossing; the thruster fires slightly before and after the node crossing, resulting in a slight drop in efficiency of the maneuver. The thrust duration in this model is bounded from below by the zero-order hold discretization. As the discretization becomes smaller, the finite thrust and impulsive maneuver solutions will converge, but this comes at the expense of more computation when building the equality constraint matrices. For this scenario, the sampling time was taken to be $T_s = 5$ s and the minimum Δv obtained with this model was 27.24 m/s.

In Figure 5.3, a sample relative trajectory over 5 orbits is shown. This is a pure cross-track maneuver, and in the absence of J_2 and eccentricity, the radial and in-track histories are numerically zero. The initial and final points for the trajectory are identical, however the cross-track velocity has changed; this is consistent with what one would expect from classical orbital mechanics. The control history for the maneuver is seen in Figure 5.4. The thrusts are periodic, and in fact the beginning and end of each thrust are symmetric about the node crossing. Again, this is consistent with what is expected of this maneuver.

Differential Semi-major Axis Change

Next, we consider the differential change of the semi-major axis. The semi-major axis change for an arbitrary elliptical orbit can be accomplished by two impulsive burns, one at periapsis and one at apoapsis [117]:

$$\begin{aligned} \Delta v_p &= \frac{na\eta}{4}\left[\frac{\delta a}{a} + \frac{\delta e}{1+e}\right] \\ \Delta v_a &= \frac{na\eta}{4}\left[\frac{\delta a}{a} - \frac{\delta e}{1-e}\right] \end{aligned} \tag{5.26}$$

where $\eta = \sqrt{1-e^2}$ and $e, \delta e = 0$. Similarly to the previous case, it is required that a tangential thrust (aligned with the velocity vector) occur at two very specific points in the orbit, periapsis and apoapsis, for the highest efficiency. The Δv predicted for the differential semi-major axis change based on the relative orbital elements is $\Delta v = 5.7845$ m/s. Interestingly, this yields exactly the same Δv lower bound predicted by Ichikawa *et al.* [73] despite using

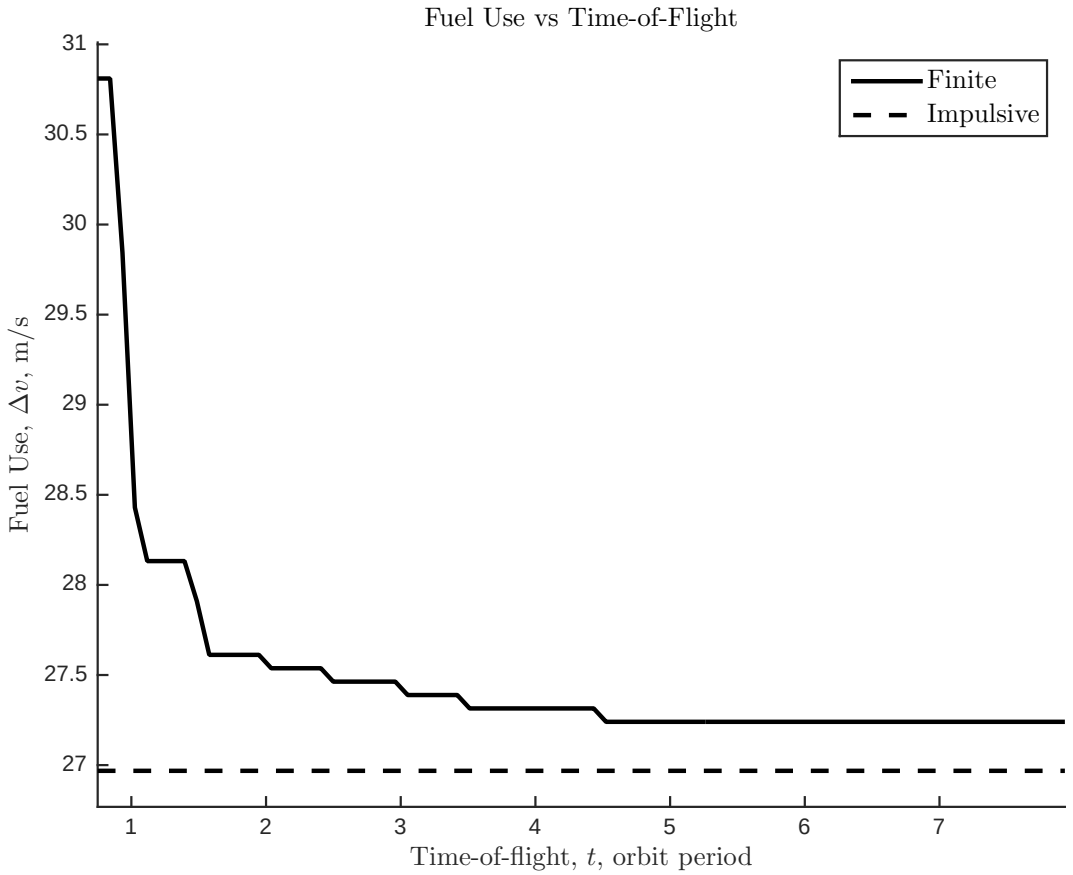

Figure 5.2: Δv vs time-of-flight

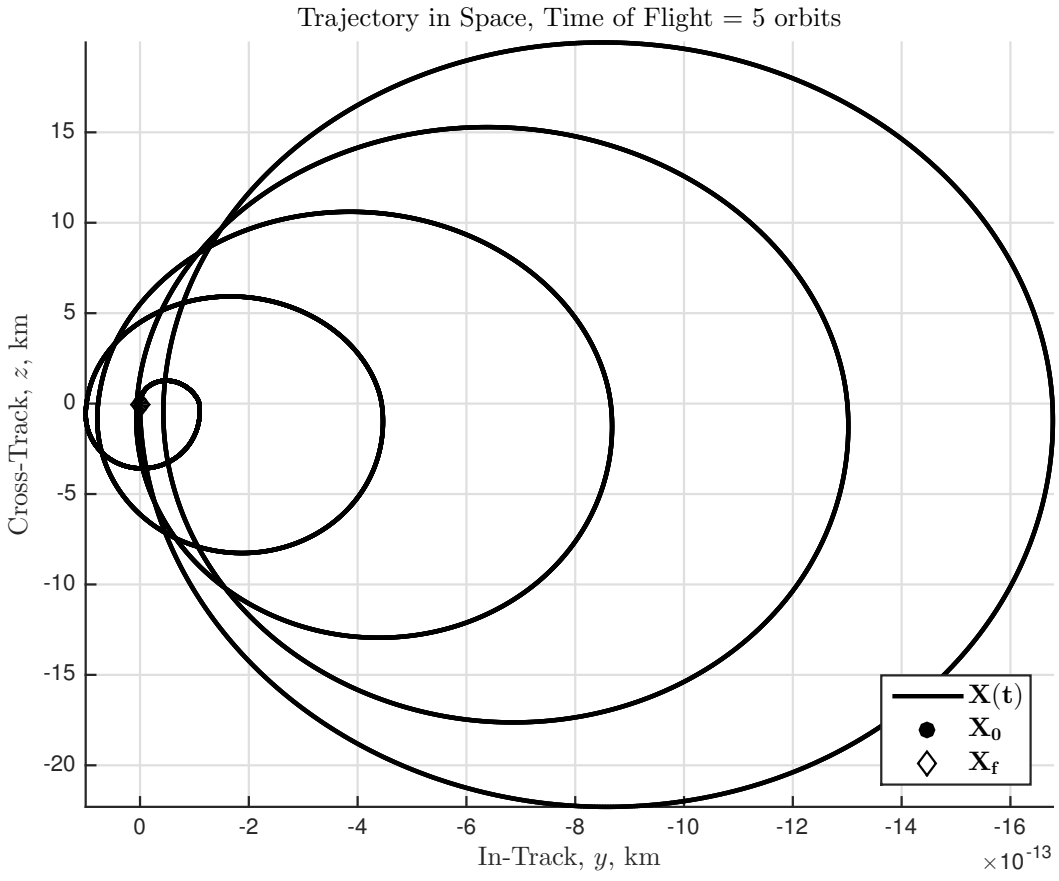

Figure 5.3: Cross-track motion of the inclination change maneuver

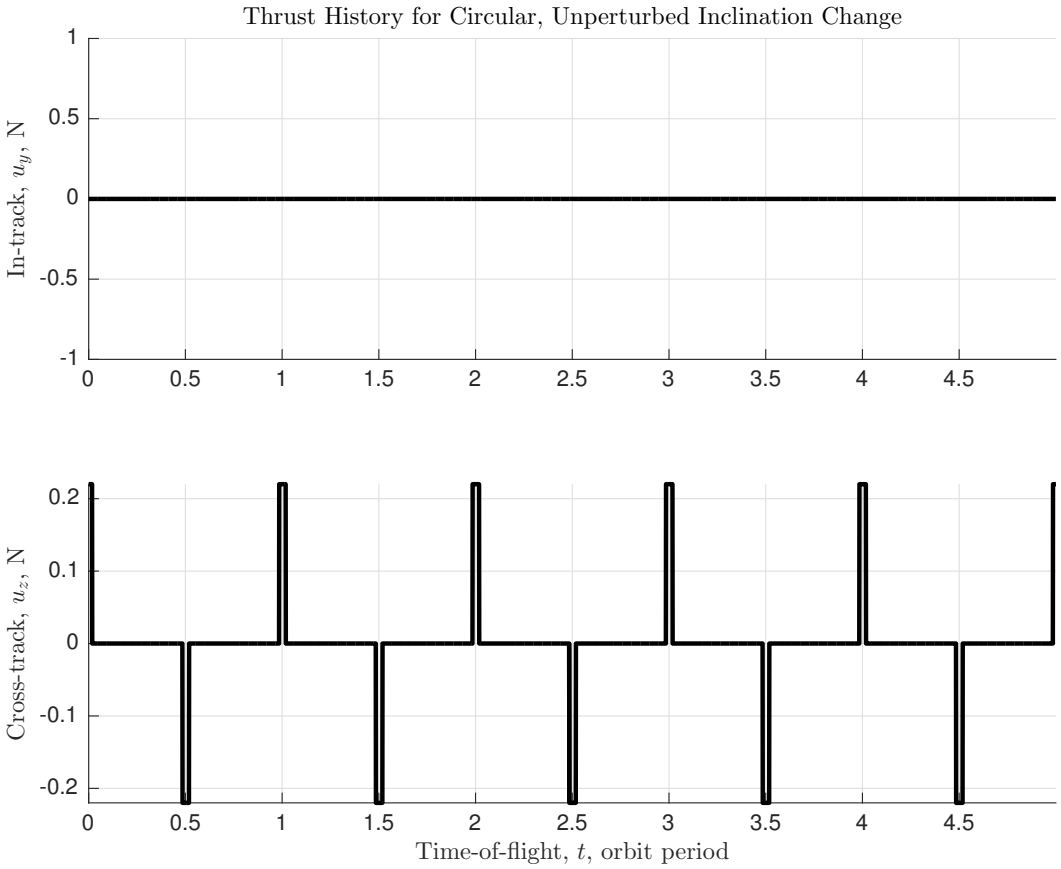

Figure 5.4: control history for cross-track maneuver

an entirely different formulation (relative orbital elements in [117] vs the HCW equations in [73]). The parameters for the relative semi-major axis change are given in Table 5.2. Again, the deputy begins from the origin and performs thrusts to move straight up.

Table 5.2: Parameters for circular, unperturbed relative semi-major axis change

Parameter	Value
Chief init. state, $(a, \theta, i, q_1, q_2, \Omega)$	$(6678 \text{ km}, 0 \text{ deg}, 28 \text{ deg}, 0, 0, 45 \text{ deg})$
Deputy init. state, $(x, \dot{x}, y, \dot{y}, z, \dot{z})$	$(0 \text{ m}, 0 \text{ m/s}, 0 \text{ m}, 0 \text{ m/s}, 0 \text{ m}, 0 \text{ m/s})$
Deputy final state, $(\delta a, \delta\theta, \delta i, \delta q_1, \delta q_2, \delta\Omega)$	$(10 \text{ km}, 0 \text{ deg}, 0 \text{ deg}, 0, 0, 0 \text{ deg})$
Max thrust, u_{max}	0.22 N
Specific impulse, I_{sp}	206 s
Deputy mass, m_{d}	15 kg

The required Δv for this maneuver as a function of the time-of-flight is shown in Figure 5.5. Similarly to the previous case, the finite thrust is not quite as efficient as a purely impulsive burn. This is again due to the finite thrust case not being able to command the requisite Δv instantaneously. The relative trajectory for the semi-major axis change over 5 orbits is shown in Figure 5.6. The motion for the circular, unperturbed case is a pure radial/in-track trajectory, and from Figure 5.7, we can see that the maneuver requires three finite thrusts, but they occur at approximately integer values of $\theta = \kappa\pi,\ \kappa \in \mathbb{N}$ apart from each other, and these thrusts are not necessarily on consecutive orbits. This is similar to the result predicted by Gaias *et al.* [52, 50] for purely impulsive, planar maneuvers, and this further validates that the linear programming approach provides finite thrusts which are consistent with what would be expected for these orbital maneuvers.

5.4.3 Trajectory Optimization for Perturbed Eccentric Orbits

Now, the J_2 perturbation and eccentricity are incorporated into the model and we show that while the addition of J_2 and eccentricity affects the fuel usage for the inclination change because of the precession of the ascending (and descending) node, the Δv required for the semi-major axis change is very nearly the same.

Differential Inclination Change

The addition of J_2 and eccentricity will affect not only the motion of the satellite over $\boldsymbol{x}_0 \mapsto \boldsymbol{x}_N$ but also the points in the orbit where the burn occurs, as well as the duration of the burn. The simulation parameters for this maneuver are given in Table 5.3 and the parameters for the genetic algorithm are given in Table 5.4.

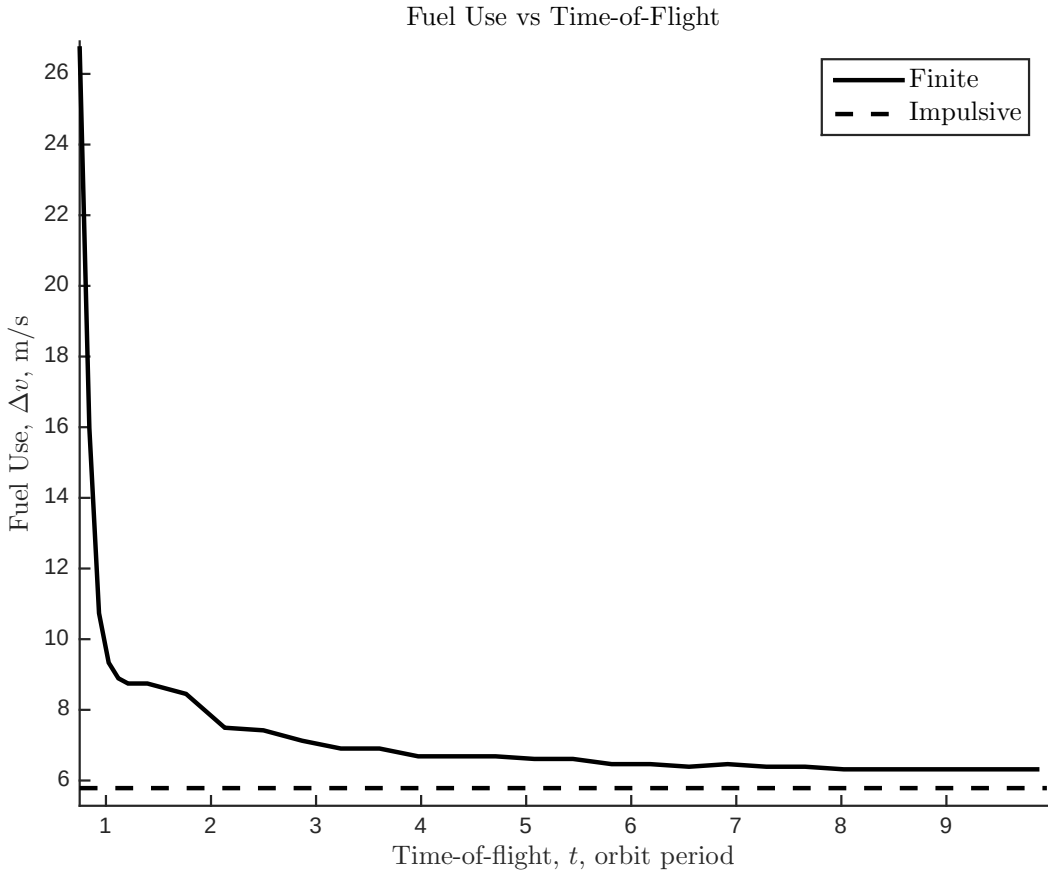

Figure 5.5: Δv vs time-of-flight

Table 5.3: Parameters for eccentric, perturbed relative inclination change

Parameter	Value
Chief init. state, $(a, \theta, i, q_1, q_2, \Omega)$	$(6678 \text{ km}, 0 \text{ deg}, 28 \text{ deg}, 0.01, 0, 45 \text{ deg})$
Deputy init. state, $(x, \dot{x}, y, \dot{y}, z, \dot{z})$	$(0 \text{ m}, 0 \text{ m/s}, 0 \text{ m}, 0 \text{ m/s}, 0 \text{ m}, 0 \text{ m/s})$
Deputy final state, $(\delta a, \delta\theta, \delta i, \delta q_1, \delta q_2, \delta\Omega)$	$(0 \text{ m}, 0 \text{ deg}, 0.2 \text{ deg}, 0, 0, 0 \text{ deg})$
Max thrust, u_{max}	0.22 N
Specific impulse, I_{sp}	206 s
Deputy mass, m_{d}	15 kg

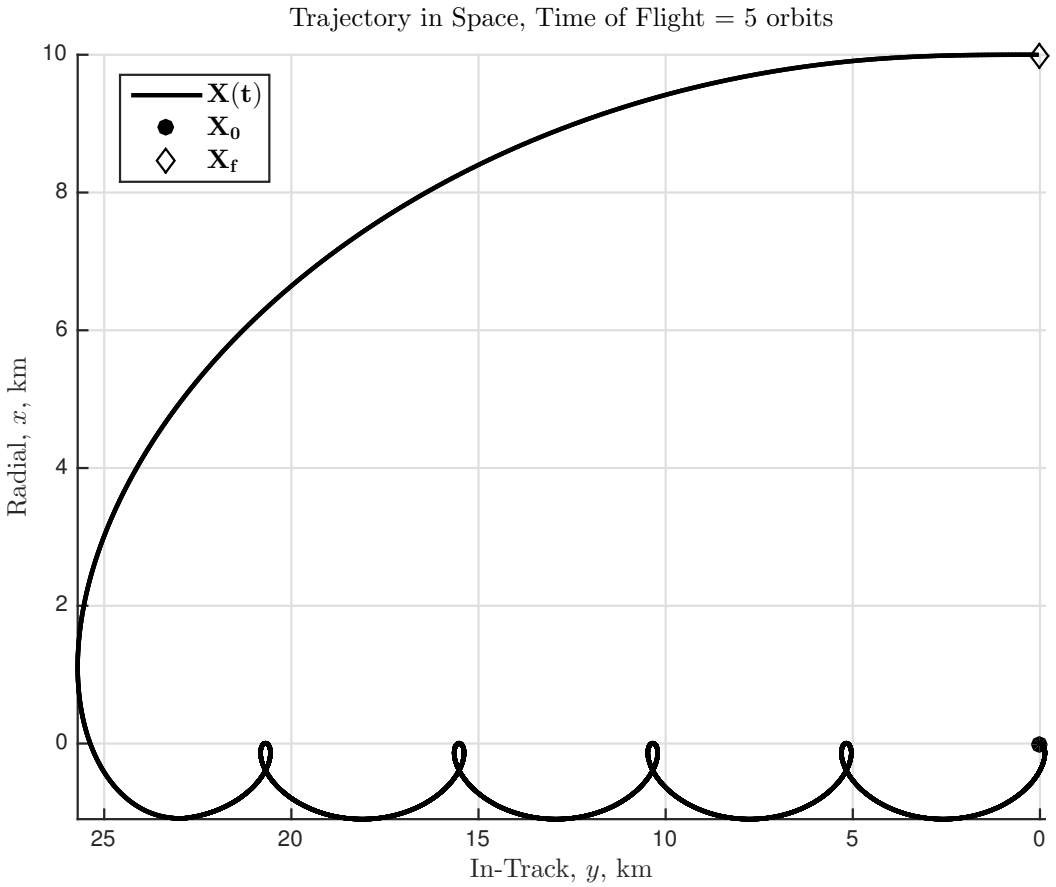

Figure 5.6: Relative trajectory for the planar maneuver

Table 5.4: Genetic algorithm for relative inclination change

Parameter	Value
No. Opt. Vars, (t_f)	1
Min. time, t_{lower}	0.75 Orbit period
Max. time, t_{upper}	6 Orbit period
Max. No. Generations, gen_{max}	20
No. chromosomes, n_ξ	20
Mutation index, -	0.2
Selection index, -	0.5

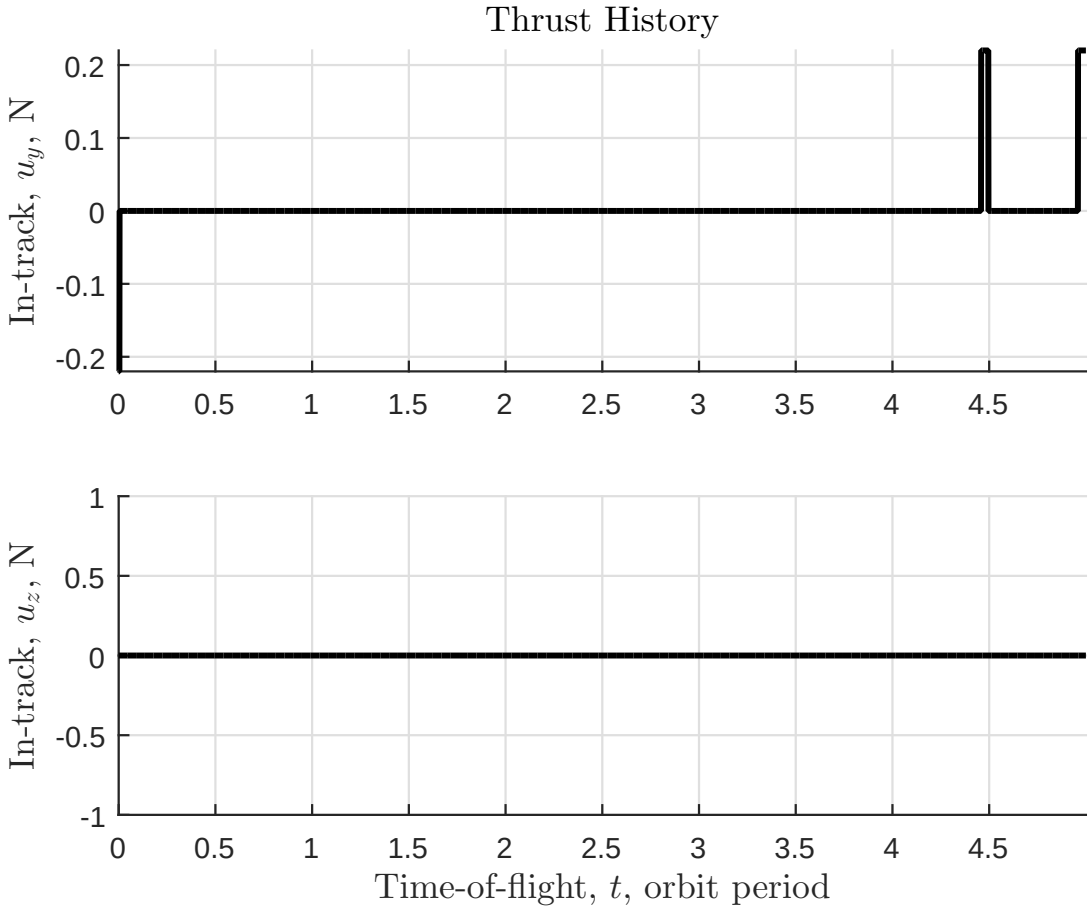

Figure 5.7: Δv vs time-of-flight

The effect that J_2 and eccentricity have on the shape of the maneuver and the structure of the thrust history become apparent upon inspecting Figure 5.8, 5.10, and 5.11. In Figure 5.8, the Δv required to accomplish the maneuver versus the time-of-flight is shown. The ideal Δv remains the same since the impulsive maneuver happens at the node crossing, however the linear programming solution requires about 1 m/s more Δv to accomplish the maneuver.

In the circular unperturbed case (see Figure 5.4), the cross track thrusts occurs at the node crossing, and the thrust duration is symmetric about the node resulting in a pure cross track maneuver. When eccentricity and J_2 are included, the motion is no longer purely cross track, and some planar thrusting must occur at periapsis and apoapis to satisfy the boundary conditions of the optimization. The cross-track thrusts are no longer symmetric about the node crossing. As seen in Figure 5.11, the thrusts actually become a little bit longer in the vicinity of the node crossing, which is a result of the differential precession of the chief and deputy nodes.

The fuel/time optimal control problem is solved using the LP with the genetic algorithm. As can be seen in Figure 5.9, the cost function becomes multi-modal for a given α. The cost function in Eq. (5.21) is fairly insensitive to small changes in α for this particular problem; since the LP cost typically takes values $\mathcal{O}(10^1)$, and time-of-flight is typically $> \mathcal{O}(10^3)$, for $\alpha < \mathcal{O}(10^3)$, the time-of-flight dominates the cost function.

Differential Semi-major Axis Change

The semi-major axis change with the addition of eccentricity and J_2 is similar to the circular, unperturbed solution. Recalling Eq. (5.26) and the fact that the quantity $\delta e = 0$, it is readily apparent that the only change in the Δv at periapsis and apoapsis will be due to η in Eq. (5.26). For the maneuver we consider, $e = 0.01$ from which it follows that $\eta \approx 0.99995$, so the total fuel use is $\Delta v = 5.78425$ m/s, very nearly the same as the circular, unperturbed solution ($\Delta v = 5.7845$ m/s). The parameters for the maneuver are given in Table 5.5 and the genetic algorithm parameters are given in Table 5.6.

Table 5.5: Parameters for eccentric, perturbed relative semi-major axis change

Parameter	Value
Chief init. state, $(a, \theta, i, q_1, q_2, \Omega)$	$(6678 \text{ km}, 0 \text{ deg}, 28 \text{ deg}, 0.01, 0, 45 \text{ deg})$
Deputy init. state, $(x, \dot{x}, y, \dot{y}, z, \dot{z})$	$(0 \text{ m}, 0 \text{ m/s}, 0 \text{ m}, 0 \text{ m/s}, 0 \text{ m}, 0 \text{ m/s})$
Deputy final state, $(\delta a, \delta\theta, \delta i, \delta q_1, \delta q_2, \delta\Omega)$	$(10 \text{ km}, 0 \text{ deg}, 0 \text{ deg}, 0, 0, 0 \text{ deg})$
Max thrust, u_{max}	0.22 N
Specific impulse, I_{sp}	206 s
Deputy mass, m_{d}	15 kg

As before, the genetic algorithm is able to find the minimum of the multi-modal cost func-

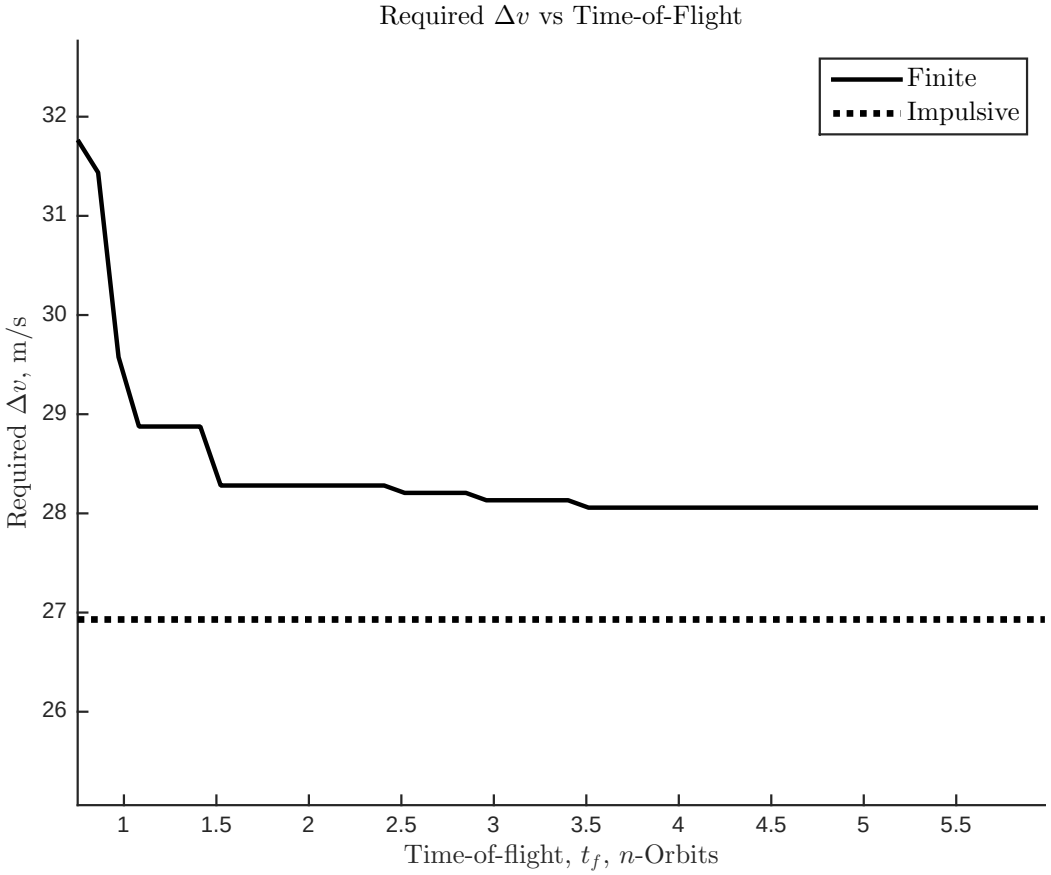

Figure 5.8: Δv vs time-of-flight for the perturbed, eccentric maneuver

Table 5.6: Genetic algorithm for relative semi-major axis change

Parameter	Value	Unit
No. Opt. Vars, (t_f)	1	-
Min. time, t_{lower}	0.75	Orbit period
Max. time, t_{upper}	6	Orbit period
Max. No. Generations, gen_{max}	20	-
No. chromosomes, n_ξ	20	-
Mutation index, -	0.2	-
Selection index, -	0.5	-

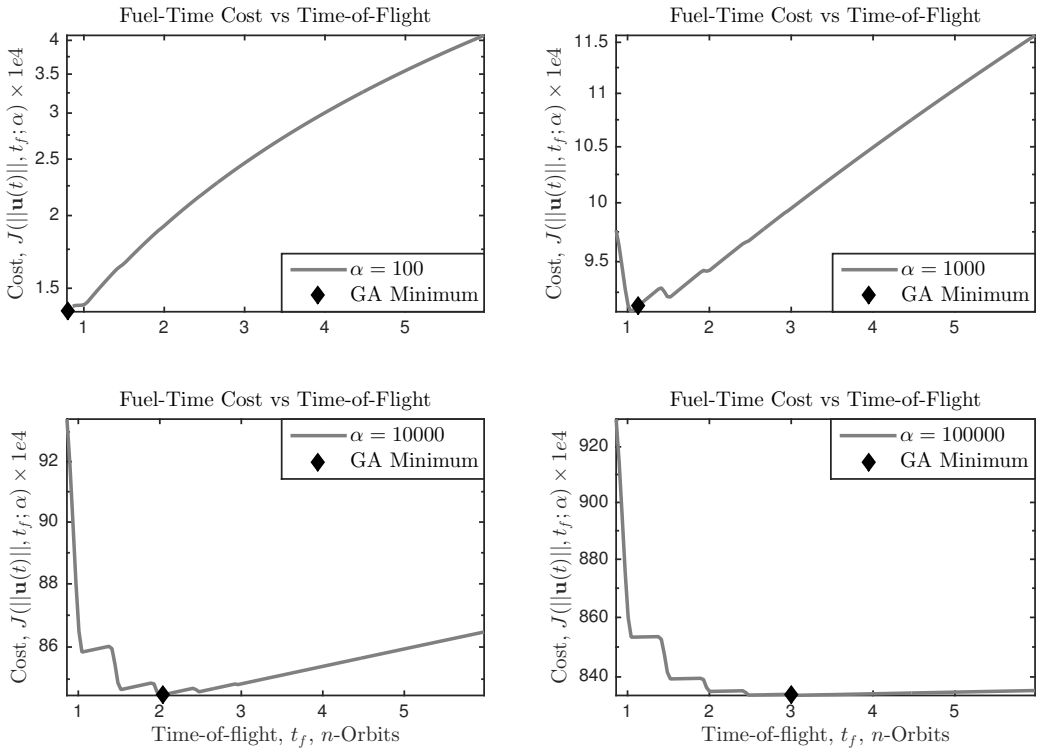

Figure 5.9: Minimum cost for different values of α

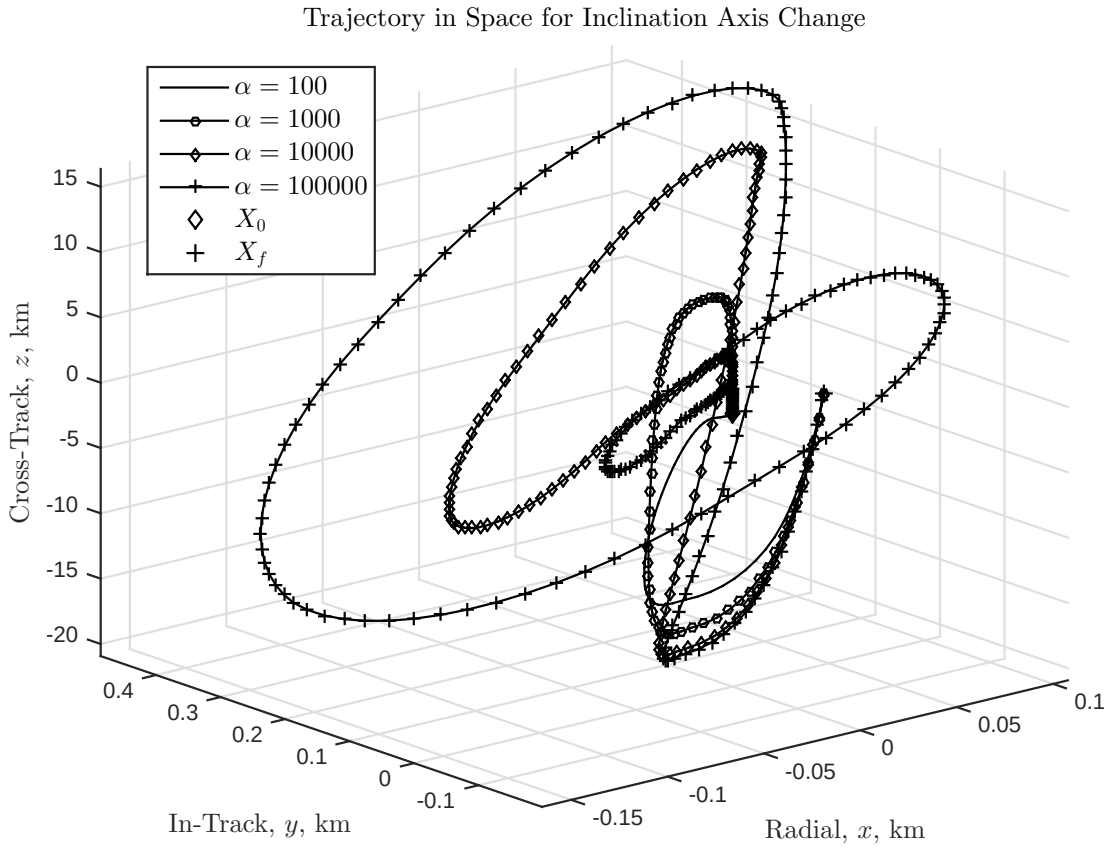

Figure 5.10: Different relative trajectories for different values of α

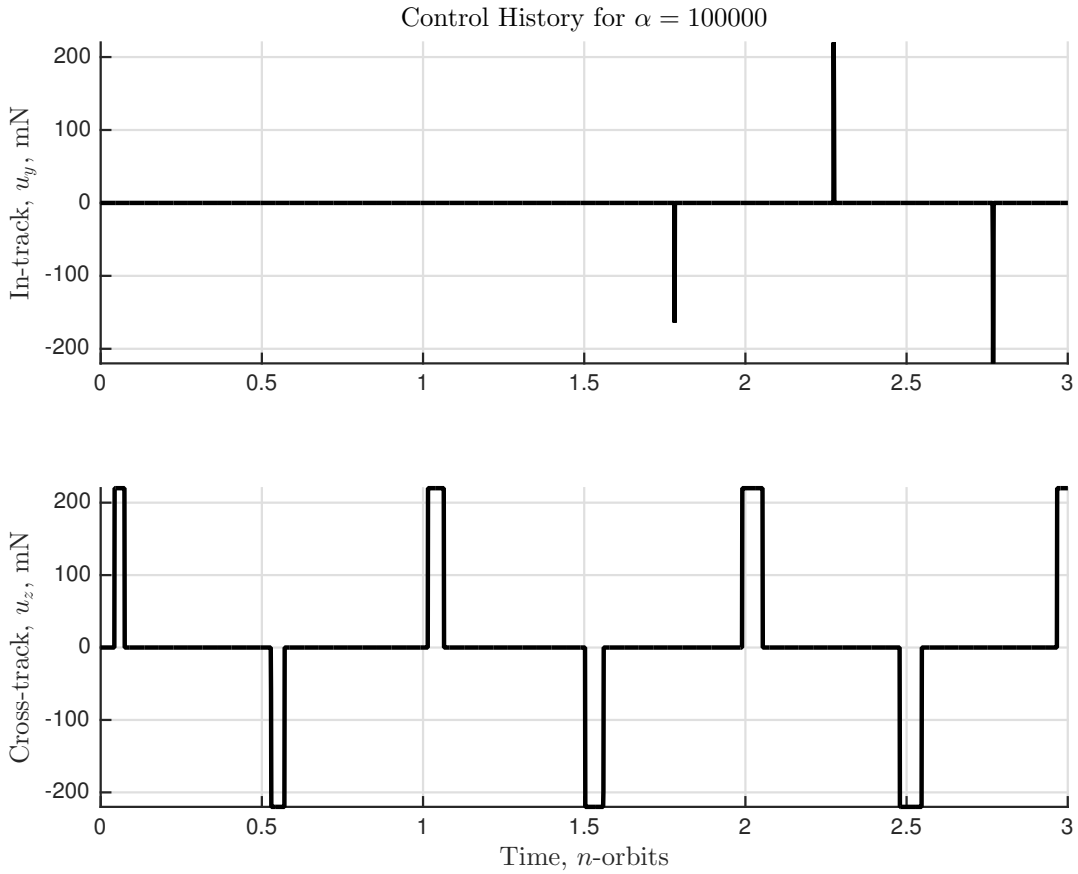

Figure 5.11: Control history for $\alpha = 100000$

tion. An interesting feature appears in this optimization however; the fuel use levels out at $\Delta v = 5.949$ m/s, which is actually lower than the solution for the circular, unperturbed validation result. The minimum fuel/time solution for both $\alpha = 10000$ and $\alpha = 100000$ is very similar, as seen in Figure 5.13.

This result is actually expected. This particular orbit has $e = 0.01$, and the lower fuel use required for this transfer highlights an important feature concerning elliptic orbits. The most effective point in an elliptic orbit to perform an altitude adjustment is at apoapsis; the satellite's velocity is lowest at this point so a given change in velocity has a larger effect. While the theoretical lower bound on the Δv required to perform altitude adjustments is very similar between the circular and slightly elliptical orbits, we find that the LP method proposed here exploits the eccentricity of the reference orbit and performs a burn at apoapsis which reduces the Δv required to accomplish the maneuver. This can be seen in Figure 5.15; the second burn in the in-track direction occurs at apoapsis. For shorter maneuver horizons, the thrust still occurs at periapsis and apoapsis, but the efficiency is reduced since the thruster is active for longer periods of time on either side of periapsis or apoapsis.

In the circular, unperturbed case, the semi-major axis change is a pure planar maneuver but eccentricity and J_2 change this. The cross-track motion created by eccentricity and J_2 are corrected in each of our simulations by a single cross-track maneuver to counteract the out-of-plane motion.

5.4.4 On Real-Time Implementation

The hybrid method of linear programming with a genetic algorithm can be used for the trajectory planning *a priori*. If a maneuver is selected beforehand, however, the LP method with the GA-STM could be implemented to compute optimal controllers in a receding horizon fashion.

The most computationally intensive parts of this method are 1) the root finding operations used when solving Kepler's equation and 2) building the equality constraint matrices for the linear program. Beyond that, since there are no integer decision variables or combinatorial constraints, the optimal control problem is a standard linear program, and highly efficient, custom-generated LP solvers can be designed to compute solutions in significantly less time than the sampling time.

5.5 Conclusions

This chapter has presented a novel method for computing fuel/time optimal maneuvers in an elliptic, J_2-perturbed relative orbit. The Gim-Alfriend relative motion model was used in conjunction with a linear program to compute a minimum-fuel transfer between two points

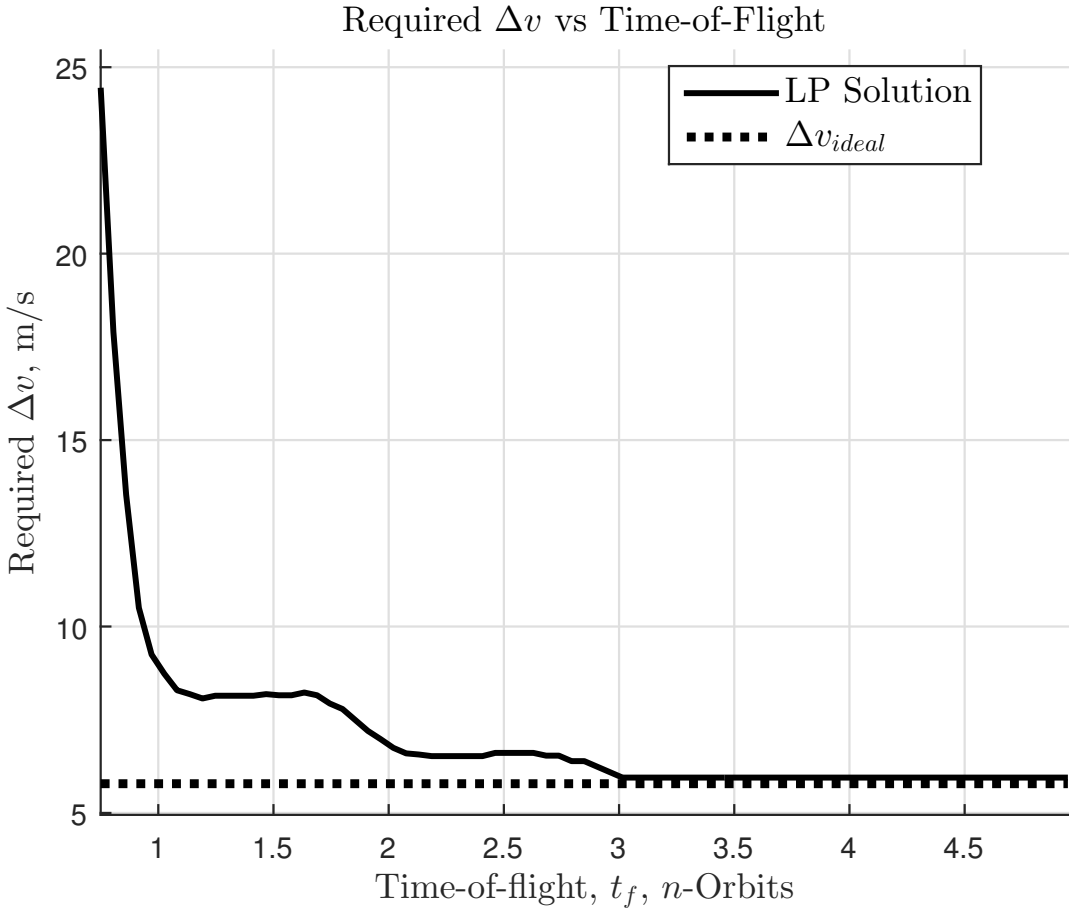

Figure 5.12: Δv vs time-of-flight

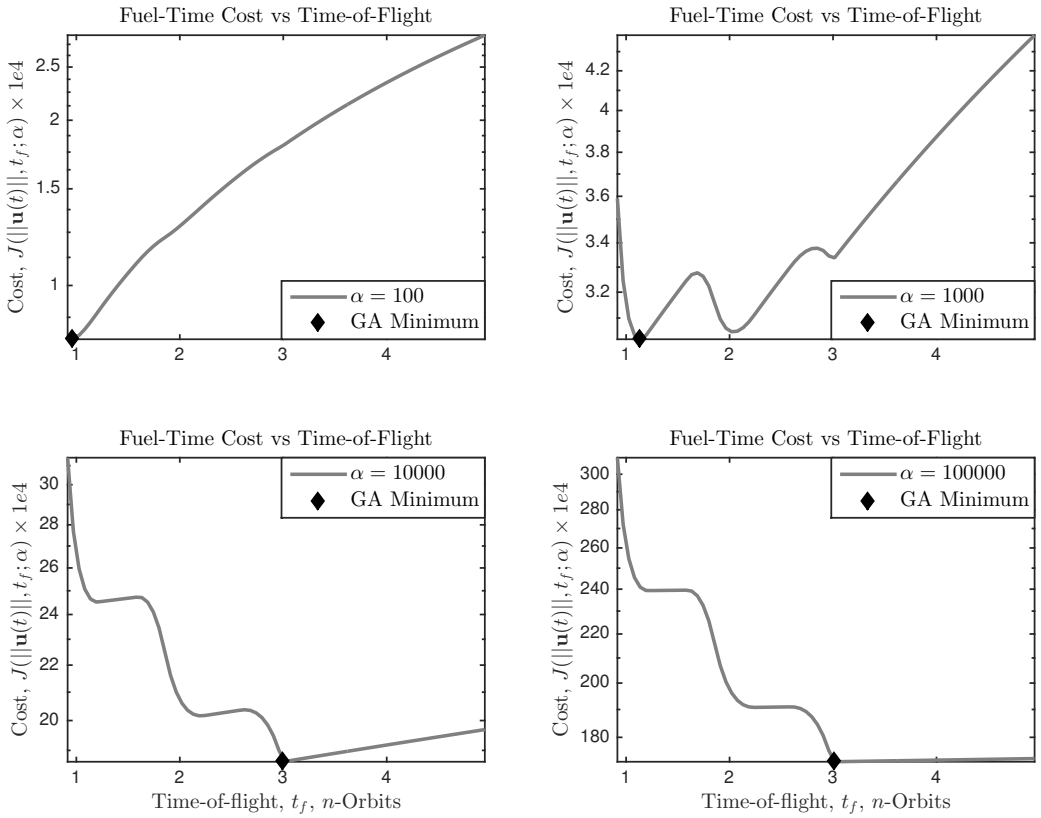

Figure 5.13: Fuel/time costs for different α

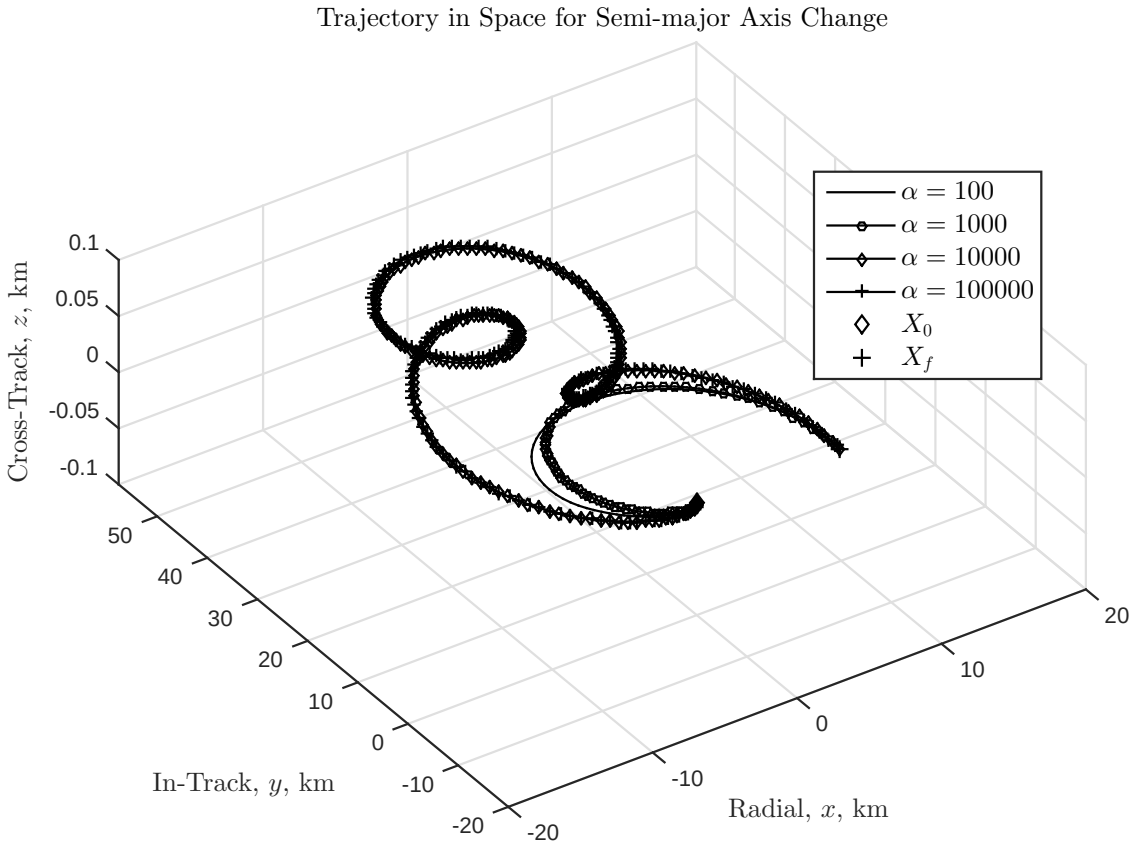

Figure 5.14: Trajectories for different α

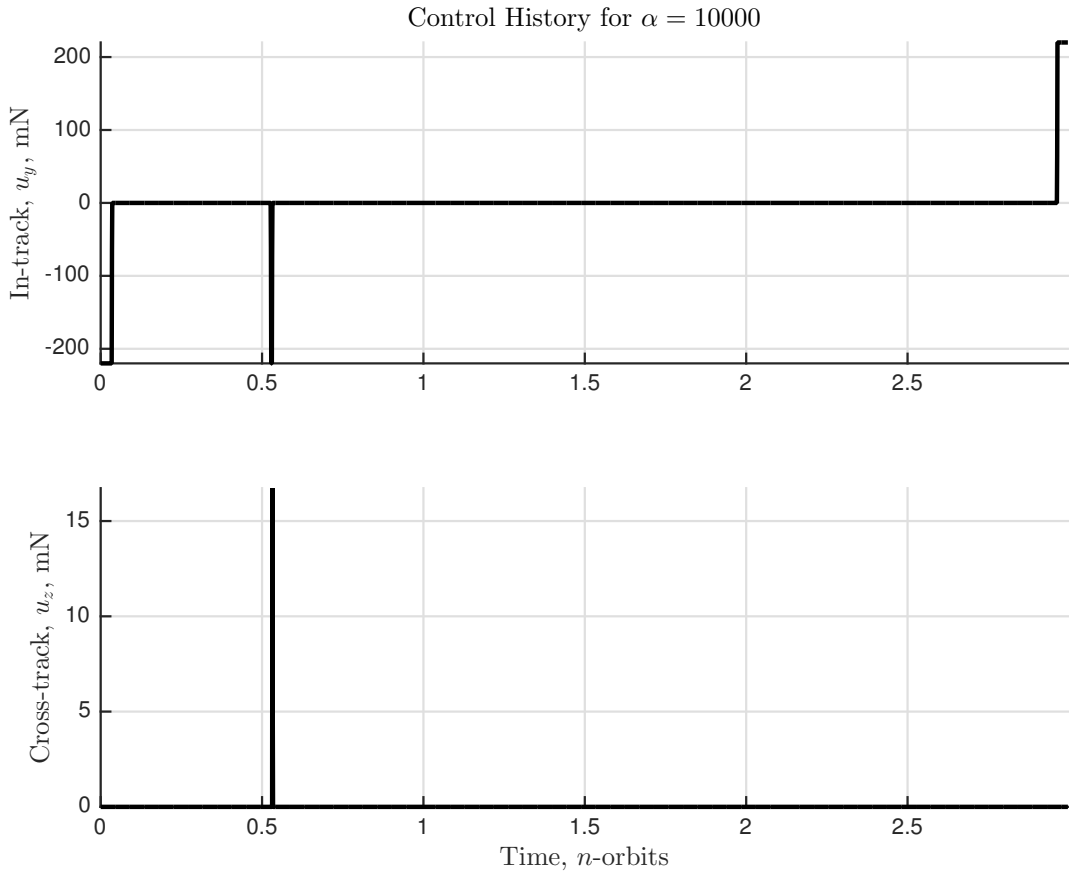

Figure 5.15: Control history for $\alpha = 10000$

in a relative orbit. In addition, a genetic algorithm was used to find the minimizing time-of-flight. Using a realistic hardware limit based on a commercially available mono-propellant rocket, we used this method to compute several fuel/time optimal transfers which are parameterized by the fuel penalty parameter α. Two well-known solutions to fundamental, impulsive orbit transfers were used to validate the results of the optimization, and it was found that the results agree with the idealized model. We conclude from this study that the proposed method can be used by trajectory planners to easily analyze the balance of time-of-flight and fuel budget for deployment of large formations. Furthermore, the results obtained here could potentially be used to generate an initial guess for a higher-fidelity optimization routine.

Chapter 6

Constrained Control of a Small Satellite for Robotic Inspection

6.1 Introduction

This paper investigates a new formulation of model predictive control (MPC) applied to spacecraft proximity operations, particularly the coupled orbit and attitude control of a "small," resource-constrained, inspector satellite.

The space-based, autonomous, inspector problem has gained considerable attention in recent years both as a control theoretic problem and as a practical engineering solution for future manned or high-value space missions. The concept of autonomous inspection is rather simple: a small, free-flying satellite is deployed from a main satellite equipped with thrusters/ attitude control system (ACS) and some type of imaging equipment and performs inspection on a region of interest on the host body. The inspector could be deployed on a routine basis for periodic inspection of elements like solar panels etc. or deployed in the event of a damage event of similar emergency [66]. The benefits of this concept of operations are three-fold:

1. Free-flying agents can reduce or eliminate blind spots on the larger system
2. They can provide near-real-time information to the main vehicle or ground control to improve response time in the event of emergency
3. For manned systems, an astronaut would not need to venture into a possibly hazardous environment

Autonomous inspection presents a number of technological challenges which must be overcome such as relative navigation, miniaturization of imaging equipment and control design, which is the focus of this paper. The small size and limited resources of the inspector satellite

present a unique challenge for control design. Possibly the most well-known system which has actually flown is the Orbital Express [88] which focused on relative navigation and the demonstration of on-orbit transfer of fuel and a spare computer.

The Naval Research Lab's **L**ow-design **I**mpact **I**nspection **Ve**hicle (LIIVe) is a program to develop techniques and algorithms for autonomous inspection at very close range (on the order of meters) of legacy systems and its concept of operations serves as a basis for our analysis. LIIVe is a 5-15 kg inspection vehicle which, when commanded, would detach from the host vehicle, and use a series of open-loop thrusts to circumnavigate the host. After the circumnavigation has been completed, the ground controllers can analyze the collected imagery and decide whether to 1) perform the circumnavigation again, 2) re-dock the inspector, or 3) command the inspector to dispose of itself (use the remaining propellant to push itself into a de-orbit phase) [66]. The control design in this paper is based on a system such as LIIVe.

This chapter includes two contributions. First, we present a coupled, nonlinear orbit/ attitude model which assumes that the thrusters are rigidly attached to the body and cannot vector their thrust. This means that any attitude error will affect the tracking ability of the trajectory controller. The model also accounts for the potential misalignment of the thrusters with the satellite's center of mass and with other thrusters which will induce a torque on the satellite each time the thruster turns on, thus causing more attitude error. The system is specialized to a 6U CubeSat in LEO, but can be applied to any spacecraft geometry in any elliptical orbit. Under the LEO assumption, the system can be linearized to yield a linear, time-invariant model which is ideal for linear control design. The second contribution is a formulation of trajectory tracking model predictive control which encodes the minimum impulse bit of a thruster as a semi-continuous variable and also includes collision constraints. This is a flexible model which results in a mixed-integer linear or quadratic program. The model allows the thruster to either take values in $[u_{\min}, u_{\max}]$ where $u_{\min} > 0$ or be turned off altogether.

The remainder of the chapter is structured as follows. First, the nonlinear orbit and attitude model is developed from first principles, and then we show how the two subsystems couple together through the thruster inputs. Then this model is linearized and specialized to a 6U CubeSat platform. Next the fuel-optimal and fuel/time optimal control solutions are presented using a mixed-integer linear program and golden section search, which are developed to serve as a baseline for the trajectory tracking maneuver. Additionally we discuss the construction of a constrained linear-quadratic attitude regulator to help the satellite recover from the thruster disturbances. Throughout our study, commercially available, flight proven hardware has been incorporated into our models to reflect realistic flight conditions. We find that the controllers proposed in this paper are feasible for currently available thruster and ACS systems. Finally, we present numerical results for both nominal and perturbed initial conditions. We show that the controllers developed in this study are able to stabilize the attitude and track the trajectory, and we find that using the mixed-integer approach to modeling the MIB yields favorable results compared to rounding down small signals to zero.

6.2 System Model

In this section, the general coupled orbit/attitude model is derived and then specialized to a 6U CubeSat. The result is a linear, time-invariant model that is ideally suited to linear control design.

6.2.1 Trajectory Model

For two satellites in close relative orbits, denote the chief as the satellite about which the deputy will maneuver, seen in Figure 6.1. We make the assumption that the relative separation of the chief and deputy is several orders of magnitude smaller than the radius of the chief. Let $\boldsymbol{r}_{\mathrm{c}} = \begin{bmatrix} X & Y & Z \end{bmatrix}^T$ be the position vector of the chief in the Earth-centered-inertial (ECI) frame, which will be referred to as $\{\hat{\boldsymbol{n}}\}$. Similarly, we let $\boldsymbol{r}_{\mathrm{d}}$ be the inertial position of the deputy. In the inertial frame, the equation of motion that describes the chief's trajectory is

$$\ddot{\boldsymbol{r}}_i = -\frac{\mu}{||\boldsymbol{r}_i||^3}\boldsymbol{r}_i, \quad i = \mathrm{c}, \mathrm{d} \tag{6.1}$$

where μ is the gravitational parameter. It is convenient to describe the relative dynamics of

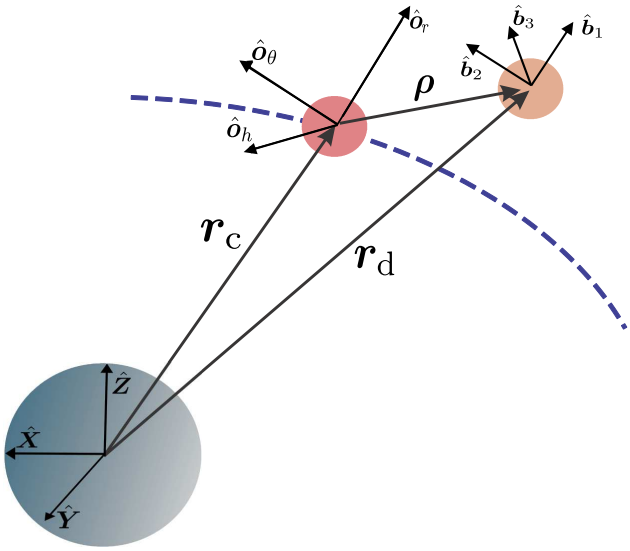

Figure 6.1: Relative trajectory geometry

the chief and deputy in a reference frame that is attached to the orbit of the chief, the orbiting or Local-Vertical, Local-Horizontal (LVLH) frame. In the LVLH frame, the separation is given by $\boldsymbol{\rho} = \begin{bmatrix} x & y & z \end{bmatrix}^T$. The orbital angular momentum of the chief is $\boldsymbol{h}_{\mathrm{c}} = \boldsymbol{r}_{\mathrm{c}} \times \dot{\boldsymbol{r}}_{\mathrm{c}}$. The

transformation from the inertial frame to the orbiting frame, $\{\hat{\boldsymbol{o}}\}$ is

$$\boldsymbol{R}_n^o = \begin{bmatrix} \dfrac{\boldsymbol{r}_\mathrm{c}}{||\boldsymbol{r}_\mathrm{c}||} & \dfrac{\boldsymbol{h}_\mathrm{c} \times \boldsymbol{r}_\mathrm{c}}{||\boldsymbol{h}_\mathrm{c} \times \boldsymbol{r}_\mathrm{c}||} & \dfrac{\boldsymbol{h}_\mathrm{c}}{||\boldsymbol{h}_\mathrm{c}||} \end{bmatrix} \tag{6.2}$$

The basis vectors for $\{o\}$ are $\hat{\boldsymbol{o}}_r$ in the radial direction, $\hat{\boldsymbol{o}}_h$ in the cross-track direction and $\hat{\boldsymbol{o}}_\theta$ in the in-track direction. The position vector for the deputy in the orbiting frame is

$$\boldsymbol{r}_\mathrm{d} = \boldsymbol{r}_\mathrm{c} + \boldsymbol{\rho} = \begin{bmatrix} r_\mathrm{c} + x & y & z \end{bmatrix}^T \tag{6.3}$$

The angular velocity of the LVLH frame with respect to the inertial frame is $\boldsymbol{\omega}_n^o = \begin{bmatrix} 0 & 0 & \dot{\theta} \end{bmatrix}^T$. The deputy's velocity with respect to the inertial frame is

$$(\dot{\boldsymbol{r}}_\mathrm{d})_n = (\dot{\boldsymbol{r}}_\mathrm{c} + \dot{\boldsymbol{\rho}})_o + S(\boldsymbol{\omega}_n^o)(\boldsymbol{r}_\mathrm{c} + \boldsymbol{\rho})_o \tag{6.4}$$

where $S(\cdot)$ is the skew-symmetric cross product operator satisfying $S(\boldsymbol{a})\boldsymbol{b} = \boldsymbol{a} \times \boldsymbol{b}$ for $\boldsymbol{a}, \boldsymbol{b} \in \mathbb{R}^3$. The deputy's acceleration is

$$(\ddot{\boldsymbol{r}}_\mathrm{d})_n = (\ddot{\boldsymbol{r}}_\mathrm{c} + \ddot{\boldsymbol{\rho}})_o + 2S(\boldsymbol{\omega}_n^o)(\dot{\boldsymbol{r}}_\mathrm{c} + \dot{\boldsymbol{\rho}})_o + S(\dot{\boldsymbol{\omega}}_n^o)(\boldsymbol{r}_\mathrm{c} + \boldsymbol{\rho})_o + S(\boldsymbol{\omega}_n^o)\left[S(\boldsymbol{\omega}_n^o)(\boldsymbol{r}_\mathrm{c} + \boldsymbol{\rho})_o\right] \tag{6.5}$$

Using Eq. (6.5) with Eq. (6.1) for $i = \mathrm{d}$, the equations of motion are

$$(\ddot{\boldsymbol{r}}_\mathrm{c} + \ddot{\boldsymbol{\rho}})_o + 2S(\boldsymbol{\omega}_n^o)(\dot{\boldsymbol{r}}_\mathrm{c} + \dot{\boldsymbol{\rho}})_o + S(\dot{\boldsymbol{\omega}}_n^o)(\boldsymbol{r}_\mathrm{c} + \boldsymbol{\rho})_o + S(\boldsymbol{\omega}_n^o)\left[S(\boldsymbol{\omega}_n^o)(\boldsymbol{r}_\mathrm{c} + \boldsymbol{\rho})_o\right] = -\frac{\mu(\boldsymbol{r}_\mathrm{c} + \boldsymbol{\rho})}{||\boldsymbol{r}_\mathrm{c} + \boldsymbol{\rho}||^3} \tag{6.6}$$

Recalling Section 2.1.2, the nonlinear equations of the relative motion (NERM) in terms of the relative separation are

$$\begin{aligned} \ddot{x} =& 2\dot{\theta}\dot{y} + \ddot{\theta}y + \dot{\theta}^2 x + \frac{\mu}{r_\mathrm{c}^2} - \frac{\mu(x + r_\mathrm{c})}{\left[(r_\mathrm{c} + x)^2 + y^2 + z^2\right]^{3/2}} \\ \ddot{y} =& -2\dot{\theta}\dot{x} - \ddot{\theta}x + \dot{\theta}^2 y - \frac{\mu y}{\left[(r_\mathrm{c} + x)^2 + y^2 + z^2\right]^{3/2}} \\ \ddot{z} =& -\frac{\mu z}{\left[(r_\mathrm{c} + x)^2 + y^2 + z^2\right]^{3/2}} \end{aligned} \tag{6.7}$$

that define a nonlinear, time-varying system. The time-varying coefficients r_c, $\dot{r}_\mathrm{c}$, $\dot{\theta}$ and $\ddot{\theta}$ satisfy the differential equations [13]

$$\ddot{r}_\mathrm{c} = r_\mathrm{c}\dot{\theta}^2 - \frac{\mu}{r_\mathrm{c}^2}, \quad \ddot{\theta} = -\frac{2\dot{r}_\mathrm{c}\dot{\theta}}{r_\mathrm{c}} \tag{6.8}$$

and $\theta = \omega + f$, where ω is the argument of periapsis and f is the true anomaly. Assuming that the orbit is approximately circular (so that $\dot{\boldsymbol{\omega}}_n^o = \boldsymbol{0}$ and the angular rate $\dot{\theta} = n$ is the

mean motion), the NERM become

$$\begin{aligned}\ddot{x} =& 2n\dot{y} + n^2 x + \frac{\mu}{a^2} - \frac{\mu(x+a)}{\left[(r_c + x)^2 + y^2 + z^2\right]^{3/2}} \\ \ddot{y} =& -2n\dot{x} + n^2 y - \frac{\mu y}{\left[a + x)^2 + y^2 + z^2\right]^{3/2}} \\ \ddot{z} =& -\frac{\mu z}{\left[(a+x)^2 + y^2 + z^2\right]^{3/2}}\end{aligned} \tag{6.9}$$

that define a nonlinear, time-invariant system. For proximity operations, it is reasonable to assume that the motion takes place in the approximately linear subspace about the chief. Linearizing about the origin and adding control forces in each direction, the well-known Hill-Clohessy-Wiltshire equations are obtained:

$$\begin{aligned}\ddot{x} &= 3n^2 x + 2n\dot{y} + \frac{u_x}{m_d} \\ \ddot{y} &= -2n\dot{x} + \frac{u_y}{m_d} \\ \ddot{z} &= -n^2 z + \frac{u_z}{m_d}\end{aligned} \tag{6.10}$$

where u_i are the control forces in the radial, in-track and cross-track directions, $\hat{\boldsymbol{o}}_i$. It can be shown that bounded, closed, relative orbits exist for initial conditions satisfying the constraint

$$\dot{y}_0 = -2nx_0 \tag{6.11}$$

The state matrix is

$$\boldsymbol{A}^t = \begin{bmatrix} 0 & 0 & 0 & 1 & 0 & 0 \\ 0 & 0 & 0 & 0 & 1 & 0 \\ 0 & 0 & 0 & 0 & 0 & 1 \\ 3n^2 & 0 & 0 & 0 & 2n & 0 \\ 0 & 0 & 0 & -2n & 0 & 0 \\ 0 & 0 & -n^2 & 0 & 0 & 0 \end{bmatrix} \tag{6.12}$$

and the linearized input matrix is

$$\boldsymbol{B}^t = \frac{1}{m_d} \begin{bmatrix} \boldsymbol{0}_{3\times 3} \\ \mathbb{I}_{3\times 3} \end{bmatrix}^T \tag{6.13}$$

where the superscript t indicates that the system describes the translational dynamics.

6.2.2 Attitude Model

Now, consider the motion of a rigid spacecraft in a circular orbit near the orbiting reference frame. The linear transformation between the principal axes of the spacecraft and the

orbiting reference frame for some arbitrary orientation can be parameterized by the 3-2-1 Euler angle sequence, where ψ is the yaw angle around the radial unit vector, θ is the pitch angle around the cross-track unit vector, and ϕ is the roll angle about the in-track unit vector, seen in Figure 6.2. The angular velocity of the body with respect to the inertial frame is

$$\boldsymbol{\omega}_n^b = \boldsymbol{\omega}_o^b + \boldsymbol{R}_o^b \boldsymbol{\omega}_n^o \implies \dot{\boldsymbol{\omega}}_n^b = \dot{\boldsymbol{\omega}}_o^b + \dot{\boldsymbol{R}}_o^b \boldsymbol{\omega}_n^o \tag{6.14}$$

where $\boldsymbol{\omega}_n^o = \begin{bmatrix} 0 & 0 & -n \end{bmatrix}^T$ is the constant angular velocity of the orbiting frame with respect to the inertial frame (because we assume the motion is in a circular orbit), and $\boldsymbol{\omega}_n^b$ is the body angular velocity with respect to the orbiting frame. The time-derivative of $\boldsymbol{R}_o^b$ is

$$\dot{\boldsymbol{R}}_o^b = -S(\boldsymbol{\omega}_o^b)\boldsymbol{R}_o^b \tag{6.15}$$

The angular displacement of the body axes with respect to the orbiting frame can be parameterized by the quaternions $\bar{\boldsymbol{q}} = \begin{bmatrix} q_0 & \boldsymbol{q}^T \end{bmatrix}^T$, and the rotation matrix of the body axes with respect to orbiting axes is

$$\boldsymbol{R}_o^b(\bar{\boldsymbol{q}}) = \mathbb{I}_{3\times 3} + 2q_0 S(\boldsymbol{q}) + 2S^2(\boldsymbol{q}) \tag{6.16}$$

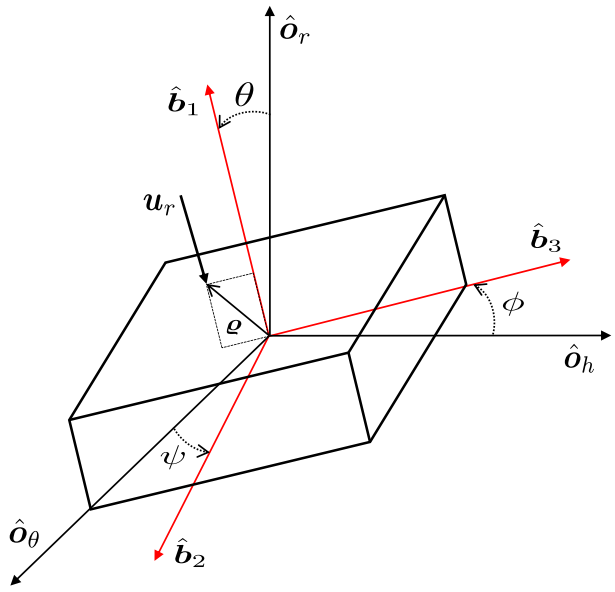

Figure 6.2: Spacecraft body axes relative to orbiting axes

The kinematic equations in terms of quaternions are

$$\begin{bmatrix} \dot{q}_0 \\ \dot{\boldsymbol{q}} \end{bmatrix} = \frac{1}{2} \begin{bmatrix} -\boldsymbol{q}^T \\ [q_0 \mathbb{I}_{3\times 3} + S(\boldsymbol{q})] \end{bmatrix} \boldsymbol{\omega}_o^b \tag{6.17}$$

and the kinematic relationships between the 3-2-1 Euler sequence and kinematics, the mapping between the angular velocities, and associated Euler angle rates are provided in [119, 70, 133]. The dynamic equations including the gravity gradient torque are

$$\dot{\boldsymbol{\omega}}_o^b = \boldsymbol{I}^{-1}\left(-S(\boldsymbol{\omega}_n^b)\boldsymbol{I}\boldsymbol{\omega}_n^b + 3n^2 S(\boldsymbol{r}_1(\bar{\boldsymbol{q}}))\boldsymbol{I}\boldsymbol{r}_1(\bar{\boldsymbol{q}}) + \boldsymbol{\tau}\right) + S(\boldsymbol{\omega}_o^b)\boldsymbol{R}_o^b(\bar{\boldsymbol{q}})\boldsymbol{\omega}_n^o \tag{6.18}$$

where $\boldsymbol{I}$ is the inertia matrix of the satellite, $\boldsymbol{\tau}$ is the control torque and $\boldsymbol{r}_1(\bar{\boldsymbol{q}})$ is the first column of the matrix $\boldsymbol{R}_o^b(\bar{\boldsymbol{q}})$ [133]. Eq (6.18) can be linearized around the equilibrium $\begin{bmatrix}\bar{\boldsymbol{q}}^T & (\boldsymbol{\omega}_o^b)^T\end{bmatrix}^T = \begin{bmatrix}1 & \boldsymbol{0}_{1\times 6}\end{bmatrix}^T$ to yield the state matrix

$$\boldsymbol{A}^r = \begin{bmatrix} 0 & 0 & 0 & 0 & 0 & 0 & 0 \\ 0 & 0 & 0 & 0 & 1/2 & 0 & 0 \\ 0 & 0 & 0 & 0 & 0 & 1/2 & 0 \\ 0 & 0 & 0 & 0 & 0 & 0 & 1/2 \\ 0 & 2n^2\frac{(I_2-I_3)}{I_1} & 0 & 0 & 0 & n\frac{(I_1-I_2+I_3)}{I_1} & 0 \\ 0 & 0 & 8n^2\frac{(I_1-I_3)}{I_2} & 0 & -n\frac{(I_2-I_1+I_3)}{I_2} & 0 & 0 \\ 0 & 0 & 0 & 6n^2\frac{(I_1-I_2)}{I_3} & 0 & 0 & 0 \end{bmatrix} \tag{6.19}$$

and the input matrix

$$\boldsymbol{B}^r = \begin{bmatrix}\boldsymbol{0}_{3\times 4} & \boldsymbol{I}^{-1}\end{bmatrix}^T \tag{6.20}$$

and I_i are the principal moments of inertia. The superscript r indicates the the systems describes the rotational dynamics.

6.2.3 Coupled Motion

As they stand, Eq (6.10), (6.17), and (6.18) have no natural coupling; in the absence of disturbances such as atmospheric drag the satellite *translational* motion and the rotational motion have no effect on each other. The gravity gradient torque couples the orbit and attitude motion together, but this is independent of the relative motion. For a small, rigid satellite in close proximity (on the order of meters) to another body, neglecting the effect of attitude error on thrust alignment can be an oversimplification of the problem. Even small alignment errors for the thrust vector can cause significant changes to the effect the thrusters have on the motion.

In reality, rotation and translation are coupled through the translational control inputs. The propulsion force applied by the thrusters depends on the spacecraft attitude:

$$\boldsymbol{u}_r = \boldsymbol{R}_o^b(\bar{\boldsymbol{q}})\boldsymbol{u}_t \tag{6.21}$$

The result is that any attitude error will cause the thrusters to be misaligned with the LVLH axes as defined in the previous sections, and the satellite would conceivably move in the wrong direction. Note that when the coupled system is linearized around the equilibrium, the rotation matrix is $\boldsymbol{R}_o^b(\bar{\boldsymbol{q}}) = \mathbb{I}_{3\times 3}$ and this coupling vanishes in the linear model.

Another source of orbit/attitude coupling comes from non-collinearity of the thrusters with a) each other and b) the center of mass. The design constraints on small satellites are such that it might not be possible to mount a thruster to be perfectly aligned with the center of mass. Each time a thruster fires, this will induce a torque on the body of the spacecraft. This will, in turn, create more attitude error by Eq. (6.21). The torque induced by a thruster in the body frame around the center of mass is

$$\boldsymbol{N} = S(\boldsymbol{\varrho})\boldsymbol{u}_r \tag{6.22}$$

where $\boldsymbol{\varrho}$ is the moment arm. The complete, nonlinear, coupled dynamic model near circular orbit with k thrusters is

$$\begin{aligned}
\begin{bmatrix}\dot{q}_0 \\ \dot{\boldsymbol{q}}\end{bmatrix} &= \frac{1}{2}\begin{bmatrix}-\boldsymbol{q}^T \\ [q_0\mathbb{I}_{3\times 3} + S(\boldsymbol{q})]\end{bmatrix}\boldsymbol{\omega}_o^b \\
\dot{\boldsymbol{\omega}}_o^b &= \boldsymbol{I}^{-1}\left(-S(\boldsymbol{\omega}_n^b)\boldsymbol{I}\boldsymbol{\omega}_n^b + 3n^2 S(\boldsymbol{r}_1(\bar{\boldsymbol{q}}))\boldsymbol{I}\boldsymbol{r}_1(\bar{\boldsymbol{q}}) + \sum_{i=1}^{k} S(\boldsymbol{\varrho}_i)\boldsymbol{u}_{r,i} + \boldsymbol{\tau}\right) + S(\boldsymbol{\omega}_o^b)\boldsymbol{R}_o^b(\bar{\boldsymbol{q}})\boldsymbol{\omega}_n^o \\
\ddot{\boldsymbol{\rho}} &= -2S(\boldsymbol{\omega}_n^o)(\dot{\boldsymbol{r}}_{\mathrm{c}} + \dot{\boldsymbol{\rho}})_o - S(\boldsymbol{\omega}_n^o)\left[S(\boldsymbol{\omega}_n^o)(\boldsymbol{r}_{\mathrm{c}} + \boldsymbol{\rho})_o\right] - \frac{\mu(\boldsymbol{r}_{\mathrm{c}} + \boldsymbol{\rho})_o}{||(\boldsymbol{r}_{\mathrm{c}} + \boldsymbol{\rho})_o||^3} - \ddot{\boldsymbol{r}}_{\mathrm{c}} + \frac{\boldsymbol{u}_r}{m_{\mathrm{d}}}
\end{aligned} \tag{6.23}$$

This model contains thirteen states and completely describes the coupled motion of a rigid body flying in close proximity to a nearly circular orbit. In theory, the model could be used on any spacecraft shape, however in this paper, the focus is on CubeSat-class spacecraft. In particular, a 6U CubeSat is used; each face of the satellite has a thruster mounted on it, and all six of the thrusters are assumed to have equal thrust capability. This doubles the dimension of the thrust input vector

$$\boldsymbol{u}_r \;=\; \boldsymbol{R}_o^b(\bar{\boldsymbol{q}})\left(\boldsymbol{u}_t^+ - \boldsymbol{u}_t^-\right) \tag{6.24}$$

where the positive and negative quantities refer to the thruster pointed in the positive or negative LVLH directions. The 6U satellite can be seen in Fig. 6.3 and we adopt the following convention for the thruster misalignment torques. Side 1 is in the ram direction, and side 6 opposes side 1 in the anti-ram direction. Side 3 is the zenith-facing direction and is opposed by side 4 in the nadir-facing direction. Finally, side 5 faces the angular momentum vector and is opposed by side 2. This convention is arbitrary, it is only required to describe the moment arm vectors for the thruster misalignment. The thruster misalignment moment arms are given in the body axes by (units in cm):

$$\begin{aligned}
\boldsymbol{\varrho}_1 &= \begin{bmatrix}1 & 0 & 1\end{bmatrix}^T & \boldsymbol{\varrho}_6 &= \begin{bmatrix}0.9 & 0 & 0.2\end{bmatrix}^T \\
\boldsymbol{\varrho}_2 &= \begin{bmatrix}-1 & 2 & 0\end{bmatrix}^T & \boldsymbol{\varrho}_5 &= \begin{bmatrix}1 & -0.2 & 0\end{bmatrix}^T \\
\boldsymbol{\varrho}_3 &= \begin{bmatrix}0 & -1 & -1\end{bmatrix}^T & \boldsymbol{\varrho}_4 &= \begin{bmatrix}0 & 2 & 2\end{bmatrix}^T
\end{aligned} \tag{6.25}$$

In practice, any spacecraft geometry could be used the orbit and attitude model used in this paper. The thruster misalignment would primarily be caused by the design constraints on the satellite body.

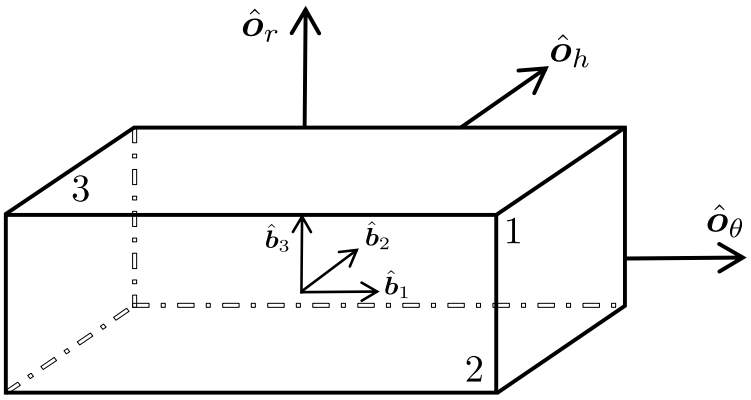

Figure 6.3: Side numbering convention for the thruster misalignment torques

6.3 Control Design

This section details the planning of a fuel optimal trajectory, followed by a novel formulation of mixed-integer model predictive control for trajectory tracking and a constrained linear-quadratic attitude regulator.

6.3.1 Minimum Fuel Trajectory Planning

Consider the continuous-time optimal control problem

$$\begin{aligned} \min_{\boldsymbol{u}} J(\boldsymbol{u}(t), t) &= \int_{t_0}^{t_f} \sum_{i=1}^{m} c_i |u_i(\tau)| \, \mathrm{d}\, \tau \\ &\text{subject to:} \\ \dot{\boldsymbol{x}}(t) &= \boldsymbol{A}(t)\boldsymbol{x}(t) + \boldsymbol{B}(t)\boldsymbol{u}(t) \\ \boldsymbol{x}(t_0), \boldsymbol{x}(t_f) &\text{ specified} \\ &\text{Collision avoidance constraints} \\ u_i &\in [-u_{\max}, u_{\max}] \subseteq \mathbb{R}^m \end{aligned} \tag{6.26}$$

where c_i are real coefficients, u_i are the control signals and the closed interval $[-u_{max}, u_{max}]$ contains all feasible control signals. The solution to this problem results in a minimum fuel transfer [78]. The optimal control sequence results in a bang-off-bang signal as seen in Figure 6.4. The discrete-time formulation of this problem was addressed in [109] where the minimum-fuel problem with collision avoidance constraints was constructed as a mixed-integer linear program (MILP). Suppose that an inspector vehicle is deployed from a chief satellite, and that the shape of the chief can be approximated to lie strictly within the

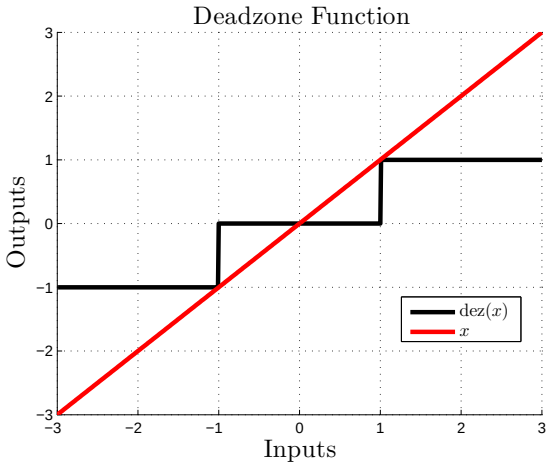

Figure 6.4: Bang-off-bang control profile

intersection of i polytopes $\mathbb{P}_i$. Each polytope is defined by the points

$$\boldsymbol{\rho}_{\min} = \begin{bmatrix} x_{\min} & y_{\min} & z_{\min} \end{bmatrix}^T_{\mathbb{P}_i} \qquad \boldsymbol{\rho}_{\max} = \begin{bmatrix} x_{\max} & y_{\max} & z_{\max} \end{bmatrix}^T_{\mathbb{P}_i} \tag{6.27}$$

The minimum-fuel optimal control problem in discrete time is

$$\begin{aligned} \min_{\{\boldsymbol{u}(k)\}_{k=0}^{N-1}} J(\boldsymbol{u}(k),k) &= \sum_{k=0}^{N-1} \boldsymbol{c}^T\boldsymbol{\theta}(k) \\ \text{subject to:} \\ \boldsymbol{x}(k+1) &= \boldsymbol{A}_k^t\boldsymbol{x}(k) + \boldsymbol{B}_k^t\boldsymbol{u}(k) \\ \boldsymbol{x}(0) &= \boldsymbol{x}_0 \;\text{ and }\; \boldsymbol{x}(N) = \boldsymbol{x}_f \\ \begin{bmatrix} \boldsymbol{u}(k) \\ -\boldsymbol{u}(k) \end{bmatrix} &\leq \begin{bmatrix} \boldsymbol{\theta}(k) \\ \boldsymbol{\theta}(k) \end{bmatrix}, \; \mathbf{0} \leq \boldsymbol{\theta}(k) \leq u_{\max}\mathbf{1} \\ \begin{bmatrix} \boldsymbol{\rho}_o(k) \\ -\boldsymbol{\rho}_o(k) \end{bmatrix} &\leq \begin{bmatrix} \boldsymbol{\rho}_{\min} \\ -\boldsymbol{\rho}_{\max} \end{bmatrix}_{\mathbb{P}_i} + \mathbf{M}\boldsymbol{o}(k) \\ \boldsymbol{o}(k) &\in \left\{ \mathbb{R}^{6\times 1} | \; o_i(k) \in \{0,1\}, \forall \, i = 1,\ldots,6 \right\} \\ \sum_{i=1}^{6} o_i(k) &\leq 5 \quad \text{for each } \mathbb{P}_i \end{aligned} \tag{6.28}$$

where $\boldsymbol{\rho}_o = \begin{bmatrix} x & y & z \end{bmatrix}^T$ is the position component of $\boldsymbol{x}(k)$, $\mathbf{M}$ is a diagonal matrix of arbitrarily large positive numbers and $o_j(k) \in \{0,1\}$ are integer constraints. When $o_j(k) = 0$, the constraint is enforced, and if $o_j(k) = 1$ then the constraint is relaxed and the multiplication by the component m_{jj} moves the upper bound outside of the solution space. In order to guarantee that at least one of the constraints is active at each time step, the final constraint in Eq. (6.28) must always be less than the number of integer collision constraints.

In the original optimal control problem in Eq. (6.26), the terms $|u_i(t)|$ are piecewise linear, convex functions. Introduction of the slack variable $\boldsymbol{\theta}(k)$ changes the cost function from a sum of piecewise linear, convex functions to a single strictly convex, linear function [15].

Eq. (6.28) provides a feasible solution for a fixed time-of-flight. It is intuitive to expect that shorter times-of-flight would yield a larger Δv (measure of fuel use), and longer times-of-flight yield a Δv that asymptotically approaches a finite lower bound (determined by the minimum input energy required by the maneuver). This suggests that for different emphases on time-of-flight vs fuel consumed, a trade study can be performed. Let $||\boldsymbol{u}(t_f)||_1$ be the optimal solution of Eq. (6.28) for a prescribed time-of-flight. Define an augmented cost function

$$\mathcal{J}(||\boldsymbol{u}(t_f)||_1; \alpha) = t_f + \alpha||\boldsymbol{u}(t_f)||_1 \tag{6.29}$$

where $\alpha > 0$ is a fuel penalty parameter; a larger value of α places heavier emphasis minimizing fuel use. In the limit that α approaches 0, the problem tends toward the minimum-time solution, and as α increases the problem tends toward a minimum-fuel solution. Planning an optimal maneuver with collision avoidance constraints results in an NP-complete mixed-integer program, so an exhaustive search of the solution space may be undesirable from a computation standpoint, particularly for longer times of flight. The cost function Eq. (6.29) is a unimodal function of the time-of-flight, so a line search technique such as golden section can be used. The golden section search allows for a "black box" optimization of Eq. (6.29). The mission planner can further classify maneuvers as "lazy," "moderate," or "aggressive" depending on how much fuel is available and how critical it is for the inspector to arrive at its target state.

A more aggressive trajectory has the benefit that it takes less time to accomplish a maneuver, but this comes at the expense of 1) increased fuel usage and 2) it can be potentially more difficult to track along the trajectory in the presence of disturbances and initial condition error. Conversely, a more relaxed maneuver may use less fuel and be easier to track but at the added expense of increased time of flight. The bounds on this time of flight are simply the minimum time of flight for a feasible solution to Eq. (6.28) and the maximum time of flight deemed acceptable for the mission at hand.

In a manner somewhat reminiscent of motion-primitive-based planning used often in robotics, a library of possible, safe maneuvers around the main vehicle can be defined *a priori*, and subsequently concatenated online [86, 56, 11].

6.3.2 Feedback Control Design

In this section, a trajectory tracking controller and constrained attitude regulator are presented to keep the satellite body axes aligned with the orbiting axes and subsequently track the fuel/time optimal trajectory. The trajectory and attitude controllers are designed separately under ideal assumptions, but will be simulated together in the complete system.

Mixed-Integer Model Predictive Control

Given a state vector $\boldsymbol{x}(k)$ and reference trajectory $\boldsymbol{r}(k)$, the tracking error is defined as

$$\boldsymbol{e}(k) \triangleq \boldsymbol{x}(k) - \boldsymbol{r}(k) \tag{6.30}$$

and the deviation of the control signal from the desired control signal is

$$\tilde{\boldsymbol{u}}(k) = \boldsymbol{u}(k) - \boldsymbol{u}_r(k) \tag{6.31}$$

where $\boldsymbol{u}_r(k)$ is the desired control signal from trajectory optimization. Initially, it is assumed that each thruster can produce any signal belonging to the convex set $[0, u_{\max}]$. recalling that $\boldsymbol{u}(k) = \boldsymbol{u}^+(k) - \boldsymbol{u}^-(k)$ the aggregate control signal is $\boldsymbol{u}(k) \in [-u_{\max}, u_{\max}]$. The model predictive controller is the solution to Problem MPC.

Problem MPC:

$$\begin{aligned}
\min_{\{\boldsymbol{u}(k))\}_{k=0}^{N}} J(\boldsymbol{x}(k), \boldsymbol{r}(k), \boldsymbol{u}(k), k)_{\ell_p} &= ||\boldsymbol{P_e}\boldsymbol{e}(N)||_{\ell_p} + \sum_{k=0}^{N-1} \left[||\boldsymbol{Q_e}\boldsymbol{e}(k)||_{\ell_p} + ||\boldsymbol{R_u}\tilde{\boldsymbol{u}}(k)||_{\ell_p}\right] \\
\boldsymbol{x}(k+1) &= \boldsymbol{A}_k^t\boldsymbol{x}(k) + \boldsymbol{B}_k^t\boldsymbol{u}(k) \\
\boldsymbol{e}(k) &= \boldsymbol{x}(k) - \boldsymbol{r}(k), \quad \boldsymbol{r}(k) \text{ given } \textit{a priori} \\
\tilde{\boldsymbol{u}}(k) &= \boldsymbol{u}(k) - \boldsymbol{u}_r(k), \quad \boldsymbol{u}_r(k) \text{ given } \textit{a priori} \\
-u_{\max}\mathbf{1} &\leq \boldsymbol{u}(k) \leq u_{\max}\mathbf{1} \\
\begin{bmatrix} \boldsymbol{\rho}_o(k) \\ -\boldsymbol{\rho}_o(k) \end{bmatrix} &\leq \begin{bmatrix} \boldsymbol{\rho}_{\min} \\ -\boldsymbol{\rho}_{\max} \end{bmatrix}_{\mathbb{P}_i} + \mathbf{M}\boldsymbol{o}(k) \\
\boldsymbol{o}(k) &\in \left\{\mathbb{R}^{6\times 1} |\ o_i(k) \in \{0,1\}, \forall\ i = 1, \ldots, 6\right\} \\
\sum_{i=1}^{6} o_i(k) &\leq 5 \quad \text{for each } \mathbb{P}_i
\end{aligned} \tag{6.32}$$

where N is the prediction horizon, ℓ_p denotes the ℓ_p-norm, and collision avoidance constraint is the same as in the trajectory optimization problem. The matrices $\boldsymbol{Q_e}$ and $\boldsymbol{R_u}$ are state and control penalty matrices (identical in function to those from LQR theory), and $\boldsymbol{P_e}$ is the solution to the discrete Riccati equation, which aids in the stability of the closed-loop system [121, 96, 87]. Rather than consider only a quadratic cost function as in the classic formulation of MPC, the 1-norm is also examined to evaluate its performance relative to the quadratic formulation. It is worth noting that an ∞-norm formulation was studied, however it was difficult to tune and yielded significantly higher fuel usage than the 1-norm and quadratic formulations. This is expected because the ∞-norm minimizes the largest component of the vector and has no effect on the rest of the values.

Now, the method by which the prediction model and cost function are built into a linear or quadratic program are briefly presented, see [30, 19, 107] for a more in-depth presentation.

Using a zero-order hold on the input, the linearized dynamics are sampled at T_s which yields the discrete transition and convolution matrices $\boldsymbol{A}_k$ and $\boldsymbol{B}_k$ respectively [114], and the tracking error dynamics are predicted over N samples in the following manner

$$\begin{aligned}
\boldsymbol{e}(0) &= \boldsymbol{e}(0) \\
\boldsymbol{e}(1) &= \boldsymbol{A}_k\boldsymbol{e}(0) + \boldsymbol{B}_k\tilde{\boldsymbol{u}}(0) \\
\boldsymbol{e}(2) &= \boldsymbol{A}_k\boldsymbol{e}(1) + \boldsymbol{B}_k\tilde{\boldsymbol{u}}(1) \\
&= \boldsymbol{A}_k^2\boldsymbol{e}(0) + \boldsymbol{A}_k\boldsymbol{B}_k\tilde{\boldsymbol{u}}(0) + \boldsymbol{B}_k\tilde{\boldsymbol{u}}(1) \\
&\vdots \\
\boldsymbol{e}(N) &= \boldsymbol{A}_k^N\boldsymbol{e}(0) + \boldsymbol{A}_k^{N-1}\boldsymbol{B}_k\tilde{\boldsymbol{u}}(0) + \boldsymbol{A}_k^{N-2}\boldsymbol{B}_k\tilde{\boldsymbol{u}}(1) + \cdots + \boldsymbol{B}_k\tilde{\boldsymbol{u}}(N-1)
\end{aligned} \tag{6.33}$$

This can be more compactly written in matrix form

$$\begin{bmatrix} \boldsymbol{e}(0) \\ \boldsymbol{e}(1) \\ \boldsymbol{e}(2) \\ \boldsymbol{e}(3) \\ \vdots \\ \boldsymbol{e}(N) \end{bmatrix} = \begin{bmatrix} \mathbb{I} \\ \boldsymbol{A}_k \\ \boldsymbol{A}_k^2 \\ \boldsymbol{A}_k^3 \\ \vdots \\ \boldsymbol{A}_k^N \end{bmatrix} \boldsymbol{e}(0) + \begin{bmatrix} \boldsymbol{0} & \boldsymbol{0} & \boldsymbol{0} & \cdots \\ \boldsymbol{B}_k & \boldsymbol{0} & \boldsymbol{0} & \cdots \\ \boldsymbol{A}_k\boldsymbol{B}_k & \boldsymbol{B}_k & \boldsymbol{0} & \cdots \\ \boldsymbol{A}_k^2\boldsymbol{B} & \boldsymbol{A}_k\boldsymbol{B}_k & \boldsymbol{B}_k & \cdots \\ \vdots & \vdots & \vdots & \cdots \\ \boldsymbol{A}_k^{N-1}\boldsymbol{B}_k & \boldsymbol{A}_k^{N-2}\boldsymbol{B}_k & \boldsymbol{A}_k^{N-3}\boldsymbol{B}_k & \cdots \end{bmatrix} \begin{bmatrix} \tilde{\boldsymbol{u}}(0) \\ \tilde{\boldsymbol{u}}(1) \\ \tilde{\boldsymbol{u}}(2) \\ \tilde{\boldsymbol{u}}(3) \\ \vdots \\ \tilde{\boldsymbol{u}}(N-1) \end{bmatrix} \tag{6.34}$$

which can then be written in the succinct form

$$\boldsymbol{E} = \mathcal{A}\boldsymbol{e}_0 + \mathcal{B}\tilde{\boldsymbol{U}} \tag{6.35}$$

The trajectory tracking problem and point regulation control design can be accomplished by the same controller since point regulation is a special case of trajectory tracking.

First the quadratic program is considered since it is the more commonly encountered formulation. Define the augmented penalty matrices

$$\begin{aligned}
\bar{\boldsymbol{Q}} &= \text{blkdiag}(\boldsymbol{Q}_e, \boldsymbol{Q}_e, \ldots, \boldsymbol{P}_e), \quad \boldsymbol{Q}_e, \boldsymbol{P}_e \succeq \boldsymbol{0},\ \bar{\boldsymbol{Q}} = \bar{\boldsymbol{Q}}^T \\
\bar{\boldsymbol{R}} &= \text{blkdiag}(\boldsymbol{R}_u, \boldsymbol{R}_u, \ldots, \boldsymbol{R}_u), \quad \boldsymbol{R}_u \succ \boldsymbol{0},\ \bar{\boldsymbol{R}} = \bar{\boldsymbol{R}}^T
\end{aligned} \tag{6.36}$$

Using the definition for the predicted error states, the cost function for Problem MPC may be rewritten. The cost function is now given by

$$\begin{aligned}
J &= \boldsymbol{E}^T\bar{\boldsymbol{Q}}\boldsymbol{E} + \tilde{\boldsymbol{U}}^T\bar{\boldsymbol{R}}\tilde{\boldsymbol{U}} \\
&= \left[\mathcal{A}\boldsymbol{x}_0 + \mathcal{B}\tilde{\boldsymbol{U}}\right]^T \bar{\boldsymbol{Q}} \left[\mathcal{A}\boldsymbol{x}_0 + \mathcal{B}\tilde{\boldsymbol{U}}\right] + \tilde{\boldsymbol{U}}^T\bar{\boldsymbol{R}}\tilde{\boldsymbol{U}} \\
&= \tilde{\boldsymbol{U}}^T\left[\mathcal{B}^T\bar{\boldsymbol{Q}}\mathcal{B} + \bar{\boldsymbol{R}}\right]\tilde{\boldsymbol{U}} + 2\left[\boldsymbol{e}_0^T\mathcal{A}^T\bar{\boldsymbol{Q}}\mathcal{B}\right]\tilde{\boldsymbol{U}} + \boldsymbol{e}_0^T\mathcal{A}^T\bar{\boldsymbol{Q}}\mathcal{A}\boldsymbol{e}_0 \\
&= \tilde{\boldsymbol{U}}^T\mathbf{H}\tilde{\boldsymbol{U}} + 2\boldsymbol{f}^T\tilde{\boldsymbol{U}} + \boldsymbol{d}
\end{aligned} \tag{6.37}$$

Note that the intermediate states $\boldsymbol{e}(k)$ are eliminated from the problem, and then optimization problem is parameterized by the initial sample $\boldsymbol{e}(0)$ and the reference trajectory. Some

additional algebra yields the standard form for the constraints on the control signals and the state constraints (which are now functions of $\tilde{\boldsymbol{u}}(k)$ parameterized by $\boldsymbol{e}(0)$), yielding a standard quadratic program in the absence of integer constraints.

The linear programming approach is somewhat more involved. In a similar fashion to the formulation of the trajectory planning program in Eq. (6.28), the sum of absolute values is replaced by a single strictly convex, linear function

$$J = \sum_{k=0}^{N-1} \gamma^{\boldsymbol{e}}(k) + \gamma^{\boldsymbol{u}}(k) \tag{6.38}$$

where $\gamma^{\boldsymbol{e}}(k)$ and $\gamma^{\boldsymbol{u}}(k)$ are slack functions which form the upper bound on J. At each time step, the following constraints are introduced [19]

$$\begin{aligned} -\gamma^{\boldsymbol{e}}(k)\mathbf{1} &\leq \pm \boldsymbol{Q}_{\boldsymbol{e}} \left(\boldsymbol{A}^k \boldsymbol{e}(0) + \sum_{j=0}^{k-1} \boldsymbol{A}^j \boldsymbol{B} \tilde{\boldsymbol{u}}(k-j-1) \right) \\ -\gamma^{\boldsymbol{e}}(N)\mathbf{1} &\leq \pm \boldsymbol{P}_{\boldsymbol{e}} \left(\boldsymbol{A}^N \boldsymbol{e}(0) + \sum_{j=0}^{N-1} \boldsymbol{A}^j \boldsymbol{B} \tilde{\boldsymbol{u}}(N-j-1) \right) \\ -\gamma^{\boldsymbol{u}}(k)\mathbf{1} &\leq \pm \boldsymbol{R}_{\boldsymbol{u}} \tilde{\boldsymbol{u}}(k) \end{aligned} \tag{6.39}$$

which yields a standard linear program when no integer constraints are present.

If the collision avoidance constraints are neglected, the optimization problem is strictly convex for $\ell_p = 1, 2, \infty$, and the problem can be solved efficiently [21]. The addition of the collision avoidance constraints makes this a mixed-integer linear or quadratic program. For the proximity operations considered in this paper, it is important to include these non-convex constraints to prevent the inspector satellite from colliding with the main vehicle if the tracking error grows too large.

The assumption that $\boldsymbol{u}(k)$ can take any value in the set $[-u_{\max}, u_{\max}]$ is rather optimistic; real spacecraft thrusters cannot necessarily achieve this. Particularly for cold gas thruster systems, the thrust profiles can resemble a nearly bang-off-bang or binary actuator. To this end, it would be advantageous to model the thruster in such a way that the minimum impulse bit is encoded in the optimization problem. We use the following semi-continuous control signal:

$$\boldsymbol{u}(k) \in \{0, 1\} \bigcup [u_{\min}, u_{\max}], \quad \Delta(\boldsymbol{u}) = u_{\max} - u_{\min} \tag{6.40}$$

where $u_{\min}$ is the MIB and $\Delta(\boldsymbol{u})$ can be thought of as the throttle range of the thruster. An example thruster constraint set for $\boldsymbol{u}(k) = [u_1(k), u_2(k)]$ can be seen in Figure 6.5. When used in the context of an optimal control problem, Eq. (6.40) results in a combinatorial optimization problem [14]. This is similar to a formulation briefly proposed by Larsson *et al.* [85] however they did not use this formulation due to computational burden.

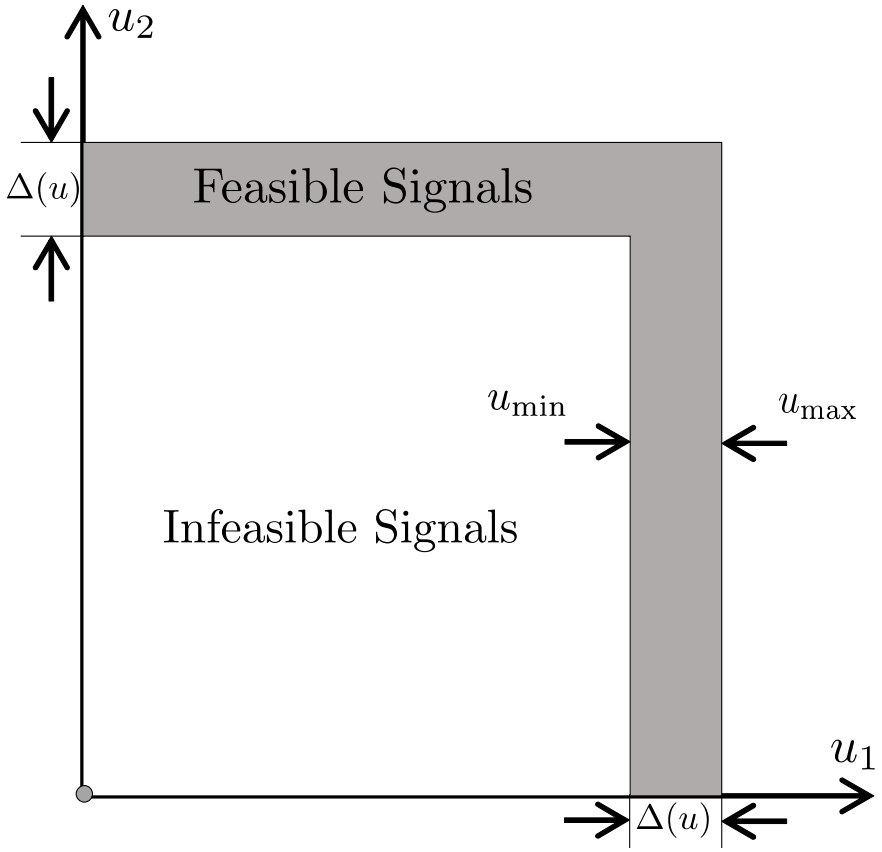

Figure 6.5: Thruster constraint modeled as a semi-continuous variable

The mixed-integer model predictive control problem is

Problem MI-MPC:

$$
\begin{aligned}
\min_{\{\boldsymbol{u}(k))\}_{k=0}^{N}} J(\boldsymbol{x}(k), \boldsymbol{r}(k), \boldsymbol{u}(k), k)_{\ell_p} &= ||\boldsymbol{P_e} \boldsymbol{e}(N)||_{\ell_p} + \sum_{k=0}^{N-1} \left[||\boldsymbol{Q_e} \boldsymbol{e}(k)||_{\ell_p} + ||\boldsymbol{R_u} \tilde{\boldsymbol{u}}(k)||_{\ell_p} \right] \\
\boldsymbol{x}(k+1) &= \boldsymbol{A}_k^t \boldsymbol{x}(k) + \boldsymbol{B}_k^t \boldsymbol{u}(k) \\
\boldsymbol{e}(k) &= \boldsymbol{x}(k) - \boldsymbol{r}(k), \quad \boldsymbol{r}(k) \text{ given } \textit{a priori} \\
\tilde{\boldsymbol{u}}(k) &= \boldsymbol{u}(k) - \boldsymbol{u}_r(k), \quad \boldsymbol{u}_r(k) \text{ given } \textit{a priori} \\
u_{\min} \boldsymbol{b}(k) &\leq \boldsymbol{u}(k) \leq u_{\max} \boldsymbol{b}(k) \\
\begin{bmatrix} \boldsymbol{\rho}_o(k) \\ -\boldsymbol{\rho}_o(k) \end{bmatrix} &\leq \begin{bmatrix} \boldsymbol{\rho}_{\min} \\ -\boldsymbol{\rho}_{\max} \end{bmatrix}_{\mathbb{P}_i} + \mathbf{M} \boldsymbol{o}(k) \\
\boldsymbol{o}(k) &\in \left\{ \mathbb{R}^{6\times 1} |\ o_i(k) \in \{0,1\}, \forall\, i = 1, \ldots, 6 \right\} \\
\boldsymbol{b}(k) &\in \left\{ \mathbb{R}^{6\times 1} |\ b_i(k) \in \{0,1\}, \forall\, i = 1, \ldots, 6 \right\} \\
\sum_{i=1}^{6} o_i(k) &\leq 5 \quad \text{for each } \mathbb{P}_i
\end{aligned}
\tag{6.41}
$$

which now has integer constraints on both the states *and* control signals. The resulting mixed-integer linear or quadratic control problem can now be solved using well-known techniques such as branch-and-bound. This transforms the problem into a hybrid system. There have been significant advances in embedded control optimization for hybrid systems [48] which suggest that real time solution of these mixed-integer programs are feasible.

In the simulations section, we compare Problem MI-MPC with a problem we call the convex-modulated approach (CM-MPC) to Problem MPC; the control signal is allowed to take any value in the convex control constraint set, and then values below $u_{\min}$ are rounded to zero, which is identical to the second approach mentioned in [62]. The problem is convex with respect to the control constraint set; if the state constraints are neglected then this problem can also be solved in polynomial time with respect to the size of the optimization. This approach is sub-optimal in that the signal is modified as a post-processing step.

Problem CM-MPC and MI-MPC are formulated as trajectory tracking problems where the fuel-optimal trajectory is previewed as part of the prediction model. This has the desirable characteristic that the fuel-optimal trajectory defines the nominal state history, and can be used as a baseline in a more realistic simulation. This also helps alleviate some of the difficulty of using linear programming-based MPC; MPC with linear cost functions (1-norm or ∞-norm) can exhibit a phenomenon called dead-beat behavior [39]. MPC is typically formulated as a point-stabilization problem and, particularly for linear cost functions, the controller can tend toward solutions that result in minimum-time behavior. Alternatively, if the controller tuning is relaxed so as to prevent the minimum-time behavior, the optimization routine may determine that the optimal sequence of moves is to do nothing, resulting in idle control. Some of this behavior can be alleviated by using variable control horizons (as in

Richards and How [108]), however with the approach presented in that work, there was no baseline for the optimal maneuver in terms of fuel consumed. The formulation presented in this paper allows for easier tuning of the controller for both Problem CM-MPC and MI-MPC as well as a basis for comparison with the optimal fuel consumption.

It is worth noting that since all of the trajectory feedback controllers presented in this section are NP-complete, it is natural to inquire about the possibility of the integer program solution time and whether the system can run faster than real time. While it is difficult to guarantee that a feasible solution to Problem CM-MPC or MI-MPC will be found in less than the sample time, T_s, the simulations in this paper adopt a standard approach to dealing with this. The integer programs are solved using branch-and-bound, and if the solution time exceeds the sampling time, then the branch-and-bound is terminated and the second solution from the previous time step is used [61]. While generally sub-optimal, it is reasonable to assume that the optimal solutions from one time step will be similar to the optimal solutions for the next time step, particularly for fast sampling time ($T_s = 1$ s for this paper). This will be discussed in the numerical results section.

Constrained Linear-Quadratic Attitude Regulator

The objective of the attitude controller is to stabilize the body axes to track the orbiting axes and reject the disturbance torques from the environment and thruster misalignments. It is assumed that the attitude and attitude rate deviations from the orbiting axes are small enough to be linear, motivating the use of the constrained linear quadratic regulator.

The state linearization in Eq. (6.19) is uncontrollable since the matrix $\boldsymbol{A}_r$ has a 1-dimensional null space corresponding to the scalar component of the quaternion. This is a result of the redundancy of the quaternion parameterization. The attitude is found to be linearly *stabilizable* by enforcing the constraint $\bar{\boldsymbol{q}}^T\bar{\boldsymbol{q}} = 1$. Linear MPC only requires that a system be stabilizable, meaning that all of the uncontrollable modes are stable. For the purposes of control design, we introduce a truncated state vector containing the vector part of the quaternion and the angular velocity:

$$\boldsymbol{w}(k) = \begin{bmatrix}\boldsymbol{q}^T(k) & (\boldsymbol{\omega}_o^b(k))^T\end{bmatrix}^T \tag{6.42}$$

and then perform control design using the partitions of $\boldsymbol{A}^r$ and $\boldsymbol{B}^r$ which correspond to the controllable states. For the trajectory design, a convex control constraint set such as $[-u_{\max}, u_{\max}]$ was an insufficient assumption. For attitude control, where the actuation can be performed by reaction wheels, magnetorquers etc. and provide very fine attitude resolution, this assumption is more realistic.

The construction of the quadratic program for the attitude controller is similar to the method by which the quadratic trajectory tracking controller was formed in the previous section, however the reference is $\mathcal{R} = \boldsymbol{0}$ in this case. The constrained linear-quadratic regulator

problem is

Problem MPC-Att:

$$\begin{aligned} \min_{\{\boldsymbol{\tau}(k)\}_{k=0}^{N}} \; & J(\boldsymbol{\tau}(k),k) = \boldsymbol{w}^T(N)\boldsymbol{P}_{\boldsymbol{w}}\boldsymbol{w}(N) + \sum_{k=0}^{N-1} \boldsymbol{w}^T(k)\boldsymbol{Q}_{\boldsymbol{w}}\boldsymbol{w}(k) + \boldsymbol{\tau}^T(k)\boldsymbol{R}_{\boldsymbol{\tau}}\boldsymbol{\tau}(k) \\ & \boldsymbol{w}(k+1) = \boldsymbol{A}_k^r\boldsymbol{w}(k) + \boldsymbol{B}_k^r\boldsymbol{\tau}(k) \\ & -\tau_{\max}\mathbf{1} \leq \boldsymbol{\tau}(k) \leq \tau_{\max}\mathbf{1} \end{aligned} \tag{6.43}$$

where $\tau_{\max}$ is the maximum torque output provided by the attitude control system (ACS) and $\boldsymbol{P}_{\boldsymbol{w}}$ is the solution to the discrete Riccati equation which aids in the stabilizing properties of the controller. The thrusters could be used to provide the attitude control in conjunction with the ACS or as a standalone ACS (see [65] for example), however the thruster misalignment torques are treated as a disturbance torque.

6.4 Numerical Results

In this section, a sample deployment and inspection mission is detailed. First the fuel/time optimization is studied and an optimal deployment maneuver is selected. Once an optimal maneuver is computed, the feedback controller is demonstrated in the presence of a higher-fidelity orbit and attitude model as well as initial condition error. Noting that the initial condition error will affect the performance of the system more than the orbital perturbations, a Monte Carlo run is presented to show the system's robustness to initial conditions and the resulting fuel-use trends from the four controllers studied. All of the simulations were modeled in Matlab using Yalmip to construct the problems [89] and Gurobi's branch-and-bound algorithm was used to solve the mixed-integer programs [58].

6.4.1 Fuel/Time Optimization

Trajectory planning typically takes place *a priori*; developing an entire trajectory in real time can take a prohibitively long time or require too much computational power. The fuel/time optimal control problem provides the mission planner with a wide search space in which to explore different trajectories' fuel consumption. The mission parameters are given in Table 6.1, and the polytopic approximation of the shuttle's shape can be seen in Fig. 6.6.

While an exhaustive search of the solution space for a general optimal control problem with non-convex collision constraints can be impractical, certain maneuvers may be easily and quickly solved, so an extensive search is feasible, and is used for the purposes of validation. The maneuver considered here begins at the edge of the egress bay of the space shuttle with a small amount of velocity along the nadir vector, and ends at the leading edge of the left wing. The thruster model used is the MOOG 58E143 cold gas thruster [98] which has a

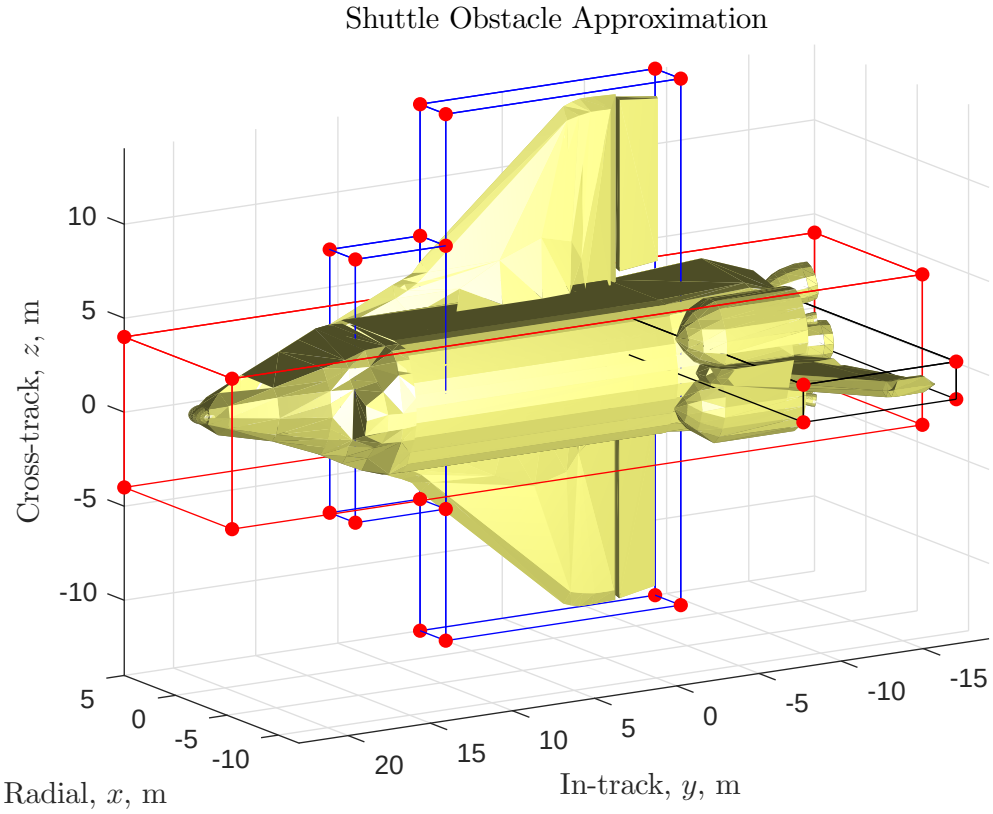

Figure 6.6: Approximation of Shuttle geometry

thrust output of 16 mN and $I_{\text{sp}} = 65$ s. A family of curves corresponding to the fuel/ time functional is seen in Fig. 6.7. For increasingly large values of α, the minimum of Eq. (6.29) shifts to the right.

Inspection of the curves in Fig. 6.7 shows that they are clearly unimodal, so the golden section search method is a reliable way to compute a solution. A similar approach is used in [18], however Blackmore *et al.* optimized a different cost function in their work. Using the golden section search for $\alpha = 800$, the minimum was found at $t_f = 333$ s, which corresponds to $\Delta v = 0.22744$ m/s. The trajectory can be seen in Figure 6.8, and the control history and change in spacecraft mass can be seen in Figures 6.9 and 6.10, respectively.

The optimal control signals for the minimum fuel problem tend to take the form of bang-off-bang control as in Figure 6.4. The inspector's thrusters are off for the majority of the maneuver, and the integer constraints on the states are not violated. An additional safety margin of 1 meter was added to the polytopes representing the shuttle to allow for extra conservatism in the collision avoidance constraints. This trajectory now will serve as pre-specified "safe" trajectory for the deployment of the inspector.

Table 6.1: Trajectory planning parameters

Parameter	Value	Unit
Semi-major axis, a	6678	km
Spacecraft mass, m	9.167	kg
Max thrust, $u_{\max}$	0.016	N
Specific impulse, I_{sp}	65	s
Deputy initial state, $\boldsymbol{x}_0$	$[7, 0.5, -0.5, -0.05, 0, 0]^T$	m, m/s
Deputy final state, $\boldsymbol{x}_f$	$[3, 7, -10, 0, 0, 0]^T$	m, m/s
Safety margin	1	m

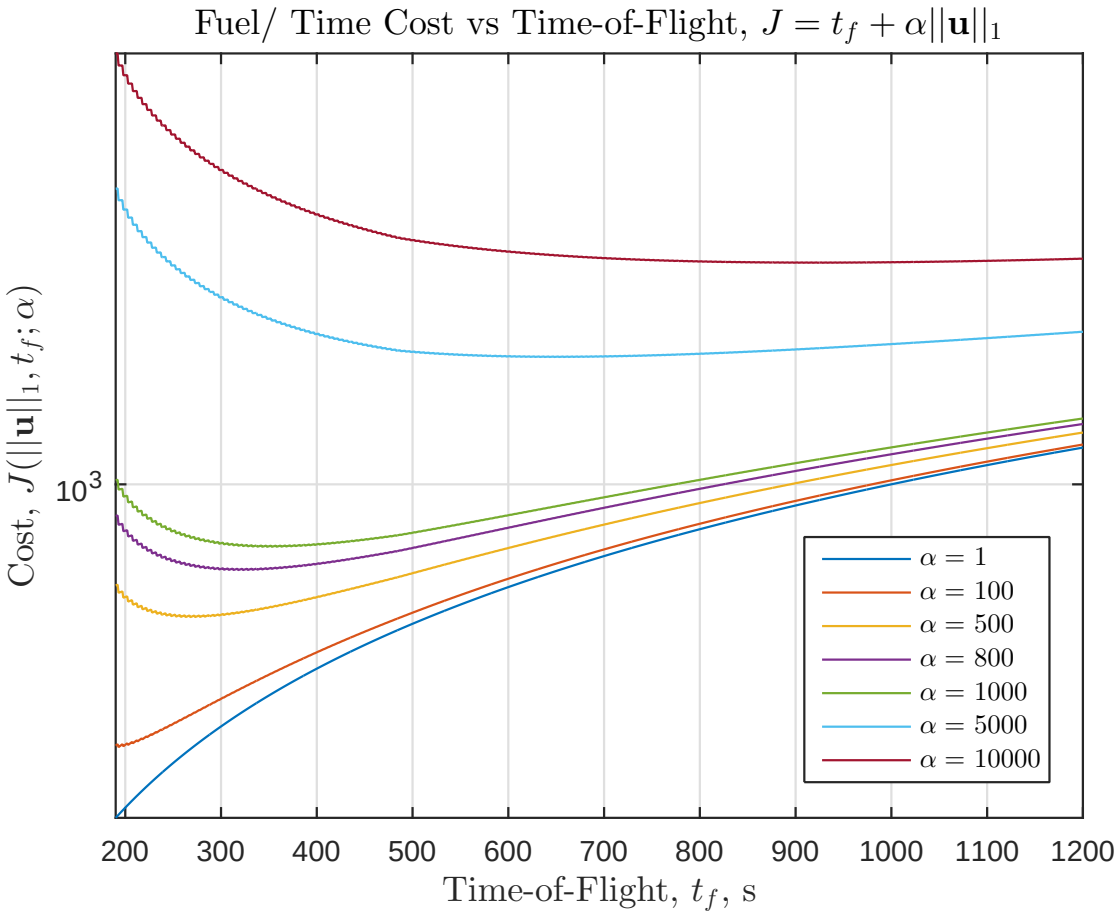

Figure 6.7: Fuel/time cost for various α

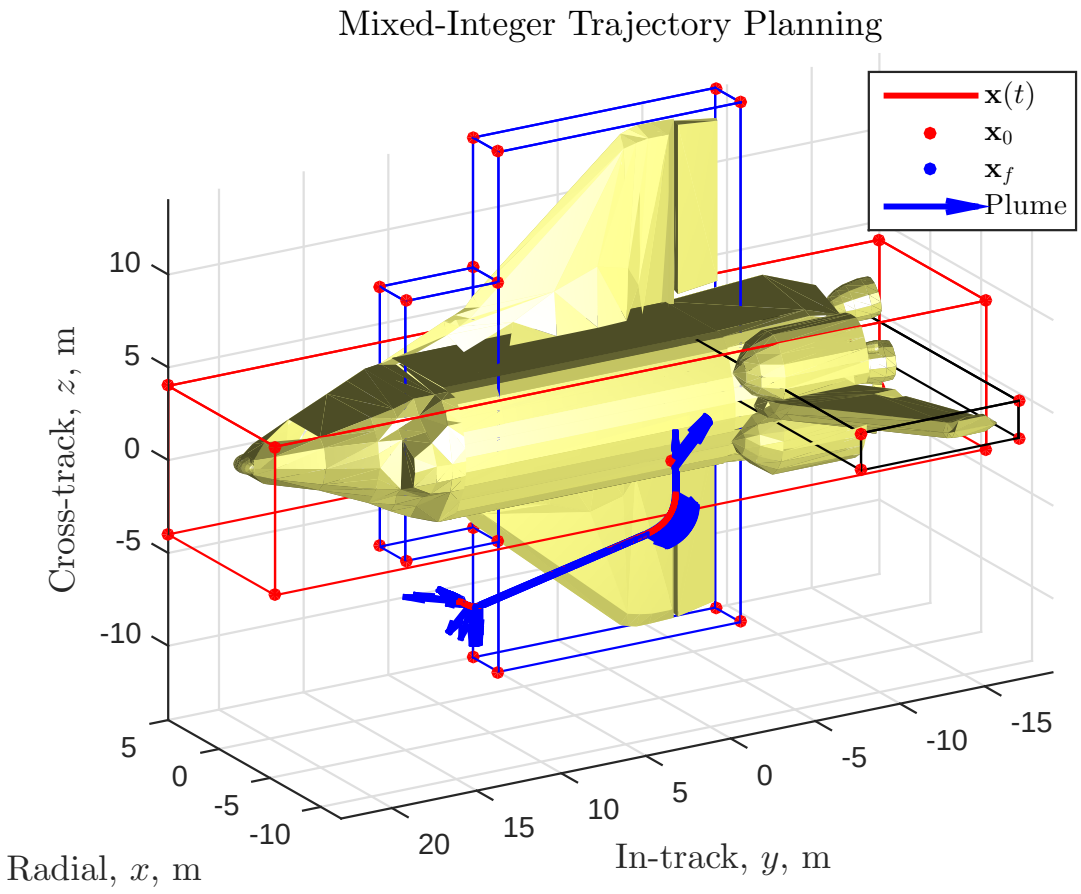

Figure 6.8: Fuel optimal trajectory for $t_f = 333$ s

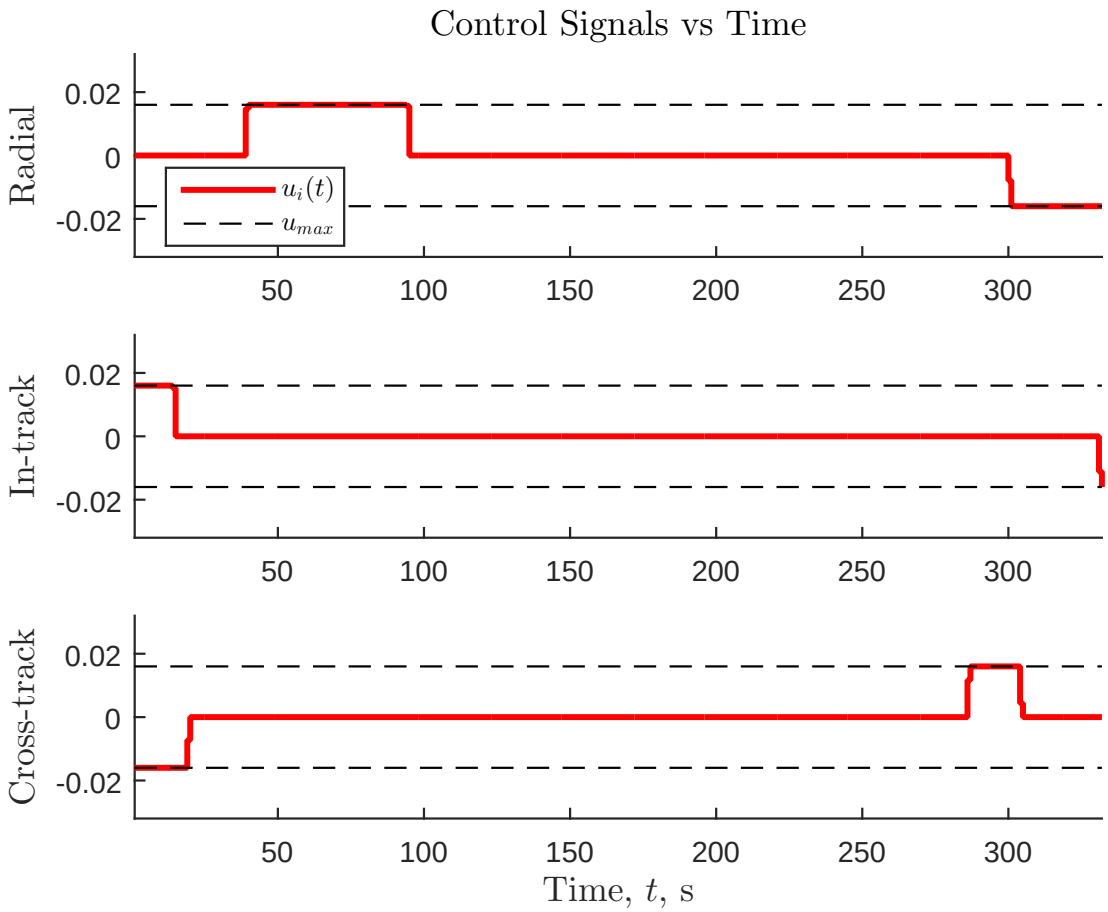

Figure 6.9: Control signals for $t_f = 333$ s

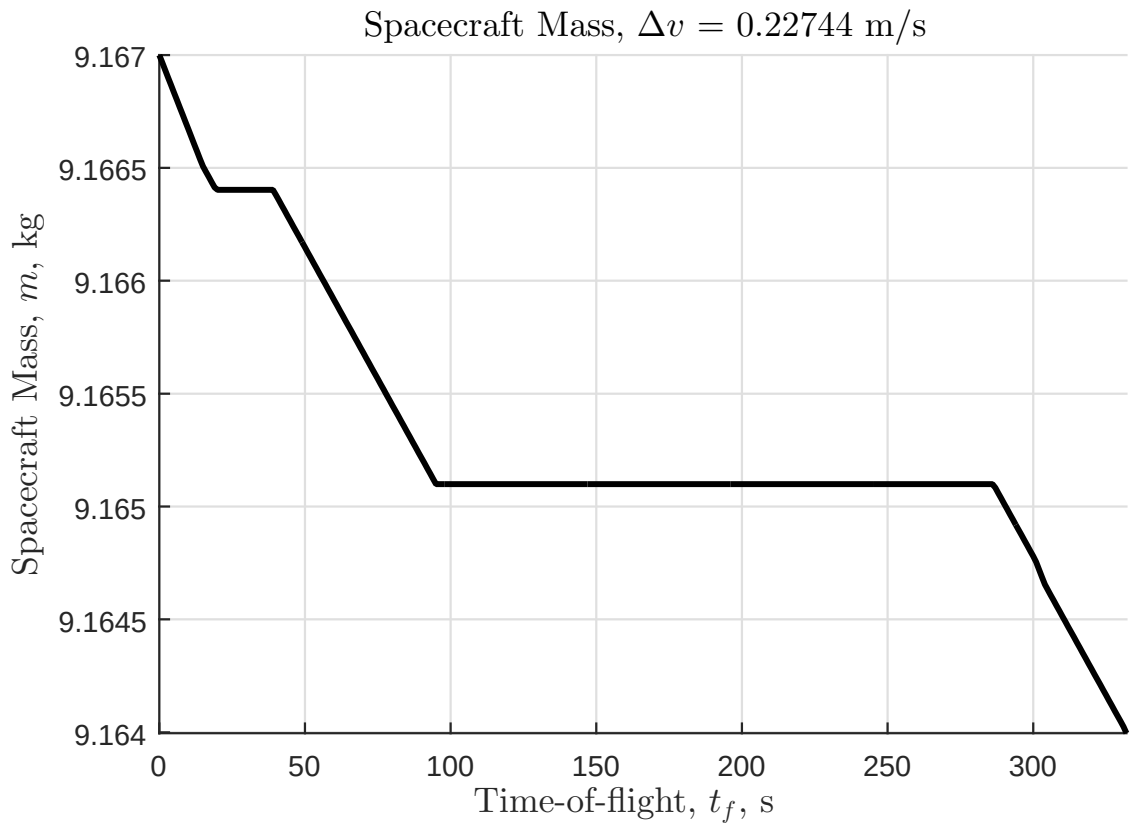

Figure 6.10: Change in spacecraft mass for $t_f = 333$ s

6.4.2 Deployment Solution- No Initial Condition Error

The optimal trajectory from the preceding section represents an idealized solution which does not account for perturbations or initial condition error. The simulation consists of two stages: 1) the 333 second optimal maneuver is tracked in the presence of disturbances then 2) the inspected satellite holds its final position for 900 seconds. These times are flexible and could be easily manipulated for different mission requirements.

The HCW model and linearized attitude model are used for the control design because they are low complexity and time-invariant. In the actual implementation, a myriad disturbances would be present, and while small, could add up over time. The trajectory is simulated on the Gauss Variational Equations (GVE) which are a nonlinear, time-varying system that describes how an arbitrary perturbation affects the orbital elements [13]. The orbital model contains the J_2 perturbation and an exponential atmospheric model, which are the two largest perturbations in LEO, and these are coupled to the nonlinear attitude model. The relationship between the differential orbital elements for the chief and deputy and the Cartesian variables in the HCW model is given by the first-order linear mapping in [119].

Simulation Algorithm:

1. Initialize chief and deputy orbital elements and deputy attitude
2. While $t \leq t_f$
   (a) Use mapping between orbital elements and Cartesian variables for deputy to compute relative state and error state, $\left[\boldsymbol{e}^T(k) \quad \dot{\boldsymbol{e}}^T(k) \quad \bar{\boldsymbol{q}}^T(k) \quad \left(\boldsymbol{\omega}_o^b(k)\right)^T\right]^T$
   (b) Drop scalar component of $\bar{\boldsymbol{q}}^T(k)$, compute controller
      i. Solve Problem MPC-Att
      ii. Solve Problem MI-MPC or CM-MPC
         A. If solution time exceeds T_s, terminate integer program
         B. Use feasible solution with smallest branch gap
   (c) Compute relative orbital elements using inverse linear mapping
   (d) Simulate coupled GVE/ nonlinear attitude over T_s
   (e) Convert relative orbital elements back to Cartesian, re-normalize $\bar{\boldsymbol{q}}^T(k)$
   (f) Return

The simulation algorithm is shown in Figure 6.11.

This simulation implements the controllers on a more realistic, higher fidelity model, which is more representative of what the inspector satellite would experience in orbit. The satellite is assumed to have the MOOG cold gas thrusters from the previous section, as well as the MAI-400 attitude determination and control system [94], upon which the control constraints are modeled. As mentioned before, the control algorithm requires that the mixed-integer program be solved in at least real-time, however faster-than-real-time would be most desirable. The standard approach when implementing these mixed-integer programs is to set the algorithm to terminate when the processor time exceeds the sampling time and use the best feasible solution. The parameters for the solutions presented in this section are provided in Table 6.2.

It was found during simulations that the 1-norm MI-MPC, as well as the 1- and 2-norm CM-MPC formulations did not experience this, and were able to be solved faster than real time. The 2-norm MI-MPC solution was terminated early less than 0.01% of the time.

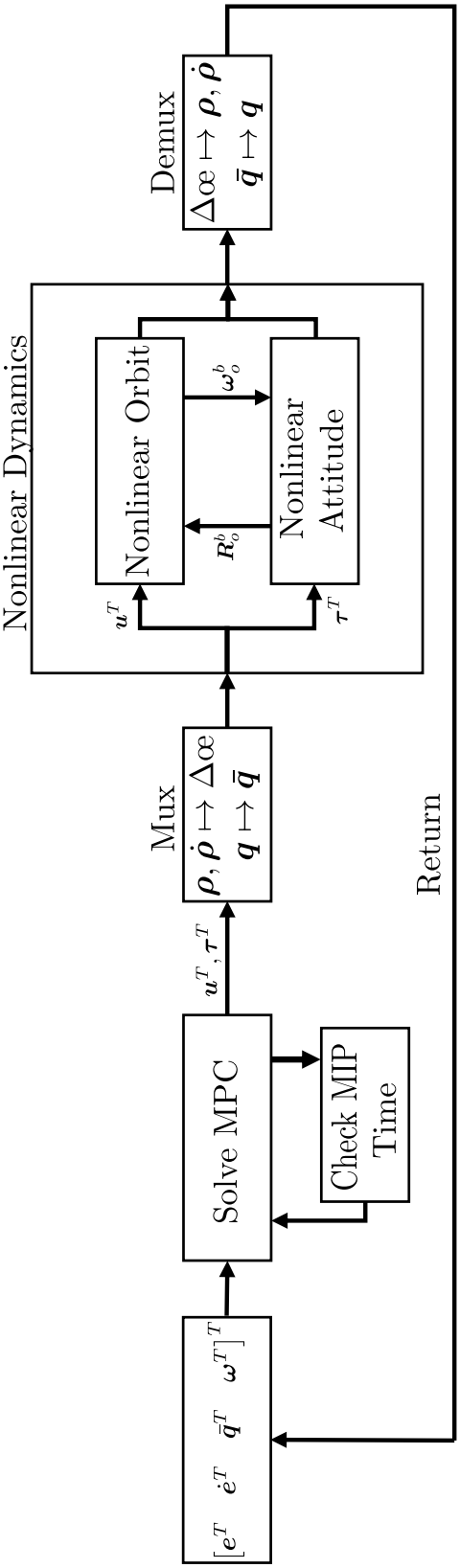

Figure 6.11: Simulation flowchart

Table 6.2: Trajectory tracking parameters

Parameter	Value	Unit
Chief orbit, $(a, e, i, \Omega, \omega, M_0)$	$(6678, 0.01, 28.5, 30, 30, 0)^T$	(km,-,deg,deg,deg,deg)
Spacecraft mass, m	9.167	kg
Principal MOI, I_i	$(0.140998, 0.10559, 0.05417)^T$	$\text{kg} \cdot \text{m}^2$
Max thrust, $u_{\max}$	0.016	N
Min thrust, $u_{\min}$	0.015984	N
Specific impulse, I_{sp}	65	s
Max torque $\tau_{\max}$	0.635	mN·m
Deputy initial state, $\boldsymbol{x}_0$	$[7, 0.5, -0.5, -0.05, 0, 0]^T$	m, m/s
Deputy final state, $\boldsymbol{x}_f$	$[3, 7, -10, 0, 0, 0]^T$	m, m/s
Deputy initial YPR/ rates	$[0, 0, 0, 0, 0, 0]$	deg, deg/s
Prediction horizon, N,	25	s
Loiter time, t_{loiter}	900	s
$\boldsymbol{Q_e}, \boldsymbol{R_u}$	$\mathbb{I}$, 1e3$\mathbb{I}$	-
$\boldsymbol{Q_w}, \boldsymbol{R_\tau}$	$\mathbb{I}$, 1e4$\mathbb{I}$	-

In Figures 6.12 and 6.14, the tracking error can be seen and the Euler angle histories can be seen in 6.13 and 6.15. The thruster histories and torque histories can be seen in 6.16, 6.17, 6.18, and 6.19, respectively. Finally, the mass histories of the spacecraft with each of the controllers are seen in Figures 6.20 and 6.21.

Without initial condition error, the attitude is still disturbed by the thrusters firing, but quickly recovered. The 1-norm MI-MPC solution requires 28% less fuel ($\Delta v = 0.26955$ m/s vs $\Delta v = 0.37691$ m/s) than the 1-norm CM-MPC solution, but at the expense of slightly more tracking error. On the other hand the 2-norm MI-MPC and CM-MPC solutions use very similar amounts of fuel, with $\Delta v = 0.26193$ m/s and $\Delta v = 0.28651$ m/s, respectively). The MI-MPC formulation has the advantage that the thruster activity is sparser, particularly for the 1-norm solution. This is expected from the heuristic that the 1-norm optimization should provide more sparsity since it has the fuel minimization directly encoded in the cost function. Furthermore, the thrusters and ACS never violate their constraints. Under nominal initial conditions, the two controllers are similar enough in terms of fuel usage that it might not be worth the extra computational burden to solve MI-MPC. In the presence of initial condition error, we find that the differences between the two formulations become more pronounced, and the MI-MPC formulation shows a marked improvement over CM-MPC.

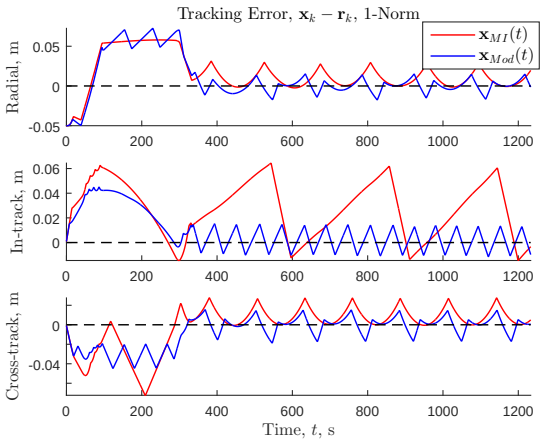

Figure 6.12: Tracking error for the 1-norm MPC formulation

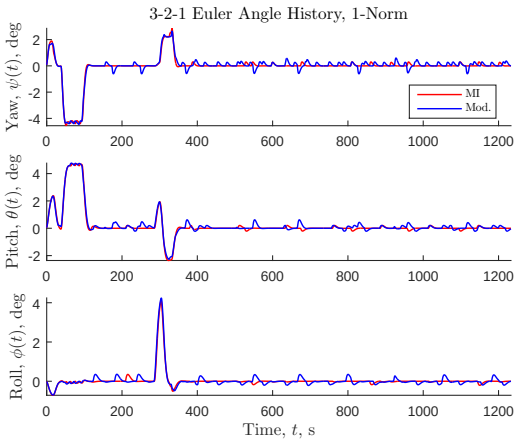

Figure 6.13: Euler angles for the 1-norm MPC formulation

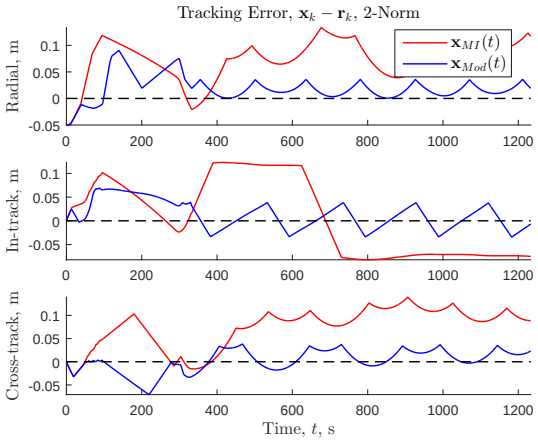

Figure 6.14: Tracking error for the 2-norm MPC formulation

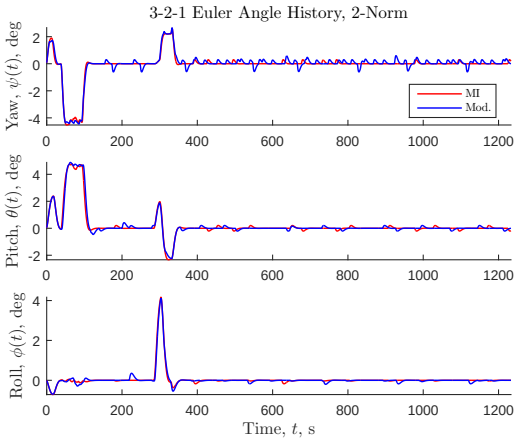

Figure 6.15: Euler angles for the 2-norm MPC formulation

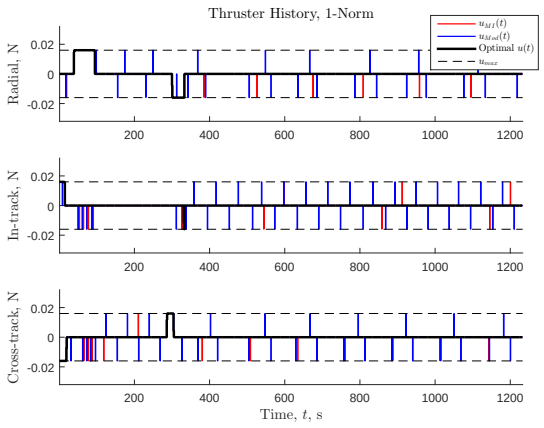

Figure 6.16: Thruster for the 1-norm MPC formulation

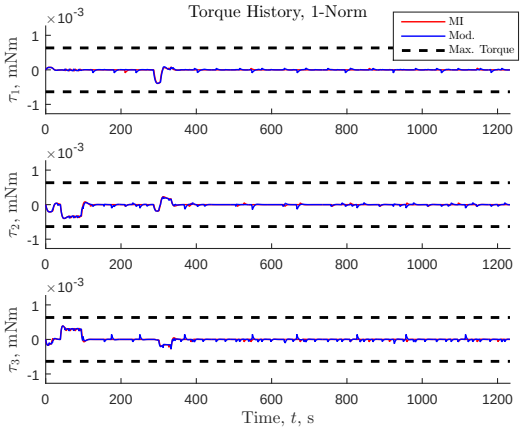

Figure 6.17: Torque history for the 1-norm MPC formulation

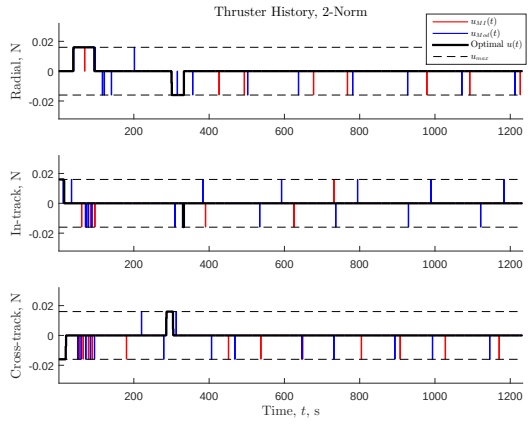

Figure 6.18: Thruster history for the 2-norm MPC formulation

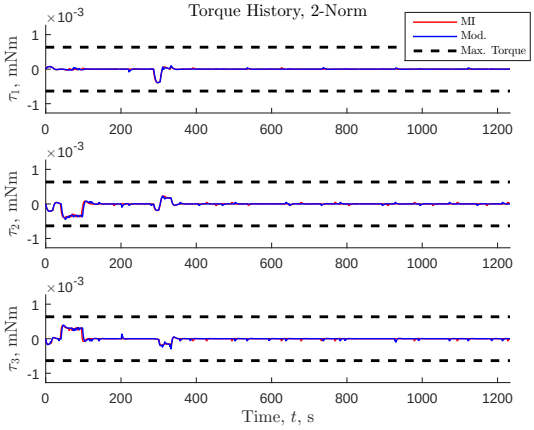

Figure 6.19: Torque history for the 2-norm MPC formulation

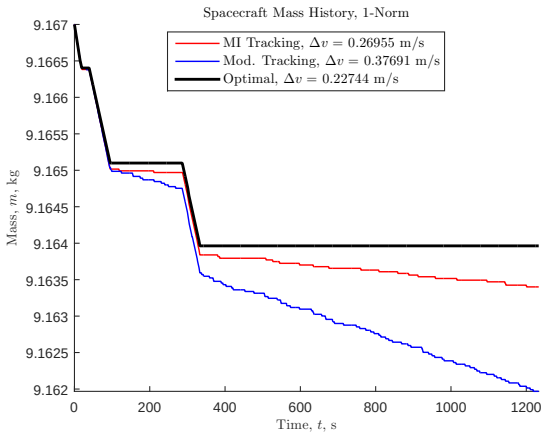

Figure 6.20: Mass history for the 1-norm MPC formulation

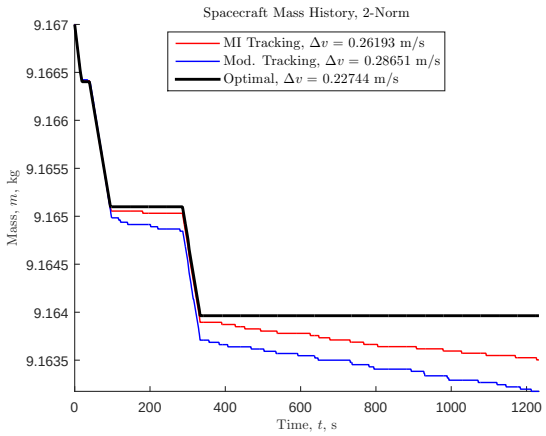

Figure 6.21: Mass history for the 2-norm MPC formulation

6.4.3 Deployment Solution- With Initial Condition Error

In this section we add initial condition error to the simulations to show that the controllers can recover successfully from an event like deployment error. Orbital eccentricity, J_2 and atmospheric drag are the factors that have the largest effects in most formation flying applications, however, over the short timescales (relative to the orbital period) and length scales considered in this paper, these effects will have little effect on the relative motion. For length scales on the order of meters, deploying the satellite accurately and with as little initial velocity as possible is crucial. If the velocities are too large, nonlinear effects can start to appear in the response of the system and can be difficult to control with a linear controller.

The nominal initial conditions for the satellite were perturbed with 20% error for the trajectory, and between 10◦ and 20° of yaw, pitch and roll error. Again, the controller is able to recover from the initial condition error and track the optimal maneuver. Figures 6.22, 6.23, 6.26 and 6.27 show the system histories for the 1-norm formulation of the problem, and Figures 6.24, 6.25, 6.28 and 6.29 show the systems histories for the 2-norm solution. The MI-MPC method presents a sparser solution and results in lower overall Δv for both the 1-norm and 2-norm formulations.

In the final set of simulations, 100 Monte Carlo runs with randomly generated initial conditions were performed. In each of the simulations, all of the controllers are able to stabilize the system to track their respective references, see Figures 6.32, 6.33, 6.36, 6.34, 6.35 and 6.37, however the MI-MPC formulation generally yields a lower Δv, seen in Figure 6.38.

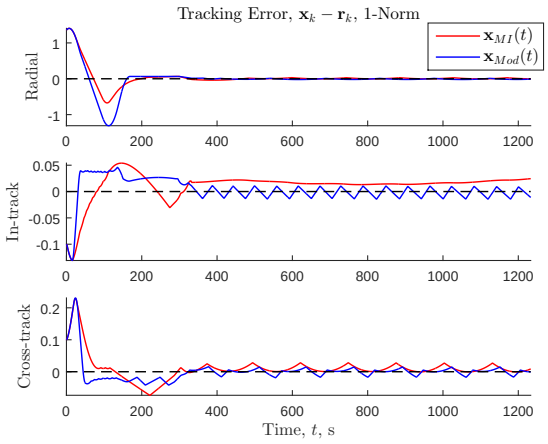

Figure 6.22: Tracking error for the 1-norm MPC formulation

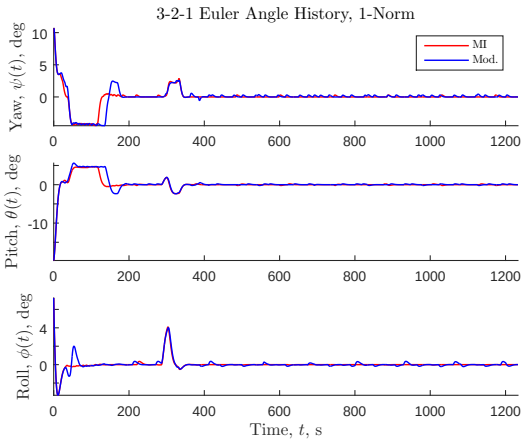

Figure 6.23: Euler angles for the 1-norm MPC formulation

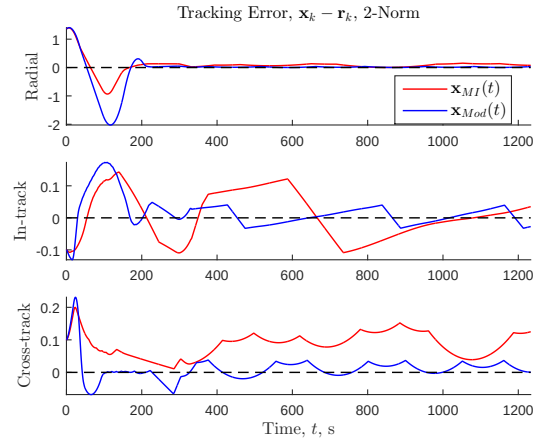

Figure 6.24: Tracking error for the 2-norm MPC formulation

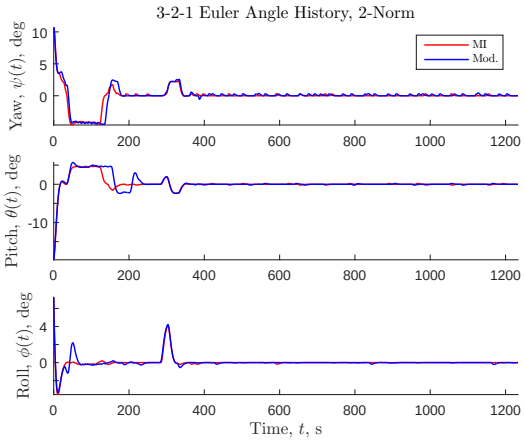

Figure 6.25: Euler angles for the 2-norm MPC formulation

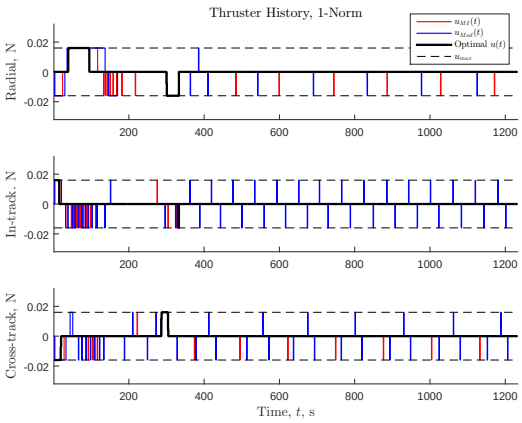

Figure 6.26: Thruster for the 1-norm MPC formulation

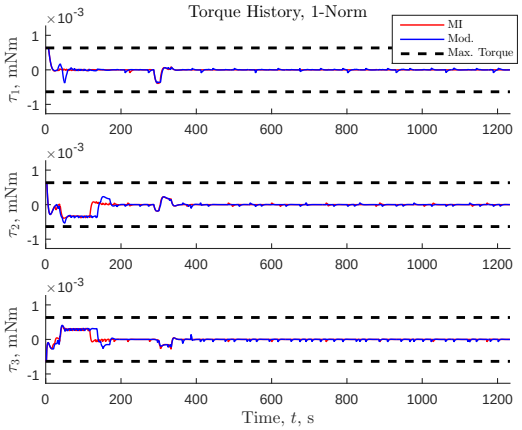

Figure 6.27: Torque history for the 1-norm MPC formulation

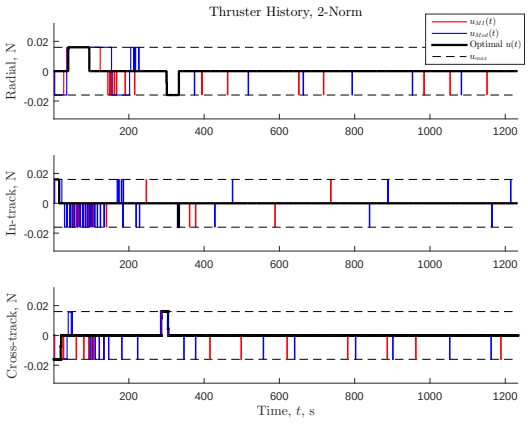

Figure 6.28: Thruster history for the 1-norm MPC formulation

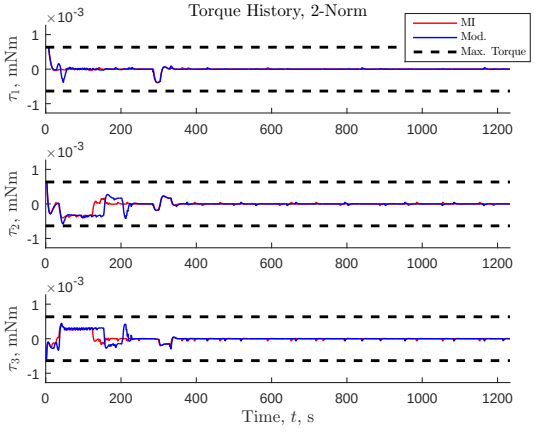

Figure 6.29: Torque history for the 1-norm MPC formulation

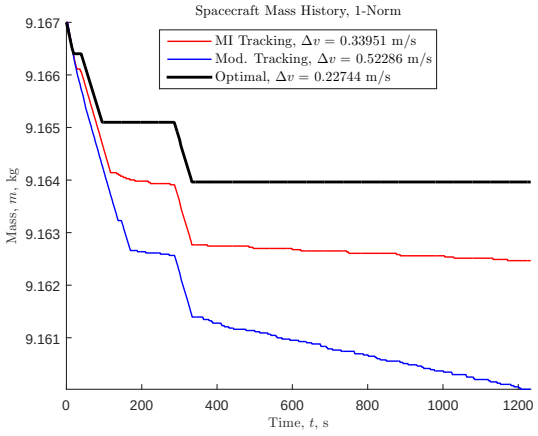

Figure 6.30: Mass history for the 1-norm MPC formulation

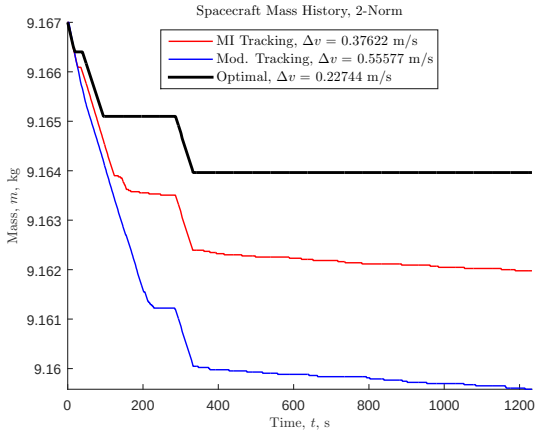

Figure 6.31: Mass history for the 2-norm MPC formulation

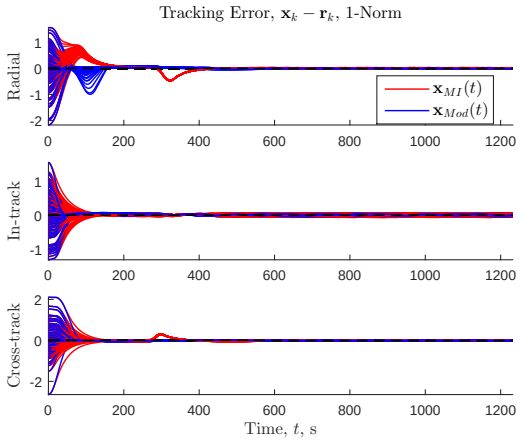

Figure 6.32: Tracking error for the 1-norm MPC formulation

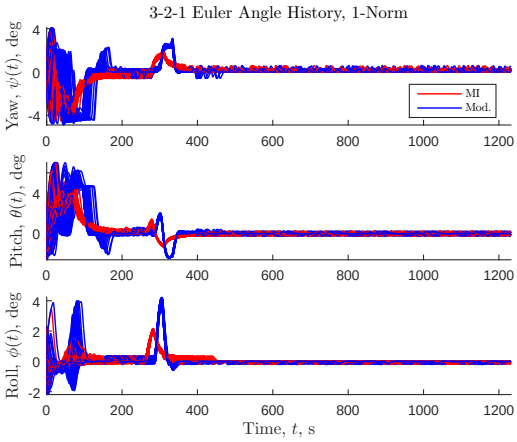

Figure 6.33: Tracking error for the 1-norm MPC formulation

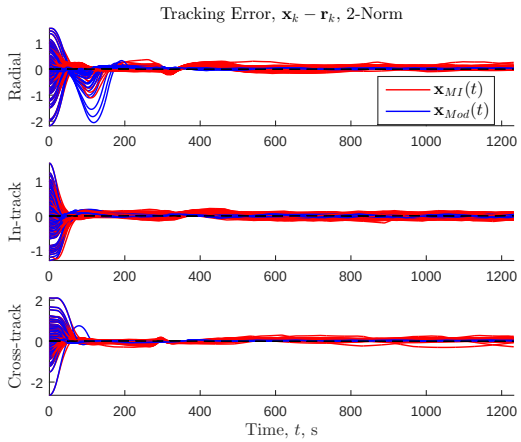

Figure 6.34: Tracking error for the 2-norm MPC formulation

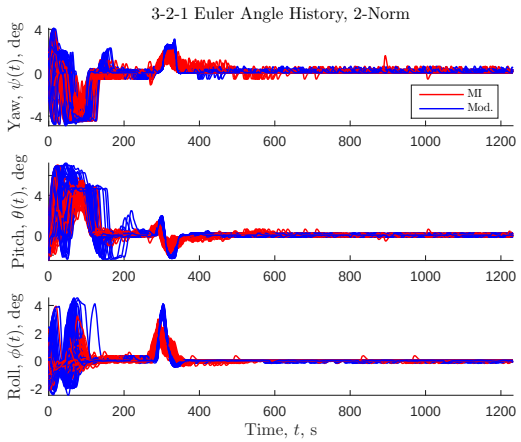

Figure 6.35: Tracking error for the 2-norm MPC formulation

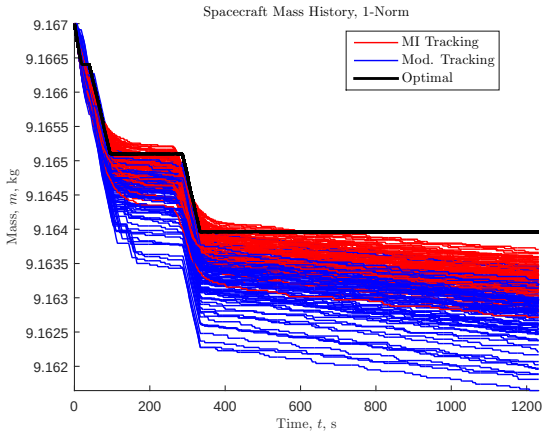

Figure 6.36: Tracking error for the 2-norm MPC formulation

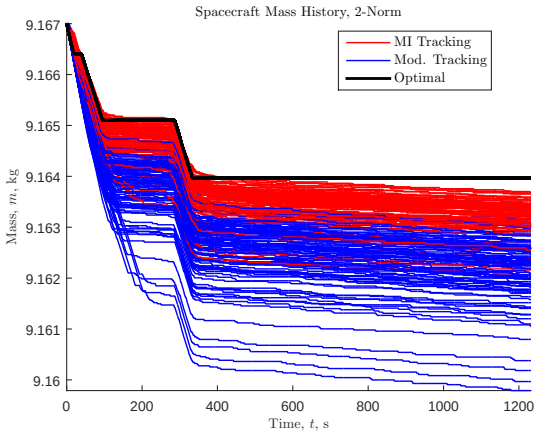

Figure 6.37: Tracking error for the 2-norm MPC formulation

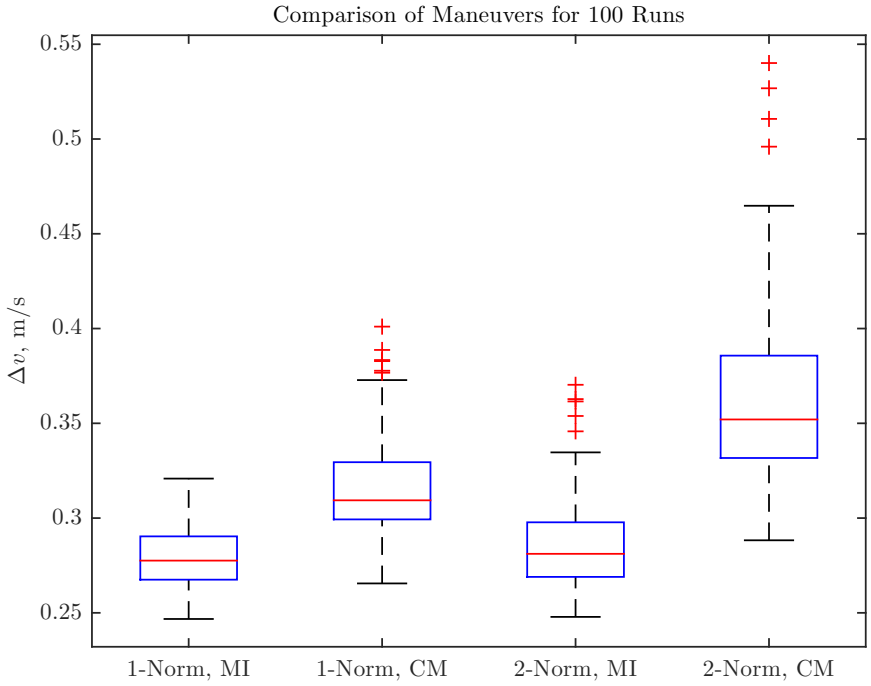

Figure 6.38: Δv for 100 different simulations with initial condition error

6.5 Conclusions

In this chapter, a coupled orbit and attitude model is derived which includes the effect of the thrusters on the attitude, and the subsequent manner in which the attitude affects the thruster alignment. The model was specialized for a 6U Cubesat which could be launched to carry out inspection missions.

Next a mixed-integer linear program was used with a golden section search was used to find the minimum cost for the fuel/time optimal control problem which provides a safe reference trajectory between two points near the chief's body. Having found the reference trajectory, four different mixed-integer based model predictive tracking controllers are used to track the reference trajectory, and a constrained linear quadratic regulator is used to stabilize the body axes of the satellite. We make note of the following:

1. The torques induced on the attitude by the thruster activity present a noticeable effect, but can be easily corrected using the constrained LQR attitude controller presented. This keeps the attitude error from growing too large and affecting the direction of the thrusters.

2. For similar tunings, the MI-MPC and CM-MPC solutions exhibit sparse control activity. The sparse activity in MI-MPC is a result of the control signals being either off ($u = 0$) or on but above the minimum impulse bit $0 < u_{\min} \leq u_{\max}$ whereas the sparsity in CM-MPC results from rounding down signals lower than the minimum impulse bit to 0.

3. The MI-MPC solution tends to have lower fuel consumption than CM-MPC in terms of Δv, and the 1-norm solution tends to have lower fuel consumption than the 2-norm solution. The only instance in which this is not the case was for the nominal initial conditions where the 2-norm MI-MPC yielded a slightly smaller Δv than the 1-norm MI-MPC.

4. While the MI-MPC formulation yields favorable Δv performance over the CM-MPC formulation, it comes at the added computational expense of having more binary variables per time step. As noted before, if one were to remove the collision avoidance constraints, Problem CM-MPC would result in a strictly convex program whereas MI-MPC still would result in a mixed-integer program.

Chapter 7

Conclusions

Modeling and control for spacecraft relative motion has numerous applications, both implemented and proposed. These applications range from science gathering missions to military applications to spacecraft servicing and inspection. While attractive in terms of the capabilities it affords to mission designers, there are still many challenges that need to be addressed to continue to advance the state of the art for effective implementation. The control design in this dissertation helps address some of these challenges, and they are summarized below, followed by recommendations for future research directions.

7.1 Summary of Contributions

The work encompassed in this dissertation ranges from primarily analytical with restrictive, idealized assumptions on the models to primarily computational with many of the assumptions relaxed to produce more realistic models.

In Chapter 3, the Hill-Clohessy-Wiltshire model served as the model for an analytical trajectory optimization study. The result of this analysis is a completely analytical, closed-form, explicit solution to the minimum-energy, under-actuated, optimal transfer problem using purely in-track and cross-track thrust. This analysis proved the necessary and sufficient conditions for the optimality of the candidate controller using the Pontryagin Principle as well as elements of linear operator theory: the controller is a guaranteed global minimum and simultaneously proves the controllability of the under-actuated system. The controller is parameterized by the time-of-flight as well as the boundary conditions of the maneuver, and we showed simplified forms for the controller for specific maneuvers. Comparison of the under-actuated maneuver with a fully-actuated maneuver developed using the same technique used for the under-actuated maneuver shows that the total cost, given by the $\mathcal{L}_2$ energy, is of the same order of magnitude, however the fully-actuated maneuver is slightly less expensive overall. This implies that the radial component of the maneuver does help

lower the overall cost, but the in-track component contributes most of the effort for the maneuver. This matches intuition about orbital maneuvers, namely, in-track thrusts are more efficient than radial thrusts.

In Chapter 4, the more general, elliptical LERM were used to compute a minimum-energy transfer and then verified by using the Pontryagin Principle on the NERM. The linear transfer was solved by numerically computing a Gramian for the transfer, and building the minimum energy transfer using the form provided in Chapter 2. The NERM transfer was formulated as a nonlinear, two-point boundary value problem, and solved numerically using Matlab's `bvp4c` solver as well as the GPOPS2 tool. Comparison of the linear and nonlinear maneuvers shows that the two solutions are nearly identical. From this we concluded that, for the class of maneuvers considered in this work, accurate trajectories can be generated using the LERM and the nonlinearities are of little consequence. Additionally better guarantees of optimality are available for linear systems than nonlinear systems. After generating the linear optimal controller, we developed a sliding mode tracking controller which tracked the (linear) optimal trajectory in the presence of orbital disturbances and nonlinearity. We showed that the sliding mode controller, which used the saturation function relaxation of the signum function is 1) asymptotically stabilizing, 2) robust to the un-modeled disturbances, and 3) forces the system to reach the boundary layer of the sliding manifold in finite time, from which it does not leave. The controllers presented in this chapter are flexible and can handle any arbitrarily elliptical orbit.

Chapter 5 extended elements of chapters 3 and 4 with the intent of developing more realistic trajectory optimization solutions. The Gim-Alfriend state transition matrix was used as the relative motion model, which models the J_2 perturbation on the relative motion to first order for any arbitrarily elliptical reference orbit. The GA-STM was then discretized using a zero-order hold on the input, and the controllability Gramian was numerically shown to be non-singular for both the fully-actuated and under-actuated cases, which guarantees controllability of the system. The system was transcribed to a linear program to solve a minimum fuel optimal control problem. Validation cases for circular, unperturbed orbits were shown to converge to classical results from impulsive orbit transfer theory. This convergence occurs in the limit that the discretization approaches zero, and the time-of-flight approaches infinity. Then, the elliptical, perturbed solutions were computed, showing similar convergence. Finally, the fuel/time optimal control problem was solved using the linear programming approach in conjunction with a genetic algorithm to find the optimal time-of-flight. This analysis showed that globally optimal solutions can be found using our method, which computes solutions for multi-revolution, finite thrust, fuel-optimal, relative transfers near perturbed, elliptical orbits.

In Chapter 6, the focus shifted from very large formation reconfiguration to very short baseline, short time-scale proximity operations problems. The primary application in this chapter was robotic inspection. A coupled orbit and attitude model was developed for this type of mission. The new model captures the coupling of the orbit and attitude through the trajectory input channels; attitude error results in the trajectory inputs firing in the wrong

direction, and thruster non-collinearities with the center of mass and each other can result in further attitude errors. To wit, the control design consisted of 1) an *a priori* trajectory planning phase where a fuel-optimal, "safe" deployment trajectory was obtained using a mixed-integer linear program and 2) a trajectory tracking phase where the attitude is stabilized to track the orbiting axes and the trajectory tracks along a the pre-planned route. Both the trajectory control and attitude control are formulated as model predictive controllers in order to encode state and control constraints into the optimization problem. The trajectory tracking controller used thrust constraints formulated as semi-continuous variables in order to capture the nearly binary nature of the thruster. This was compared with another common approach which rounds signals below the minimum-impulse bit down to zero. We showed that the semi-continuous variable approach saved more fuel and resulted in sparser control activity than the sub-optimal approach for both 1-norm and 2-norm formulations of the MPC algorithm when simulated on a more realistic orbit model.

7.2 Recommendations for Future Work

The primary direction for future work is continued analysis of the control design for proximity operations. There are four areas where improvements might be made: 1) using different models for the trajectory and attitude, 2) exploration of convexification techniques to make the proximity operations controllers more efficient, 3) alternative formulations of model predictive control, and 3) adding in state estimation to the proximity operations problem.

The proximity operations scenario modeled in this dissertation used the HCW equations for the trajectory which we assumed was a "good enough" model due to the short time-scales and baselines of the maneuvers. Analysis of other motion models, such as the model proposed by Gaias *et al.* [51] which incorporates J_2 and differential drag or the small eccentricity theory proposed by Yan and Alfriend [8] which is an approximation of the GA-STM, may reveal that further fuel savings are obtained on the realistic orbit simulation.

The novel method of encoding the minimum-impulse bit into a mixed-integer program may not be the most ideal way to deal with the problem. We compared the method with one of the methods presented by Hartley *et al.* [62] which most closely matched our control design objectives and assumptions. We showed that it provides some fuel savings, however the savings come at the expense of added computational complexity and branching behavior in the mixed-integer program solution. While there has been some excellent progress in the field of real-time optimization for mixed logical systems, we did not explore that in this work. The control constraint set could be convexified to improve the solution time for the optimization (the optimization already runs faster than real time, but still requires early termination occasionally, as noted in chapter 6). The convexification, even if it is not a lossless convexification, could significantly improve the performance of the proposed system.

Closely related to the previous paragraph are improvements to the model predictive control

design. Future work could include either explicit model predictive control based on dynamic programming, or gain-scheduled model predictive control. Explicit model predictive control was originally considered for part of this dissertation, however the explicit MPC algorithm was based on dynamic programming, and suffered from the curse of dimensionality. Explicit MPC results in a multi-parametric program and a piecewise affine system; the controller is computed *a priori* for all possible combinations of states and controls over a set of polyhedra, and then the controller is converted to a look-up table. The *a priori* computational effort can be extremely large for longer time horizons, but the controller implementation is very fast online. This could be used to significantly speed up the real-time capability of the proposed method. Then, it would be an interesting problem to implement some of these controllers in a bench simulation on more realistic flight computers to verify their efficacy.

Gain-scheduled model predictive control is recommended to handle the nonlinearity arising from the changing mass of the system; as fuel is depleted, the mass of the satellite as well as its inertia tensor will accordingly change. Gain-scheduling could address this through treating the system as a linear, parameter-varying system where the scheduling variables are the inertia properties of the system. There has been some excellent work on explicit MPC for LPV systems by Löfberg *et al.* [16]. This could help relax the assumption that the mass and inertia tensor stay constant throughout the maneuver, which is inherently untrue though it can be an appropriate assumption.

Finally, incorporating state estimation for both the attitude and trajectory could help improve the realism of the system proposed in Chapter 6. In reality, all spacecraft control problems are output feedback, where the output contains some estimate of the state subject to noisy measurements. This was not considered in this dissertation since the focus was on state feedback. Additionally, 6U CubeSats were considered as the basis model for proximity operations, but different spacecraft form factors and control allocation could certainly be analyzed.

Bibliography

[1] Ossama Abdelkhalik and Daniele Mortari. N-Impulse Orbit Transfer Using Genetic Algorithms. *Journal of Spacecraft and Rockets*, 44(2), March-April 2007.

[2] Nabih N Abdelmalek. Solutions of Minimum Time Problem and Minimum Fuel Problem for Discrete Linear Admissible Control Systems. *International Journal of Systems Science*, 9(8):849–855, 1978.

[3] David Adam. Gravity Measurement: Amazing GRACE. *Nature*, 416(6876):10–11, 2002.

[4] Aerojet. *Aerojet Monopropellant Rocket Datasheet*, 04 2006. Rev. 2006-018.

[5] European Space Agency. *Publications of the Cluster-II and Double Star Missions*, 11 December 2015 (access 23 January 2016).

[6] Miguel Aguirre-Martinez and Nico Sneeuw. Needs and tools for future gravity measuring missions. *Space science reviews*, 108(1-2):409–416, 2003.

[7] Buzz Aldrin. *Line-of-sight guidance techniques for manned orbital rendezvous*. PhD thesis, Massachusetts Institute of Technology, 1963.

[8] K. T. Alfriend and H. Yan. Evaluation and comparison of relative motion theories. *Journal of Guidance, Control and Dynamics*, 28(2), March-April 2005.

[9] Kyle T. Alfriend, Hanspeter Schaub, and Dong-Woo Gim. Gravitational perturbations, nonlinearity and circular orbit assumption effect on formation flying control strategies. In *Proceedings of the Annual AAS Rocky Mountain Conference*, pages 139–158, Breckenridge, CO, Feb. 2–6 2000.

[10] Kyle T. Alfriend, Srinivas R. Vadali, Pini Gurfil, Jonathan P. How, and Louis S. Breger. *Spacecraft Formation Flying- Dynamics, Control and Navigation*. Elsevier Astrodynamics Series. Butterworth-Heinemann, 30 Corporate Drive, Suite 400, Burlington, MA 01803, USA, 2010.

[11] Ony Arifianto and Mazen Farhood. Optimal control of a small fixed-wing UAV about concatenated trajectories. *Control Engineering Practice*, 40:113 – 132, 2015.

[12] David A Barnhart, Roger C Hunter, Alan R Weston, Vincent J Chioma, Mark Steiner, and William Larsen. Xss-10 micro-satellite demonstration. In *Proceedings of the AIAA Defense and Civil Space Programs Conference and Exhibit*, 1998.

[13] Richard Battin. *An Introduction to the Mathematics and Methods of Astrodynamics*. AIAA Education Series, New York, N.Y., 1987.

[14] Alberto Bemporad and Manfred Morari. Control of systems integrating logic, dynamics, and constraints. *Automatica*, 35(3):407 – 427, 1999.

[15] Dimitris Bertsimas and John Tsitsiklis. *Introduction to Linear Optimization*. Athena Scientific, P.O. Box 805, Nashua, NH 03061, 1997.

[16] Thomas Besselmann, Johan Löfberg, and Manfred Morari. Explicit MPC for LPV systems: stability and optimality. *IEEE Transactions on Automatic Control*, 57(9):2322–2332, 2012.

[17] John T. Betts. Survey of Numerical Methods for Trajectory Optimization. *Journal of Guidance, Control, and Dynamics*, 21(2), March-April 1998.

[18] Lars Blackmore, Behçet Açikmeşe, and Danial Scharf. Minimum-Landing-Error Powered-Descent Guidance for Mars Landing Using Convex Optimization. *Journal fo Guidance, Control, and Dynamics*, 33(4), July-August 2010.

[19] F Borrelli, A Bemporad, and M Morari. Predictive control. *Draft Available at: http://www. mpc. berkeley. edu/mpc-course-material (in preparation)*, 2012.

[20] Albert B Bosse, W James Barnds, Michael A Brown, N Glenn Creamer, Andy Feerst, C Glen Henshaw, Alan S Hope, Bernard E Kelm, Patricia A Klein, Frank Pipitone, et al. Sumo: spacecraft for the universal modification of orbits. In *Proc. of SPIE Vol*, volume 5419, page 37.

[21] Stephen Boyd and Lieven Vandenberghe. *Convex Optimization*. Cambridge University Press, 2004.

[22] Louis Breger. Model Predictive Control for Formation Flying Spacecraft. Master's thesis, Massachusetts Institute of Technology, June 2004.

[23] Louis Breger. *Control of Spacecraft in Proximity Orbits*. PhD thesis, Massachusetts Institute of Technology, June 2007.

[24] Louis Breger and Jonathan P. How. Gauss' Variational Equation-Based Dynamics and Control For Formation Flying Satellites. *Journal of Guidance, Control and Dynamics*, 30(2):437–448, 2007.

[25] R.W. Brockett. *Finite-Dimensional Linear Systems*. John Wiley and Sons, 1970.

[26] Roger A. Broucke. Solution of the Elliptic Rendezvous Problem with Time as the Independent Variable. *Journal of Guidance, Control and Dynamics*, 26(4), 2003.

[27] Owen Brown and Paul Eremenko. Fractionated Space Architectures: A Vision for Responsive Space. In *AIAA Responsive Space Conference*, number RS4-2006-1002, April 2006.

[28] John A. Burns. *Introduction to Calculus of Variations and Control, with Modern Applications*. Applied Mathematics and Nonlinear Science. Chapman and Hall/ CRC, 2013.

[29] Randal Burns, Craig McLaughlin, Jesse Leitner, Maurice Martin, et al. Techsat 21: formation design, control, and simulation. In *Aerospace Conference Proceedings, 2000 IEEE*, volume 7, pages 19–25. IEEE, 2000.

[30] Eduardo Camacho and Carlos Bordons. *Model Predictive Control*. Advanced Textbooks in Control and Signal Processing. Springer London, 2007.

[31] Thomas Carter. Fuel-Optimal Maneuvers of a Spacecraft Relative to a Point in Circular Orbit. *Journal of Guidance, Control and Dynamics*, 7(6):710–716, 1984.

[32] Thomas Carter and Mayer Humi. Fuel-Optimal Rendezvous Near a Point in a General Keplerian Orbit. *Journal of Guidance, Control and Dynamics*, 10(6):567–573, 1987.

[33] G. Chisham, M. Lester, S.E. Milan, M.P. Freeman, W.A. Bristow, A. Grocott, K.A. McWilliams, J.M. Ruohoniemi, T.K. Yeoman, P.L. Dyson, R.A. Greenwald, T. Kikuchi, M. Pinnock, J.P.S. Rash, N. Sato, G.J. Sofko, J.-P. Villain, and A.D.M. Walker. A decade of the Super Dual Auroral Radar Network (SuperDARN): scientific achievements, new techniques and future directions. *Surveys in Geophysics*, 28(1):33–109, 2007.

[34] H. Choset, R. Knepper, J. Flasher, S. Walker, A. Alford, D. Jackson, D. Kortenkamp, R. Burridge, and J. Fernandez. Path planning and control for aercam, a free-flying inspection robot in space. In *Robotics and Automation, 1999. Proceedings. 1999 IEEE International Conference on*, volume 2, pages 1396–1403 vol.2, 1999.

[35] W. H. Clohessy and R. S. Wiltshire. Terminal Guidance System for Satellite Rendezvous. *The Astronautical Journal*, 1960.

[36] Martin J Corless and Art Frazho. *Linear Systems and Control: an Operator Perspective*. CRC Press, 2003.

[37] Simone D'Amico, J-S Ardaens, and Robin Larsson. Spaceborne autonomous formation-flying experiment on the prisma mission. *Journal of Guidance, Control, and Dynamics*, 35(3):834–850, 2012.

[38] Alok Das and Richard Cobb. Techsat 21-space missions using collaborating constellations of satellites. 1998.

[39] Prashant Dave, Dennis A. Willing, Gautham K. Kudva, Joseph F. Pekny, and Francis J. Doyle. LP methods in MPC of large-scale systems: Application to paper-machine CD control. *AIChE Journal*, 43(4):1016–1031, 1997.

[40] Mark Dowson. The Ariane 5 Software Failure. *SIGSOFT Softw. Eng. Notes*, 22(2):84–, March 1997.

[41] S DAmico, E Gill, M Garcia, and O Montenbruck. GPS-based real-time navigation for the PRISMA formation flying mission. In *3rd ESA workshop on satellite navigation user equipment technologies, NAVITEC*, pages 11–13, 2006.

[42] Simone DAmico, Eberhard Gill, and Oliver Montenbruck. Relative orbit control design for the prisma formation flying mission. In *AIAA GNC Conference*, 2006.

[43] Greg D. Earle. personal communication.

[44] C Ph Escoubet. Cluster-II: scientific objectives and data dissemination.

[45] CP Escoubet, M Fehringer, and M Goldstein. Introduction the Cluster mission. In *Annales Geophysicae*, volume 19, pages 1197–1200, 2001.

[46] C.P. Escoubet, R. Schmidt, and M.L. Goldstein. Cluster – science and mission overview. *Space Science Reviews*, 79(1):11–32.

[47] CP Escoubet, MGGT Taylor, A Masson, H Laakso, J Volpp, M Hapgood, and ML Goldstein. Dynamical processes in space: Cluster results. In *Annales Geophysicae*, volume 31, pages 1045–1059. Copernicus GmbH, 2013.

[48] Damian Frick, Alexander Domahidi, and Manfred Morari. Embedded optimization for mixed logical dynamical systems. *Computers and Chemical Engineering*, 72:21 – 33, 2015. A Tribute to Ignacio E. Grossmann.

[49] Robert B Friend. Orbital express program summary and mission overview. In *SPIE Defense and Security Symposium*, pages 695803–695803. International Society for Optics and Photonics, 2008.

[50] G Gaias and S DAmico. Impulsive maneuvers for formation reconfiguration using relative orbital elements. *Journal of Guidance, Control, and Dynamics*, 38(6):1036–1049, 2014.

[51] Gabriella Gaias, Jean-Sébastien Ardaens, and Oliver Montenbruck. Model of j_2 perturbed satellite relative motion with time-varying differential drag. *Celestial Mechanics and Dynamical Astronomy*, 123(4):411–433, 2015.

[52] Gabriella Gaias, Simone D'Amico, and Jean-Sébastien Ardaens. Generalised multi–impulsive manoeuvres for optimum spacecraft rendezvous in near–circular orbit. *International Journal of Space Science and Engineering*, 3(1):68–88, 2015.

[53] Marco Gallieri and Jan M Maciejowski. Lasso MPC: Smart regulation of over-actuated systems. In *American Control Conference (ACC), 2012*, pages 1217–1222. IEEE, 2012.

[54] Harold Gehman, John Barry, Duane Deal, James Hallock, Kenneth Hess, G. Scott Hubbard, John Logsdon, Douglas Osheroff, Sally Ride, Roger Tetrault, Stephen Turcotte, Steven Wallace, and Sheila Widnall. *Columbia* Accident Investigation Board. Technical report, National Aeronautics and Space Administration, August 2003.

[55] Dong-Woo Gim and Kyle T. Alfriend. State Transition Matrix of Relative Motion for the Perturbed Noncircular Reference Orbit. *Journal of Guidance, Control and Dynamics*, 26(6):956–971, 2003.

[56] David J. Grymin, Charles B. Neas, and Mazen Farhood. A hierarchical approach for primitive-based motion planning and control of autonomous vehicles. *Robotics and Autonomous Systems*, 62(2):214 – 228, 2014.

[57] M. Guelman and M. Aleshin. Optimal Bounded Low-Thrust Rendezvous with Fixed Terminal-Approach Direction. *Journal of Guidance, Control and Dynamics*, 24(2):378–385, 2001.

[58] Inc. Gurobi Optimization. Gurobi optimizer reference manual, 2015.

[59] Jean-Fracoise Hamel and Jean de Lafontaine. Neighboring Optimum Feedback Control Law for Earth-Orbiting Formation-Flying Spacecraft. *Journal of Guidance, Control and Dynamics*, 32(1):290–299, 2009.

[60] David M Harland. *The story of space station MIR*. Springer Science & Business Media, 2007.

[61] Edward N Hartley. A Tutorial on Model Predictive Control for Spacecraft Rendezvous. 2015.

[62] Edward N Hartley, Marco Gallieri, and Jan M Maciejowski. Terminal spacecraft rendezvous and capture with lasso model predictive control. *International Journal of Control*, 86(11):2104–2113, 2013.

[63] Edward N. Hartley, Paul A. Trodden, Arthur G. Richards, and Jan M. Maciejowski. Model predictive control system design and implementation for spacecraft rendezvous. *Control Engineering Practice*, 20(7):695 – 713, 2012.

[64] Randy L. Haupt and Sue Ellen Haupt. *Practical Genetic Algorithms*. John Wiley and Sons, Hoboken, NJ, second edition edition, 2004.

[65] Oyvind Hegrenaes, Jan Tommy Gravdahl, and Petter Tondel. Spacecraft attitude control using explicit model predictive control. *Automatica*, 41(12):2107 – 2114, 2005.

[66] Carl Henshaw, Liam Healy, and Stephen Roderick. LIIVe: A Small, Low-Cost Autonomous Inspection Vehicle. In *AIAA SPACE 2009 Conference and Exposition*, pages 1–9. AIAA Reston, VA, 2009.

[67] Gerald R Hintz. Survey of orbit element sets. *Journal of Guidance, Control, and Dynamics*, 31(3):785–790, 2008.

[68] Xu Huang, Ye Yan, and Yang Zhou. Analytical Solutions to Optimal Under-actuated Spacecraft Formation Reconfiguration. *Advances in Space Research*, 56(10):2151–2166, 2015.

[69] Chris W Hughes, Carl Wunsch, and Victor Zlotnicki. Satellite peers through the oceans from space. *Eos, Transactions American Geophysical Union*, 81(7):68–68, 2000.

[70] Peter C Hughes. *Spacecraft Attitude Dynamics*. Dover Publishing, 2004.

[71] Liu Hui and Junfeng Li. Terminal Sliding Mode Control for Spacecraft Formation Flying. *Aerospace and Electronic Systems, IEEE Transactions on*, 45(3):835–846, July 2009.

[72] David G. Hull. *Optimal Control Theory for Applications*. Mechanical Engineering Series. Springer New York, 2003.

[73] Akira Ichikawa and Yoshihiro Ichimura. Optimal impulsive relative orbit transfer along a circular orbit. *Journal of guidance, control, and dynamics*, 31(4):1014–1027, 2008.

[74] Gökhan Inalhan, Michael Tillerson, and Jonathan How. Relative Dynamics and Control of Spacecraft Formations in Eccentric Orbits. *AIAA Journal of Guidance, Dynamics and Control*, 25(1):48–59, 2002.

[75] Jean Albert Kechichian. Motion in General Elliptic Orbit with Respect to a Dragging and Precessing Coordinate Frame. *Journal of the Astronautical Sciences*, 46(1):25–45, January-March 1998.

[76] Hassan Khalil. *Nonlinear Systems*. Prentice Hall, Upper Saddle River, NJ 070458, third edition, 2002.

[77] Young Ha Kim and David Spencer. Optimal Spacecraft Rendezvous Using Genetic Algorithms. *Journal of Spacecraft and Rockets*, 39(6), Nov.-Dec. 2002.

[78] Donald E. Kirk. *Optimal Control Theory- An Introduction*. Dover Publishing, 2004.

[79] Marin Kobilarov and Sergio Pellegrino. Trajectory Planning for CubeSat Short-Time-Scale Proximity Operations. *Journal of Guidance, Control and Dynamics*, 37(2):566–579, 2014.

[80] Raymond Kristiansen. *Dynamic synchronization of spacecraft*. PhD thesis, Norwegian University of Science and Technology, 2008.

[81] Raymond Kristiansen, Esten Grøtli, Per J Nicklasson, and Jan T Gravdahl. A model of relative translation and rotation in leader-follower spacecraft formations. *Modeling, Identification and Control*, 28(1):3–13, 2007.

[82] Raymond Kristiansen, Per Johan Nicklasson, and Jan Tommy Gravdahl. Spacecraft coordination control in 6dof: Integrator backstepping vs passivity-based control. *Automatica*, 44(11):2896–2901, 2008.

[83] MIT Space Systems Laboratory. *About SPHERES*, 2014 (access 8 February 2016).

[84] Christopher Lane and Penina Axelrad. Formation design in eccentric orbits using linearized equations of relative motion. *Journal of Guidance, Control and Dynamics*, 29(1), January-February 2006.

[85] R Larsson, S Berge, P Bodin, and Ulf T Jönsson. Fuel efficient relative orbit control strategies for formation flying and rendezvous within prisma. *Advances in the Astronautical Sciences*, 125:25–40, 2006.

[86] Steven M. LaValle. *Planning Algorithms*. Cambridge University Press, New York, NY, USA, 2006.

[87] M. Lazar, W.P.M.H. Heemels, S. Weiland, and A. Bemporad. Stabilizing model predictive control of hybrid systems. *Automatic Control, IEEE Transactions on*, 51(11):1813–1818, Nov 2006.

[88] Manny R. Leinz, Chih-Tsai Chen, Michael W. Beaven, Thomas P. Weismuller, David L. Caballero, William B. Gaumer, Peter W. Sabasteanski, Peter A. Scott, and Mark A. Lundgren. Orbital Express Autonomous Rendezvous and Capture Sensor System (ARCSS) flight test results, 2008.

[89] J. Löfberg. YALMIP : A Toolbox for Modeling and Optimization in MATLAB . In *Proceedings of the CACSD Conference*, Taipei, Taiwan, 2004.

[90] Anne Long, Mitra Farahmand, and Russell Carpenter. Navigation operations for the magnetospheric multiscale mission. 2015.

[91] Ya-Zhong Luo, Guo-Jin Tang, and Hai yang Li. Optimization of multiple-impulse minimum-time rendezvous with impulse constraints using a hybrid genetic algorithm. *Aerospace Science and Technology*, 10(6):534 – 540, 2006.

[92] Maurice Martin, Pete Klupar, Steve Kilberg, and James Winter. Techsat 21 and revolutionizing space missions using microsatellites. 2001.

[93] Maurice Martin and Michael Stallard. Distributed satellite missions and technologies-the techsat 21 program. In *Space Technology Conference and Exposition*, pages 28–30, 1999.

[94] Maryland Aerospace, Inc. *MAI-400 ADCS Specification Sheet.*

[95] Timothy Massey and Yuri Shtessel. Continuous Traditional and High-Order Sliding Modes for Satellite Formation Control. *Journal of Guidance, Control and Dynamics*, 28(4):826–831, 2005.

[96] D.Q. Mayne, J.B. Rawlings, C.V. Rao, and P.O.M. Scokaert. Constrained model predictive control: Stability and optimality. *Automatica*, 36(6):789 – 814, 2000.

[97] Geoffrey R. McVittie, Krishna Dev Kumar, and Guangjun Liu. Reduced Input Control of an Underactuated Satellite Formation. In *AIAA Guidance, Navigation and Control Conference*, number AIAA 2010-7710, August 2010.

[98] Moog Systems Group. *Cold Gas Thrusters Datasheet*, 2013.

[99] Joseph B. Mueller, Paul R. Griesemer, and Stephanie J. Thomas. Avoidance Maneuver Planning Incorporating Station-Keeping Constraints and Automatic Relaxation. *Journal of Aerospace Information Systems*, 10(6):306–322, 2013.

[100] Tom A Mulder. Orbital express autonomous rendezvous and capture flight operationsPart 2 of 2: AR&C Exercises 4, 5, and End-of-Life. *AIAA Paper*, 6768, 2008.

[101] Hyeongjun Park, S. Di Cairano, and I. Kolmanovsky. Model predictive control for spacecraft rendezvous and docking with a rotating/tumbling platform and for debris avoidance. In *American Control Conference (ACC), 2011*, pages 1922–1927, June 2011.

[102] Michael A. Patterson and Anil V. Rao. GPOPS-II: A MATLAB Software for Solving Multiple-Phase Optimal Control Problems Using *hp*-Adaptive Gaussian Quadrature Collocation Methods and Sparse Nonlinear Programming. *ACM Trans. Math. Softw.*, 41(1):1:1–1:37, October 2014.

[103] D.J. Pearson. The Glideslope Approach. *Advances in the Astronautical Sciences*, 69:109–123, 1989.

[104] Christopher Petersen, Andris Jaunzemis, Morgan Baldwin, MJ Holzinger, and IV Kolmanovsky. Model Predictive Control and Extended Command Governor for Improving Robustness of Relative Motion Guidance and Control.

[105] Mauro Pontani and Bruce Conway. Minimum-Fuel, Finite-Thrust Relative Orbit Maneuvers via Indirect Heuristic Method. *Journal of Guidance, Control and Dynamics*, 38(5), May 2015.

[106] Anil V Rao. A survey of numerical methods for optimal control. *Advances in the Astronautical Sciences*, 135(1):497–528, 2009.

[107] Christopher V. Rao and James B. Rawlings. Linear programming and model predictive control. *Journal of Process Control*, 10(23):283 – 289, 2000.

[108] Arthur Richards and Jonathan How. Model predictive control of vehicle maneuvers with guaranteed completion time and robust feasibility. In *American Control Conference, 2003. Proceedings of the 2003*, volume 5, pages 4034–4040 vol.5, June 2003.

[109] Arthur Richards, Tom Schouwenaars, Jonathan How, and Eric Feron. Spacecraft Trajectory Planning with Avoidance Constraints Using Mixed-Integer Linear Programming. *Journal of Guidance, Control and Dynamics*, 25(4), 2002.

[110] F. S. Rodrigues, M. C. Kelley, P. A. Roddy, D. E. Hunton, R. F. Pfaff, O. de La Beaujardiere, and G. S. Bust. C/NOFS Observations of Intermediate and Transitional Scale-size Equatorial Spread F Irregularities. *Geophysical Research Letters*, 36(18):n/a–n/a, 2009.

[111] Andrew Rogers, Craig Woolsey, and Robert McGwier. Under-Actuated Controllability for Spacecraft Rendezvous. Technical Report 01, Virginia Center for Autonomous Systems, 2014.

[112] Andrew Rogers, Craig Woolsey, and Robert McGwier. Nonlinear tracking of optimal maneuvers in spacecraft formations. In *American Control Conference (ACC), 2015*, pages 5859–5864, July 2015.

[113] Christopher W. T. Roscoe, Jason J. Westphal, Jacob D. Griesbach, and Hanspeter Schaub. Formation Establishment and Reconfiguration Using Differential Elements in J_2-Perturbed Orbits. *AIAA Journal of Guidance, Control, and Dynamics*, 38(9):1725–1740, Sept. 2015.

[114] Wilson Rugh. *Linear System Theory*. Prentice Hall, 1993.

[115] Alexander JB Russell, Tomas Karlsson, and Andrew N Wright. Magnetospheric signatures of ionospheric density cavities observed by cluster. *Journal of Geophysical Research: Space Physics*, 120(3):1876–1887, 2015.

[116] M. Sabatini, D. Izzo, and R. Bevilacqua. Special Inclinations Allowing Minimal Drift Orbits for Formation Flying Satellites. *Journal of Guidance, Control and Dynamics*, 31(1), January-February 2008.

[117] Hanspeter Schaub and Kyle T. Alfriend. Impulsive Feedback Control to Establish Specific Mean Orbit Elements of Spacecraft Formations. *Journal of Guidance, Dynamics and Control*, 24(4):739–745, 2001.

[118] Hanspeter Schaub and Kyle T. Alfriend. J_2-Invariant Relative Orbits for Spacecraft Formations. *Celestial Mechanics and Dynamical Astronomy*, 79(2), 2001.

[119] Hanspeter Schaub and John Junkins. *Analytical Mechanics of Space Systems*. AIAA Education Series, Reston, Virginia, 2009.

[120] Samuel Schweigart and Raymond Sedwick. High-fidelity linearized j_2 model for satellite formation flight. *Journal of Guidance, Control and Dynamics*, 25(6):1073–1080, November-December 2002.

[121] P.O.M. Scokaert and J.B. Rawlings. Constrained linear quadratic regulation. *Automatic Control, IEEE Transactions on*, 43(8):1163–1169, Aug 1998.

[122] A Surjalal Sharma and Steven A Curtis. Magnetospheric multiscale mission. In *Nonequilibrium Phenomena in Plasmas*, pages 179–195. Springer, 2005.

[123] Ryan Sherrill. *Dynamics and Control of Satellite Relative Motion in Elliptic Orbits using Lyapunov-Floquet Theory*. PhD thesis, Auburn University, May 2013.

[124] Andrew J Sinclair and John E Hurtado. The eleventh motion constant of the two-body problem. *Celestial Mechanics and Dynamical Astronomy*, 110(3):189–198, 2011.

[125] Tarunraj Singh. *Optimal Reference Shaping for Dyanmic Systems*. CRC Press, 2009.

[126] M.G.G.T. Taylor, C.P. Escoubet, H. Laakso, A. Masson, and M.L. Goldstein. The cluster mission: Space plasma in three dimensions. In Harri Laakso, Matthew Taylor, and C. Philippe Escoubet, editors, *The Cluster Active Archive*, Astrophysics and Space Science Proceedings, pages 309–330. Springer Netherlands, 2010.

[127] Michael Tillerson, Gokhan Inalhan, and Jonathan P. How. Coordination and Control of Distributed Spacecraft Systems Using Convex Optimization Techniques. *International Journal of Robust and Nonlinear Control*, 12:207–242, 2002.

[128] David Vallado. *Fundamentals of Astrodynamics and Applications*. Space Technology Library. Springer Microcosm Press, third edition, 2007.

[129] MJH Walker. A set of modified equinoctial orbit elements (errata). *Celestial Mechanics and Dynamical Astronomy*, 38(4):391–392, 1986.

[130] MJH Walker, B Ireland, and J Owens. A set of modified equinoctial orbit elements. *Celestial Mechanics and Dynamical Astronomy*, 36(4):409–419, 1985.

[131] A. Weiss, M. Baldwin, R.S. Erwin, and I. Kolmanovsky. Model predictive control for spacecraft rendezvous and docking: Strategies for handling constraints and case studies. *Control Systems Technology, IEEE Transactions on*, 23(4):1638–1647, July 2015.

[132] David A Whelan, E Allen Adler, Samuel B Wilson III, and Gordon M Roesler Jr. Darpa orbital express program: effecting a revolution in space-based systems. In *International Symposium on Optical Science and Technology*, pages 48–56. International Society for Optics and Photonics, 2000.

[133] Bong Wie. *Space Vehicle Dynamics and Control*. AIAA Education Series. AIAA, second edition, 2008.

[134] William E. Wiesel. *Modern Astrodynamics*. Aphelion Press, 2652 Yalonda Ct. Beavercreek OH 45434, second edition, 2010.

[135] Koji Yamanaka and Finn Ankersen. New State Transistion Matrix for Relative Motion on an Arbitrary Elliptical Orbit. *Journal of Guidance, Control and Dynamics*, 25(1), 2002.

[136] Hui Yan and Kyle T. Alfriend. Approximate Minimum Energy Control Laws for Low-Thrust Formation Reconfiguration. *Journal of Guidance, Control and Dynamics*, 30(4), July-August 2007.

[137] Hui Yan and Qi Gong. Feedback Control for Formation Flying Maintainence Using State Transition Matrix. *Journal of the Astronautical Sciences*, 59(1-2), June 2012.

[138] Hsi-Han Yeh, Eric Nelson, and Andrew Sparks. Nonlinear Tracking Control for Satellite Formations. *Journal of Guidance, Control and Dynamics*, 25(2):376–386, 2002.

[139] Renato Zanetti. Optimal Glideslope Guidance for Spacecraft Rendezvous. *AIAA Journal of Guidance, Dynamics and Control*, 34(5):1593–1597, 2011.